

**AN IMPLANTABLE NANO-ENABLED BIO-ROBOTIC INTRACRANIAL DEVICE
FOR TARGETED AND PROLONGED DRUG DELIVERY**

Maluta Steven Mufamadi



A thesis submitted to the Faculty of Health Sciences, University of the
Witwatersrand,
in fulfillment of the requirements for the degree of
Doctor of Philosophy

Supervisors

Professor Viness Pillay

University of the Witwatersrand, Department of Pharmacy and Pharmacology,
Johannesburg, South Africa

Co-Supervisors

Prof. Girish Modi

University of the Witwatersrand, Department of Neurosciences, Johannesburg,
South Africa

Dr Dinesh Naidoo

University of the Witwatersrand, Department of Neurosciences, Johannesburg,
South Africa

Prof Sunny E. Iyuke

School of Chemical and Metallurgical Engineering Johannesburg, South Africa

DECLARATION

I, Maluta Steven Mufamadi declare that this thesis is my own work. It has being submitted for the degree of Doctor of Philosophy in the Faculty of Health Sciences at the University of the Witwatersrand, Johannesburg, South Africa. It has not been submitted before for any degree or examination at this or any other University.

.....

Signature

This day of

RESEARCH PUBLICATIONS ARISING FROM THIS WORK

1. Ligand-functionalized nanoliposomes for targeted delivery of galantamine. Maluta S. Mufamadi, Yahya E. Choonara, Pradeep Kumar, Girish Modi, Dinesh Naidoo, Sanday van Vuuren, Valence MK Ndesendo, Lisa C. du Toit, Sunny E. Iyuke, Viness Pillay. *International Journal of Pharmaceutics*, 2013, 448:267-281.
2. Effect of surface-engineered nanoliposomes by chelating ligands on modulation of neurotoxicity associated with β -amyloid aggregates of Alzheimer disease. Maluta S. Mufamadi, Yahya E. Choonara, Pradeep Kumar, Girish Modi, Dinesh Naidoo, Valence M. K. Ndesendo, Lisa C. Du Toit and Viness Pillay. *Journal of Pharmaceutical Research*, 2012, 29 (11): 3075-3089.
3. Design, biomolecular modeling and evaluation of surface-engineered nanoliposomes for the management of Alzheimer's disease. M.S. Mufamadi, Y.E. Choonara, L.C. du Toit, G. Modi, D. Naidoo, P. Kumar, V.M.K. Ndesendo, L. Meyer, S.E. Iyuke, V. Pillay. *European Journal of Neurology* 2012, 19 (Supplement 1), 90-457, Neurotoxicology.
4. Exploration of a composite nano-medical device for the delivery of neuroprotectant- nanocarriers into targeted neuronal cells of Alzheimer's disease. M.S. Mufamadi, Y.E. Choonara, L.C. du Toit, G. Modi, D. Naidoo, P. Kumar, V.M.K. Ndesendo, L. Meyer, S.E. Iyuke, V. Pillay. *European Journal of Neurology* 2012, 19 (Supplement 1), 90-457, Ageing and Dementia.

5. Physicomechanical transitions of an implantable nano-enabled Bio-robotic Intracranial Device for Alzheimers disease management for validation of *in vivo* behavior in a simulated brain environment. M.S. Mufamadi, Y.E. Choonara, L.C. du Toit, G. Modi, D. Naidoo, P. Kumar, V.M.K. Ndesendo, L. Meyer, S.E. Iyuke, V. Pillay. European Journal of Neurology 19 (Supplement X), 66-343, Ageing and Dementia.

6. A review on composite liposomal technologies for specialized drug delivery. Maluta S. Mufamadi, Viness Pillay, Yahya E. Choonara, Lisa C. Du Toit, Girish Modi, Dinesh Naidoo and Valence M. K. Ndesendo. Journal of Drug Delivery doi:10.1155/2011/939851

7. Biomedical Imaging and mechanical dynamics validated the physicochemical properties of the Bio-Robotic Intracranial Device *in vitro*. Maluta S. Mufamadi, Yahya E. Choonara, Lisa C. du Toit, Pradeep Kumar, Girish Modi, Dinesh Naidoo, Clement Penny, Sunny E. Iyuke, Viness Pillay. Submitted to AAPs PharmSciTech.

8. Bio-Construction of an Implantable Nano-Enabled Bio-Robotic Intracranial Device for Advanced Delivery Galantamine into CNS. Maluta S. Mufamadi, Yahya E. Choonara, Lisa C. du Toit, Pradeep Kumar, Girish Modi, Dinesh Naidoo, Clement Penny, Sunny E. Iyuke, Viness Pillay. Submitted to Journal of Pharmaceutical Sciences.

RESEARCH PRESENTATIONS ARISING FROM THIS WORK

1. Maluta S. Mufamadi, Yahya E. Choonara, Girish Modi, Dinesh Naidoo, Lisa C. du Toit, Sunny E. Iyuke, Viness Pillay. An Implantable composite intracranial device for prolong delivery of liposomal nanomedicine into the brain. Medical Research Council (MRC) Early Career Scientist Convention, Parow, Medical Campus, Cape Town, October 23, 2014.
2. Maluta S. Mufamadi, Yahya E. Choonara, Lisa C. du Toit, Girish Modi, Dinesh Naidoo, Pradeep Kumar, Valence M.K. Ndesendo, Leith C.R Meyer, Sunny E. Iyuke, Viness Pillay. Bio-construction of composite intracranial device for prolonged delivery of liposomal nanomedicine into the brain. MRC Early Career Scientist Convention, Parow, Medical Campus, Cape Town, October 16, 2013.
3. Maluta Steven Mufamadi, Kewei Yang, Roman Ott, Andress Fisch, Bernd Riebesehl, Harry Tiemessen. Microfluidic technology for manufacturing of stealth liposomal nanomedicine. Novartis Next Generation Scientist Research day, D&I Development and NIBR, Basel, Switzerland, August 27, 2013.
4. Maluta S. Mufamadi, Yahya E. Choonara, Lisa C. du Toit, Girish Modi, Dinesh Naidoo, Pradeep Kumar, Valence M.K. Ndesendo, Leith C.R Meyer, Sunny E. Iyuke, Viness Pillay. Exploration of a composite nano-medical device for the delivery of neuroprotectant-nanocarriers into targeted neuronal cells of Alzheimer's disease. 16th Congress of the European Federation of

Neurological Societies (EFNS), Ageing and Dementia, Stockholm, Sweden, Europe, September 08 - 11, 2012.

5. Maluta S. Mufamadi, Yahya E. Choonara, Lisa C. du Toit, Girish Modi, Dinesh Naidoo, Pradeep Kumar, Valence M.K. Ndesendo, Leith C.R Meyer, Sunny E. Iyuke, Viness Pillay. Exploration of a composite nano-medical device for the delivery of neuroprotectant-nanocarriers into targeted neuronal cells of Alzheimer's disease. 16th Congress of the European Federation of Neurological Societies (EFNS), Ageing and Dementia, Stockholm, Sweden, Europe, September 08 - 11, 2012 (e-poster).
6. Maluta S. Mufamadi, Yahya E. Choonara, Lisa C. du Toit, Girish Modi, Dinesh Naidoo, Pradeep Kumar, Valence M.K. Ndesendo, Leith C.R Meyer, Sunny E. Iyuke, Viness Pillay. Design, biomolecular modeling and evaluation of surface-engineered nanoliposomes for the management of Alzheimer's disease. 16th Congress of the European Federation of Neurological Societies (EFNS), Neurotoxicology/Occupational Neurology, Stockholm, Sweden, Europe, September 08 - 11, 2012.
7. Maluta S. Mufamadi, Yahya E. Choonara, Lisa C. du Toit, Girish Modi, Dinesh Naidoo, Pradeep Kumar, Valence M.K. Ndesendo, Leith C.R Meyer, Sunny E. Iyuke, Viness Pillay. Physicomechanical transitions of an implantable nano-enabled Bio-robotic Intracranial Device for Alzheimers disease management for validation of *in vivo* behavior in a simulated brain environment.16th

Congress of the European Federation of Neurological Societies (EFNS), Ageing and Dementia, Stockholm, Sweden, Europe, September 08-11, 2012.

8. Maluta S. Mufamadi, Yahya E. Choonara, Lisa C. du Toit, Girish Modi, Dinesh Naidoo, Pradeep Kumar, Valence M.K. Ndesendo, Sunny E. Iyuke, Viness Pillay. Bio-Architecture of an implantable nano-enabled Bio-robotic Intracranial Device for optimized CNS drug delivery. Wits Faculty of Health Sciences Research Day & Postgraduate Expo 2012. Wits Medical School, Parktown, JHB, South African. September 19, 2012.
9. Maluta Steven Mufamadi, Viness Pillay, Yahya E. Choonara, Lisa C. Du Toit, Girish Modi, Dinesh Naidoo. Elucidation of the cytotoxicity and intracellular uptake of surface modified nanoliposomes by chelating ligands. Annual Meeting of the American Association of Pharmaceutical Scientists, Washington DC, United States of America, October 23-27, 2011.
10. Maluta Steven Mufamadi, Viness Pillay, Yahya E. Choonara, Lisa C. Du Toit, Girish Modi, Dinesh Naidoo. Surface-modified nanoliposomes by chelating ligands to modulate neurotoxicity associated with β -amyloid aggregation in Alzheimer's disease. Annual Meeting of the American Association of Pharmaceutical Scientists (AAPS), Washington DC, United States of America, October 23-27, 2011.
11. Maluta Steven Mufamadi, Viness Pillay, Yahya E. Choonara, Lisa C. Du Toit, Girish Modi, Dinesh Naidoo. Fabrication and characterization of an

implantable nano-enabled Bio-robotic Intracranial Device for enhanced drug delivery into targeted neuronal cells of Alzheimer's disease. Annual Meeting of the American Association of Pharmaceutical Scientists, Washington DC, United States of America, October 23-27, 2011.

12. Maluta Steven Mufamadi, Viness Pillay, Yahya E. Choonara, Lisa C. Du Toit, Girish Modi, Dinesh Naidoo. Development of functionalized nanoliposomes using a box-menken experimental design to validate improvement of galantamine uptake by neuronal cells. Annual Meeting of the American Association of Pharmaceutical Scientists, Washington DC, United States of America, October 23-27, 2011.
13. Maluta Steven Mufamadi, Viness Pillay, Yahya E. Choonara, Lisa C. Du Toit, Girish Modi, Dinesh Naidoo. Formulation and physicochemical characterization of surface-modified nanoliposomes by chelating ligands. Annual Meeting of the American Association of Pharmaceutical Scientists, Washington DC, United States of America, October 23-27, 2011.
14. Maluta Steven Mufamadi, Viness Pillay, Yahya E. Choonara, Lisa C. Du Toit, Girish Modi, Dinesh Naidoo. An implantable nano-enabled Bio-robotic Intracranial Device for neurotherapeutic applications. 6th International Conference of South African Pharmaceutical and Pharmacological Sciences Society (ICPPS), ICPPS, University of KZN, South Africa, September 25-27, 2011.

15. Maluta Steven Mufamadi, Viness Pillay, Yahya E. Choonara, Lisa C. Du Toit, Girish Modi, Dinesh Naidoo. Application of ligand-functionalize nanoliposomes to reduce the neurotoxicity associated with β -amyloid aggregation in Alzheimer's disease. 6th International Conference of South African Pharmaceutical and Pharmacological Sciences Society (ICPPS), ICPPS, University of KZN, South Africa, September 25-27, 2011.

16. Maluta Steven Mufamadi, Viness Pillay, Yahya E. Choonara, Lisa C. Du Toit, Girish Modi, Dinesh Naidoo. Design of an implantable nano-enabled Bio-Robotic Intracranial Device as a new approach to improve drug delivery for Alzheimer's patients. 2nd Annual Alzheimer's One-Day Seminar "Making it real: Living with Alzheimer's", University of Witwatersrand, Parktown, Johannesburg, September 1st, 2011.

17. Maluta Steven Mufamadi, Viness Pillay, Yahya E. Choonara, Lisa C. Du Toit, Girish Modi, Dinesh Naidoo. An implantable nano-enabled Bio-Robotic Intracranial Device for the delivery of antiaging drug in Alzheimer's disease. 3rd Biennial Research Day. The School of Therapeutic Sciences, University of Witwatersrand, Parktown, Johannesburg, August 24, 2011.

ABSTRACT

Alzheimer's disease (AD) is the most prevalent and progressive neurodegenerative disorder (ND). It is characterized by a progressive decline of cognitive function, complete loss of memory, deterioration of visual capacity and the inability to function independently. According to the World Health Organization (WHO) it is estimated that about 26 million people suffer with AD worldwide. Although the etiology of AD is not fully understood, the aggregation of β -amyloid (A) peptides that are associated with the formation of extracellular neurotoxic senile plaques and neurofibrillary tangles comprising hyperphosphorylated tau proteins have been recognized as the primary constituents that play a crucial role in AD. Several potential neurotherapeutic agents that can improve the management of AD such as metal chelators and alkaloid drugs have been approved by the US Food and Drug Administration (FDA) and European Medicines Agency (EMA). Metal chelators [e.g. histidine, Ethylenediaminetetraacetic acid (EDTA) and zinc acetate (ZnAc)] are the main therapy used for modulating A β peptide aggregation with biological metals (such as zinc and copper ions) which is associated with promoting neurotoxicity in AD. While alkaloid drugs, such as donepezil, galantamine and rivastigmine, are used to inhibit the enzyme acetylcholinesterase (AChE); memantine is used to block the N-methyl-D-aspartate (NMDA) receptors associated with pathological activation. Despite the availability of these indispensable drugs, the clinical utility of these drugs is hampered by their poor retention and difficulty in bypassing the highly restrictive Blood Brain Barrier (BBB). Therefore this study aimed at developing novel nanoliposomes (NLPs) surface-engineered with chelating and synthetic peptides that are capable of crossing the BBB thus improving delivery efficacy and modulating the extracellular neurotoxicity associated with β -Amyloid aggregates of AD. Furthermore, since this system was designed for a chronic condition, a temporary depot-based polymeric system was integrated for further enhancement of the liposomal half-life, storage and prolonged drug delivery over a period of 50 days. The surface-engineered NLPs produced were spherical in shape, 100-149 \pm 28nm ~ size, with a zeta potential range of -9.59 to -37.3mV and a polydispersity index (Pdl) of 0.02-0.2. A Box-Behnken experimental design was employed for maximizing the ligand coupling efficiency (40-78%) and drug entrapment efficiency (DEE) that ranged from 42-79%. The optimized peptide-based ligand NLP formulation showed sustained drug release (30% of drug released within 48 hours). Chelating ligands on the surface of NLPs showed 50-68% modulation of neurotoxicity on PC12 neuronal cells induced by ZnA β (1-42) or CuA β (1-42) aggregates. When drug-loaded functionalized NLPs were embedded within the temporal hydrophilic hydrogel network/scaffold as an implantable nano-enabled bio-robotic intracranial device (BICD), the physicochemical and physicochemical dynamics showed improvement of liposomal structure such as the stability, and homogeneity in distribution of the liposomes within the internal core of the hydrogel networks and post-lyophilized scaffold. *In vitro* studies in simulated cerebrospinal fluid (CSF) showed prolonged release behavior of the drug-loaded functionalized NLPs from the BICD with 50-70% released over 50 days. Scanning Electron Microscopy (SEM) and confocal microscopy confirmed intact liposomal structures within the temporal polymeric scaffold/depot post-fixation and post-lyophilization. *Ex vivo* studies confirmed cell proliferation and a low level of lactate dehydrogenase (LDH), which is associated with cell membrane damage/injury, after PC12 neuronal cells were exposed to the BICD. In addition, when PC12 neuronal cells were exposed to the BICD high accumulation of galantamine (GAL) into these PC12 neuronal cells was observed post-cultivation. This outcome indicated that the released drug-loaded functionalized NLPs from the BICD were still in their intact form and capable of serving as bio-robotic markers for the delivery of GAL into the neuronal cells in response to AD. Furthermore, intracellular activity validated that the synthetic peptide has the potency for targeted delivery of the drug-loaded NLPs post-release of the BICD in *ex vivo* studies. Overall, results from this study revealed that the BICD device had superior cytocompatibility and may be suitable for application as a prolonged and targeted delivery system for GAL into neuronal cells to treat AD.

PATENT FILED

1. Microfluidic technology for the manufacture of stealth liposomal nanomedicines. *Inventors:* Maluta Steven Mufamadi, Kewei Yang, Roman Ott, Andreas Fisch, Bernd Riebesehl, Harry Tiemessen. Patent Application Filed: Novartis Patent Application date, 20 August 2013, Novartis Pharma AG, Basel, Switzerland.
2. An implantable device for targeted and prolonged drug delivery. *Inventors:* Maluta Steven Mufamadi, Viness Pillay, Yahya E. Choonara, Girish Modi, Dinesh Naidoo and Lisa C. du Toit. Patent Application Filed: SA Patent Application Number 2010/07276, 12 October 2010.
3. A Drug Delivery Device. *Inventors:* Thiresen Govender, Viness Pillay, Yahya Essop Choonara, Lisa Claire du Toit, Girish Modi, Dinesh Naidoo, Maluta Steven Mufamadi. Patent Application Filed: World Intellectual Property Organization, International Application No. PCT/IB2011/055345. 2012.

RESEARCH ACCOLADES

1. Novartis Internship, Next Generation Scientists Program.

Diversity and Inclusion Development and NIBR, Basel, Switzerland, 1 June-August 31, 2013. Microfluidic technology for manufacturing of stealth liposomal nanomedicine.

2. Best Research Paper Publication Award for Pharmaceuticals.

Academy of Pharmaceutical Sciences Conference, Cape Town, 4-6 October 2013. Effect of Surface-Engineered Nanoliposomes by Chelating Ligands on Modulation of Neurotoxicity Associated with β -amyloid Aggregates of Alzheimer Disease. Maluta S. Mufamadi, Yahya E. Choonara, Pradeep Kumar, Girish Modi, Dinesh Naidoo, Valence M. K. Ndesendo, Lisa C. Du Toit and Viness Pillay. Journal of Pharmaceutical Research. 2012; 29(11): 3075-3089.

Postgraduates PhD Scholarship Awards

1. National Health Scholar Programme (NHSP), Doctoral Scholarship South Africa, 2013.
2. Technology Innovation Agency (TIA) Doctoral Scholarship grant holder, South Africa, 2012.
3. National Research Foundation (NRF) Scare Skill Doctoral Scholarship, South Africa, 2010-2011.

International Conference Travel Grant Awards

1. Wits University, Faculty of Health Sciences International Conference Travelling Grant to attend 16th Congress of the European Federation of Neurological Societies (EFNS), Ageing and Dementia, Stockholm, Sweden, Europe, September 08 - 11, 2012.
2. Medical Research Council (MRC) of South Africa Travel Grant (Grant Holder) to attend 16th Congress of the European Federation of Neurological Societies

(EFNS), Ageing and Dementia, Stockholm, Sweden, Europe, September 08 - 11, 2012.

3. National Research Foundation (NRF) Scarce Skills Postgraduate Conference Travel Grant to attend Annual Meeting of the American Association of Pharmaceutical Scientists, Washington DC, United States of America, October 23-27, 2011.
4. Wits Health Consortium Postgraduate Conference Travel Grant to attend Annual Meeting of the American Association of Pharmaceutical Scientists, Washington DC, United States of America, October 23-27, 2011.
5. Wits University Postgraduate Conference Travel Grant to Annual Meeting of the American Association of Pharmaceutical Scientists, Washington DC, United States of America, October 23-27, 2011.

ACKNOWLEDGMENTS

First and foremost, I would like to express my deepest gratitude and appreciation to my supervisor Prof. Viness Pillay for believing in me, for his immaculate supervision and guidance throughout this study. I appreciate his devotion in ensuring the successful accomplishment of this research work and for keeping on inspiring me towards academic excellence and maturity. My further gratitude goes toward my co-supervisors, Prof Girish Modi, Prof Yahya Essop Choonara and Prof Sunny E. Iyuke for their merited guidance from the beginning during the build-up of the protocol until completion of the research work. In addition, I would like to acknowledge Prof Girish Modi for providing me with valuable neuropharmaceutical expertise and exceptional advice toward completion of my research papers. I would also like to acknowledge Prof Yahya Essop Choonara for his outstanding contribution, kindness, remarkable advice and encouragement throughout the research work. My gratitude also goes to Dr Lisa Clare Du Toit, Mr. Pradeep Kumar and Dr Valence Ndesendo for their advice and assistance with so much research expertise. Furthermore, my gratitude goes to Prof. Sandy van Vuuren for her advice, for providing valuable cellular expertise, and for providing permission to use one of her laboratory for culturing our neuronal cells. I would also like to thank Mrs. Pam Sharp, Ms. Caroline Lalkhan and Prof. Alexander Ziegler of the Microscopy and Microanalysis Unit of the University of the Witwatersrand for providing technical support towards Electron Microscopy analysis. I take this opportunity to thank Dr. Clement Penny for providing technical support and allowing me to use the Fluorescence Microscopy in his laboratory.

To all support members of staff in our Department of Pharmacy and Pharmacology thanks for their kind assistance, moral support and providing me with all technical support required toward the completion of each experiment until the concluding part of this research work. To all my colleagues in the Wits Advanced Drug Delivery Platform (WADDP) thanks so much for all the support, encouragements and your great endurance on this demanding journey.

To my wife Linda Mufamadi, I do not have enough words to appreciate all the support and encouragement you have offered during this journey. Thank you for having faith in me and for allowing me to nourish my academic dreams. To my mother, Peter, Avhatakali and Greaves Mufamadi (my brothers) and Dr. Abdullah Ely (my friend), thank you for your encouragement and support during this degree, and for always being there for me. I would like to express my deepest gratitude to the financial assistance whom makes this study possible by provide me with the scholarships; National Health Scholar Programme (NHSP), Technology Innovation Agency (TIA), and National Research Foundation (NRF) Scare Skills. Finally, but certainly not the least, I would like to gratefully acknowledge God Almighty, who gave me faith, strength and courage to carry out this study, in Jesus name, amen.

DEDICATION

This thesis is dedicated to my children, Olugaho Makondelele Mutondwa and Kharendwe Munei Mufamadi.

TABLE OF CONTENTS

CHAPTER 1 INTRODUCTION

1.1.	Introduction	1
1.1.1.	Background on Alzheimer's disease	1
1.1.2.	Current neuroprotectants used for the management of Alzheimer's disease	4
1.1.3.	Challenges associated with current neuroprotectant for Alzheimer's disease	5
1.2.	Novel drug delivery systems for the treatment of Alzheimer's disease	5
1.3.	Approaches to the problem	7
1.4.	Aim and Objectives of this research	10
1.5.	Overview of this thesis	12

CHAPTER 2
A LITERATURE REVIEW ON COMPOSITE LIPOSOMAL TECHNOLOGIES FOR
SPECIALIZED DRUG DELIVERY

2.1.	Introduction	16
2.2.	Liposome-based technology	18
2.2.1.	Conventional liposomes	19
2.2.2.	Stealth liposomes	20
2.2.3.	Targeted liposomes	21
2.2.4.	Additional diverse liposomes types	25
2.2.4.1.	Virosomes and stimuli-responsive liposomes	25
2.2.4.2.	Gene-based liposomes	27
2.3.	Temporary depot polymeric-based systems for liposomal coupling	29
2.3.1.	Injectable polymeric scaffolds	30
2.3.2.	Prefabricated polymeric scaffolds	31
2.4.	Natural product-based liposomal drug delivery systems	32
2.4.1.	Collagen-based liposomal drug delivery systems	32
2.4.2.	Gelatin-based liposomal drug delivery systems	35
2.4.3.	Chitosan-based liposomal drug delivery systems	36
2.4.4.	Fibrin-based liposomal drug delivery systems	38
2.4.5.	Alginate-based liposomal drug delivery systems	38
2.4.6.	Dextran-based liposomal drug delivery systems	40
2.5.	Liposomal drug delivery systems based on synthetic polymers	41
2.5.1.	Carbopol-based liposomal drug delivery systems	41
2.5.2.	Polyvinyl alcohol-based liposomal drug delivery systems	42
2.6.	Techniques for embedding drug-loaded liposomes within depot polymeric-based systems	44
2.7.	Modulating drug release from liposomes within polymeric depot systems	46
2.8.	The successes and challenges emerging from composite liposome and polymeric-based technologies	47
2.9.	Future perspective	49

CHAPTER 3
DEVELOPMENT OF SURFACE-ENGINEERED NANOLIPOSOMES FOR
MODULATING THE NEUROTOXICITY ASSOCIATED WITH β AMYLOID
AGGREGATES IN ALZHEIMER'S DISEASE

3.1.	Introduction	51
3.2.	Materials and Methods	54
3.2.1.	Materials	54
3.2.2.	Preparation of the nanoliposomes	55
3.2.3.	Surface modification of the nanoliposomes employing chelating ligands	56
3.2.4.	Evaluation of the conjugation efficiency of chelating ligands on the nanoliposomes surface	57
3.2.5.	Determination of particle size and zeta potential of the modified Nanoliposomes	57
3.2.6.	Chemical structure analysis of the modified chelating ligand-bound nanoliposomes	58
3.2.7.	Evaluation of the surface morphology and architecture of the modified nanoliposomes	58
3.2.7.1.	Scanning Electron Microscopy examination	58
3.2.7.2.	Transmission Electron Microscopy examination	58
3.2.8.	<i>In vitro</i> studies on the formation of $A\beta$ (1-42) aggregates	59
3.2.9.	Assessment of the effect of the modified chelating ligand-bound resolubilization of $A\beta$ (1-42) peptides	59
3.2.10.	PC12 neuronal cells culture studies	60
3.2.10.1.	<i>Ex vivo</i> neurotoxicity assay of metal ions and $A\beta$ 1-40 aggregates	60
3.2.10.2.	Neurotoxicity analysis of the modified chelating ligand-bound nanoliposomes	61
3.2.10.3.	<i>Ex vivo</i> uptake of the modified chelating ligand-bound nanoliposomes by PC12 neuronal cells	61
3.2.11.	Static Lattice Atomistic Simulations	62
3.3.	Results and Discussion	63
3.3.1.	Conjugation efficiency of chelating ligands on the surface of the nanoliposomes	63
3.3.2.	Physicochemical properties of the targeted nanoliposomes	63
3.3.3.	Assessment of the modified nanoliposomes chemical structure variations	65
3.3.4.	Morphological characterization of the modified nanoliposomes	66
3.3.5.	<i>In vitro</i> metals ions and $A\beta$ (1-42) resolubilization assay	67
3.3.6.	<i>Ex vivo</i> neurotoxicity assay of metals ions and $A\beta$ (1-42) aggregates	69
3.3.7.	Effect of modified chelating ligand-bound nanoliposomes on the	

	modulation of neurotoxicity	70
3.3.8.	<i>Ex vivo</i> uptake of modified chelating ligand-bound nanoliposomes	72
3.3.9.	Molecular mechanics energy relationship analysis	75
3.3.10.	Formation of the nanoliposomal system	76
3.3.11.	Energy transformations involving metal binding, aggregation and chelation	78
3.4.	Concluding remarks	80

CHAPTER 4

**FORMULATION OF THE LIGAND-FUNCTIONALIZED NANOLIPOSOMES FOR
TARGETED DELIVERY OF GALANTAMINE IN ALZHEIMER'S DISEASE**

4.1.	Introduction	82
4.2.	Materials and Methods	85
4.2.1.	Materials	85
4.2.2.	Preparation of the nanoliposomes	86
4.2.3.	Optimization of the ligand-functionalized nanoliposomes	86
4.2.4.	Surface-engineering of synthetic peptide ligands onto the nanoliposomes	88
4.2.5.	Determination of the drug entrapment efficiency of the ligand - functionalized nanoliposomes	90
4.2.6.	Physicochemical characterization of the ligand-functionalized nanoliposomes	90
4.2.7.	Analyses of the molecular structural variation due to nanoliposomes formulation	91
4.2.8.	Thermal characterization of the ligand-functionalized nanoliposomes	91
4.2.9.	Particle size and distribution analysis of the ligand-functionalized nanoliposomes	92
4.2.10.	Zeta potential analysis of the ligand-functionalized nanoliposomes	93
4.2.11.	Morphological characterization of the nanoliposomes	93
4.2.12.	Evaluation of the <i>in vitro</i> release of galantamine from the ligand functionalized nanoliposomes	94
4.2.13.	<i>Ex vivo</i> cytotoxicity and cell uptake studies	95
4.2.13.1.	Neuronal cell culture and preservation	95
4.2.13.2.	<i>Ex vivo</i> cytotoxicity assay of the ligand-functionalized nanoliposomes	95
4.2.13.3.	<i>Ex vivo</i> uptake of the ligand-functionalized nanoliposomes	96
4.2.13.4.	Cellular uptake and intracellular localization of the ligand-functionalized nanoliposomes	97
4.2.14.	Static lattice atomistic simulations for polymer-peptide interaction analysis	97
4.3.	Results and Discussion	99
4.3.1.	Characterization of the peptide-based ligand coupled onto the nanoliposomes surface	99
4.3.2.	Assessment of structural variations in the ligand-functionalized nanoliposomes	99
4.3.3.	Drug entrapment efficiency within the ligand-functionalized nanoliposomes	102
4.3.4.	Determination of the particle size distribution and zeta potential	102
4.3.5.	Characterization of the surface morphology of the ligand	

	functionalized nanoliposomes	104
4.3.6.	Thermal behavior of the ligand-functionalized nanoliposomes	106
4.3.7.	<i>In vitro</i> drug release from the ligand-functionalized nanoliposomes	108
4.3.8.	Responses optimization of the galantamine-loaded ligand-functionalized nanoliposomes	111
4.3.9.	<i>Ex vivo</i> analysis of the ligand-functionalized nanoliposomes	113
4.3.9.1.	<i>Ex vivo</i> cytotoxicity assay of the ligand-functionalized nanoliposomes	113
4.3.9.2.	<i>Ex vivo</i> uptake of labeled ligand-functionalized nanoliposomes	114
4.3.10.	Molecular Mechanics Energy Relationship analysis	118
4.3.11.	<i>In silico</i> formation of nanoliposomal system	119
4.3.12.	Investigation of the amphiphilic properties involving polymer peptide aggregation	121
4.4.	Concluding remarks	125

CHAPTER 5
IN VITRO SYNTHESIS AND CHARACTERISATION OF THE CROSS-LINKED
CHITOSAN-EUDRAGIT RSPO-POLYVINYL ALCOHOL HYDROGEL FOR THE
PREPARATION OF THE NANO-ENABLED BIO-ROBOTIC INTRACRANIAL
DEVICE

5.1.	Introduction	127
5.2.	Materials and Methods	131
5.2.1.	Materials	131
5.2.2.	Fabrication of the gas-filled or fluorescence-labeled functionalized nanoliposomes	132
5.2.2.1.	Particle size analysis of gas-filled functionalized nanoliposomes	133
5.2.2.2.	Morphological characterization of the gas-filled functionalized nanoliposomes	133
5.2.2.3.	<i>In vitro</i> investigation of the stability of the gas-filled functionalized nanoliposomes	133
5.2.3.	Synthesis of the cross-linked Chitosan-Eudragit RSPO-Polyvinyl alcohol hydrogel	134
5.2.3.1.	Molecular structural transition of the cross-linked Chitosan-Eudragit RSPO-Polyvinyl alcohol hydrogel	135
5.2.3.2.	Rheological properties of the cross-linked Chitosan-Eudragit RSPO-Polyvinyl alcohol hydrogel	135
5.2.4.	Fabrication of the Bio-Robotic Intracranial Device	136
5.2.4.1.	Ultrasound imaging of the gas-filled functionalized nanoliposomes embedded within the Bio-Robotic Intracranial Device	136
5.2.4.2.	Real-time imaging of fluorescence-labeled functionalized nanoliposomes embedded within a Bio-Robotic Intracranial Device	137
5.2.4.3.	Optical fluorescence microscopy imaging of fluorescence-labeled functionalized nanoliposomes embedded within the Bio-Robotic Intracranial Device	138
5.3.	Results and Discussion	139
5.3.1.	<i>In vitro</i> characterization of the gas-filled functionalized nanoliposomes	139
5.3.1.1.	Determination of the particle size distribution of the gas-filled functionalized nanoliposomes	139
5.3.1.2.	<i>In vitro</i> stability of the gas-filled functionalized nanoliposomes	141
5.3.2.	Physicochemical characterization of the cross-linked Chitosan-Eudragit RSPO-Polyvinyl alcohol hydrogel	143
5.3.2.1.	Molecular structural transition of the cross-linked Chitosan-Eudragit RSPO-Polyvinyl alcohol hydrogel	143

5.3.2.2.	Rheological properties of the cross-linked Chitosan-Eudragit RSPO-Polyvinyl alcohol hydrogel	145
5.3.3.	Characterization of the Bio-Robotic Intracranial Device using imaging system	150
5.3.3.1.	Ultrasound imaging of gas-filled functionalized nanoliposomes embedded within the Bio-Robotic Intracranial Device	150
5.3.3.2.	Fluorescence imaging of the fluorescence-labeled Bio-Robotic Intracranial Device	153
5.4.	Concluding remarks	157

CHAPTER 6
EX VIVO CYTOTOXICITY ANALYSIS OF THE NANO-ENABLED BIO-ROBOTIC INTRACRANIAL DEVICE FOR PROLONGED GALANTAMINE RELEASE

6.1.	Introduction	160
6.2.	Materials and Methods	164
6.2.1.	Materials	164
6.2.2.	Bio-construction of a nano-enabled Bio-Robotic Intracranial Device	164
6.2.3.	Thermal analysis of the cross-linked Chitosan-Eudragit RSPO-Polyvinyl alcohol scaffold	165
6.2.3.1.	Differential Scanning Calorimetry of the cross-linked Chitosan-Eudragit RSPO-Polyvinyl alcohol scaffold	165
6.2.3.2.	Thermogravimetric analysis of the cross-linked Chitosan-Eudragit RSPO-Polyvinyl alcohol scaffold	166
6.2.4.	Surface morphological characterization of the cross-linked Chitosan-Eudragit RSPO-Polyvinyl alcohol scaffold	166
6.2.5.	Physicomechanical characterization of the cross-linked Chitosan-Eudragit RSPO-Polyvinyl alcohol	167
6.2.5.1.	Textural analysis of the cross-linked Chitosan-Eudragit RSPO-Polyvinyl alcohol scaffold	168
6.2.5.2.	Determination of the water content in cross-linked Chitosan-Eudragit RSPO-Polyvinyl alcohol scaffold	169
6.2.5.3.	Hydration study of the cross-linked Chitosan-Eudragit RSPO-Polyvinyl alcohol scaffold	169
6.2.5.4.	Swelling characteristics of cross-linked Chitosan-Eudragit RSPO-Polyvinyl alcohol scaffold	169
6.2.5.5.	Matrix erosion of the cross-linked Chitosan-Eudragit RSPO-Polyvinyl alcohol scaffold	170
6.2.6.	Morphology and structure characterization of the Bio-Robotic Intracranial Device	170
6.2.7.	<i>In vitro</i> release drug-loaded functionalized nanoliposomes from Bio-Robotic Intracranial Device	171
6.2.8.	<i>Ex vivo</i> characterization of the Bio-Robotic Intracranial Device	172
6.2.8.1.	Cell Seeding on the Bio-Robotic Intracranial Device	172
6.2.8.2.	Morphological characterization of the Bio-Robotic Intracranial Device seeded with PC12 neuronal cells	172
6.2.8.3.	Cytocompatibility of the Bio-Robotic Intracranial Device in the PC12 Neuronal cells	173
6.2.8.4.	Cell uptake of the FTIC-labeled functionalized nanoliposomes post release from the Bio-Robotic Intracranial Device	174

6.3.	Results and Discussion	175
6.3.1.	Thermal properties of the cross-linked Chitosan-Eudragit RSPO-Polyvinyl alcohol scaffold	175
6.3.1.1.	Differential Scanning Calorimetry analysis of the cross-linked Chitosan-Eudragit RSPO-Polyvinyl alcohol scaffold	175
6.3.1.2.	Thermogravimetric analysis of the cross-linked Chitosan-Eudragit RSPO-Polyvinyl alcohol scaffold	176
6.3.2.	Surface morphology of the cross-linked Chitosan-Eudragit RSPO-Polyvinyl alcohol scaffold	180
6.3.3.	Physicochemical and physicomechanical characterization of the cross-linked Chitosan-Eudragit RSPO-Polyvinyl alcohol scaffold	182
6.3.3.1.	Textural properties of the cross-linked Chitosan-Eudragit RSPO-Polyvinyl alcohol scaffold	183
6.3.3.2.	Water contents in lyophilized cross-linked Chitosan-Eudragit RSPO-Polyvinyl alcohol scaffold	185
6.3.3.3.	Magnetic Resonance Imaging and swelling characteristics of the cross-linked Chitosan-Eudragit RSPO-Polyvinyl alcohol scaffold	185
6.3.3.4.	Matrix erosion of the Chitosan-Eudragit RSPO-Polyvinyl alcohol scaffold	187
6.3.4.	Morphology characterization of the Bio-Robotic Intracranial Device	188
6.3.5.	<i>In vitro</i> drug release from functionalized nanoliposomes post-embedded from the Bio-Robotic Intracranial Device	189
6.3.6.	<i>Ex vivo</i> characterization of the Bio-Robotic Intracranial Device	193
6.3.6.1.	Morphology characterization of the PC12 neuronal cells seeded on the surface of the Bio-Robotic Intracranial Device	193
6.3.6.2.	Cytocompatibility of the Bio-Robotic Intracranial Device in the PC12 neuronal cells	195
6.3.6.3.	<i>Ex vivo</i> uptake of the drug-loaded functionalized nanoliposomes post-embedded within Bio-Robotic Intracranial Device	197
6.4.	Concluding remarks	199

CHAPTER 7
IN VIVO DEVELOPMENT OF THE PRE-CLINICAL MODEL FOR ALZHEIMER'S
DISEASE USING NON-TRANSGENIC SPRAGUE DAWLEY RATS FOR THE
ASSESSMENT OF THE BICD PERFORMANCE

7.1.	Introduction	201
7.2.	Materials and Methods	203
7.2.1.	Sprague Dawley rats and husbandry	203
7.2.2.	Preparation of aggregated A β (25-35) peptide and microscopy characterization	203
7.2.3.	Experimental design of non-transgenic rat model of Alzheimer's Disease	204
7.2.3.1.	Intra-Cisterna Magna administration of aggregated A β (25-35) peptide	205
7.2.3.2.	Euthanasia and brain tissue collection	205
7.2.3.3.	Histopathology of brain tissues	205
7.2.3.4.	Histochemical stains on the brain section	206
7.3.	Results and Discussion	207
7.3.1.	<i>In vitro</i> characterization of aggregation and fibril morphology of the peptide	207
7.3.1.1.	Morphological examination by Transmission Electron Microscopy	207
7.3.1.2.	Morphological examination by Fluorescence microscopy	208
7.3.2.	Brain tissues for paraffin wax embedding and mounting	209
7.3.3.	Histopathology examinations	209
7.3.4.	Amyloid deposits formations	213
7.3.4.1.	Thioflavin stain	213
7.3.4.2.	Congo Red stain	214
7.4.	Conclusions and remarks	216

CHAPTER 8
CONCLUSION AND RECOMMENDATIONS

8.1.	Conclusions	218
8.2.	Recommendations	220
	REFERENCES	223
	APPENDICES	266
	A: Research publications	266
	B: Conference abstracts presented	274
	C: Patent publications	289
	D: University of the Witwatersrand Animal Ethics Screening Committee Clearance certificate	290
	E: Certificate to confirm the Novartis Next Generation Scientist Program Completion	292

LIST OF FIGURES

Figure 1.1:	Possible aetiology associated with AD; a) extra-cellular β -amyloid ($A\beta$) plaques, b) β -amyloid aggregation with a biological ions and c) intracellular neurofibrillary tangles	3
Figure 1.2:	The structure of donepezil, rivastigmine, galantamine and Memantine, being the drugs for treating AD conditions	4
Figure 2.1:	Schematic representation of liposome-based systems (adapted from Zucker et al., 2009)	24
Figure 2.2:	Schematic depicting of stealth PEGylated liposome (Adapted from Ray et al., 2008)	26
Figure 2.3:	A schematic representation of the targeted liposome delivery system depicting the cyclic RGD peptides that targets the $\alpha v \beta 3$ integrin receptors on the vascular tumor cells (adapted from Nallamotheu et al., 2006)	26
Figure 2.4:	A schematic representation of a virosome (source: Pevion Biotech Ltd., 2010)	28
Figure 2.5:	A schematic representation of a DNA-liposome complex (adapted from Uchegbu. 1999)	28
Figure 2.6:	A schematic depicting the optimization of liposomal gene delivery (adapted from Uchegbu. 1999)	29
Figure 2.7:	Schematic depicting drug delivery from pre-encapsulated drug loaded liposomes incorporated within an injectable hydrogel based system (adapted from Ta et al., 2008)	32
Figure 2.8:	Schematic depicting drug delivery from fabricated polymeric based depot system incorporated within drug-loaded liposomes, with eventual entry through a cell membrane (adapted from Stenekes et al., 2000)	34
Figure 2.9:	A schematic representation of a collagen-based liposome (adapted from Kang et al., 2010)	34
Figure 3.1:	FTIR spectra of (a) native CuAc, ZnAc, histidine and EDTA and (b) unmodified NLPs and surface-modified NLPs with histidine, ZnAc, EDTA and CuAc	66
Figure 3.2:	TEM micrographs of a) unmodified NLPs and modified NLPs with b) ZnAc, c) CuAc, d) histidine and e) EDTA	67

Figure 3.3:	Typical SEM image of the modified NLPs synthesized	67
Figure 3.4:	Resolubilization of (a) ZnA β (1-42) aggregates and (b) Cu A β (1-42) aggregates by modified NLPs	69
Figure 3.5:	Effect of ZnA β (1-42) and CuA β (1-42) aggregates on cell viability,(b) effect of the modified NLPs on reversing neurotoxicity of ZnA β (1-42) aggregates and (c) effect of the modified NLPs on neurotoxicity induced by CuA β (1-42) aggregates	72
Figure 3.6:	Cellular uptake profiles of modified NLPs in the presence of (a) Cu(II) ions and (b) Zn(II) ions	73
Figure 3.7:	Light and fluorescent microscopy analysis of PC12 cell line incubated in for 24 h (a) with labeled FITC or rhodamine NLPs; (b) surface engineered with CuAc; (c) surface engineered ZnAc, (d) surface engineered EDTA and (e) surface engineered Histidine	75
Figure 3.8:	Visualization of (a) geometrical preferences (color codes: C (cyan),O (red), N (blue), P (yellow) and H (white); and (b) Connolly molecular electrostatic potential surfaces (color codes: DSPE-PEG (yellow), DSPC (blue) and CHOL (red)) in translucent display mode showcasing the nanoliposomal after molecular simulation in vacuum	77
Figure 3.9:	Visualization of geometrical preferences of (a) A β (10-21)-Cu (II) and (b) A β (10-21)-Cu(II)-EDTA after molecular simulation in vacuum	79
Figure 3.10:	Visualization of geometrical preferences of (a) A β (10-21)-Zn(II) and (b) A β (10-21)-Zn(II)-EDTA after molecular simulation in vacuum	80
Figure 4.1:	Schematic representation of FITC or GAL-loaded ligand functionalized NLPs showing; a) drug-loaded NLPs, b) GAL-loaded functionalized NLPs with ligand 1, c) ligand 2 and d) ligand 3	89
Figure 4.2:	Typical FTIR profiles of the NLPs showing; a) native NLPs, b) GAL-loaded NLPs and c) GAL loaded ligand-functionalized NLPs	101
Figure 4.3:	Typical physical profile distributions showing; a) average particle size and b) zeta potential distributions of the GAL-loaded ligand functionalized NLPs	105
Figure 4.4:	Darkfield (1) and brightfield (2) TEM micrographs of NLPs showing a1-a2) native NLPs, b1-b2) GAL-loaded NLPs and	

	c1-b2) GAL-loaded ligand-functionalized NLPs	106
Figure 4.5:	TMDSC profiles for the NLPs showing; a) native NLPs, b) GAL-loaded NLPs and c) GAL-loaded ligand functionalized NLPs	108
Figure 4.6:	Drug release profiles obtained from the ligand-functionalized NLPs formulated as per the Box-Behnken design template showing a) formulation 1-5, b) formulations 6-10 and c) formulations 1-15 in PBS (pH7.4; 37°C) over 48 hours	110
Figure 4.7:	Desirability plots obtained for the optimized ligand functionalized NLPs at each response	112
Figure 4.8:	Drug release profile obtained for the optimized ligand functionalized NLPs formulation in PBS (pH7.4; 37°C) over 48 hours	113
Figure 4.9:	Cytotoxicity profiles showing a) native ligands (1, 2 and 3) and b) non functionalized as well as functionalized NLPs (functionalized formulations R1-R4, respectively)	116
Figure 4.10:	<i>Ex vivo</i> PC12 neuronal cells uptake of the ligand-functionalized NLPs with a) non-functionalized NLPs (R1) and R2-R4 coupled with 1mg/mL peptide, b) R2-R4 coupled with 10mg/mL peptide and c) GAL uptake by PC12 neuronal cells (R1-R4) after 24 hours of incubation	117
Figure 4.11:	Confocal microscopy images representing the population of fluorescence PC12 neuronal cells associated with uptake of the NLPs with (A) 2D images: 1a) R1, 2a) R2, 3a) R3 and 4a) R4 and histograms 1b) R1, 2b) R2, 3c) R3, and 4d) R4; (B) Pseudo3D images of the topographical view of cells and its fluorescence intensity and distribution after treatment with 1) non functionalized NLPs and 2) ligand-functionalized NLPs and (C) SEM image exhibiting the cell surface morphology	118
Figure 4.12:	Visualization of geometrical preferences of a DSPE molecule in complexation with the ligands showing a) ligand 1, b) ligand 2 and c) ligand 3 after molecular simulations in vacuum	124
Figure 4.13:	Visualization of geometrical preferences showing a) DSPE, b) DSPE-ligand 1, c) DSPE-ligand 2, and d) DSPE-ligand 3 after molecular simulation in a solvated system consisting of 200 H ₂ O molecules	125
Figure 5.1:	Schematic demonstrating ultrasound imaging analysis of the BICD, a) Vevo [®] 2100 Visual Sonics instrument; b1) EcoGel 100 [™] , b2) latter device; and b3) transducer array on top of EcoGel 100 [™] and BICD	137

Figure 5.2:	Schematic demonstrating detection of the labeled-BICD employing Cell-viZio™ imaging analysis connected with optical proflex™ fiber probe	138
Figure 5.3:	Physicochemical characterization of the functionalized NLPs, a typical a) particle size, b) zeta potential, and c) TEM micrographs, c1) 10x, c2) 50x magnification	140
Figure 5.4:	Transmission and backscattering images of the functionalized NLPs obtained using Turbiscan LAb spectra post samples scanned at $\lambda=880\text{nm}$ every 5 minutes for an hour, a) MLVs b), native NLPs and c) gas-filled functionalized NLPs	142
Figure 5.5:	FTIR spectra of the cross-linked CEP hydrogels; a) cross-linked CEP hydrogel fabricated from, native polymers; CHT, 2) EU, 3) PVA and 4) CHT-EU-PVA-GA, b) CEP hydrogel fabricated by the native polymers: 1) CHT, 2) EU, 3) PEO and (4) CHT-EU-PEO-GA	145
Figure 5.6:	Flow behaviour of CEP hydrogel (F1-6) and BICD. a) F1-3, b) F4-6, c) non-cross-linked and cross-linked CEP hydrogel, d) typical cross-linked CEP hydrogel and BICD	147
Figure 5.7:	Viscoelastic moduli (G' and G'') and complex viscosity of formulation a) F1-3 and F4-6 at 37°C	150
Figure 5.8:	Ultrasound images of the gas-filled functionalized NLPs embedded within the BICD, a) native CEP hydrogel; b) CEP hydrogel induced inter-bubbles, c) SF6-filled native NLPs d) SF6-filled functionalized NLPs	152
Figure 5.9:	Ultrasound images of the gas-filled functionalized NLPs embedded within the BICD employing different loading techniques: a) loading into CEP hydrogel prior to cross-linking; b) loading post cross-linked and c) loading using 1mL syringe injection	152
Figure 5.10:	Typical ultrasound images of SF6-functionalized NLPs post embedded within CEP hydrogels fabricated out of different polymeric components. Cross-linked CEP hydrogels a) CHT-EU-PVA-GA and b) CHT-EU-PEO-GA	153
Figure 5.11:	Cell-viZio images of FITC-labeled functionalized NLPs distribution within the CEP hydrogels of the BICD. a) FITC-labeled functionalized NLPs b) FITC-labeled and gas-filled functionalized NLPs within the cross-linked CEP hydrogel (CHT-EU-PVA-GA) and c) FITC-labeled functionalized NLPs, d) FITC-labeled and gas-filled functionalized NLPs within the cross-linked CEP scaffold (CHT-EU-PEO-GA).	155

Figure 5.12: Typical Cell-viZio profiles of the double fluorescence-labeled BICD. a) Control cross-linked CEP hydrogel (unlabeled), b) cross-linked CEP hydrogel stained with DAPI or trypan blue, and c) double fluorescence-labeled BICD	156
Figure 5.13: Typical fluorescence images of the BICD. a1-3) rhodamine, b) FITC-labeled functionalized NLPs and c) cross-linked CEP hydrogel stained with DAPI or trypan blue	157
Figure 6.1: DSC profiles of the CEP scaffold; native a) CHT, b) EU, and c) PVA, d) non-cross-linked CEP scaffold and e) cross-linked CEP scaffold	176
Figure 6.2: TGA thermographs of the cross-linked CEP scaffold; native a) CHT, b) EU and c) PVA, and d) cross-linked CEP scaffold	179
Figure 6.3: SEM micrograph of the CEP scaffolds, a1-2) (F1), b1 2) F2, c1-2) F3, d1-2) scaffold edge and e1-2) magnified view of a pore of the CEP scaffold magnification 450-1000x	182
Figure 6.4: Typical Isothermal linear plot of the CEP scaffold	182
Figure 6.5: Typical textual profiles of the cross-linked CEP scaffold; a) deformation energy, b) matrix resilience and c) matrix hardness	184
Figure 6.6: Swelling profiles of the CEP scaffold (F1-F3) in sCSF condition over 24 hours; a) non-cross-linked CEP scaffold, b) cross-linked CEP scaffold, c) CEP scaffold outside hydration medium, d) 30 minutes, e) 12 and f) 24 hours inside hydration medium	187
Figure 6.7: Weight loss profiles of the CEP scaffold (F1-F3) in sCSF condition over 24 hour; a) non-cross-linked CEP scaffold and b) cross-linked CEP scaffold	188
Figure 6.8: Typical SEM micrographs and fluorescence images of the BICD a1-2) drug-loaded functionalized NLPs post embedded within the BICD at 40x magnification, b) high magnification 50x and c) fluorescence images of the control unlabeled CEP scaffold and d) rhodamine-labeled functionalized NLPs within the surface and deeper region of the BICD	189
Figure 6.9: <i>In vitro</i> drug release from the functionalized NLPs post embedded within the CEP scaffold of the BICD over 50 days in a sCSF, a), BICD formulations, D1, b) D2) and c) D3 (with non-cross-linked and cross-linked CEP)	192
Figure 6.10: Typical drug-loaded functionalized NLPs profile showing (a)	

particle size (nm) and b) zeta potential (mV)	193
Figure 6.11: SEM and stereomicrograph of native CEP scaffold and CEP scaffold (F1-F3) of the BICD post seeded with PC12 neuronal cells at day 28 of <i>ex vivo</i> incubation	195
Figure 6.12: LDH release profiles measured from PC12 neuronal cells treatment with functionalized drug-loaded NLPs, CEP scaffold and BICD	196
Figure 6.13: PC12 neuronal of the drug-loaded functionalized NLPs released post embedded within the BICD (D1, D2 and D3) in cellular environment over 28 days	198
Figure 6.14: Topographical view of fluorescence Pseudo 3D images of the PC12 neuronal cells post exposed with the BICD. Images were acquired at day a) 3, b) 7, c) 14, d) 21 and e) 28 using confocal microscopy	199
Figure 7.1: Schematic diagram representing the study design and number number of Sprague Dawley rats used for the development of a model for AD for preclinical studies	204
Figure 7.2: TEM micrographs of (a) A β (25-35) peptides, b) aggregated A β (25-35) peptides at 1 μ g/ μ l concentration and c) at 3 μ g/ μ l concentration	207
Figure 7.3: Fluorescent microscopy analysis of (a) A β (25-35) peptides, b) aggregated A β (25-35) peptides at 1 μ g/ μ l concentration and c) at 3 μ g/ μ l concentration	208
Figure 7.4: Digital images displayed wax embedded brain tissues sections and mounted section on the glass slide and stained (haematoxylin and eosin, ThT and congo red stain)	210
Figure 7.5: Histological slides of the brain sections of the experimental animals post-ICM injection with aggregated A β (25-35) peptides, a) Cortex, b) Hypocampus, c) Cerebral white matter, d) Pia mater on cerebrum, e) Lat verticle, f) Coroid in vertricle, g) White cerebrum, h) peduncle cerebel, i) Medulla oblongata, j) Cerebellum and l) Cerebel white matter	212
Figure 7.6: Sprague Dawley rats brain sections representing the morphology of the amyloid-like deposits post ThT staining, a1-3) group 1, animals received ICM treatment with 1 μ g/ μ l of the aggregated A β (25-35) peptides, b1-3) group 2, animals received ICM treatment with 3 μ g/ μ l of the aggregated (25-35) peptides and c1-3) control group (3), animals without ICM injection, with magnification x40	214

Figure 7.7: Sprague Dawley rats brain sections representing the morphology of the amyloid-like deposits post ThT staining, a1-3) group 1, animals received ICM treatment with 1µg/µl of the aggregated Aβ(25-35) peptides, b1-3) group 2, animals received ICM treatment with 3µg/µl of the aggregated Aβ(25-35) peptides and c1-3) control group (3), animals without ICM injection

216

LIST OF TABLES

Table 3.1.	Compositions of NLPs formulations with chelating ligand	56
Table 3.2.	Physicochemical characterization of the unmodified and modified NLPs	64
Table 4.1.	Box-Behnken Experimental design template for producing the NLPs with quantity of DSPC, CHOL and DSPE used in the each experimental formulation	87
Table 4.2.	Independent formulation variables and measured responses employed	88
Table 4.3.	TMDSC settings employed for thermal analysis of the NLPs	92
Table 4.4.	Characterization of the 15 formulations generated by the Box-Behnken experimental design	103
Table 4.5.	Particle size distribution, polydispersity index, and zeta potential of the 15 Box-Behnken experimental design formulations evaluated	104
Table 4.6.	Comparative experimental and fitted values of the optimized ligand-functionalized NLPs	112
Table 5.1.	Compositions of CEP hydrogel cross-linked with 5% GA	134
Table 5.2.	The alteration in particle size of the functionalized NLPs following incorporation of various gases	141
Table 6.1.	Composition of the cross-linked CEP scaffolds formulations employing CHT, EU, PVA and GA as cross-linker	165
Table 6.2.	Composition of the different BICD formulations	165
Table 6.3.	Evacuation and heating phase parameters employed during porositometric analysis of the CEP scaffold	167
Table 6.4.	Textural parameters employed for determine CEP scaffold, matrix hardness, deformation energy and matrix resilience	168
Table 6.5.	Decomposition temperature of native polymers (CHT, EU and PVA) components and cross-linked CEP scaffold	179
Table 6.6.	Textural profiles of the dry and hydrated cross-linked CEP scaffold	183

Table 6.7. <i>In vitro</i> release characterization of the BICD formulations	192
Table 7.1. Morphological pathology of the brain tissues of the Sprague Dawley rats post-ICM injection with aggregated A β (25-35) peptides	211

LIST OF ABBREVIATIONS

A β	β -amyloid
ADC	AIDS Dementia Complex
AD	Alzheimer's Disease
APP	A β precursor glycoprotein
ANN	Artificial Neural Networks
BICD	Bio-Robotic Intracranial Device
BBB	Blood-Brain Barrier
BV	blood vessels
CNS	Central Nervous System
CHT	Chitosan
CHOL	Cholesterol
CQ	Clioquinol
CE	Conjugation efficiency
CLSM	Confocal Laser Scanning Microscopy
CuAc	Cacetate
CuCl ₂	Copper chloride
DAPI	4,6-Diamidino-2-phenylindole
DCC	N, N'-dicyclohexylcarbodiimide
DE	Deformation energy
DEE	Drug entrapment efficiency
DLS	Dynamic Light Scattering
DMSO	Dimethylsulfoxide
DOPE	1, 2-dioleoyl- <i>sn</i> glycero-3-phosphoethanolamine
DR	Drug release
DSPC	Distearoyl- <i>sn</i> -glycero-phosphatidylcholine
DSC	Differential scanning calorimetry
DSPE	1,2-distearoyl- <i>sn</i> -glycero-3-phosphatidyl-ethanolamine- methoxypolyethyleneglycol-2000
DT	Decomposition temperature
EDTA	Ethylenediaminetetraacetic acid

EU	Eudragit® RSPO
FDA	USA Food and Drug Administration
FITC	Fluorescein isothiocyanate
FTIR	Fourier Transform Infra-Red
GA	Glutaraldehyde
GAL	Galantamine
G'	Elastic storage
G''	Viscous loss moduli
HIS	Histidine
HLB	Hydrophilic-lipophilic-balance
ICM	Intra-cisterna magna
ICV	Intracerebroventricular
kDa	Kilodaltons
KH ₂ PO ₄	Potassium dihydrogen phosphate
LDH	Lactate dehydrogenase
LM	Leptomeninges
MAN	p-aminophenyl- α -D-manno-pyranoside
MDT	Mean Dissolution Time
MH	Matrix hardness
MMER	Molecular mechanics energy relationship
MR	Matrix resilience
MRI	Magnetic Resonance Imaging
nAChRs	Nicotinic acetylcholine receptors
NaOH	Sodium hydroxide
NDs	Neurodegenerative Disorders
NHS	N-hydroxysulfosuccinimide
NLPs	Nanoliposomes
NP	Neuroparenchyma
PCE	Peptide coupling efficiency
Pdi	Polydispersity index
PD	Parkinson Disease
PEG	Poly (ethylene glycol)
PEO	Polyethylene oxide
PVA	Polyvinyl alcohol

PSD	Particle size distribution
RES	Reticuloendothelial System
sCSF	Simulated cerebrospinal fluid
SEC-R	Serpin enzyme complexes Receptor
SEM	Scanning Electron Microscopy
SF6	Sulfur hexafluoride
TEM	Transmission Electron Microscopy
TF	Transferring
TGA	Thermogravimetric analysis
ThT	Thioflavin T
TMDSC	Temperature Modulated Differential Scanning Calorimetry
WHO	World Health Organization
ZnAc	Zinc acetate
ZnCl ₂	zinc chloride
ZP	zeta potential

CHAPTER 1

BACKGROUND AND RATIONALE FOR THIS RESEARCH

1.1. Introduction

Neurodegenerative Disorders (NDs) are a group of chronic, progressive disorders characterized by the gradual loss of neurons in discrete areas of the Central Nervous System (CNS) (Gao and Hong, 2008). NDs such as Parkinson Disease (PD) and Alzheimer's Disease (AD), CNS neoplasms (brain tumors), and AIDS Dementia Complex (ADC) are still challenging NDs in terms of treatment efficacy (Iversen et al., 1995; Fleming et al., 2005; Fernandes et al., 2007; Riemenschneider and Reifenberger, 2009). The current study focused on advancing the neuroprotection in NDs, specifically in AD.

1.1.1. Background of Alzheimer's disease

AD is the most common disease of the CNS marked by decline in memory and cognitive performance, and defects in visual and motor coordination (Cummings, 2004; Hauptmann et al., 2004). A study by Brookmeyer and co-workers (2007) reported that AD is becoming a significant disease, which is spontaneously affecting many individuals around the world, including in developing countries. AD is declared epidemic with an estimated about 33.9 million people suffering with AD worldwide. In the United States of America alone, about 5.2 million people are living with AD today. According to the World Health Organization (WHO), the prevalence and risk for AD

is reported to be rise up, with estimation that there will be 65,7 million people with AD worldwide by 2030 (Perry, 2008). Since AD is disease of aging, many studies report that the prevalence of AD increases exponentially with aging from 65-100 years, with estimated incidence rates as follows: 0.4-2% in people aged between 65-69 years, 10-12% in people aged around 90 years old and about 40% of those over age 100 years (Barnes and Yaffe, 2011; Corrada et al., 2011).

Although the etiology of AD is not fully understood, AD is still the most common form of dementia. The disease is characterized by an accumulation of extra-cellular β -amyloid ($A\beta$) plaques and intracellular neurofibrillary tangles composed of tau amyloid fibrils (Kowalska., 2004). On one hand, there is considerable evidence that the $A\beta$ peptide has to undergo a process of polymerization in order to produce neurotoxic forms of amyloid (Selkoe, 1994; Selkoe, 2002). In the case of $A\beta$ plaques, many studies evidently reported that senile plaques are caused by 40 or 42 amino acid peptides which are generated by the proteolytic cleavage (β and γ secretase enzymes) of the $A\beta$ precursor glycoprotein (APP) (Figure 1.1a). These $A\beta$ peptides are known to act as a pathogenic seed for $A\beta$ aggregation and amyloid plaque formation because they are more hydrophobic compared to the shorter amyloid peptides (De Strooper and Annaert, 2000). On the other hand, there is considerable evidence that the extracellular soluble $A\beta$ peptide has to undergo a process of aggregation with biological metals ions (such as zinc and copper ions) in order to form insoluble $A\beta$ peptide, which is substantiated to promote neurotoxic $A\beta$ peptide forms of plaques in AD (Figure 1.1b) (Daxiong et al., 2008). In the case of intracellular neurofibrillary tangles, many studies also evidently reported that amyloid fibrils are formed when the tau protein (which is composed of a microtubule

structure) beginnings to become unstable and their filamentous start to aggregate in a principal component of paired helical filaments (Figure 1c) (Goebert and Crowther, 1991).

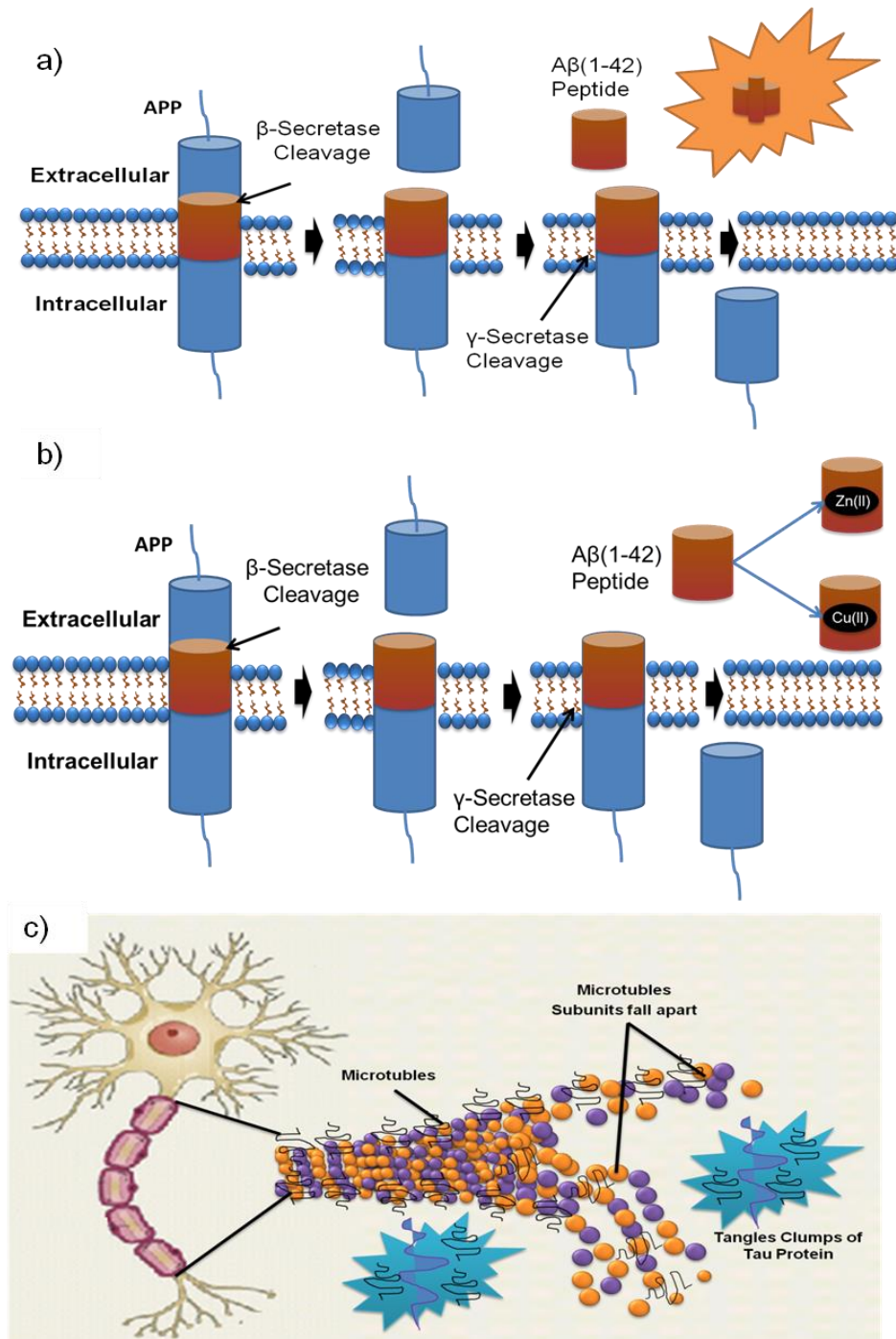


Figure 1.1: Possible etiology associated with AD; a) extra-cellular β -amyloid ($A\beta$) plaques, b) β -amyloid aggregation with biological ions, and c) intraneuronal neurofibrillary tangles (Goebert and Crowther, 1991; Kowalska, 2004; Daxiong et al., 2008).

1.1.2. Current neuroprotectants used for the management of Alzheimer's disease

The cholinesterase inhibitors (ChEIs) such as donepezil, rivastigmine and galantamine (GAL) are first-line neuroprotectants for the management of AD (Masuda, 2004). Donepezil, rivastigmine and GAL are selected as drugs of choice based on their capability to inhibit acetylcholinesterase whereas rivastigmine inhibits the enzyme butyrylcholinesterase (Stahl, 2000). Another added neuroprotectant for AD is memantine that acts as N-methyl-D-aspartate (NMDA) receptor antagonist by blocking the pathological activation (Danysz and Parsons, 2003) (Figure 1.2). The evidence suggests that the NMDA receptor is induced by excessively high synaptic levels of glutamate (Reisberg et al., 2003; Lipton, 2005). A recent study demonstrated significant effects when memantine and donepezil were combined for AD management (Atri et al., 2013). Supplementary agents include antioxidants, such as Vitamin C, Vitamin E, and beta-carotene, which can also be considered as anti-aging therapy to provide protection against oxidative damage in AD patients (Frei, 1994; Gella and Durancy, 2009).

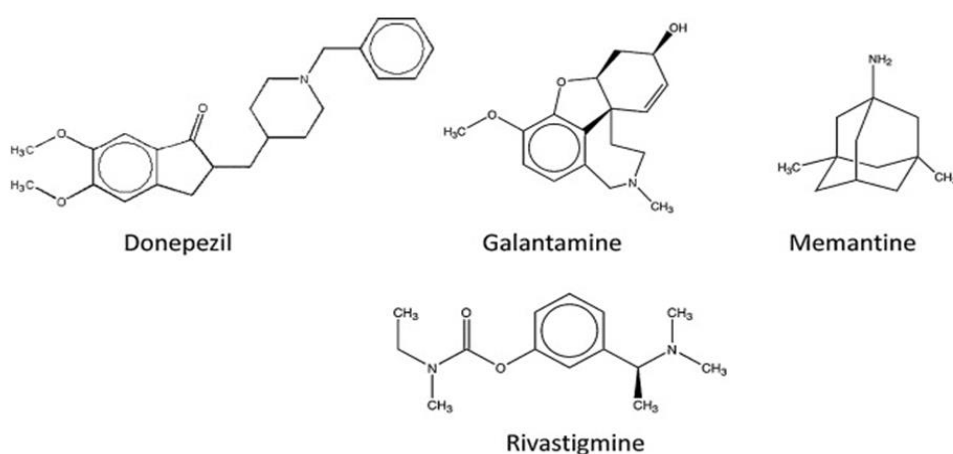


Figure 1.2: The structure of donepezil, rivastigmine, galantamine and memantine, being the drugs for treating AD conditions.

1.1.3. Challenges associated with current neuroprotectants for Alzheimer's disease

One of the current challenges for the effective treatment of NDs is the need to bridge the gap between the indispensable drug therapies that are available and the improvement in the mode of drug delivery to ensure minimal drug toxicity, improved efficacy and a superior quality of life for patients challenged with NDs (Popovic and Brundin, 2006). The treatment of NDs following systemic drug administration is still challenging due to the existence of the highly restrictive Blood-Brain Barrier (BBB) (Popovic and Brundin, 2006). According to Wang and co-workers (2002), the BBB restricts the entry of substances entering the brain based on particle size and endothelial permeability. The BBB is composed of tight cell junctions and ATP-dependent efflux pumps that restricts the delivery of drug molecules into the brain, thus making the therapy of NDs via the systemic route significantly difficult (Abbott and Romeo, 1996; Wang et al., 2002; Alavijeh et al., 2005). Although lipophilic molecules, peptides, nutrients and polymers may satisfy penetrability requirements, these molecules are associated with the inability to access and penetrate targeted regions within the brain, or are inherently non-specifically taken up by sensitive normal tissues and cells (Popovic and Brundin, 2006).

1.2. Novel drug delivery systems for the treatment of Alzheimer's disease

Intracranially implantable devices engineered from biodegradable or non-biodegradable polymers have been previously investigated for the treatment of brain tumors and NDs (Iversen et al., 1995; Wang et al., 2002; Benoit et al., 2000).

Various systems, including drug-loaded microparticles and disc/rod-shaped devices may be used to control the drug release rate and optimize the concentration of the drug at the site of action in the brain over prolonged periods of time (Siepmann et al., 2006). The advantages of using such implantable polymeric devices is that a single intracranial implant would be sufficient to provide neuroprotectant drug levels at the site of action over a prolonged period of time and improve patient compliance due to a significant reduction in drug dosing frequencies and peripheral side-effects (Haesslein et al., 2006; Siepmann and Gopferich, 2001). However, in order to effectively overcome the impediments posed by the BBB, functionalized or site-targeting nanoliposomes (NLPs) may be designed with the ability to deliver drugs at the desired site of action (either within specific regions of brain tissue or at the surface of targeted cells within the CNS) that can provide higher localized concentrations of the drug for uptake into target cells (Forssen and Willis, 1998).

Pharmaceutical nanotechnology is known to involve the creation and utilization of polymeric materials, devices or systems on the nanometer scale such as nanospheres, nanocapsules, nanobubbles, nanotubes and nanofibres (Siepmann and Gopferich, 2001; Sahoo and Labhasetwar, 2003). Nano-enabled drug delivery systems provide great promise for the improvement of the pharmaceutical and therapeutic properties of neuroprotectant drugs (Pillay et al., 2009). Nanostructures (such as NLPs) have the following advantages; 1) they are small in size, which allows them to cross the BBB, 2) they are able to be embedded in a polymeric or lipid matrix, thus offering significant versatility for achieving site-specific CNS drug delivery, and 3) they are capable of releasing the incorporated drug in a passive pre-determined or active programmable manner over a prolonged period of time. In

addition, by utilizing the strategy of direct intracranial implantation of a nano-enabled device, the neuroprotectant drug bioavailability may be significantly improved and the side-effects (the majority of which are peripherally induced) and/or the toxicity profile of the drug may be drastically minimized due to the lower doses and more targeted drug delivery approach.

1.3. Approaches to the problem

The development of novel strategies for the enhancement of the CNS drug delivery to a specific region of brain tissue/cells directly from an intracranially implanted polymeric device is of great interest (Olivier, 2005). Newer synthetic molecular design strategies for targeting neuroprotectant drugs or other biomolecules to a specific region of the CNS is attractive due to the potential to allow the administration of potent therapeutic agents only to diseased tissues or cells, thereby enhancing drug efficacy and minimizing side-effects. The design of a nano-enabled drug delivery device comprising of NLPs conjugated with targeting ligands that bind to receptors which are common or specific to certain NDs may provide an ingenious solution to improving the treatment of NDs. Permutter and co-workers (1990), identified a candidate receptor known as the Serpin enzyme complexes Receptor (Sec-R) domain of A1 elastase on the surface of hepatocytes, glial cell mono-layers and neutrophils for recognition of α 1 AT-elastase. Sequence motifs bearing homology with this pentapeptide domain were found in the A β peptide common in AD (Joslin et al., 1991; Boland et al., 1995). Sec-R is also shown to mediate internalization of A β -peptide in neuronal cell-lines (PC12) (Boland et al., 1995). A previous study performed by Ziady and co-workers (1997) demonstrated how

synthetic peptide (C1315) coupled within the surface of poly-L-lysine for advance gene transfer into heptoma cell-lines via the Sec-R. However, another study by Boland and co-workers (1995), demonstrated that the A β (25-35) peptide (insoluble) was not recognized at all by Sec-R and retained its full toxic/aggregating properties. In another study by Paula-Lima and co-workers (2009), it was demonstrated that human apolipoprotein A-I (ApoA-I) sequence motifs shared homology with the A β peptide. The study also demonstrated binding between Apol A1 to A β peptide and preventing A β peptide from inducing neurotoxicity that is commonly found in AD. Therefore, in order to surmount these restrictions, an implantable device encapsulating functionalized NLPs with targeting ligand (with Apol A1 sequence) for delivering neuroprotectant drug to a specific receptor (Sec-R) was developed in this study.

This study attempts to develop a Bio-robotic Intracranial Device (BICD), which would be capable of delivering alkaloid drugs particularly galantamine (GAL) to a specific site in the neurodegenerative brain and control the release of drugs over a prolonged period of time after direct implantation into the frontal lobe of the brain. The GAL was previously rendered unsatisfactory for management of ADs in terms of neuroprotectant efficacy, bioavailability, long-term pharmaceutical stability, targeted drug delivery, reduction in severe peripheral side-effects and frequent drug dosing intervals, which result into poor patient compliance. The BICD will possess the intrinsic capability to respond to NDs (including disease states, injury and/or inflammation). The system will be designed on pharmaceutical nanotechnology principles comprising biodegradable and biocompatible polymeric NLPs fixated within a neuro-compliant scaffold, incorporating drugs selected on the basis of

pharmaceutical product prototyping and/or the treatment of NDs particularly AD. The NLPs will be functionalized with synthetic peptide and also act as drug reservoirs for precise drug targeting. Targeting ligands (of the synthetic peptide type) will be designed that will bind to Sec-R receptors, and will be conjugated onto the surface of NLPs, to serve as bio-robotic markers for selected NDs.

Numerous approaches for the utilization of site-directing ligands have been developed for liposomes / microbubble targeting (Eniola and Hammer, 2005; Weller et al., 2005). Examples of several classes of such ligands include, 1) antibodies, 2) carbohydrates, 3) peptides, 4) other polysaccharides and, 5) oligonucleotide aptamers (Forssen and Willis, 1998; Shihorkar and Vyas, 2001). Various types of coupling strategies for conjugating liposomes or microbubbles with targeting ligands, employing covalent or non-covalent binding have been developed, and include biotinylated PEG-phospholipid and a streptavidin-conjugate antibody (Schnyder et al., 2004) and protein to pegylated phospholipids by cleavable or metabolically stable linker strategies (Olivier, 2005; Schnyder and Huwyler, 2005).

The BICD was designed in a multi-component manner. The first component would employ a modified “intelligent” polymeric scaffold based on previous engineering approaches in our laboratories that would be able to release NLPs in a passive or actively pre-programmed manner. The second component would be in the development of the NLPs for specific site-targeting and delivery of drugs within specific regions of the brain tissue in close proximity to degenerative neurons. The NLPs would function in response to stimuli that subsequently target molecular markers of NDs, such as the β -amyloid plaques commonly found in AD.

The structure of the NLPs was conceptualized as follows: 1) the GAL would be incorporated into the core of the NLPs, 2) inert sulfur hexafluoride (SF₆) were entrapped into the core region of the lipid monolayers, and 3) site-directing ligands were conjugated onto surface of the NLPs for binding or interacting with specific cellular receptors such as Sec-R. These strategies should allow the NLPs to be sustained over a prolonged periods within degenerative tissues or at sites of inflammation within the brain that are often seen with the neuropathology of NDs such as PD, AD, ADC and brain tumors such as PCNSL.

The BICD provides an improvement to the GAL delivery into the brain for AD management. *In vitro* and *ex vivo* studies were tested on the BICD, the following were determined; the potential of synthetic peptide on target delivery of GAL-loaded NLPs into PC12 neuronal cell via Sec-R, and physicochemical and physicochemical behaviour of cross-linked CEP hydrogel and/or scaffold. In addition, the BICD should ensure prolonged delivery and/or uptake and cytocompatibility of GAL-loaded functionalized NLPs in a simulated cerebrospinal fluid (sCSF) condition and PC12 neuronal cell environment.

1.4. Aim and objectives of this research

The aim of this study was to break the frontiers in CNS drug delivery by designing a nano-enabled BICD that was capable of delivering GAL into a specific region of the brain in response to the presence of specific NDs. The BICD should be able to prolong release of GAL-loaded functionalized NLPs over a period of 50 days in a sCSF condition. The following were proposed as the objectives of this study:

1. To review current composite liposomal technologies based on integration of the liposome-based and polymeric-based technologies that are capable to act as a temporal depot for prolonged drug release *in vitro*, *ex vivo* and *in vivo*.
2. To perform a preformulation study on surface engineered drug-loaded NLPs with chelating ligands that are proposed for modulating of neurotoxicity associated with β -amyloid aggregates of AD.
3. To design unique biocompatible and bio-robotic NLPs that are composed of targeting ligands of the synthetic peptide-type, poly (ethylene glycol) (PEG), and GAL-entrapped within the phospholipid core structure through remote loading in the presence of ammonium sulphate.
4. To optimize constructed drug-loaded functionalized NLPs with synthetic peptide employing the Artificial Neural Networks (ANN) approach.
5. To assess *ex vivo* cytotoxicity and biocompatibility of the drug-loaded functionalized NLPs.
6. To assess the feasibility of employing targeting ligands to bind and facilitate uptake of drug-loaded NLPs through the specific receptor Sec-R that is over expressed in AD.
7. To design a nano-enabled BICD that meets several criteria dictated by vague concept of the disease or disorder or inflammatory conditions within the brain through a rigorous approach.
8. To investigate the biomechanical and physicochemical dynamics of the BICD in both the hydrogel state and lyophilized state, during pre- or post-fabrication of the nano-enabled structure.
9. To visualize the morphological architecture of the BICD, stability and distribution of drug-loaded functionalized NLPs post embedded in the temporal polymeric

depot of scaffold of the BICD, employing Scanning Electron Microscopy (SEM) and imaging microscopy system such as ultrasound imaging, real-time fluorescence imaging (Cellvizio) and optical fluorescence imaging (Microscope).

10. To explore and examine of the BICD for prolonged release of the drug-loaded functionalized NLPs in their intact form in simulated cerebrospinal fluid (sCSF) over 50 days.
11. To assess PC12 neuronal cells membrane damage/injury and cytotoxicity post treatment with BICD.
12. To validate the potency of the functionalized NLPs with synthetic peptide for targeted delivery post-escape from the lyophilized BICD *ex vivo*.
13. To develop non-transgenic Sprague dawley rats model of AD for the assessment of the BICD performance *in vivo*.

1.5. Overview of this thesis

Chapter 1 outlined the problem identification and rationale for selection of the drug delivery system for this research. The study protocol provides current challenges for the effective treatment of the AD, the need to bridge the gap between the indispensable drug therapies and break the frontiers in CNS drug delivery to ensure minimal drug toxicity, and to provide improved efficacy and a superior quality to life for patients challenged with NDs specifically AD.

Chapter 2 provided a comprehensive literature review of the current liposome-based and polymeric-based technologies, as well as the integration of liposome-based technology within a temporary depot polymeric-based technology for sustained or

prolonged drug release. This section provides detailed approaches, advantages and disadvantages on different types of liposome-based technology and depot polymeric scaffold technologies, various methods for embedding drug-loaded liposomes within a depot polymeric-based technology, and various approaches to enhance prolonged drug release within a temporal depot polymeric-based technology.

Chapter 3 described the pre-formulation, chemometric molecular modeling and surface engineering drug-loaded NLPs with chelating ligands aimed at modulation of neurotoxicity associated with A β aggregates of the AD. Ethylenediaminetetraacetic acid (EDTA), histidine and zinc acetate (ZnAc) as a chelating ligands surface engineered on the surface of NLPs employing either covalent or non-covalent bonding provided evidence of resolubilized ZnA β (1-42) or CuA β (1-42) aggregates *in vitro*. *Ex vivo* results elucidated the effectiveness of chelating ligand-bound NLPs for prevention of CuA β (1-42) or ZnA β (1-42) aggregate buildup associated with neurotoxicity in PC12 neuronal cells, as well as promotion of intracellular uptake in the presence of Cu(II) or Zn(II) metal ions. Furthermore, *in silico* molecular mechanistic studies were also employed to corroborate the experimental findings by exploring the spatial disposition of energy minimized molecular structures.

Chapter 4 described the development and optimization of the synthetic peptide ligand for functionalized GAL-loaded NLPs for targeted delivery into PC12 neuronal cells for to managing AD. A Box-Behnken experimental design optimized the fabricated NLPs, which were constructed with synthetic phospholipids [(1, 2 distearoyl-sn-glycero-3-phosphocholine (DSPC) and phosphatidylethanol-aminedistearoyl-methoxy polyethyleneglycol conjugate (DSPE-mPEG2000)] and

cholesterol that lead to significant maximum drug entrapment efficiency and the synthetic peptide, Lys-Val-Leu-Phe-Leu-Ser conjugated onto the surface of the NLPs to provided effective intracellular delivery of an GAL into PC12 neuronal cells. Furthermore, *ex vivo* results revealed that the functionalized NLPs had superior cytocompatibility and post-engineering of peptides onto the surface of drug-loaded NLPs enhanced high GAL accumulation into PC12 neuronal cells through the sec-R in a mediated manner.

Chapter 5 described and evaluated the feasibility of entrapment of GAL-loaded functionalized NLPs into the polymeric-based technology, which in this research was a hydrogel network. Distribution and morphological architecture of embedded functionalized NLPs into hydrogel networks were validated *in vitro* employing bio-imaging such as fluorescence and ultrasound imaging. Nano-enabled structure stability was validated by characterization of physicochemical and physicomechanical properties of the developed nanocomposite hydrogel produced by merged liposome-based and polymeric-based technologies in the presence of cross-linking agents.

Chapter 6 explored and examined the biocompatibility of the nano-enabled BICD for prolonged GAL release in a simulated cerebrospinal fluid (sCSF). *In vitro* studies in sCSF showed prolonged release behavior of the drug-loaded functionalized NLPs with 50-70% GAL release over 50 days. In an *ex vivo* study, BICD provided a platform to act as a bio-robotic marker for the precise delivery of the drug into the brain cells in response to AD. High GAL accumulation within PC12 neuronal cells post-cultivation indicate that the targeting moieties (of the synthetic peptide type) still

had potency for targeted delivery of the drug-loaded NLPs post-escape from lyophilized BICD.

Chapter 7 examined the induction of amyloid-like deposits into the brain tissues of non-transgenic Sprague dawley rats post intra-cisterna magna (ICM) administration of aggregated A β (25-35) peptide. *In vitro* self-assembly and aggregation of A β (25-35) peptide and the morphological structure was validated employing Transmission Electron Microscopy (TEM) and Immunofluorescence microscopy. Histopathological examination of the neuroparenchyma, blood vessels and leptomeninges morphology was evaluated on the brain sections, which was stained with hematoxylin and eosin stain. The formation of amyloid-like deposits at day 14 post-ICM administration with aggregated A β (25-35) peptide was validate employing thioflavin T and Congo Red staining.

Chapter 8 presented the overall the conclusive remarks on the smart BICD, as well as recommendations for future studies in animal models of AD and in chronic patients with the AD.

CHAPTER 2

A LITERATURE REVIEW ON COMPOSITE LIPOSOMAL TECHNOLOGIES FOR SPECIALIZED DRUG DELIVERY

2.1. Introduction

Over the past few decades, liposomes have received widespread attention as a carrier system for therapeutically active compounds, due to their unique characteristics such as capability to incorporate hydrophilic and hydrophobic drugs, good biocompatibility, low toxicity, lack of immune system activation, and targeted delivery of bioactive compounds to the site of action (Mastrobattista et al., 2002; Schnyder and Huwyler, 2005; Immordino et al., 2006; Chen et al., 2010). Additionally, some achievements since the discovery of liposomes are controlled size from microscale to nanoscale and surface-engineered polymer conjugates functionalized with peptide, protein, and antibody (Bangham and Miller, 1974; Yousefi, et al., 2009). Although liposomes have been extensively studied as promising carriers for therapeutically active compounds, some of the drawbacks of liposomes used in pharmaceuticals is the rapid degradation by the reticuloendothelial system (RES) and inability to achieve sustained drug delivery over a prolonged period of time (Torchilin, 2005). New approaches are needed to overcome these challenges. Two polymeric approaches have been suggested thus far. The first approach involves modification of the surface of liposomes with hydrophilic polymers such polyethylene glycol (PEG) while the second one is to integrate the pre-encapsulated drug-loaded liposomes within depot polymer-based systems (Immordino et al., 2006). A study conducted by Stenekes and co-workers (2000)

reported the success of using temporary depot of polymeric materials to control the release of the loaded liposomes for pharmaceutical applications. This achievement leads to new applications, which requires collaborative research between pharmaceuticals, biomaterials, chemistry, molecular, and cell biology. Numerous studies in this context have been reported in the literature dealing with temporary depot delivery system to control the release of pre-encapsulated drug-loaded liposomes (Hara and Miyake, 2001; Wallace and Rosenblatt, 2003; Chung and Tsai, 2006; Mulik and Murthy, 2009). The proposed system was developed to integrate the advantages while avoid the disadvantages of both liposome-based and polymeric-based systems. The liposome-based systems are known to possess limitations such as instability, short half-life, and rapid clearance. However, they are more biocompatible than the polymer-based systems (Mahato, 2005). On other hand, the polymer-based systems are known to be more stable and provide improved sustained delivery compared to liposome-based systems. However, one of the major setbacks is poor biocompatibility which is associated with loss of the bioactive (i.e., the drug) during fabrication conditions such as heat of sonication or exposure to organic solvents (Chung et al., 2006; Immordino et al., 2006). The benefits of a composite system, however, include improvement of liposomes stability, the ability of the liposome to prolonged drug release, and preservation of the bioactiveness of the drugs in polymeric-based technology. In addition, increased efficacy may be achieved from this integrated delivery system when compared to that of purely polymeric-based or liposome-based systems. The aim of this Chapter therefore, is to review the current liposome-based and polymeric-based technologies, as well as the integration of liposome-based technology within temporary depot polymeric-based technology for sustained drug release. The discussion will focus on different types of

liposome-based technology and depot polymeric scaffold technologies, various methods for embedding drug-loaded liposomes within a depot, and diverse approaches reported to control the rate of sustained drug release from depot systems over a prolonged period.

2.2. Liposome-based technology

A liposome is a tiny vesicle consisting of an aqueous core entrapped within one or more natural phospholipids forming closed bilayered structures (Figure 2.1) (Bangham et al., 1974). Liposomes have been extensively used as potential delivery systems for a variety of compounds primarily due to their high degree of biocompatibility and the enormous diversity of structures and compositions (Vasir et al., 2005; Fang et al., 2006). The lipid components of liposomes are predominantly phosphatidylcholines derived from egg or soybean lecithin's (Fang et al., 2006). Liposomes are biphasic a feature that renders them the ability to act as carriers for both lipophilic and hydrophilic drugs. It has been observed that drug molecules are located differently in the liposomal environment and depending upon their solubility and partitioning characteristics, they exhibit different entrapment and release properties (Fang et al., 2006; Zucker et al., 2009). Lipophilic drugs are generally entrapped almost completely in the lipid bilayers of liposomes and since they are poorly water soluble, problems like loss of an entrapped drug on storage are rarely encountered. Hydrophilic drugs may either be entrapped inside the aqueous cores of liposomes or be located in the external water phase. Noteworthy is that the encapsulation percentage of hydrophilic drugs by liposomes depends on the bilayer composition and preparation procedure of the liposomes (Manconi et al., 2002;

Johnsson and Edwards, 2003). Since liposome discovery by Bangham and co-workers (1974), several different embodiments of liposome-based technology have been developed to meet diverse pharmaceutical criteria (Torchilin, 2005). Liposome-based technology has progressed from the first generation “conventional vesicles,” to stealth liposomes, targeted liposomes, and more recently stimuli-sensitive liposomes (Immordino et al., 2006; Bharali et al., 2009). Essentially, liposomes are classified according to their size range, being 50-5000nm in diameter. This resulted into two categories of liposomes namely multilamellar vesicles and unilamellar vesicles (Bharali et al., 2009). Unilamellar vesicles consist of single bilayer with a size range of 50-250nm while multilamellar vesicles consist of two or more lipid bilayers with a size range of 500-5000 nm (Harashima et al., 1999; Immordino et al., 2006).

2.2.1. Conventional liposomes

Conventional liposome-based technology is the first generation of liposome to be used in pharmaceutical applications (Abra et al., 2002; Cattell et al., 2004; Immordino et al., 2006). Conventional liposome formulations are mainly comprised of natural phospholipids or lipids such as 1, 2-distearoyl-sn-glycero-3-phosphatidyl choline (DSPC), sphingomyelin, egg phosphatidylcholines, and monosialoganglioside. Since this formulation is made up of phospholipids only, liposomal formulations have encountered many challenges; one of the major ones being the instability in plasma, which results in short blood circulation half-life (Senior and Gregoriadis, 1982; Frank, 1993; Riché et al., 2004; Torchilin, 2005). Liposomes that are negatively or positively charged have been reported to have shorter half-lives, higher toxicity, and are rapidly removed from the circulation (Senior and Gregoriadis, 1982; Nishikawa et

al., 1990; Soenen et al., 2009). Several other attempts to overcome these challenges have been made, specifically in the manipulation of the lipid membrane. One of the attempts focused on the manipulation of cholesterol. Addition of cholesterol to conventional formulations reduces rapid release of the encapsulated bioactive compound into the plasma (Damen et al., 1981). Furthermore, studies by Tran and co-workers (2009) demonstrated liposome stability after addition of “helper” lipids such as cholesterol and 1, 2-dioleoyl-*snglycero*-3-phosphoethanolamine (DOPE). Harashima and co-workers (1994) demonstrated that phagocytosis of liposomes were dependent on the size of the liposome formulation. Larger size or multilamellar liposomes with a size range of 500-5000nm are the first to be eliminated from the systemic circulation. Nanosized liposomes or small unilamellar vesicles with a size range of 20-50nm are only eliminated later (Gabizon and D. Papahadjopoulos, 1988; Harashima et al., 1994; Torchilin, 2005). The following commercial products: Ambisone, Myocet and Daunoxome, and drug such as Daunorubicin have received clinical approval using conventional liposome technologies (Mondal et al., 2010; Allen and Martin, 2004; Veerareddy and Vobalaboina, 2004). Although small unilamellar liposomes were reported to have potential for a decreased macrophage uptake, insufficient drug entrapment is still a major disadvantage. On the basis of these studies, the success of cholesterol and other phospholipids did not completely overcome the major challenges.

2.2.2. Stealth liposomes

Stealth liposome technology is one of the most often used liposome-based systems for delivery of active molecules (Cattel et al., 2004; Immordino et al., 2006). This strategy was developed to overcome most of the challenges encountered by

conventional liposome technology such as the inability to evade interception by the immune system, toxicity due to charged liposomes, low blood circulation half-life, and steric stability (Torchilin, 2005; Cattel et al., 2004; Soenen et al., 2009). The stealth liposome strategy was achieved simply by modifying the surface of the liposome membrane; a process that was achieved by engineering hydrophilic polymer conjugates (Li and Huang, 2010). The employed hydrophilic polymers were either natural or synthetic polymers such polyethylene glycol (PEG), chitosan (CHT), silk-fibroin, and polyvinyl alcohol (PVA) (Gobin et al., 2006; Nakano et al., 2008; Wang et al., 2010; Ruizhen et al, 2011). Several properties that would add advantages to the polymeric conjugate include such as high biocompatibility, non-toxicity, low immunogenicity, and antigenicity (Immordino et al., 2006; Ruizhen et al, 2011). Although the majority of hydrophilic polymers meet the above criteria, PEG remains the most widely used polymer conjugate. It is specifically employed to increase the hydrophilicity of the liposome surface via a cross-linked lipid (Allen et al., 2002; Atyabi et al., 2009). PEGylated liposomal doxorubicin (DOXIL/Caelyx) is the exceptional example of stealth liposome technology to be approved by both the USA Food and Drug Administration (FDA) and Europe Federation (Krown et al., 2004). Although prominent results were achieved from this model such as reduction of macrophage uptake, long circulation, and low toxicity, passive targeting is still a major disadvantage since liposomes can deliver active molecules not only to abnormal cells but also to sensitive normal cells (Scherphof et al., 1985).

2.2.3. Targeted liposomes

Targeted liposome based system was suggested after conventional stealth liposome failed to evade uptake of active molecules by sensitive normal cells or nonspecific

targets *in vivo* (Sapra and Allen, 2003; Medina et al., 2004). Unlike stealth liposomes, site-specific targeting liposomes have been engineered or functionalized with different types of targeting moieties such antibodies, peptide, glycoprotein, oligopeptide, polysaccharide, growth factors, folic acid, carbohydrate, and receptors (Torchilin, 2008; Li et al 2009; Song et al., 2009; Shmeeda et al., 2010; Takara et al., 2010; Ying et al., 2010). In addition, targeted ligand can further increase the rate of liposomal drug accumulation in the ideal tissues/cells via over expressed receptors, antigen, and unregulated selectin (Stewart et al., 2008; Hossen et al., 2010; Simonis et al., 2010; Yu et al., 2010. Hua et al., 2011).

Peptides, protein, and antibodies have been most extensively studied as ligands for directing drug-loaded liposomes to sites of action, due to their molecular structures, which are essentially composed of known amino acid sequences. Furthermore, it has been reported that ligands can be conjugated onto pegylated liposomes via different types of coupling methods, such as covalent and non-covalent binding. Covalent coupling occurs when novel ligands are indirectly engineered on the surface of liposome through a hydrophobic anchor via thioether, hydrazone bonds, avidin-biotin interaction, cross-linking between carboxylic acids and/or amines (Nobs et al., 2004). Non-covalent coupling is observed when novel ligands are directly added to the mixture of phospholipids during liposomal formulation (Fang et al., 2006). Li and co-workers (2009) attempted to generate dual ligand liposome conjugates aimed at targeting multiple receptor types on the cell surface receptors. *Ex vivo* studies demonstrated the success of the dual ligand approach in improving the selectivity when compared to a single ligand approach. In another study, Ying and co-workers (2010) formulated dual targeted liposomes with various targeted

moieties such as p-aminophenyl- α -D-manno-pyranoside (MAN) and transferrin (TF). The study was conducted both *ex vivo* (in C6 glioma cells) and *in vivo* (in C6 brain glioma-bearing rats). The following were compared: free daunorubicin, daunorubicin liposomes, daunorubicin liposomes modified with MAN, and daunorubicin liposomes modified with TF as the controls, and daunorubicin liposomes modified with MAN and TF. Daunorubicin liposomes modified with dual ligands such as MAN and TF showed a more significant increase in neuroprotectant efficacy, when compared with the drug alone, drug-loaded liposome, or single ligand modified surface of the liposome. However, the efficacy of these approaches faces limitations because protein circulation and gene expression cannot be sustained for long periods of time (Torchilin, 2005).

Commercially available liposomes were surface engineered with monoclonal antibody and are now commercially available (Lukyanov et al., 2004). The overall advantage of this model of liposome is an increase in active molecules or drug reach targeted cells via endocytosis (Torchilin, 2005). In another study, Nallamothu and co-workers (2006) demonstrated the usefulness of Combretastatin A4 as novel antivasular agent. This compound portrays its anticancer activity by inducing irreversible vascular shutdown in solid tumors (Zoldakova et al., 2010). Despite its anticancer potential, the drug has been shown to have several undesirable side effects to the underlying normal tissues (Young and Chaplin, 2004). These problems may be alleviated by targeting the drug specifically to the solid tumor vasculature. Studies have shown that certain cell adhesion molecules such as $\alpha v \beta 3$ integrin receptors are overexpressed on actively proliferating endothelium of the tumor vasculature (Kumar et al., 2000; Hynes. 2002). These surface markers discriminate

tumor endothelial cells from the normal endothelial cells and they can be used as a target for antivascular drug delivery (Nollamothe et al., 2006). Nallamothe and co-workers (2006) could demonstrate that peptides with Arginine-Glycine-Aspartine (A-G-A) amino acid sequence constrained in a cyclic polyethylene-glycol (PEG)-based liposome framework can bind to the $\alpha v\beta 3$ integrin receptors. Based on this analogy, they could design a targeted liposome delivery system for combretastatin A4 with cyclic (RDG) peptides as targeting ligands (Figure 2.2). Targeting of combretastatin A4 to irradiated tumors using this delivery system resulted into significant tumor growth delay (Figure 2.3) (Nollamothe et al., 2006).

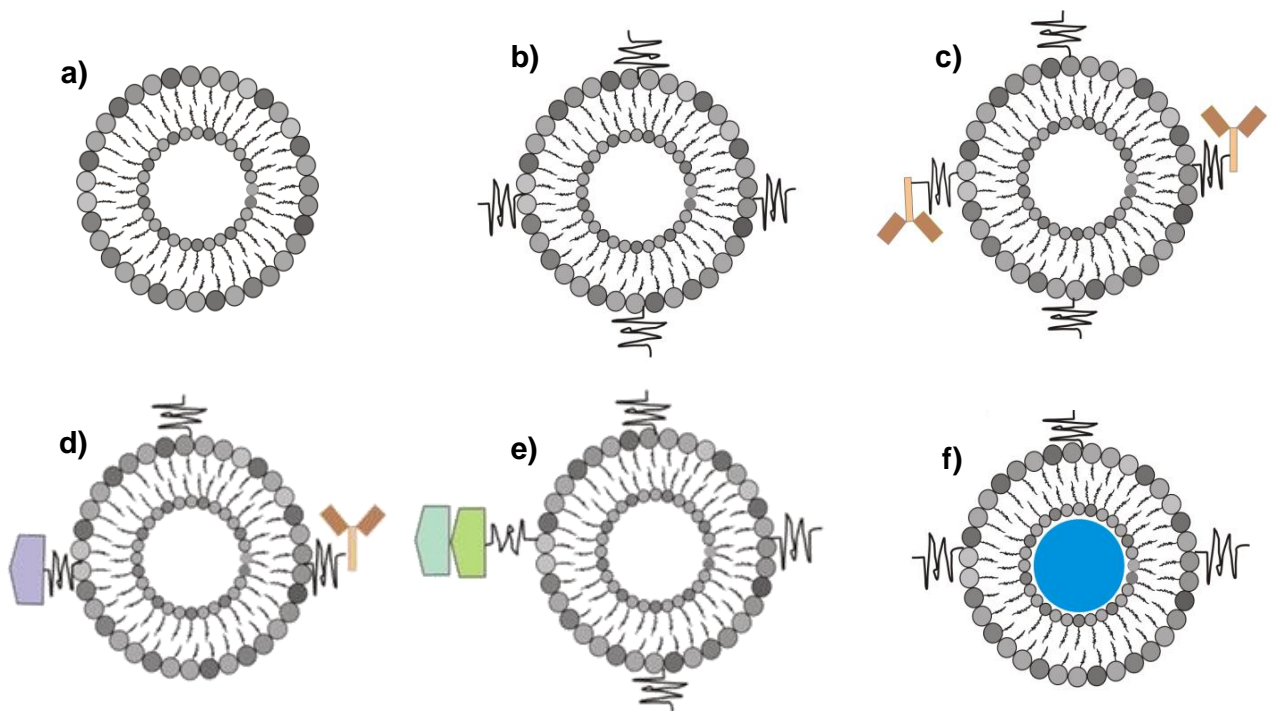


Figure 2.1: Schematic representation of liposome-based systems. (a) Conventional liposomes. (b) Stealth liposomes coated with a polymeric conjugate such as PEG. (c) Stealth liposomes coupled with a functionalized ligand, (d) liposomes with a single ligand and antibody, (e) Duplicated ligand with repeated peptide sequence, (f) liposomes loaded with perfluorocarbon gas (adapted from Zucker et al., 2009).

2.2.4. Additional diverse liposomes types

2.2.4.1. Virosomes and stimuli-responsive liposomes

Liposomal technologies, such as conventional, stealth, and targeted liposomes have already received clinical approval (Kim et al., 2001; Goyal et al., 2005). New generation types of liposomes have been developed to increase bioactive molecule delivery to the cytoplasm by escape endosome (Liu et al., 2006; Pradhan et al., 2010). New approaches that employ liposomes as pharmaceutical carriers are virosomes and stimuli-type liposomes. The stimulating agents in this case include pH, light, magnetism, temperature, and ultrasonic waves. A virosome (Figure 2.4) is another type of liposome formulation. It comprises non-covalent coupling of a liposome and a fusogenic viral envelop (Kaneda, 2000). A stimuli-sensitive liposome is a type of liposome that generally depends on different environmental factors in order to trigger drug, protein, and gene delivery. A study conducted by Schroeder and co-workers (2009), Liu and co-workers (2006), and Lentacker and co-workers (2009) demonstrated that the exposure of the liposome loaded with perfluorocarbon gas to ultrasound waves triggered drug and gene delivery into the cytoplasm of the targeted cells through cell membrane pores. Their data demonstrated that the liposome-loaded magnetic agents triggered drug delivery to the specific site *in vivo*, using an externally applied magnetic field. The enhancement of endosomal release of drug-loaded liposome into the cytoplasm was reported to be influenced by the utilization of pH-sensitive liposomes or by attachment of pH-sensitive fusogenic peptide ligands (Anabousi et al., 2006; Bellavance et al., 2010). Most recently, a review article published by Chen and co-workers (2010) described the generation of

stable liposomes utilizing lyophilization techniques, which may be used for future production of more models for liposome

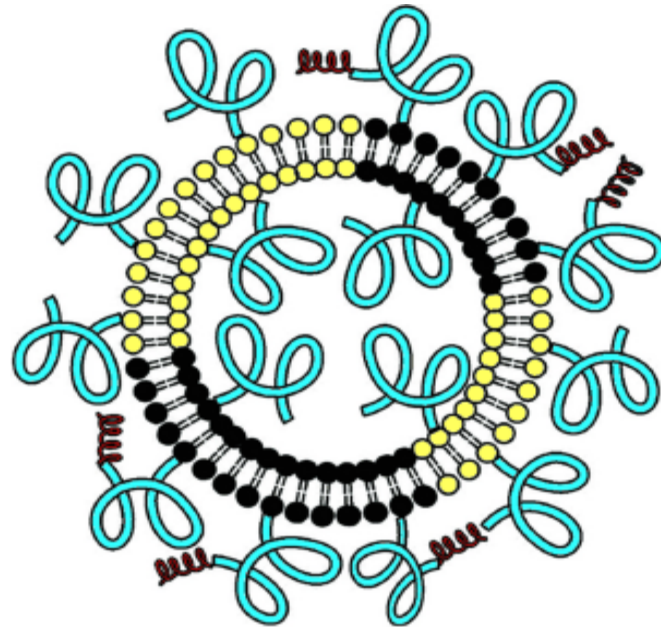


Figure 2.2: Schematic depicting a stealth PEGylated liposome (adapted from Rai et al., 2008).

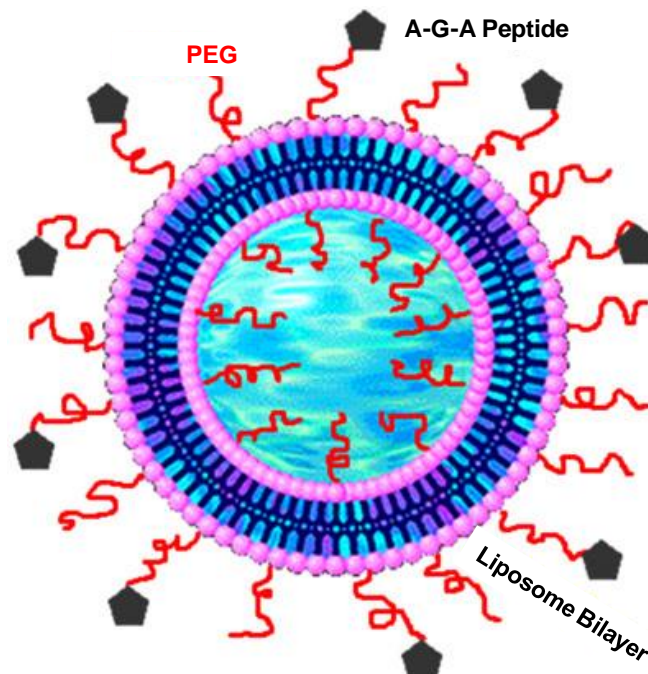


Figure 2.3: A schematic representation of the targeted liposome delivery system depicting the cyclic RGD peptides that targets the $\alpha v \beta 3$ integrin receptors on vascular tumor cells (adapted from Nallamothu et al., 2006).

2.2.4.2. Gene-based liposomes

The characterization of human genome coupled with recombinant DNA technology has created opportunities for gene therapy that never existed before (Uchegbu, 1999). Candidate diseases for such technology include cancer (Dass and Choong, 2006), arteriosclerosis (Feldman and Steg, 1997), cystic fibrosis (Griesenbach et al., 1998), haemophilia, sickle cell anaemia, and other genetic diseases. Ideally, the administration of the gene of interest should result in the expression of the therapeutic protein. However, the delivery of the large anionic bioactive DNA across cell has been one of the most difficult endeavours. DNA is easily degraded by circulating and intracellular deoxyribonucleases. Notwithstanding, it must also be delivered intact across the cell and nucleolar membranes to the nucleus (Uchegbu, 1999).

Liposomes have thus proved to achieve efficient intracellular delivery of DNA (Smith et al., 1997; Kim et al., 2009). Such liposomes are prepared from phospholipids with an amine hydrophilic head group. The amines may be either quaternary ammonium, tertiary, secondary, or primary, and the liposomes prepared in this way are commonly referred to as cationic liposomes, since they possess a positive surface charge at physiological pH. The use of cationic liposomes as gene delivery systems was firstly enforced in the late 1980s when *in vitro* studies by Felgner and co-workers (1987) could demonstrate that the complexation of genes with liposomes may promote gene uptake by cells *in vitro*. Since then, cationic liposomes of varying description have been used to promote the cellular uptake of DNA with resultant therapeutic protein expression by various organs *in vivo*. Figure 2.5 is a schematic representation of a DNA-liposome complex. Although the experimental data have

demonstrated that cationic liposomes can facilitate the transfer of DNA into live mammalian cells, there are still major problems that need to be overcome. These include a reduction in the rapid clearance of cationic liposomes and the production of efficiently targeted liposomes. At the cellular level, the problems may be overcome by improving receptor-mediated uptake employing appropriate ligands. The endowment of liposomes with endosomal escape mechanisms, coupled with more efficient translocation of DNA to the nucleus and the efficient dissociation of the liposome complex just before the entry of free DNA into the nucleus might provide an optimal cornerstone solution to the problem. This proposition is depicted in Figure 2.6.

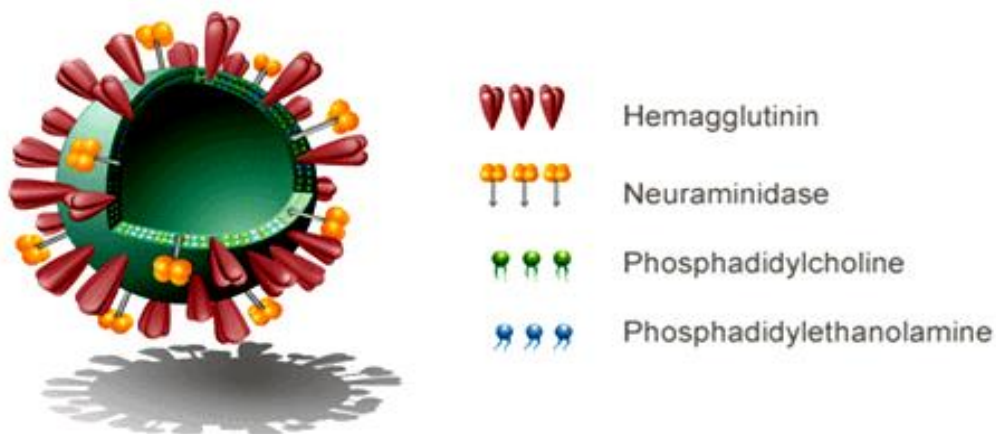


Figure 2.4: A schematic representation of a virosome (source: Pevion Biotech Ltd. 2010).

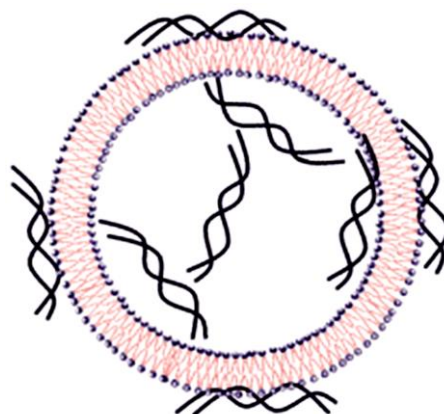


Figure 2.5: A schematic representation of a DNA-liposome complex (adapted from Uchegbu, 1999).

2.3. Temporary depot polymeric-based systems for liposomal coupling

Polymer-based systems, such as hydrogel or prefabricated scaffolds have been used as depots for drugs, regenerative cells, protein, growth factor, and pre-encapsulated drug loaded liposome for sustained release (Meyenburg et al., 2000; Stenekes et al., 2000; Peptu et al., 2008; Mulik et al., 2009; Wolf et al., 2009; Kojima et al., 2009; Hafeman et al., 2010). Various polymers have been researched for this application based on their fundamental properties such as biodegradability, biocompatibility, non-toxicity, and the noninflammatory tendency. Natural and synthetic biodegradable polymeric systems such CHT, collagen, gelatin, fibrin, alginate, dextran, carbopol, and polyvinyl alcohol have been employed as temporary depot-forming agents since they meet most of the above requirements (Kawakami et al., 2001; Berger et al., 2004; Chung et al., 2006; Kojima et al., 2009).

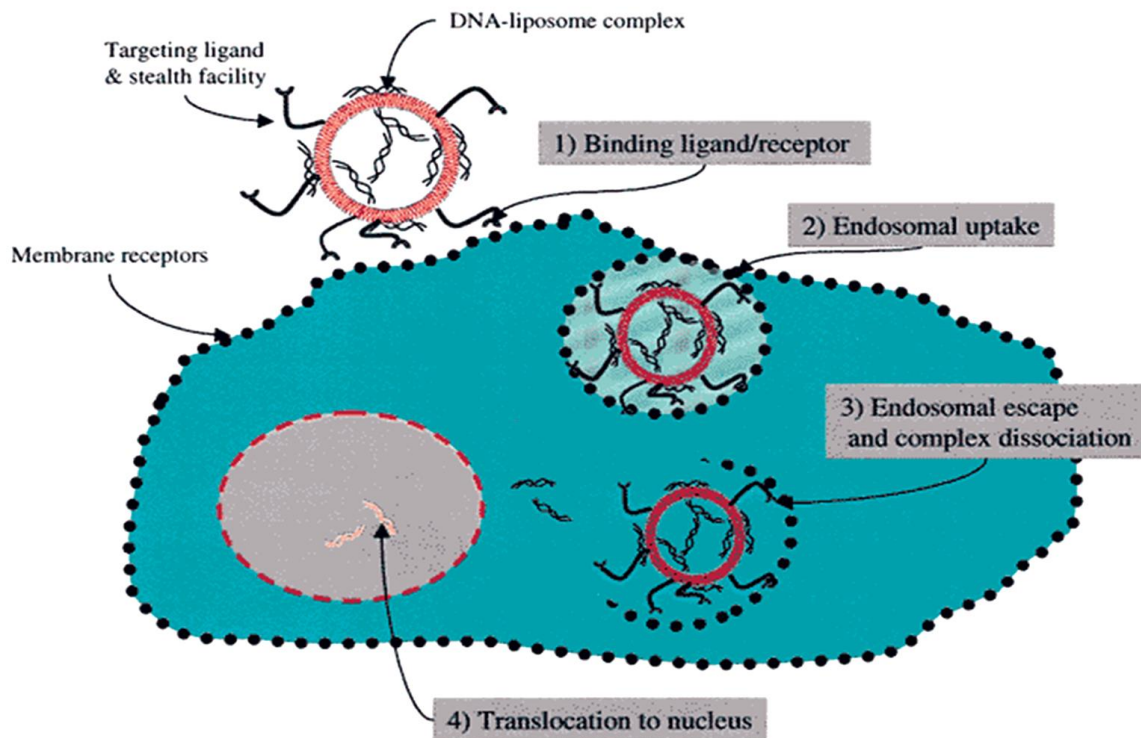


Figure 2.6: A schematic depicting the optimization of liposomal gene delivery (source: Uchegbu, 1999).

2.3.1. Injectable polymeric scaffolds

The strategy for generating an ideal depot for an active compound or bioactive molecule-loaded liposome with the benefit of local drug retention and sustained release over prolonged time has recently received much attention in both pharmaceutical and bioengineering research (Exner and Saidel, 2008; Hafeman et al., 2010). The *in-situ* forming injectable polymer was among the most successful models, since it was able to encapsulate protein and/or bioactive molecules or function as a pre-encapsulated drug-loaded liposomal formulation that was in liquid form (Patel et al., 2010; Paleos et al., 2004). This solution or suspension mixture could then be injected into the target organ with a needle to form a semisolid scaffold and finally an implant. The success in shifting from liquid formulation to semisolid and finally to an implant was a result of various desirable polymeric properties and stimulating agents such as water, light, temperature, and pH, that facilitated such processes within the polymer such as precipitation, cross-linking, and polymerization (Exner and Saidel, 2008; Ta et al., 2008; Lee et al., 2009; Deligkaris et al., 2010).

Since the majority of hydrogels were composed of natural or synthetic biodegradable polymers, bioactive molecules were released via passive diffusion, matrix pore formation, or polymeric degradation (Holland et al., 2005; Yu, et al., 2008; Bhattarai et al., 2010; Krebs et al., 2010). Furthermore, semisolid implant formation was reported as being dependant on the polymeric state such as phase inversion, low-glass transition temperature, or on hydrogels that formed by the aid of cross-linking reagents and chemo- or thermal sensitization (McHugh et al., 2005; Zhang et al., 2010). In addition, the system could deliver drug directly or indirectly to the targeted sites, through subcutaneous injection and/or intratumoral injection (Figure 2.7) (Ta et

al., 2008). Overall, the semisolid temporary depots offer several advantages such as enhanced local drug retention, sustained release, and potential for long-term storage. However, repeated injections and passive drug release are still a factor that limits their use as ideal pharmaceutical carriers.

2.3.2. Prefabricated polymeric scaffolds

Prefabricated polymeric scaffolds have gained a lot of attention as depots for delivery of bioactive molecules, regenerative cells, growth factors, and pre-encapsulated bioactive loaded liposome (Narita et al., 2009; Tabesh et al, 2009). Unlike injectable *in situ* scaffolds in which a semisolid scaffold is achieved after injection, prefabricated polymer scaffold solid depot materials are formed outside the body, and then surgically implanted (Chung and Park, 2007). In addition, prefabrication polymeric scaffold can be designed to meet the required characteristics of an ideal scaffold. Desirable attributes of an ideal scaffold are: three-dimensional structure, appropriate surface chemistry, fabrication from materials which are biodegradable or bioresorbable, should not induce any adverse response, scaled pore capacity, and highly reproducible shape and size (McHugh et al., 2005; Tabesh et al., 2009). Different fabrication techniques have been used to achieve the above criteria, such as fiber bonding, emulsion freeze drying, solvent casting, high-pressure processing, gas foaming, and electrospinning (Chung and Park, 2007; Bhardwaj and Kundu, 2010; Salerno et al., 2010; Sin et al., 2010). Various polymers that have been researched for this application are either biodegradable or nonbiodegradable, synthetic or natural, or a combination of the two (Hara and Miyake, 2001; Ghaffari et al., 2006). The major challenge of prefabricated polymeric scaffolds is that a nonbiodegradable polymeric device requires surgical removal at the end of

treatment, which is associated with pain (Eglin and Alini, 2008). However, the benefit on sustained or prolonged release for the pre-encapsulated drug-loaded scaffold has been reported and declared successful (Krebs et al., 2010). Stenekes and co-workers (2000) demonstrated that liposome embedded inside a biodegradable depot polymeric scaffold was able to sustain drug release over a prolonged period of time (Figure 2.8). In addition, the released liposome was found intact after many days of storage within the inside depot polymeric scaffold.

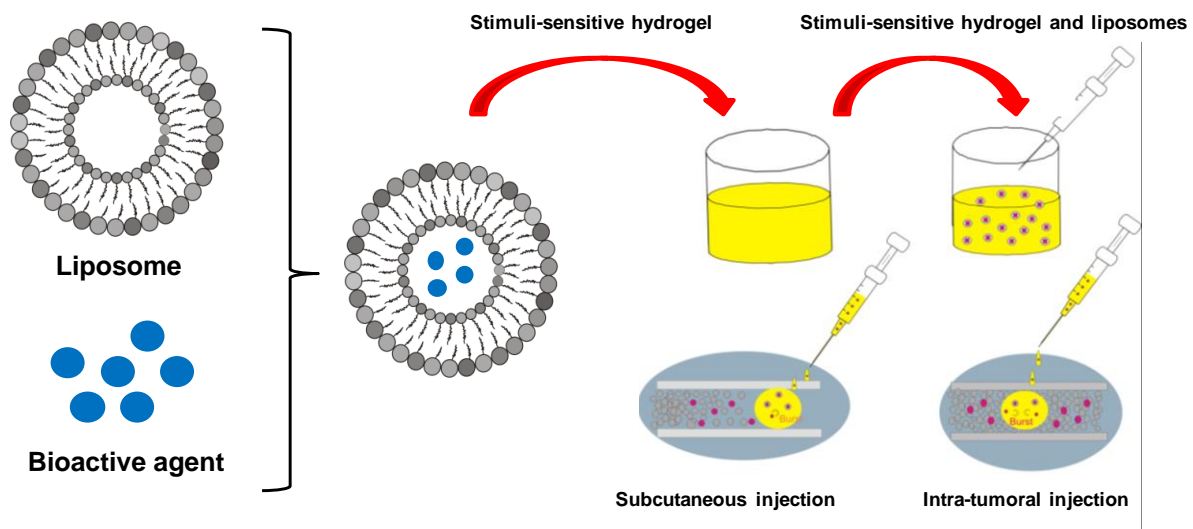


Figure 2.7: Schematic depicting drug delivery from pre-encapsulated drug-loaded liposomes incorporated within an injectable hydrogel-based system (adapted from Ta et al., 2008).

2.4. Natural product-based liposomal drug delivery systems

2.4.1. Collagen-based liposomal drug delivery systems

Collagen is a major natural protein component in mammals that is fabricated from glycine-proline-(hydroxy) proline repeats to form a triple helix molecular structure (Kojima et al., 2009). So far, nineteen types of collagen molecules have been isolated, characterized, and reported in both medical and pharmaceutical

applications (Holladay et al., 2009; Chen and Shana, 2010; Parenteau-Bareil et al., 2010). Collagen has been widely used in pharmaceutical applications due to the fulfilment of many requirements of a drug delivery system such as good biocompatibility, low antigenicity, and degradability upon implantation (Yang et al., 2004). Furthermore, collagen gels are one of the first natural polymers to be used as a promising matrix for drug delivery and tissue engineering (Weiner et al., 1985). Biodegradable collagen-based systems have served as 3D scaffold for cell culture, survival of transfected fibroblasts, and gene therapy (Holladay et al., 2009; Wolf et al., 2009). In this case, collagen scaffolds were fabricated through introducing various chemical cross-linking agents (i.e., glutaraldehyde, formaldehyde, carbodiimide) or by physical treatments (i.e., UV irradiation, freeze-drying, and heating) (Kikuchi et al., 2004; Lu et al., 2009; Tierney et al., 2009; Chen and Shana, 2010; Davidenko et al., 2010).

The combination of liposomes and collagen-based technologies has been long achieved since the early 80s (Weiner et al., 1985). In this case, drugs and other bioactive agents were firstly encapsulated in the liposomes and then embedded inside a depot composed of collagen-based systems, including scaffolds and gels. The combination of these two technologies (i.e., liposomes and collagen-based system) has improved storage stability, prolonged the drug release rate, and increased the therapeutic efficacy (Tabandeh et al., 2003; Pederson et al., 2003; Kojima et al., 2009). In addition, a study that was conducted by Marston and co-workers (2005) demonstrated that temperature sensitive liposomes and collagen thermally trigger the release of calcium and phosphate salts. Multiple collagen-based systems for pharmaceutical carrier applications are currently available for clinical

purposes (Kang et al., 2010). Figure 2.9 is schematic representation of collagen-based liposome.

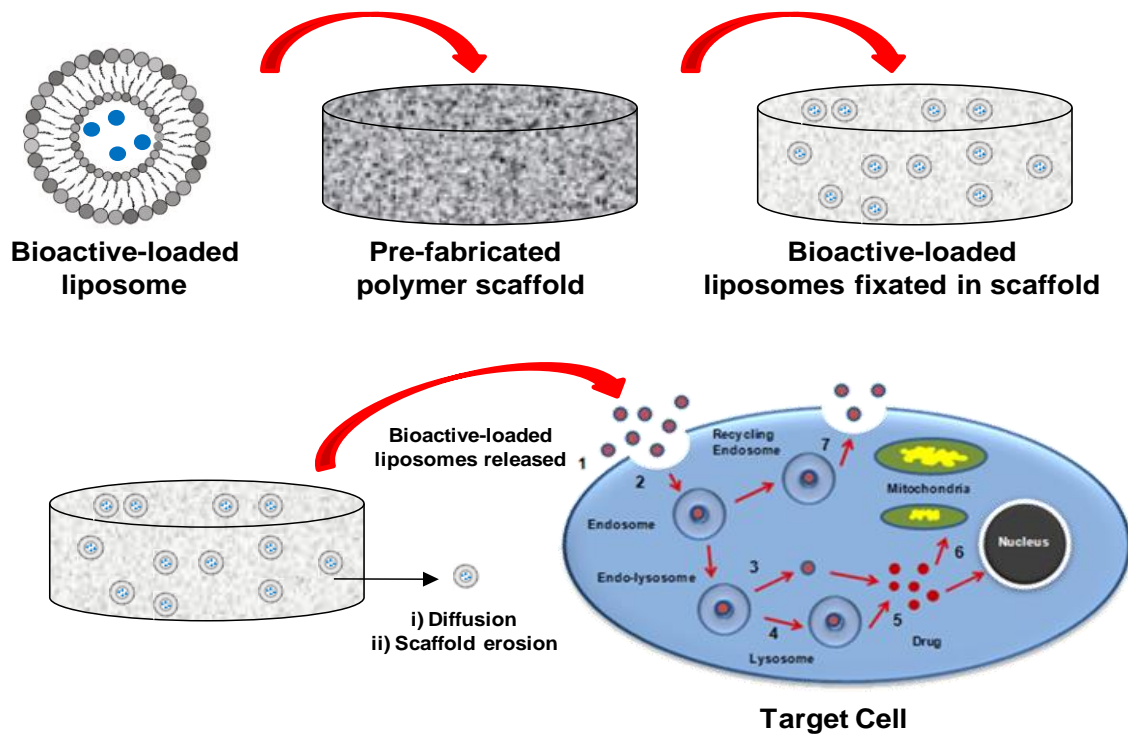


Figure 2.8: Schematic depicting drug delivery from fabricated polymeric based depot system incorporated within drug-loaded liposomes, with eventual entry through a cell membrane (adapted from Stenekes et al., 2000).

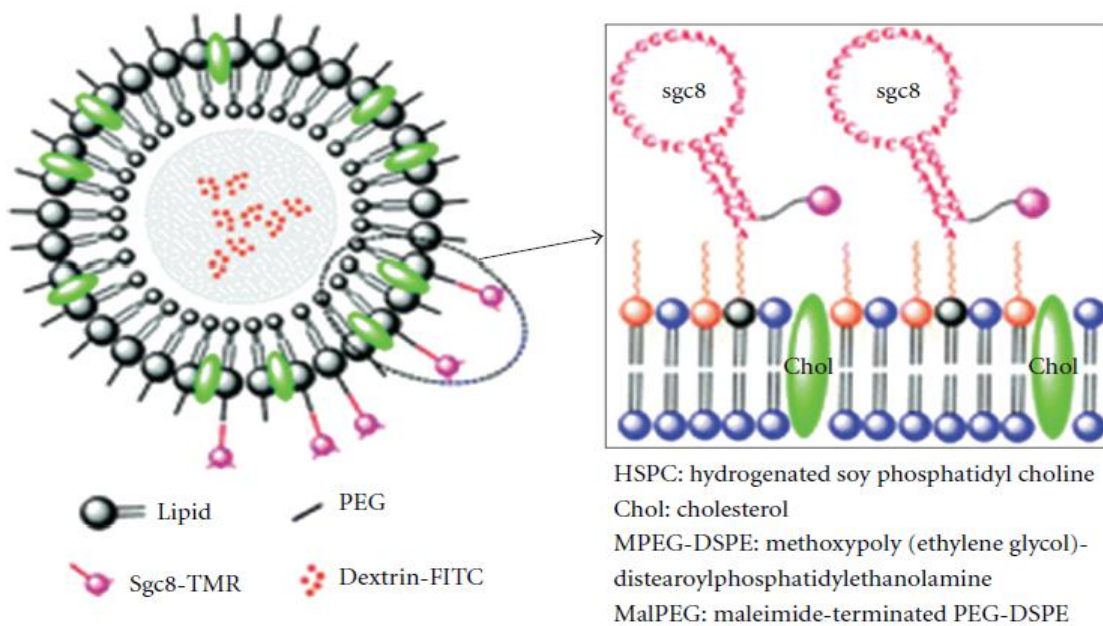


Figure 2.9: A schematic representation of a collagen-based liposome (source: Kang et al., 2010).

2.4.2. Gelatin-based liposomal drug delivery systems

Gelatin is a common natural polymer or protein, which is normally produced by denaturing collagen (Hao et al., 2009). It has been used in pharmaceutical and medical applications due to its outstanding properties such as biodegradability, biocompatibility, and low antigenicity (Narita et al., 2010). In addition, gelatin can be easy to manipulate due to its isoelectric point that allows it to change from negative to positive charge in an appropriate physiological environment or during the fabrication, a property that has found it being very attractive to many pharmaceutical researchers (Young et al., 2005). Gelatin is one of the natural polymers used as support material for gene delivery, cell culture, and more recently tissue engineering. Gelatin-based systems have the ability to control release of bioactive agents such as drugs, protein, and dual growth factors (Holland et al., 2005; Narita et al., 2009; Ofokansi et al., 2010).

It has been reported that it is possible to incorporate liposome-loaded bioactive compounds into PEG-gelatin gel, which function as porous scaffold gelatin-based temporary depots with controlled drug release over prolonged periods of time (DiTizio et al., 1998; Burke et al., 2007).

However, some setbacks have been identified, and they are said to be associated with the use of gelatin-based systems in pharmaceutical applications. These setbacks include poor mechanical strength and ineffectiveness in the management of infected sites (Parenteau-Bareil et al., 2010). A combination of a collagen-based system with liposomes has been proposed to achieve the stability of the system and controlled release profiles of the incorporated compounds. The success of these

formulations, (i.e., gelatin, hydrogel, and scaffolds) was enhanced by cross-linking agents such as glutaraldehyde, sugar, and enzyme transglutaminase. It was also discovered that the cross-linking density of gelatin was able to affect the rate of degradation and rate of bioactive agents release from gelatin vehicles or from liposomes embedded inside gelatin-based systems (Samad et al., 2009; Zhang et al., 2010; Kuwahara et al., 2010; Cheng et al., 2011). Another study by Peptu and co-workers (2008) reported a controlled release of liposome-encapsulated calcein fluorescence dye or calcein labeled with rhodamine from temporary depot of gelatin-based system, which is made up of gelatin carboxymethyl cellulose films. In the same study, the release rate of loaded liposomes were found to depend mostly on the quantity of liposomes entrapped inside the films, degree of swelling of the film, film network density, and the film geometry, which was supported by glutaraldehyde cross-linking agents. In a similar study, DiTzio and co-workers (1998), demonstrated the success of prevention of bacterial adhesion to catheters by ciprofloxacin-loaded liposomes. In this, ciprofloxacin-loaded liposomes entrapped inside a poly(ethylene-glycol) gelatin hydrogel prior characterized *in vitro*. Another study by Burke and co-workers (2007) demonstrated that there was a successive release of oxidizing reagent (sodium periodate) from thermal liposome entrapped inside a stimuli-responsive gelatinous derivative hydrogel. In general, the combination of collagen with liposome has been reported to improve liposome stability and the controlled release of incorporated bioactive agents within liposome formulations.

2.4.3. Chitosan-based liposomal drug delivery systems

CHT is a natural linear bio-polyaminosaccharide polymer obtained by *N*-deacetylation of chitin, which is fabricated from the exoskeleton of marine

crustaceans such as shrimps, crabs, prawns, and fungi (Berger et al., 2004; Pillai et al., 2009). It has been broadly investigated in pharmaceutical applications as a bioactive molecule delivery method or as depot of pharmaceutical carriers due to its desirable properties such as muco-adhesiveness, biodegradability, biocompatibility, and non-toxicity (Prabaharan, 2008; Kean and Thanou, 2010; Mao et al., 2010; Park et al., 2010).

The combination of CHT with liposome technologies is considered as being a promising approach in the drug delivery arena. More recently, CHT technology has been reported as being a depot for liposomal drug delivery systems in the form of porous hydrogel or scaffold. CHT-based hydrogels were generated with or without a cross-linking agent such as glutaraldehyde or by interacting with different types of divalent and polyvalent anions (Hejazi and Amiji, 2003; Kas; 1997; Mulik et al., 2009). Novel *in situ* gelling formulations of hydrogels such as thermosensitive and mucobioadhesive hydrogels have been recently been proposed as a depot for liposomes for sustained drug release over a prolong period of time (Illum, 2003; Mulik et al., 2009). CHT scaffold matrix can be fabricated with unique structure by simple approaches such lyophilization technique, by use of crosslinked agents of CHT solution/hydrogels followed by incubation in the liquid nitrogen, or by employing liquid carbon dioxide, solid-liquid separation, and, most recently, supercritical immersion precipitation techniques (Chung et al., 2006; Chun et al., 2008; Duarte et al., 2010; Ji et al., 2010). A study conducted by Mulik and co-worker (2010) demonstrated that liposomes were able to encapsulate cytarabine after incorporation within CHT hydrogels for sustained drug release *in vivo* at body temperature (Mulik et al., 2009).

2.4.4. Fibrin-based liposomal drug delivery systems

Fibrin is a biodegradable polymer obtained by polymerization of fibrinogen in the presence of thrombin enzyme (Nihouannen et al., 2006). The concept of developing fibrin-based technology as a temporary depot in both pharmaceutical and bioengineering fields has received considerable attention over the past decades (Meyenburg et al., 2000; Sasagawa et al., 2010). The unique properties of the fibrin-based systems such biodegradability and non toxicity, have been reported to influence the delivery efficiency of growth factors, genes, proteins, various cells and drugs (Spicer and Mikos, 2010; Huang et al, 2010; Des Rieux et al., 2009; Christman et al., 2004; Soon et al., 2010; Briganti et al., 2010; Lei et al., 2009). The fabrication of semirigid fibrin scaffold upon injection has been achieved under physiological conditions at the site of interest with rapid polymerization (Christman et al., 2004). Furthermore, fibrin scaffolds have also been used as temporary depots for drug delivery vehicles by incorporation of drug-loaded liposomes alone, or by incorporation of liposomes into a CHT matrix (containing bioactive agent molecules such as protein, drugs and genes) within the depot composed of the fibrin-based systems. The combination of two widespread devices, fibrin and liposome technologies, resulted in sustained bioactive agent release over prolonged periods of time (Chung et al., 2006; Wang et al. 2008; Des Rieux et al., 2009; Kulkarni et al., 2009; Lei et al., 2009).

2.4.5. Alginate-based liposomal drug delivery systems

Alginate also serves as an example of a naturally occurring linear polysaccharide. It is extracted from seaweed, algae, and bacteria (Gombotz and Wee, 1998; Saude et al., 2002; Willerth and Sakiyama-Elbert, 2007). The fundamental chemical structure

of alginate is composed of (1-4)-b-D-mannuronic acid (M) and (1-4)-a-L-guluronic acid (G) units in the form of homopolymeric (MM- or GG-blocks) and heteropolymeric sequences (MG or GM-blocks) (Gao et al., 2009). Alginate and their derivatives are widely used by many pharmaceutical scientists for drug delivery and tissue engineering applications due to its many unique properties such as biocompatibility, biodegradability, low toxicity, non-immunogenicity, water solubility, relatively low cost, gelling ability, stabilizing properties, and high viscosity in aqueous solutions (George and Abraham, 2006; Li et al., 2007). Since alginate is anionic, fabrication of alginate hydrogels has successively been achieved through a reaction with cross-linking agents such as divalent or trivalent cations mainly calcium ions, water-soluble carbodiimide, and/or glutaraldehyde (Xu et al., 2003). The cross-linking methodology may be conducted at room temperature and physiological pH (Jeon et al., 2009). The success in fabricating highly porous 3D alginate scaffolds has been through lyophilization (Mohan and Nair, 2005).

Thus far, alginate based systems have been successfully used as a matrix for the encapsulation of stem cells and for controlled release of proteins, genes, and drugs (Nixon and Yeung, 1989; Tilakaratne et al., 2007; Kong et al., 2008; Wang et al., 2009; Khanna et al., 2010). In addition, alginate based systems have been used as depots for bioactive agent loaded liposomes, for slow drug release (Monshipouri and Rudolph, 1995; Hara and Miyake, 2001). Highly increased efficacy has been reported from these integrated delivery systems when compared to polymeric-based systems or liposome-based systems alone (Kaneda, 2000; Schroeder et al., 2009). Machluf and co-workers (1997) have reported radio labeled protein release from liposomes encapsulated within microspheres of the calcium-crosslinked alginate.

Another study by Hara and Miyake (2001) demonstrated the release of calcein (which is a fluorescent dye) and insulin from calcium alginate gel-entrapped large multilamellar liposomal vesicles *in vivo*.

2.4.6. Dextran-based liposomal drug delivery systems

Dextran is a natural linear polymer of glucose linked by a 1-6 linked-glucoyranside, and some branching of 1, 3 linked side-chains (Mehta, 2000). Dextran is synthesized from sucrose by certain lactic-acid bacteria, the best-known being *Leuconostoc mesenteroides* and *Streptococcus mutans*. There are two commercial preparations available, namely dextran 40 kilodaltons (kDa) (Rheomacrodex) and dextran 70 Kilodaltons (kDa) (Macrodex) (Hornig et al., 2009; Sun et al., 2010). In pharmaceuticals, dextran has been used as model for drug delivery due to its unique characteristics that differentiate it from other types of polysaccharide. This includes water solubility, biocompatibility, and biodegradability (Shrivastava and Shrivastava, 2010). In recent studies, dextran has been regarded as a potential polysaccharide polymer that can sustain the delivery of proteins, vaccines, and drugs (Van Tomme and Hennink, 2007; Jin et al., 2008; Bachelder et al., 2010; Qi et al., 2010).

Interleukin-2, which is a highly effective anticancer drug, is among the success obtained in delivering a combination of drug-loaded liposome and injectable dextran hydrogel (De Groot et al., 2002). Injectable and degradable dextran based systems for drug delivery was generated by a cross-linking reaction with photo-polymerization or free radical polymerization (Maia et al., 2005). In another study by Yeo and Kohane (2008), it was demonstrated that it is possible to fabricate dextran-based hydrogel using dextran derivatives such as carboxymethyldextran derived by

aldehyde-modification or carboxymethylcellulose. In the same study, dextran-based systems were reported to inhibit peritoneal adhesions due to cytotoxicity. Cytotoxicity study was demonstrated in mesothelial cells and macrophages, and it is reported to be associated with a crosslinked agent (Yeo and Kohane, 2008). A study by Stenekes and co-workers (2000) demonstrated the successive encapsulation of a drug-loaded liposome depot into a dextran polymer-based system. The dextran polymeric-based systems were fabricated using a two phase system, the first phase was water and poly (ethylene glycol) and the second one water methacrylated dextran. The slower degradation of dextran polymeric material resulted in sustained liposome release over a period of 100 days (Stenekes et al., 2000). Liposomes released from the depot were reported to be intact, and there was no significant change in liposomal size. In a gene therapy study by Liptay and co-workers (1998), it was reported that recombinant DNA (which contains chloramphenicol acetyltransferase) was successively encapsulated in cationic liposomes and then integrated within dextran. This system was reported to be a suitable delivery system since it could stop transfection efficiency within the colon epithelium wall *in vivo* (Liptay et al., 1998).

2.5. Liposomal drug delivery systems based on synthetic polymers

2.5.1. Carbopol®-based liposomal drug delivery systems

Carbopol hydrogel formulation is a synthetic type of hydrogel, which is a polyacrylic acid derivative. Carbopol® 980, Carbopol® 974NF resin, and Carbopol® 940 have been widely used as pharmaceutical carriers due to their outstanding properties such as bioadhesivity, biocompatibility, and low toxicity (Durrani, 1992; Budai, 2007; Tang,

2007). Carbopol® can swell quickly in water and adhere to the intestinal mucus because the functional carboxylic acid groups (-COOH) can form hydrogen bridges to interpenetrate the mucus layer (Junginger and Verhoef, 1998; Rajput et al., 2010). Furthermore, Carbopol® can inhibit the activity of the dominant enzymes in the gastrointestinal tract due to the possession of carboxylic groups in its structure (Junginger and Verhoef, 1998). In a study that was conducted by Tang and co-workers (2007), the formulation of Carbopol®-containing super porous hydrogel composites showed that swelling behaviour was influenced by ionic strength in addition of the salt, at different pH values. In recent studies, Hosny (2010a; 2010b) reported the possibility of incorporating drug-loaded liposomes within a Carbopol® hydrogel-based system, which acted as a temporary depot. They conducted the study *in vitro* with the aim of improving low viscosity and poor sustainability of release over a prolonged period of time, which are associated with liposomal setbacks. The results suggested that the degree of encapsulation and prolongation of drug release rate of either drugs or drug-loaded liposomes in temporary depots of Carbopol® depends on the properties of the vesicles, such as charge and rigidity. In another study, ciprofloxacin and galifloxacin were also encapsulated within liposomes and thereafter integrated within the temporary depot of the Carbopol®-based system. These studies revealed that loaded liposome integrated within a Carbopol-based system was a suitable model of drug delivery for both ocular and vaginal disorders (Pavelić, 2005; Mourtas et al., 2007; Hosny 2010a; Hosny 2010b).

2.5.2. Polyvinyl alcohol-based liposomal drug delivery systems

Polyvinyl alcohol (PVA) is a water soluble highly hydrophilic synthetic polymer, with a molecular mass of 80 kilodaltons (kDa). PVA can be used in a widely range of

applications such industrial, medical, and food products (DeMerlis and Schoneker, 2003; Macquarie and Hardy, 2005; Pan and Kopecek, 2005). In addition, PVA has gained a lot of attention in pharmaceutical applications due to some attractive properties such as low toxicity, excellent film-forming, biodegradability, emulsifying capacity, biocompatibility, and adhesive properties (Horiike et al., 2002; Bourke et al., 2003). PVA-based hydrogel or scaffolds have been fabricated using chemical cross-linking agents such as citric acid derivative, glutaraldehyde, and formaldehyde, or by physical cross-linking processes such as ultraviolet photo cross-linking, freezing-thawing, and radiation (Yang, et al., 2004; Abdelwahed et al., 2006; Burke et al; 2007).

Various studies have been performed on the effects of PVA-based polymers on the release rate of pre-encapsulated drug-loaded liposomes. In these combination systems, PVA was postulated to enhance liposome viscosity, rendering them more stable and less permeable, thus providing a sustained release liposomal delivery system (Budai et al., 2007). A recent study conducted by Litvinchuk and co-workers (2009) demonstrated that the success of calcein-loaded liposome embedded inside a temporary depot was influenced by photo cross-linking. In the same study, the fluorescence intensity was reported to result in a sustained release effect as observed from day 0 to 120, in both phosphate buffer saline and blood plasma *in vitro*. Overall, the study demonstrated that PVA as a temporary depot offers several advantages to liposomal delivery systems. These include; liposome stability, viscosity, and prolong drug release. Ciprofloxacin, a synthetic chemotherapeutic antibiotic was reported to have been successfully integrated into liposome and PVA-based delivery systems (Budai et al., 2007).

2.6. Techniques for embedding drug-loaded liposomes within depot Polymeric-based systems

Different techniques of loading the drug within temporary depot polymeric-based systems either by using natural or synthetic polymers have been reported by many researchers (Stenekes et al., 2000; Tabandeh et al., 2003; Chung et al., 2006; Budai et al., 2007; Mulik et al., , 2009). However, several disadvantages were found to be associated with this approach such as loss of the efficacy of the drugs during the fabrication process due to the acidic, basic, and/or toxic effect of the solvents employed, heat of sonication, or biochemical interactions with polymeric-based materials such human fibrin gel (Sandor et al., 2002; Chung et al., 2006). To avoid these setbacks, new techniques were suggested by firstly pre-encapsulating the drugs within liposomes and then embedding the drug-loaded liposome into the temporary depot polymeric-based system. This approach attracted many researchers as it improved drug delivery and at the same time preserved drug bioactivity (Chung et al., 2006; Gobin et al., 2006; Budai et al., 2007; Wang et al., 2008; Hosny, 2010a). The success of this technique was also reported after pre-encapsulating drug-loaded liposomes into fibrinogen solution, then injecting the mixture into porous CHT films (Chung et al., 2006, Wang et al., 2008).

Another approach using synthetic PVA was made in which thin films of liposomes were hydrated above their glass transition temperature together with PVA as the hydration solution in order to enhance liposomes entrapment into the temporary depot of PVA based system (Budai et al., 2007). A thermosensitive hydrogel was also investigated using a CHT derivative. In this case, drug-loaded liposomes were loaded in prechilled solutions of CHT solution until an iso-osmotic pressure was

achieved within the CHT solution (Mulik et al., 2009). In another study that was conducted by Gobin and co-workers (2006), it was demonstrated that drug-loaded liposomes were incorporated within a polymeric-based system with agitation and subsequent lyophilisation after being frozen overnight at -80°C . Tabandeh and Aboufazel (2003), suggested a nitrogen refrigeration approach. In this case, pre-encapsulated drug-loaded liposomes were mixed together with collagen solution and then frozen in liquid nitrogen for 24 hours. Since soluble collagen was used in the study, adequate concentrations of collagen were suggested in order to facilitate the drug release and avoid the chain mobility associated with collagen.

A more recent study has demonstrated an enhanced process of drug-encapsulated liposomes into Carbopol[®] hydrogel by using deionized water as a vehicle (i.e., employing a hydration approach) (Hosny, 2010a). This involved the development of an effective prolonged-release liposomal hydrogel formulation containing ciprofloxacin for ocular therapy. Drug delivery in ocular therapy has for long been a difficult task to accomplish because of the poor drug bioavailability that is mainly due to the precorneal loss factors. These factors include tear dynamics, insufficient residence time in the conjunctiva sac, and non-productive absorption (Sultana et al., 2006; Budai et al., 2007). Thus far, fluoroquinolones have shown excellent activity against most of the frequently occurring Gram-positive and Gram-negative ocular pathogens (Hosny, 2010a). Earlier generations of fluoroquinolones (e.g., ofloxacin) often presented with a problem of developing resistance at a fast rate (Chaudhry et al., 1999; Jauch et al., 1999). Ciprofloxacin is active against a broad spectrum of aerobic Gram-positive and Gram-negative bacteria. In addition, resistance to this drug develops slowly and has shown to cause a minimal toxicity (Hosny, 2010a).

Ciprofloxacin is currently the drug of choice as an anti-infective ocular agent (Campoli-Richards et al., 1988; Appelbaum and Hunter, 2000). Efficacy of the marketed ophthalmic fluoroquinolone products, mostly aqueous solutions, is limited by poor ocular bioavailability, compelling the frequent dosing regimen, and uncompromised patient compliance (Lin et al., 1996; Wiechens et al., 1999). Thus, a prolonged release ciprofloxacin liposomal hydrogel has proven to be a suitable delivery system for ocular infections.

2.7. Modulating drug release from liposomes within polymeric depot systems

Sustained release of therapeutically active compounds loaded with liposomes in a depot incorporated into polymeric-based system offers the possibility of reducing the dosing frequency, which may lead to the reduction of side effects and therefore sustained drug action (Mulik et al., 2009). A study conducted by Machluf and co-workers (1997) demonstrated that radio-labeled protein-loaded liposomes could be embedded within two membrane layers of a polymeric-based system such as calcium cross-linked alginate and alginate integrated with poly (l-lysine) for sustained release of radio-labeled bovine serum albumin both *in vitro* and *in vivo*. In another set of studies, it was postulated that the success of liposomes release from polymeric-based systems could be due to mesh size of the matrix, size of liposome, diffusion, chemical, pH, and/or enzyme factor (Weiner et al., 1985; Kibat et al., 1990; Meyenburg et al., 2000; Stenekes et al., 2000). In another study by Dhoot and Wheatley (2003), liposome release from barium-alginate depots was reported to be influenced by the cross-linking ions. Leakiness of liposomes during the encapsulation process was due to high lipid content (i.e., cholesterol) during liposomes fabrication for which a high liposomal escape was also observed. In study

by van Dijk-wolthuis and co-workers (1997) demonstrate sufficient drug release in the liposome embedded within degradable polymer-based system, while liposome embedded with non-degradable polymer-based system resulting into insufficient drug release. In addition, high release from degradable polymer-based system was shown to be governing by degradation of the polymeric matrix.

Nixon and Yeung (1989) conducted a study together with Stenekes and co-workers (2000) in which they demonstrate that liposomes with low and high membrane fluidity were successfully released from a polymeric-based system in their intact form and with preserved size for approximately 60 days. Although pre-encapsulated drug-loaded liposomes could show controlled drug release from the depot, the majority of these studies have shown that the obtained drug release profiles depended on the liposomal burst effect rather than the diffusion process (Machluf et al., 1997; Chung et al. 2006; Wang et al., 2008).

2.8. The successes and challenges emerging from composite liposome and polymeric-based technologies

The combination of liposome-based systems and polymeric-based systems for sustained release of therapeutically active compounds has been demonstrated to be successful in pharmaceutical applications. Sustained release profiles of different bioactive molecules such as genes, drugs, protein, and growth factor from liposomes encapsulated in either natural or synthetic biodegradable polymeric material have been obtained (Hara and Miyake, 2001; Dai et al., 2006; Mulik et al., 2009). The success of this drug delivery combination depends mostly on encapsulation efficacy and the type of drug release profile that is obtained. Efficiency in encapsulating drug-

loaded liposomes was reported to be dependent on several techniques, such as cross-linking agents [glutaraldehyde (GA), formaldehyde, carbodiimide] or physical treatments (i.e., UV irradiation, freeze-drying), during the fabrication process (Jeon et al., 2009; Kulkarni et al., 2009). Sustained release kinetics of the pre-encapsulated drug-loaded liposomes depends most on the degradation rate of the polymeric materials. This combined system has added a remarkable advantage to both technologies (i.e., liposome-based and polymeric-based), though more so to the liposome technology since polymeric materials are more stable than liposomes.

The following were achieved properties post embedment of the liposomes into a polymeric based system: (i) sustained release over prolonged periods of time, (ii) improved viscosity, (iii) stability of liposomes, and (iv) improved half-life for both the drugs and liposomes. In polymeric-based system incorporated with liposomes, drug delivery efficacy and preservation of drug bioactivity has been achieved. This is due to the fact that liposomes have a higher degree of biocompatibility when compared to polymeric materials (Stenekes et al., 2000; Gobin et al., 2006). Although this composite system demonstrated improved success, there are still some major challenges that need to be overcome. Incorporation of toxic organic solvent or high heat during the fabrication process can inhibit the activity of some bioactive molecules such as protein (Sandor et al., 2002; Chung et al., 2006). Furthermore, since drug-loaded liposome release profiles seem to depend most on degradation of polymeric materials, the majority of drug-loaded liposome may remain enmeshed within the depot, or insufficient initial release at commencement of treatment may be a problem. At the same time, overdose may occur during the high degradation period. In either case, degradable polymeric materials have demonstrated more

efficacy than nonbiodegradable polymeric material since, insufficient drug release was reported from the latter depot (van Dijk-Wolthuis et al., 1997).

2.9. Future perspective

Significant development has been reported with regard to the combination of the liposome-based technology with temporary depot polymeric-based technology in sustaining drug release over prolonged period. However, the combination of both drug delivery technologies into a single model of drug delivery has been reported to be associated with inadequate drug release. Since both materials can be easily manipulated, design of a novel temporary depot of the polymeric-based technologies to enhance therapeutic efficacy or improve the drug release profile is of a great interest. Integration of the more advanced types of liposome-based technologies such as targeted- or stimuli-sensitive liposomes in this system can enhance therapeutic efficacy. In addition, targeted liposomes formulations, with targeted moieties such as antibodies, peptide, glycoprotein, polysaccharide, growth factors, carbohydrate, and receptors may increase liposomal drug accumulation in the tissues/cells via overexpressed receptors, antigen, and unregulated selectin. Sensitivity of liposomes to pH, light, magnetism, temperature, and ultrasonic waves can enhance therapeutic efficacy. Some polymeric systems have demonstrated some disadvantages in this application such as non biodegradability that results in insufficient drug release. The use of a combination liposomal-based system with natural and/or synthetic polymeric biodegradable and/or nonbiodegradable polymers may add strength to the depot while improving the liposomal release profile. Although organic solvents are normally added during fabrication, non toxicity should be rigorously assessed in *ex vivo* studies. In summary, the combination system, as a

model of sustained release of drug-loaded liposomes from temporary polymeric depots, has been declared successful but system improvements are demanded. Since this system is implantable, it may be useful in future for the management of chronic diseases such as Aid Dementia Complex, Tuberculosis, Cancer, or Neurodegenerative disorders, such as Parkinson's and Alzheimer's disease, which normally require regular doses over prolonged periods of time.

CHAPTER 3

**DEVELOPMENT OF SURFACE-ENGINEERED NANOLIPOSOMES FOR
MODULATING THE NEUROTOXICITY ASSOCIATED WITH β AMYLOID
AGGREGATES IN ALZHEIMER'S DISEASE**

3.1. Introduction

Different hypotheses associated with Alzheimers disease (AD) etiology have been reported. This includes considerable evidence that extracellular soluble A β peptide has to undergo a process of aggregation with biological metals ions (such as zinc, copper and iron ions) in order to form insoluble A β peptide, which is substantiated to promote neurotoxic A β peptide forms of plaques in AD (see Chapter 1, Section 1.1.1) (Small and Bornstein, 2001; Citron, 2002; De Felice et al., 2004; Lublin and Gandy, 2010). This condition is greatly influenced by a breakdown in the homeostatic mechanisms, resulting in abnormal or overexpressed biological transition metal ions, such as zinc and copper ions and thereafter established amyloidogenic form or cytotoxic A β aggregation post reacting with soluble A β (1-40) and A β (1-42) (Lovell et al., 1998; Dong et al., 2003; Bush and Tanzi, 2008; Duce et al., 2010). A study by Feaga and co-workers (2006) postulated that neurotoxicity of the A β aggregation is associated with oxidative damage. In addition, the study also evidently elucidated that monomeric or soluble A β peptide binds to copper in a linear bis-His geometry, thereafter they undergo a complexed reaction with reactive oxygen species. The binding between copper and A β (1-16) peptide is strongly

demonstrated to be modulated by histidine residue-coordination via the imidazole ring (Ma et al., 2006).

Several neuroprotectant metal chelators or chelating agents (such as 5-chloro-7-iodo-8-hydroxyquinoline (clioquinol) (CQ), Ethylenediaminetetraacetic acid (EDTA), histidine residues and zinc acetate (ZnAc) that can restore biometal homeostasis and prevent/reverse A β aggregation, have been explored in both *in vitro* and *in vivo* studies (Bush and Tanzi, 2008; Zatta et al., 2009). A study conducted by Opazo and co-workers (2005) demonstrated that the beneficial effects of CQ is that it is able to reduce the size and number of A β plaques in transgenic AD in mice. In another study by Bush (2002), it was revealed that CQ restored intracellular zinc and copper ions levels through ionophore processes in which CQ: Cu or CQ: Zn complexes mediated the transport of metal ions into the cell. The study also confirmed that CQ: Cu or CQ: Zn intracellular complexes induced the up-regulation of matrix metalloproteases ultimately promoting the digestion of amyloid oligomers.

EDTA is most widely used as a chelating agent due to its claw-like molecular structure that binds to transition metals with a high affinity constant to form EDTA complexes (such as Cu-EDTA and Zn-EDTA) (Conway et al., 1999). Chelation therapy with EDTA has been approved by the US Food and Drug Administration (FDA) for the management of symptoms associated with cardiovascular disease, more recently with AD (Seely et al., 2005; Liu et al., 2009). In another chelation form of therapy, histidine residues were demonstrated to have copper binding or zinc binding activity in AD (Nair et al., 2010). In a study conducted by Chikha and co-workers (2002) it was demonstrated that surface engineered lipid-based carriers with

histidine-rich peptide or protein improved transition metal bindings. In addition, the chelating ligand zinc acetate (ZnAc) has been validated as being the compound of choice for the treatment and management of Wilson's disease (WD) (Marcellini et al., 2005). ZnAc accomplishes its effectiveness as a chelating ligand by means of blocking copper absorption, which ultimately induces hepatic metallothionein synthesis thus resulting in the alleviation of the toxic effects of copper in intestinal mucosal cells (Shimizu et al., 1999). In other countries particularly the United States and a few European countries, ZnAc is currently available as prescription medicine for WD under the tradename Galzin® and Wilzin® respectively (Squitti and Zito, 2009).

Despite these potential chelating agents (i.e. histidine, EDTA and ZnAc), clinical improvement or management of diseases in the CNS such as AD is hampered by poor absorption, toxic side-effects and the difficulty to bypass the highly restrictive Blood-Brain Barrier (BBB) thus hindering further investigation (Popovic and Brundin, 2006). In order to avoid these disadvantages while improving delivery efficacy and reducing toxicity associated with side-effects, sterically stabilized nanoliposomes (NLPs) have been developed as potential delivery vehicles for such CNS conditions (Cui et al., 2005; Schnyder and Huwyler, 2005; Liu et al., 2006; Atyabi et al., 2009; Modi et al., 2010). NLPs are prominent candidates due to their unique characteristics such as low toxicity and capability of crossing the BBB (Chikha and Li, 2002; Kamidate et al., 2002; Kizelsztejn et al., 2009; Liu et al., 2009; Yigit et al., 2009; Phachonpai et al., 2010; Ying et al., 2010). This unique approach of chelating ligand delivery systems utilizing NLPs may significantly advance the efficacy of chelating agents in the management of AD.

The research described in this Chapter was to develop novel NLPs that were surface-engineered with chelating ligands such as EDTA, histidine and ZnAc. The chelating ligands conjugated on the surface of NLPs using either covalent or non-covalent procedures were validated. In addition, the possibility of the modified chelating ligand-bound NLPs to resolubilize or disaggregate ZnA β (1-42) or CuA β (1-42) aggregates using a Label Guard™ Microliter Cell Nano-Photometer™ (Implen GmbH, Munich, Germany) was investigated via quantifying the concentration of proteins. In addition, this Chapter was also attempting on validate that novel modified chelating ligand-bound NLPs (EDTA, histidine and ZnAc) could rendered resolubilization of the ZnA β (1-42) or CuA β (1-42) aggregates *in vitro*. *Ex vivo*, experiments have demonstrated that ZnA β (1-42) or CuA β (1-42) aggregates induced neurotoxicity to PC12 neuronal cells. Furthermore, it was confirmed that the neurotoxicity associated with A β aggregates was reversed after employing the modified chelating ligand-bound NLPs. The modified NLPs assessed in terms of the chelating ligands (EDTA, histidine and ZnAc) facilitate intracellular delivery with the influence of Cu(II) and Zn(II) metal ions *ex vivo*. Molecular Mechanics Energy Relationships (MMER) was employed to corroborate the experimental findings by exploring the spatial disposition of energy minimized molecular structures.

3.2. Materials and Methods

3.2.1. Materials

The following chemical phospholipids (1, 2 distearoyl-sn-glycero-3-phosphocholine) (DSPC), cholesterol (CHOL), phosphatidylethanolaminedistearoyl-methoxy polyethyleneglycol conjugate (DSPE-mPEG2000), phosphatidylethanolamine -

rhodamine-B triethylamine salts (Rh-DSPE), fluorescein isothiocyanate (FITC), ethylenediaminetetraacetic acid (EDTA), L-histidine, β -amyloid (1-42) synthetic peptide, N, N'-dicyclohexylcarbodiimide (DCC) and N-hydroxysulfosuccinimide (NHS) were purchased from Sigma-Aldrich (St. Louise, MO, USA). Zinc acetate (ZnAc), copper acetate (CuAc), copper chloride (CuCl₂) and zinc chloride (ZnCl₂) were purchased from Saarchem (Pty) Ltd. (Brakpan, South Africa). Membrane filters (0.22 μ m) were purchased from Millipore® (Billerica, MA, USA). The CytoTox-Glo™ Cytotoxicity Assay, which measures cell viability, was purchased from Promega Corporation (Madison, WI, USA). All other chemicals used in the experiments were of analytical grade and were employed as received.

3.2.2. Preparation of the nanoliposomes

NLPs were prepared using an adapted reverse-phase evaporation technique developed by Suzuki and co-workers (2007). Briefly, DSPC, CHOL and DSPE-mPEG conjugate (with rhodamine or FITC labeled markers) were dissolved in an organic solvent phase of chloroform/methanol (9:1). Pluronic F68 (5%^{w/v}) was then added as a surfactant (Table 3.1). The mixture was then blended with a probe sonicator (Sonics & Materials, Inc., CT, USA) followed by solvent removal by rotary evaporation (Rotavapor® RII, Büchi Labortechnik AG, Switzerland) maintained at 60°C to obtain a thin lipid film. The appropriate volume of phosphate buffered saline (PBS) (preheated to 60°C) was added and the vessel vigorously agitated on a rotary mixer to produce multilamellar vesicles (MLVs). The MLVs were then sonicated at 60°C for 5 minutes to produce unilamellar liposomes. Size distribution was obtained by gradually extruding through a 0.22 μ m pore size polycarbonate membrane filter

and the samples obtained were allowed to stabilize at 4°C in a refrigerator until further analysis.

Table 3.1. Compositions of nanoliposomes formulations with chelating ligand

F#	DSPC/CHOL/DSPE/P68 (m/m/m/m)	CuAc (mM)	ZnAc (mM)	His (mM)	EDTA (mM)
1	55/62.5/12.5/5	0	0	0	0
2	55/62.5/12.5/5	50	0	0	0
3	55/62.5/12.5/5	0	82	0	0
4	55/62.5/12.5/5	0	0	65	0
5	55/65.5/12.5/5	0	0	0	34

F#: Formulation

3.2.3. Surface modification of the nanoliposomes using chelating ligands

NLPs with DSPE-mPEG-COOH were used to conjugate the chelating ligand using either covalent or non-covalent conjugation procedures (Yagi et al., 2000; Janssen et al., 2003; Verma et al., 2003; Zhua et al., 2007). Briefly, activated NLPs (with 45mg/mL NHS and 60mg/mL DCC) and chelating ligands (65mM of histidine and 34mM of EDTA) were conjugated using a covalent procedure. A non-covalent conjugation procedure was employed for surface modification of NLPs with ZnAc (50mM) and CuAc (82mM) in PBS buffer at pH 7.4. The reaction was allowed to agitate continuously overnight at room temperature. Organic solvents were removal by rotary evaporation by rotary evaporation (Rotavapor® RII, Büchi Labortechnik AG, Switzerland) maintained at 60°C for 3 hours. Finally, the reactions mixtures either covalent or non-covalent conjugated were extensively dialyzed against PBS at pH7.4 for 48 hours to remove unconjugated chelating ligands.

3.2.4. Evaluation of the conjugation efficiency of chelating ligands on the nanoliposomes surface

Evaluation of the conjugation efficiency of chelating ligands (CuAc, EDTA, histidine and ZnAc) on the surface of NLPs was conducted using a NanoPhotometer™ spectrophotometer (Implen GmbH, Munich, Germany). Briefly, 2mL of 1% Triton x100 in methanol was added to 4mL solution of modified NLPs. The suspensions were allowed to react for 2 hours at 45°C in a laboratory oven. The absorbance of the final solution was read on a NanoPhotometer™ at λ_{\max} =220-245nm (230nm for CuAc and histidine, 220nm for ZnAc and 245nm for EDTA) against a blank sample of unmodified NLPs. The conjugation efficiency (CE) was used to confirm the total quantity of chelating ligands coupled or conjugated onto the surface of NLPs and was calculated using equation (Eq. 3.1).

$$CE\% = \frac{\text{Actual quantity of chelating ligand on NLPs}}{\text{Theoretical quantity of chelating ligand employed}} \times 100 \dots \dots \dots \text{Eq. 3.1}$$

3.2.5. Determination of size and zeta potential of the modified nanoliposomes

Determination of the average particle size, polydispersity index (Pdi) and zeta potential of unmodified NLPs and modified NLPs (with chelating ligands) were analyzed using a Zetasizer NanoZS instrument (Malvern Instruments (Pty) Ltd., Worcestershire, UK) at 25°C. All NLPs particle size and zeta potential measurements were performed in the same manner, whereby each sample was diluted (1 in 10) with deionized water using disposable cuvettes for each run (quartz cuvettes). Each test was performed in triplicate and the average value in each case was reported accordingly.

3.2.6. Chemical structure analysis of the modified chelating ligand-bound nanoliposomes

FTIR spectroscopy was performed on the modified NLPs in order to characterize the potential interaction between the chelating ligands and the surface-conjugated NLPs. Samples were compressed into 1x13mm disks using a Beckmann Hydraulic Press (Beckman Instruments Inc., Fullerton, USA), and then analyzed at high resolution with wavenumbers ranging from 4,000-400 cm^{-1} on a Nicolet Impact 400D FTIR Spectrophotometer coupled with Omnic FTIR research grade software (Nicolet Instrument Corp., Madison, WI, USA).

3.2.7. Evaluation of the surface morphology and architecture of the modified nanoliposomes

3.2.7.1. Scanning Electron Microscopy examination

Scanning electron microscopy (SEM) (Jeol JSM-120, Tokyo, Japan) was undertaken to reveal the surface morphology of the NLPs. A small quantity of lyophilized NLPs and modified chelating ligand-bound NLPs were secured on a metallic sample stub and sputter-coated with a layer of carbon. Each sample was viewed under varying magnifications at an accelerating voltage of 20 kV.

3.2.7.2. Transmission Electron Microscopy examination

Unmodified NLPs and modified chelating ligand-bound NLPs (with CuAc, EDTA, histidine or ZnAc) dispersions were diluted approximately 1:10 with PBS buffer at pH7.4 and deep inside sonication bath at 37°C for 5 minutes. One drop of the diluted sample was placed on a carbon-coated copper grid for 5 minutes followed by

removal of the excess liquid that was carried using a filter paper and air-dried. The films on the copper grid were examined using Transmission Electron Microscopy (TEM) (Jeol 1200 EX, Japan) at 10,000x magnification.

3.2.8. *In vitro* studies on the formation of A β (1-42) aggregates

To assess the effect of Cu(II) or Zn(II) metal ions on the formation of A β aggregates, *in vitro* analysis was performed as previously described (Chikha et al., 2002). Briefly 5mM of A β (1-42) peptide was incubated with CuCl₂ (20mM) and ZnCl₂ (20mM) in 25mM Tris/150mM NaCl buffer (pH7.4; 37°C) for 24 hours. Samples were then centrifuged (Optima® LE-80 K, Beckman, USA) at 10,000 rpm for 20 minutes. The supernatant aliquots were directly analyzed using a Nano-Photometer™ Spectrophotometer (Implen GmbH, Munich, Germany) at a λ_{max} 280nm for total soluble A β (1-42) peptide percentage computation. All experiments were performed in triplicate.

3.2.9 Assessment of the effect of the modified chelating ligand-bound nanoliposomes on resolubilization of A β (1-42) peptides

To determine the resolubilization percentage of A β (1-42) peptides through chelation of the modified NLPs, CuA β (1-42) or ZnA β (1-42) aggregates were incubated with either unmodified or modified chelating ligand-bound NLPs (82mM CuAc, 34mM EDTA, 65mM histidine and 50mM ZnAc) for 24 hours. Thereafter reaction mixtures in 0.5% Triton X-100 (for induce lysing to liposomal structure) in methanol were vortexed briefly and incubated at 45°C in a laboratory oven for 2 hours. The samples were then centrifuged (Optima® LE-80K, Beckman, USA) at 10,000 rpm for 20 minutes. The supernatant aliquots were then analyzed using the Label Guard™

Microliter Cell of the NanoPhotometer™ (Implen GmbH, Munich, Germany) for computation of the protein concentration as a percentage. The total percent of A β (1-42) in the soluble fraction was determined in triplicate.

3.2.10. PC12 neuronal cells culture studies

PC12 neuronal cells were purchased from the Health Science Research Resources Bank (HSRRB, Osaka, Japan) (Greene and Tischler, 1974). The cells were cultured in RPMI-1640 media (with L-glutamine and sodium bicarbonate) supplemented with 5% fetal bovine serum, 10% horse serum (both heat inactivated) and 1% penicillin/streptomycin (Sigma-Aldrich; St. Louise, MO, USA). The cells were then maintained in an incubator (RS Biotech Galaxy, Irvine, UK) with a humidified atmosphere of 5% CO₂ at 37°C.

3.2.10.1. *Ex vivo* neurotoxicity assay of metal ions and A β 1-42 aggregates

Neurotoxicity on PC12 neuronal cells was detected by a CytoTox-Glo™ Cytotoxicity assay (Promega Co. Madison, USA). Since CytoTox-Glo™ cytotoxicity reagents contain the AAF-Glo Assay™ substrate and rLuciferase that cannot cross intact cell membranes, only external release protease (normal from dead cells) may cleave the proluminescent substrate which generated a luminescent signal from luciferase (Zhang et al., 2009). Briefly, PC12 neuronal cells were incubated with ZnA β (1-42) or CuA β (1-42) aggregates at 37°C in a CO₂ incubator (RS Biotech Galaxy, Irvine, UK) for 24 hours. An appropriate quantity of CytoTox-Glo™ reagent containing the substrate was added to each well as per the Promega Co. protocol. The cytotoxicity assay was performed by incubation of the CytoTox-Glo™ substrate with treated cells at room temperature for 15 minutes. The supernatant was collected through

centrifuging (Optima® LE-80 K, Beckman, USA) at 1,800 rpm for 20 minutes. For cell viability studies, the pellet was further lysed with CytoTox-Glo™ buffer, which was followed by incubation at room temperature for 15 minutes. Dead and live cell signals were measured by a luminometer (Victor™X3, Perkin Elmer Inc., USA).

3.2.10.2. Neurotoxicity analysis of the modified chelating ligand-bound nanoliposomes

The effect of modified chelating ligand-bound NLPs on neurotoxicity associated with A β aggregates was determined by the CytoTox-Glo™ Cytotoxicity assay as previously describe Cho and co-workers (2008). Briefly, PC12 neuronal cells were first exposed for 24 hours to CuA β (1-42) aggregates or ZnA β (1-42) aggregates which is associated with neurotoxicity, the after treated with filtered sterile unmodified NLPs and modified chelating ligand-bound NLPs (82mM CuAc, 34mM EDTA; 65mM histidine and 50mM ZnAc) in RPMI 1649 media for 24 hours at 37°C. Dead and live cell signals were analyzed using a luminometer (Victor™X3, Perkin Elmer Inc., and USA).

3.2.10.3. *Ex vivo* uptake of the modified chelating ligand-bound nanoliposomes by PC12 neuronal cells

The *ex vivo* uptake of the modified chelating ligand-bound NLPs was investigated on PC12 neuronal cells using Confocal Laser Scanning Microscopy (CLSM, Leica Microsystems, Wetzlar, Germany). PC12 neuronal cells were seeded at a density of 10,000 cells for 24 hours in a 96 cells/well culture plate. The cells were thereafter incubated with 20mM CuCl₂ solution or 20mM ZnCl₂ solutions in RPMI media for 2 hours at 37°C in a CO₂ incubator. The *ex vivo* uptake capacity was performed on

50 μ L of fluorescent-labeled unmodified NLPs and 50 μ L of fluorescent-labeled NLPs surface modified with chelating ligands (CuAc, EDTA, histidine and ZnAc) in RPMI 1640 free FBS. Cells were cultured in identical condition as previously described in Chapter 3, section 3.2.10 of this thesis. After 4 hours of incubation, cells were re-suspended in fresh RPMI 1640 media supplemented with 10% FBS and 5% Horse serum. At 0, 6, 12, 18 and 24 hours of incubation at 37°C under CO₂, the cells were washed four times with culture medium. The intracellular delivery efficiency was detected by a fluorometer filter (Victor™X3 Perkin Elmer Inc. USA) at excitation and emission wavelengths of 450nm and 482nm, respectively. CLSM visualized the bound fluorescent-labeled modified NLPs with PC12 neuronal cells.

3.2.11. Static Lattice Atomistic Simulations

All modelling procedures and computations, including energy minimizations in Molecular Mechanics (MM+), were performed using HyperChem™ 8.0.8 Molecular Modelling software (Hypercube Inc., Gainesville, FL, USA) and ChemBio3D Ultra 11.0 (CambridgeSoft Corporation, UK). DSPC and DSPC-PEG polymers were drawn using ChemBio3D Ultra in their syndiotactic stereochemistry as 3D models whereas the structure of A β 10-21 was built using the Sequence Editor Module on HyperChem 8.0.8. The structure of EDTA and CHOL were built with natural bond angles as defined by the software algorithm. The models were initially energy-minimized using MM+Force Field and the resulting structures were energy-minimized using the AMBER 3 (Assisted Model Building and Energy Refinements) Force Field. The conformer having the lowest energy was used to create the polymer-polymer and protein chelators complexes. A complex between molecules was assembled by disposing the molecules in a parallel way, and the same procedure of energy-

minimization was repeated to generate the final models: DSPE-PEG/DSPC/CHOL, A β 10-21-Cu (II), A β 10-21-Cu (II)-EDTA, A β 10-21-Zn (II) and A β 10-21-Zn (II)-EDTA. Full geometrical optimization was performed in vacuum employing the Polak-Ribiere Conjugate Gradient algorithm until an RMS gradient of 0.001kcal/mol was reached. Force Field options in the AMBER (with all H-atoms explicitly included) and MM+ (extended to incorporate non-bonded limits, restraints, and periodic boundary conditions) methods were set as defaults (Kumar et al., 2011).

3.3. Results and Discussion

3.3.1. Conjugation efficiency of chelating ligands on the surface of the nanoliposomes

The conjugation efficiencies of the modified chelating ligand-bound NLPs for CuAc, ZnAc, histidine and EDTA were determined using a NanoPhotometer™ spectrophotometer (Implen GmbH, Munich, Germany). Results indicated that the coupling efficiencies of the NLPs surface modified with ZnAc, histidine and EDTA were 65%, 76%, and 68%, respectively (Table 3.2). Comparably, the NLPs surface-modified with CuAc had a conjugation efficiency of 30%. These results justify the desirable formation of the modified NLPs with chelating ligands, which is suitable for enhancing the delivery of chelating agents into brain cells associated with AD.

3.3.2. Physicochemical properties of the targeted nanoliposomes

Physicochemical characterization of the surface-modified NLPs (with CuAc, ZnAc, histidine and EDTA) such as the average particle size and zeta potential was measured using Dynamic Light Scattering (Zetasizer NanoZS, Malvern Instrument,

UK). Table 3.2 shows the average particle size obtained for the unmodified NLPs. For the modified NLPs, the results were as follows: i) 178nm for CuAc-modified NLPs; ii) 130nm for EDTA-modified NLPs; iii) 125nm for histidine-modified NLPs and vi) 127nm for ZnAc-modified NLPs. The Pdi value of the modified NLPs with chelating ligands (EDTA, histidine and ZnAc) ranged between 0.235-0.445, while the Pdi value for CuAc was 0.920. The zeta potential values were highly negative on all NLPs. For the unmodified NLPs, the zeta potential value was -28.7mV while for modified NLPs it was -37.3mV. NLPs modified with ZnAc had a zeta potential of -9.59mV while for NLPs modified with histidine and EDTA the zeta potential values were -35.8mV and -36.1mV respectively (Table 3.2). Worth noting is that when NLPs were modified with CuAc, the zeta potential decreased from been a highly negative charge toward a more neutral charge (-9.59mV) (closer to neutrality). Overall, the results indicated that NLPs modified with chelating ligands contributed towards the increase of a net negative charge for the zeta potential value and a relative increase in particle size. Thus, the zeta potential (range from -28.7 to -37.3) of NLPs modified with chelating ligands such as EDTA, histidine and ZnAc, conclude that the produced negative charge NLPs will have better storage stability than CuAc.

Table 3.2. Physicochemical characterization of the unmodified and modified NLPs

F#	DLS^a size (nm)	Polydispersity Index (0-1)	Zeta Potential (mV)	Conjugation Efficiency (%)
Unmodified NLPs	100	0.217	-28.7	-
1	178	0.92	-9.59	30
2	127	0.445	-37.3	65
3	125	0.235	-35.8	76
4	130	0.251	-36.1	68

^aDynamic Light Scattering (DLS)

3.3.3. Assessment of the modified nanoliposomes chemical structure variations

FTIR spectra is one of the most powerful chemical analytical techniques used for analyzing IR spectra, vibration, and characteristics of chemical functional groups of phospholipids (Weers and Scheuing, 1991). FTIR spectra were generated to characterize the potential interactions of the NLPs and chelating ligands. As clearly depicted in Figure 3.1, FTIR spectroscopy confirmed that there were molecular structural changes in the modified NLPs compared to the unmodified NLPs with chelating ligands. The FTIR spectra of modified NLPs displayed characteristic bond formations at the following band widths respectively, 1194.09 cm^{-1} (histidine), 1734.84 cm^{-1} and 1624.62 cm^{-1} (ZnAc), 1243.61 cm^{-1} (EDTA) and 1672.00, 1779.00 cm^{-1} as well as at 3222.85 cm^{-1} (CuAc). These peaks were absent in FTIR spectra of the unmodified NLPs. Overall, results showed that there were interactions between the NLPs and chelating ligands, which culminated into the formation of the novel modified NLPs that were surface-engineered.

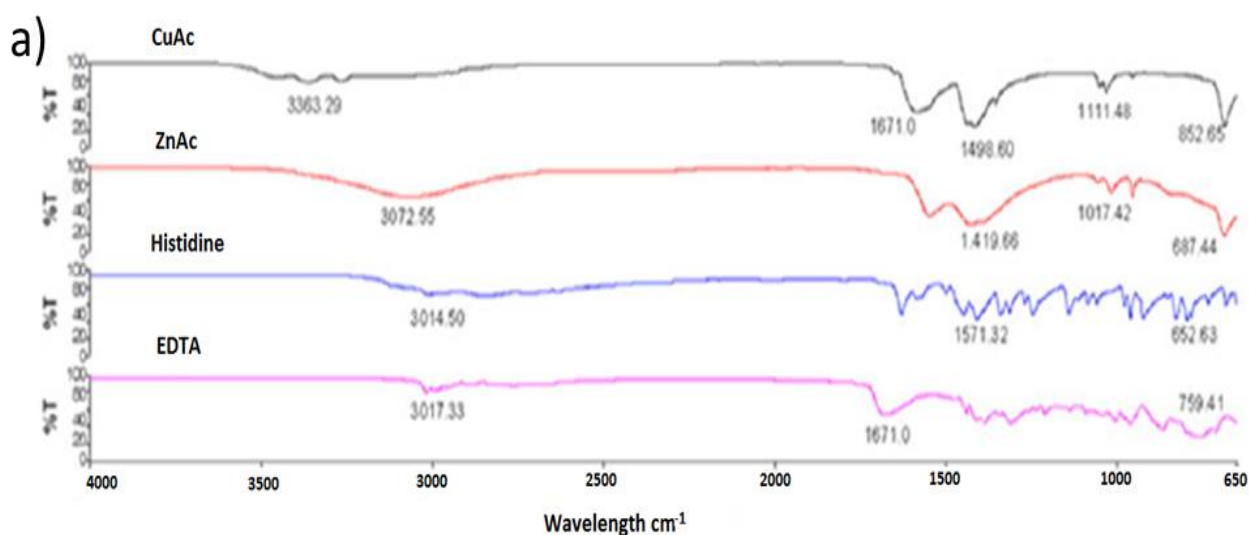


Figure 3.1: Contd. on pg 66

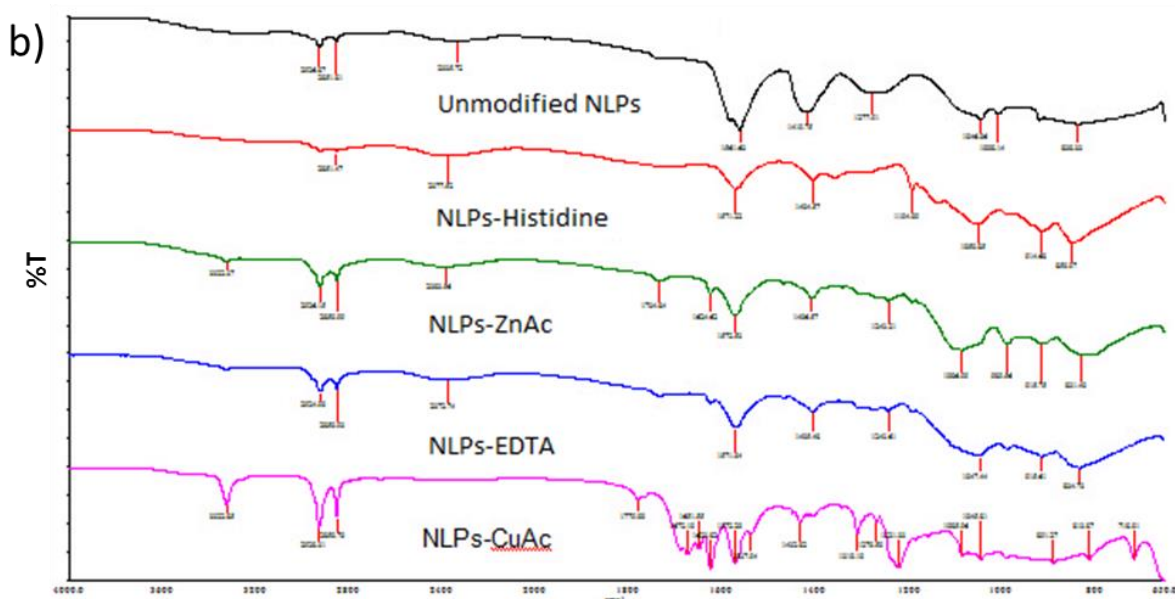


Figure 3.1: FTIR spectra of the (a) native CuAc, ZnAc, histidine and EDTA and (b) unmodified NLPs and surface-modified NLPs with histidine, ZnAc, EDTA and CuAc.

3.3.4. Morphological characterization of the modified nanoliposomes

TEM micrographs of modified chelating ligand-bound NLPs (with ZnAc, CuAc, histidine and EDTA) are shown in Figure 3.2. TEM images revealed homogeneity and uniformity of the, a) unmodified NLPs and modified NLPs with chelating ligand (b) ZnAc, c) CuAc, d) histidine and e) EDTA. The images also indicated that the unmodified NLPs and modified NLPs produced were of a nanosize range and were spherical in shape. Typical SEM image of the modified NLPs chelating ligand presented with uniform surface morphology (Figure 3.3). Results also confirmed that chelating ligands were surface-engineered onto the NLPs by either covalent or non-covalent bonding that contributed to the surface morphology.

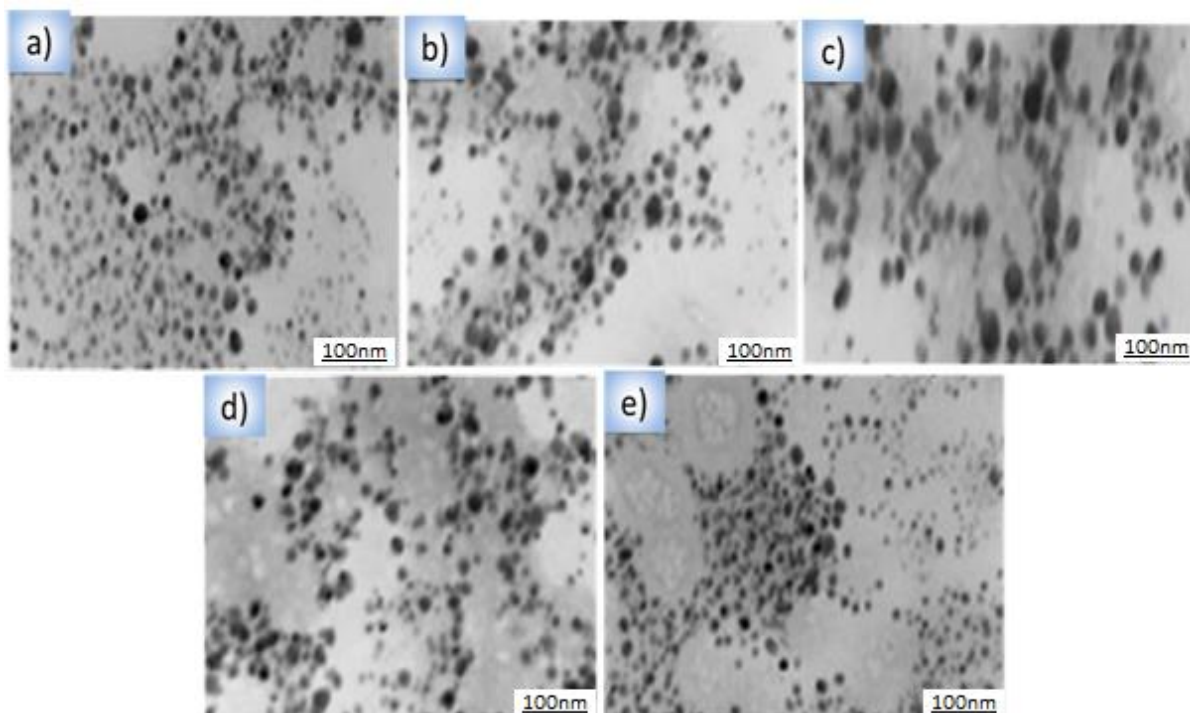


Figure 3.2: TEM micrographs of the a) unmodified NLPs and modified NLPs with b) ZnAc, c) CuAc, d) histidine and e) EDTA.

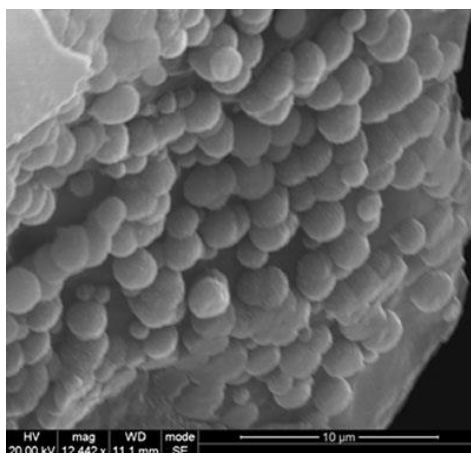


Figure 3.3: Typical SEM image of the modified NLPs synthesized (Magnification x12000).

3.3.5. *In vitro* metals Ions and A β (1-42) resolubilization assay

The modified chelating ligand-bound NLPs modulated with ZnA β (1-42) or CuA β (1-42) aggregates were confirmed *in vitro* (Strozyk et al., 2009). As shown in Figure 3.4a, the percentage of soluble A β (1-42) peptide achieved by resolubilization of ZnA β (1-42) aggregates with unmodified NLPs was 30%, while with modified NLPs

this value increased to 40% for CuAc modified NLPs, 50% for ZnAc-modified NLPs, 70% for histidine-modified NLPs and 82% for EDTA-modified NLPs. Figure 3.4b, shows the percentages of soluble A β (1-42) achieved by resolubilization of CuA β (1-42) aggregates with modified chelating ligand-bound NLPs. Unmodified NLPs showed 30% resolubilization while modified NLPs were 42% for CuAc-modified NLPs, 69% for ZnAc-modified NLPs, 60% for histidine-modified NLPs and 80% for EDTA-modified NLPs. Unmodified NLPs and CuAc modified NLPs did not show any significant effect on resolubilization of either ZnA β (1-42) or CuA β (1-42) aggregates after a 24 hours reaction at 37°C. The high percentages of soluble A β (1-42) peptide confirmed that the surface-engineered NLPs with chelating ligands were effective in resolubilization/disaggregation of ZnA β (1-42) and CuA β (1-42) aggregates.

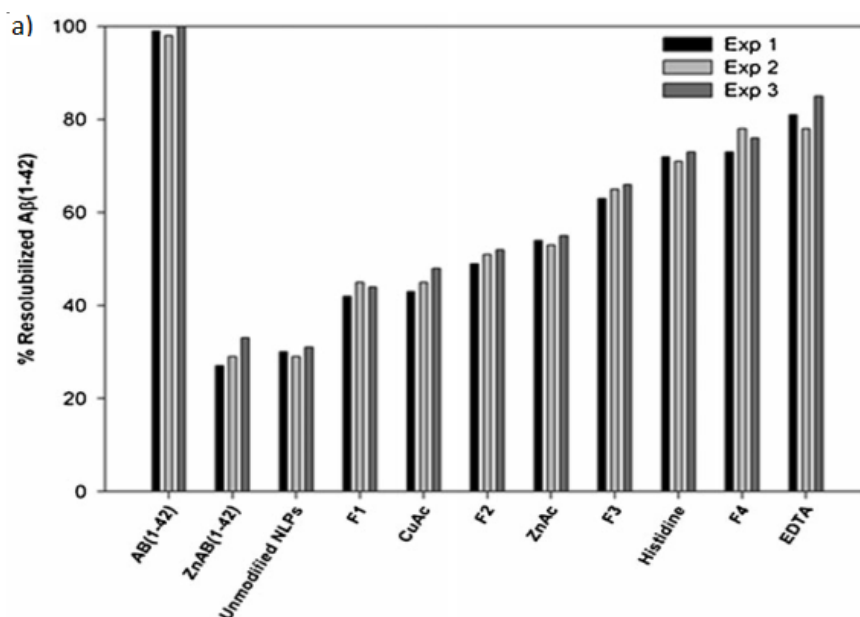


Figure 3.4: *Contd. on pg 69*

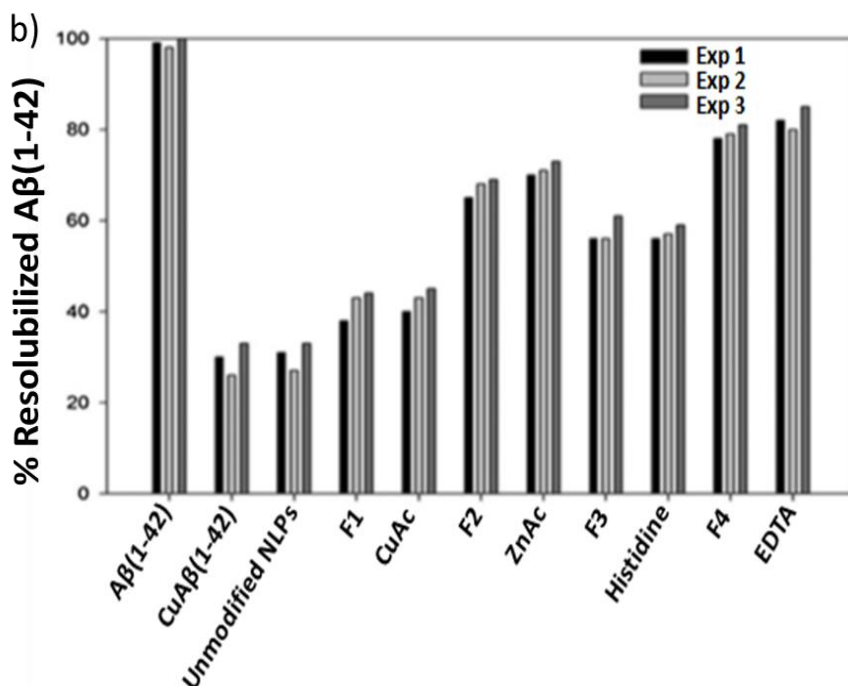


Figure 3.4: Resolubilization of the (a) ZnAβ(1-42) aggregates and (b) CuAβ(1-42) aggregates by modified NLPs. NLPs surface modified with chelating ligand (F1,CuAc), F2, ZnAc; F3, histidine and F4, EDTA.

3.3.6. *Ex vivo* neurotoxicity assay of metals ions and Aβ1-42 aggregates

The neurotoxicity profiles of metal ions Zn(II) and Cu(II)], Aβ (1-42) peptide and ZnAβ(1-42) or CuAβ(1-42) aggregates on PC12 neuronal cells are shown in Figure 3.5a. Cu(II) and Zn(II) ions showed low or no significant effect on cell viability when compared to untreated PC12 neuronal cells. At 5mM of the Aβ(1-42) peptide concentration, a small decrease in cell viability was observed. However, when PC12 neuronal cells were exposed to ZnAβ(1-42) or CuAβ(1-42) aggregates this resulted in a 60-70% decrease in PC12 neuronal cells viability. These results confirmed that both ZnAβ(1-42) and CuAβ(1-42) aggregates induced neurotoxicity when exposed to PC12 neuronal cells. Metal ions such Cu(II) and Zn(II) as well as soluble Aβ (1-42) peptides showed no effects during *ex vivo* studies. This suggested that the metal ions and soluble Aβ(1-42) peptide have low cytotoxicity or stimulate low neurotoxicity on PC12 neuronal cells.

3.3.7. Effect of modified chelating ligand-bound nanoliposomes on the modulation of neurotoxicity

Figure 3.5b-c depict the analytical data obtained for the determination of the effect of modified NLPs on the modulation of neurotoxicity of PC12 neuronal cells induced by ZnA β (1-42) or CuA β (1-42) aggregates. The analysis revealed non-restoration of cell viability after exposure to toxic ZnA β (1-42) aggregates and subsequent treatment with CuAc-bound NLPs (38% cellular survival). In addition, the data showed an increase in cellular survival after treating neurotoxic PC12 neuronal cells with ZnAc-bound NLPs (50% cellular survival), 66% for histidine-bound NLPs and 68% for EDTA-bound NLPs in *ex vivo* studies (Figure 3.5b). Figure 3.5c showed an increase in cell survival after exposure to cells with toxic CuA β (1-42) aggregates and subsequent treatment with modified chelating ligand-bound NLPs. Treatment with ZnAc-, histidine- and EDTA-bound NLPs resulted in 75% cellular survival. However, when CuAc-bound NLPs were used to modulate neurotoxicity associated with toxic CuA β (1-42) aggregates, it did not show any significant effect (30 % cellular survival) on the restoration of cell viability. The data displayed the same trend as the *in vitro* study, which confirmed that the modified chelating ligand-bound NLPs, particularly ZnAc, histidine and EDTA were able to modulate both toxic CuA β (1-42) and ZnA β (1-42) aggregates *in vitro* and *ex vivo*.

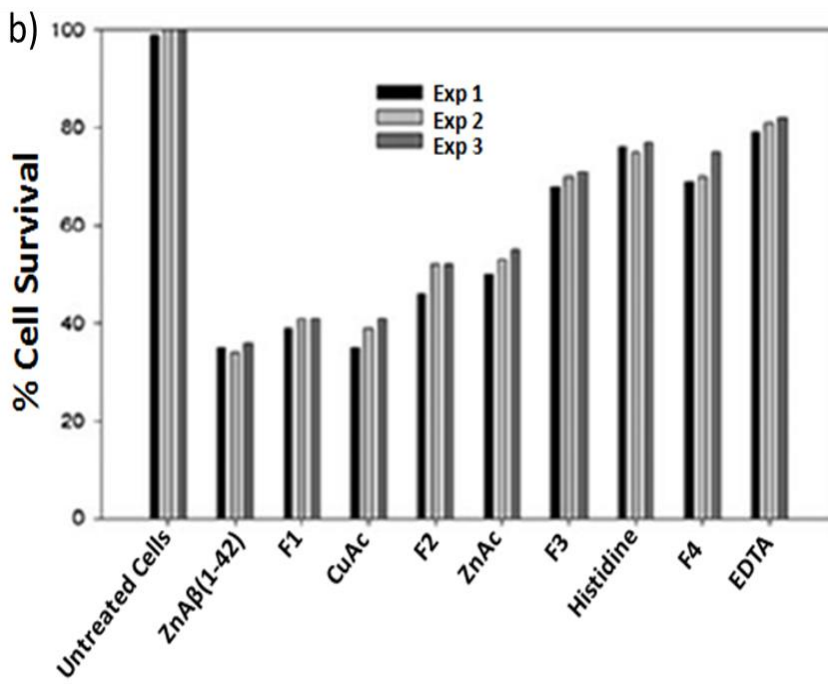
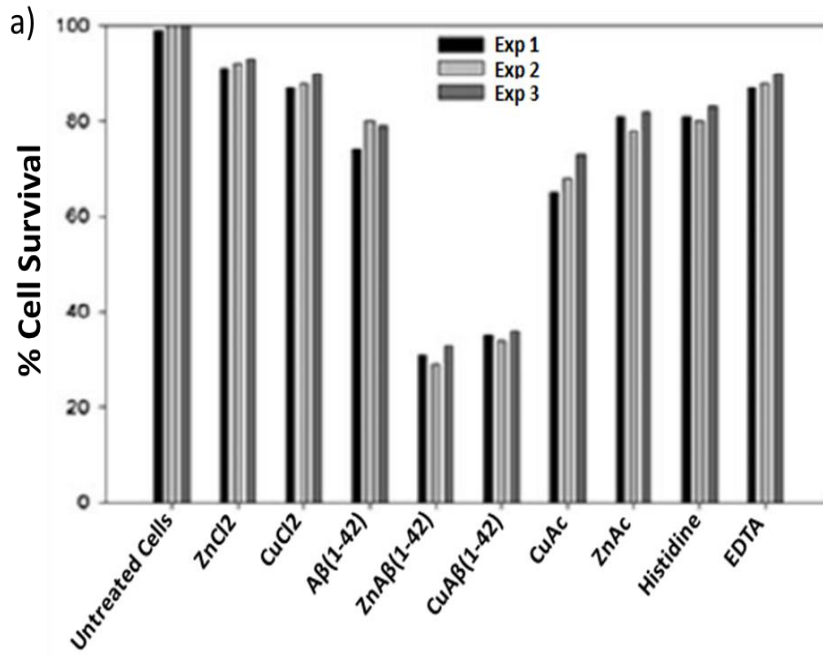


Figure 3.5: Contd. on pg 72

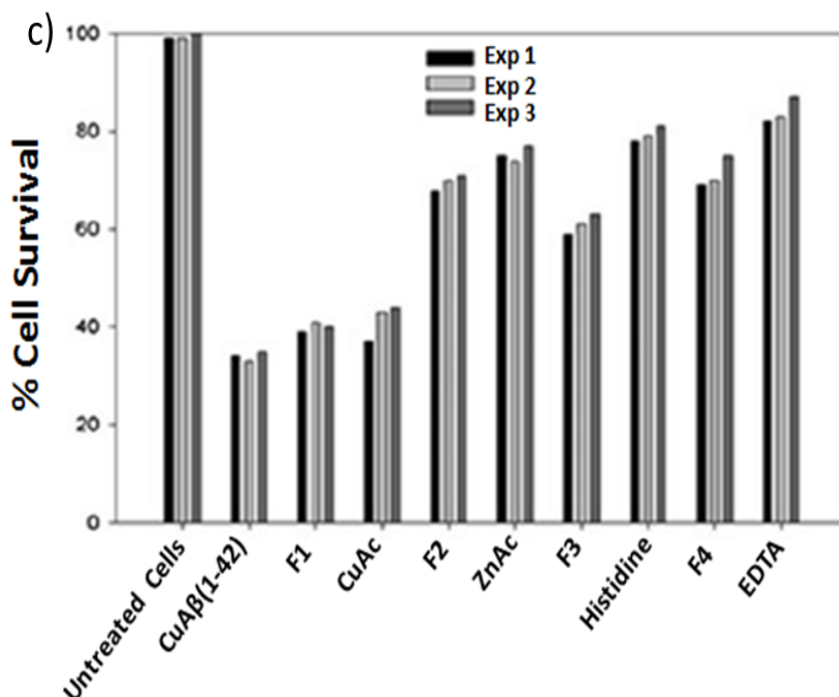


Figure 3.5: Effect of ZnAβ(1-42) and CuAβ(1-42) aggregates on cell viability, (b) effect of the modified NLPs on reversing neurotoxicity of ZnAβ(1-42) aggregates and (c) effect of the modified NLPs on neurotoxicity induced by CuAβ(1-42) aggregates. NLPs surface modified with chelating ligands (F1,CuAc), F2, ZnAc; F3, histidine and F4, EDTA.

3.3.8. *Ex vivo* uptake of modified chelating ligand-bound nanoliposomes

To investigate the effect of the chelating ligands (EDTA, histidine and ZnAc) on mediated NLPs internalization, *ex vivo* samples were characterized by CSEM and fluorescence imaging (Victor™X3 Perkin Elmer Inc., USA). Analysis was performed in the presence of the metal ions Cu(II) or Zn(II) ions and results are shown in Figures 3.6 and 3.7. Results depicted cellular uptake by the labeled NLPs in the presence of Cu(II) after 24 hours. Modified NLPs (EDTA, histidine and ZnAc) were most efficiently taken up by PC12 neuronal cells in the presence of Cu(II) from 6-24 hours (Figure 3.6a). Figure 3.6b shows that modified NLPs (with EDTA, histidine and ZnAc) were most efficiently taken up by PC12 cells when compared with unmodified NLPs in the presence of Zn(II). Unmodified NLPs and CuAc-bound NLPs showed no

significant fluorescence activity in the presence of either Zn(II) or Cu(II). Confocal images did not show any significant difference on the uptake of modified NLPs by the cells since the results were field dependent (Figure 3.7). Overall, these studies demonstrated that the modified chelating ligand bound NLPs had a greater cellular uptake in the presence of either Zn(II) or Cu(II) ions. This data also indicated that intracellular uptake of NLPs was mediated by the surface engineered chelating ligands on the NLPs.

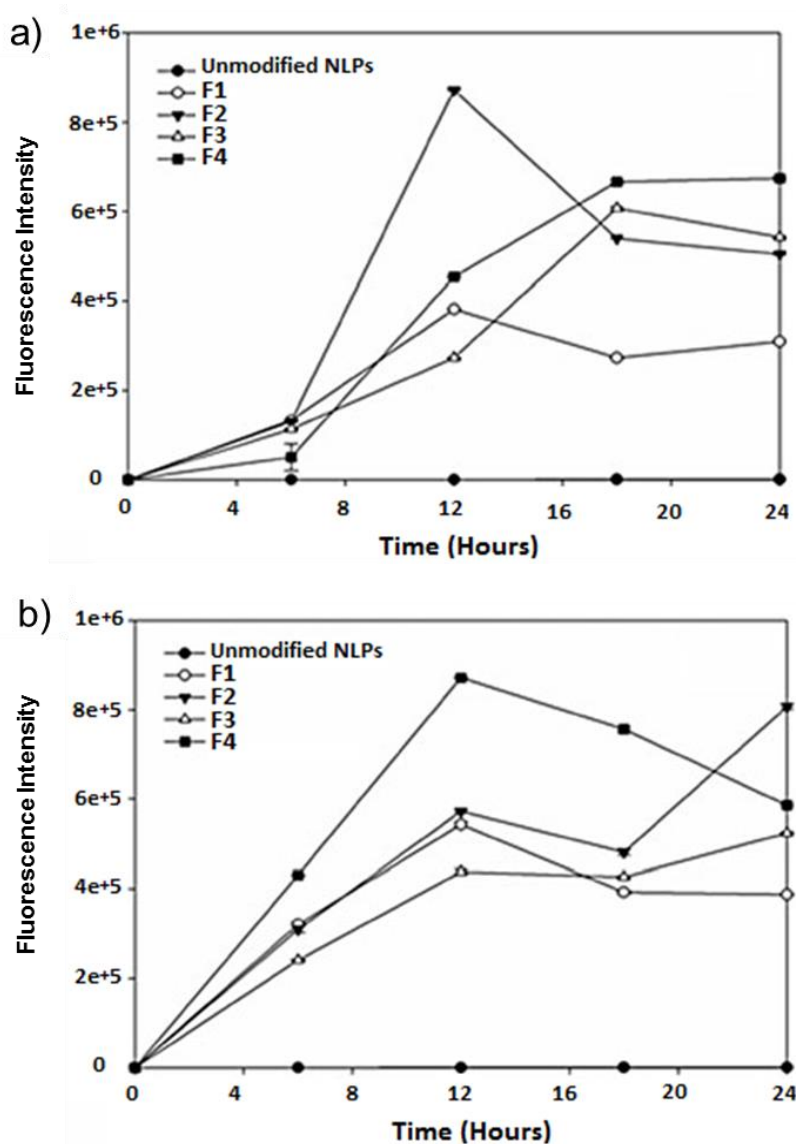


Figure 3.6: Cellular uptake profiles of modified NLPs in the presence of (a) Cu (II) ions and (b) Zn(II) ions. NLPs surface modified with chelating ligand (F1, CuAc), F2, ZnAc; F3, histidine and F4, EDTA

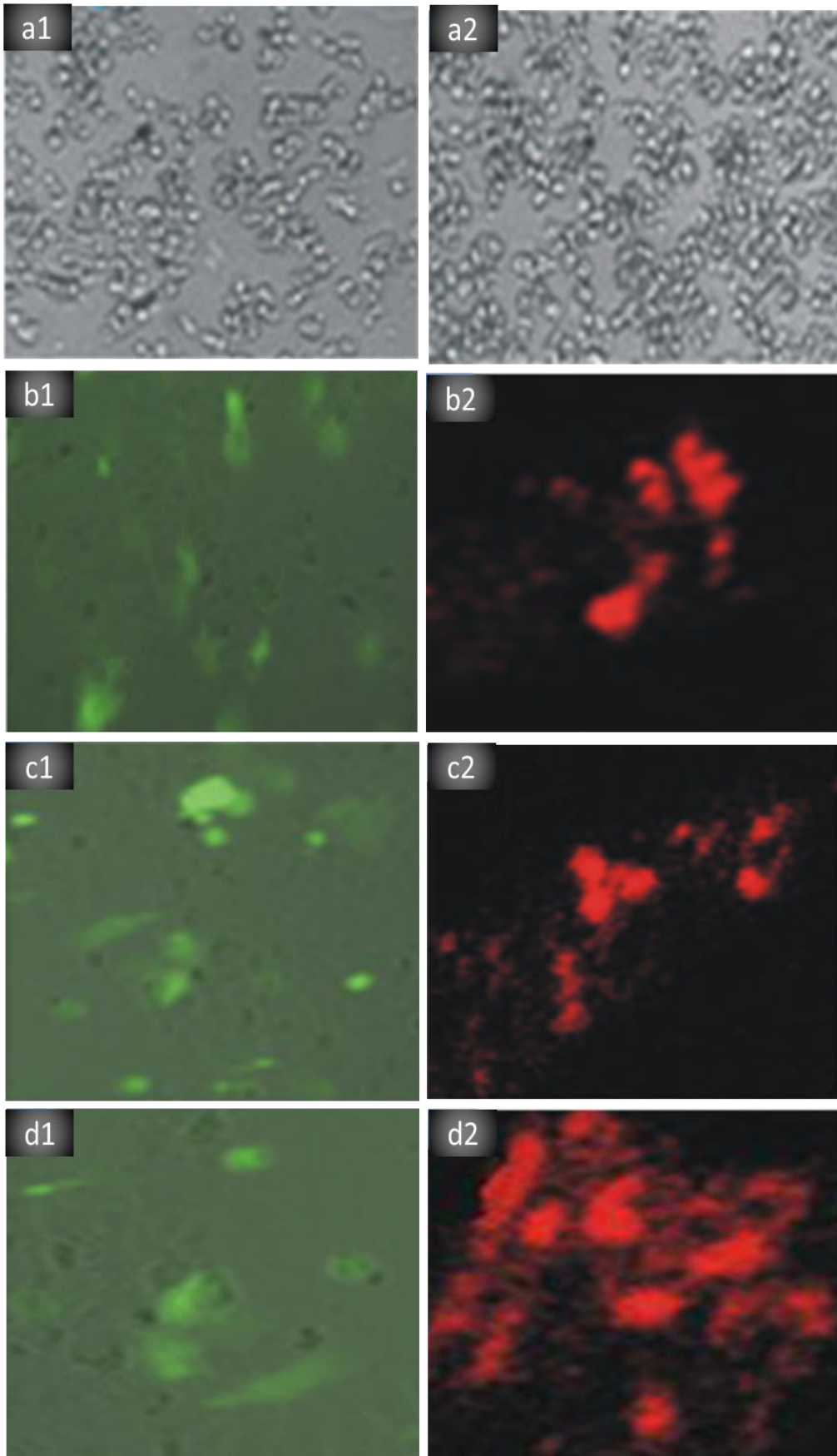


Figure 3.7: *Contd. on pg 75*

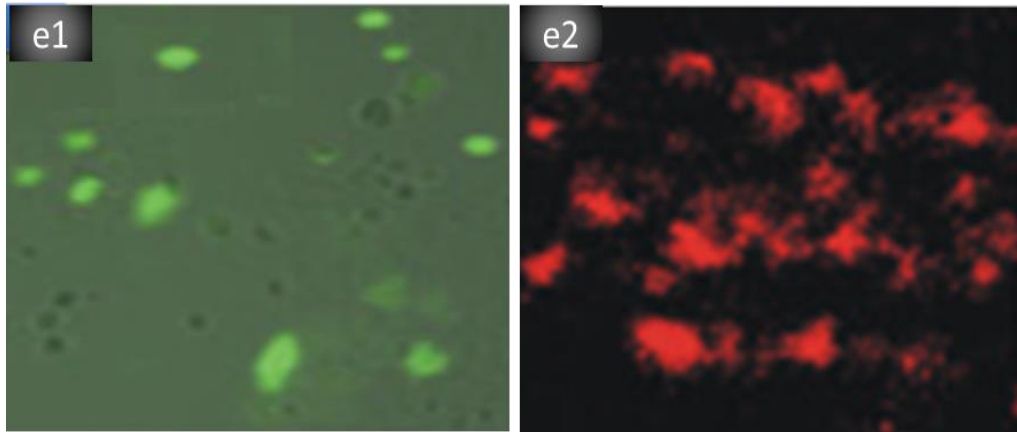


Figure 3.7: Light and fluorescent microscopy analysis of PC12 cell line incubated in for 24 hours (a1-2) with labeled FITC or rhodamine NLPs; (b1-2) surface engineered with CuAc; (c1-2) surface engineered ZnAc, (d1-2) surface engineered EDTA and (e1-2) surface-engineered histidine (Magnification 100x).

3.3.9. Molecular mechanics energy relationship (MMER) analysis

MMER, a method for analytico-mathematical representation of potential energy surfaces, was used to provide evidence of the contributions of valence terms, non-covalent Coulombic terms, and non-covalent van der Waals interactions for chelation and nanostructure formation. The MMER model for potential energy in various molecular complexes can be written as shown in Eq. 3.2.

$$E_{\text{molecule/complex}} = V_{\Sigma} = V_b + V_{\theta} + V_{\varphi} + V_{ij} + V_{hb} + V_{el} \dots\dots\dots \text{Eq.3.2}$$

Where, V_{Σ} is related to total steric energy for an optimized structure, V_b corresponds to bond stretching contributions, V_{θ} denotes bond angle contributions, V_{φ} represents torsional contribution arising from deviations from optimum dihedral angles, V_{ij} incorporates van der Waals interactions due to non-bonded interatomic distances, V_{hb} symbolizes hydrogen-bond energy function and V_{el} denoted the electrostatic energy (Choonara et al., 2011). In the present study, the global energy relationships

for the various complexes derived after assisted model building and energy refinements are shown in Eqs. 3.3-3.13

$$E_{\text{DSPE-PEG}} = 57.33 V_{\Sigma} = 2.49 V_b + 17.35 V_{\theta} + 42.18 V_{\varphi} - 4.68 V_{ij} - 0.005 V_h \dots \text{Eq.3.3}$$

$$E_{\text{DSPC}} = 19.31 V_{\Sigma} = 0.91 V_b + 6.30 V_{\theta} + 4.26 V_{\varphi} + 7.85 V_{ij} - 0.0007 V_{hb} \dots \text{Eq.3.4}$$

$$E_{\text{DSPE-PEG/DSPC}} = 49.36 V_{\Sigma} = 2.43 V_b + 16.32 V_{\theta} + 39.76 V_{\varphi} + - 8.96 V_{ij} - 0.19 V_{hb} \dots \text{Eq.3.5}$$

$$\Delta E = -27.273 \text{kcal/mol}$$

$$E_{\text{CHOL4}} = 152.984 V_{\Sigma} = 7.56 V_b + 45.76 V_{\theta} + 56.68 V_{\varphi} + 42.97 V_{ij} \dots \text{Eq.3.6}$$

$$E_{\text{DSPE-PEG/DSPC/CHOL}} = 149.83 V_{\Sigma} = 9.65 V_b + 62.29 V_{\theta} + 102.22 V_{\varphi} - 24.29 V_{ij} - 0.032 V_{hb} \dots \text{Eq.3.7}$$

$$\Delta E = -79.786 \text{kcal/mol}$$

$$E_{\text{A}\beta\text{-21}} = -131.39 V_{\Sigma} = 3.26 V_b + 58.04 V_{\theta} + 15.17 V_{\varphi} - 18.41 V_{ij} - 4.22 V_{hb} - 185.23 V_{el} \dots \text{Eq.3.8}$$

$$E_{\text{A}\beta\text{-Cu(II)}} = -133.51 V_{\Sigma} = 3.24 V_b + 58.12 V_{\theta} + 15.14 V_{\varphi} - 20.52 V_{ij} - 4.25 V_{hb} - 185.24 V_{el} \dots \text{Eq.3.9}$$

$$\Delta E = -2.122 \text{kcal/mol}$$

$$E_{\text{A}\beta\text{-Zn(II)}} = -137.07 V_{\Sigma} = 3.23 V_b + 58.15 V_{\theta} + 15.07 V_{\varphi} - 24.13 V_{ij} - 4.24 V_{hb} - 185.15 V_{el} \dots \text{Eq.3.10}$$

$$\Delta E = -5.683 \text{kcal/mol}$$

$$E_{\text{EDTA}} = 6.13 V_{\Sigma} = 0.42 V_b + 1.27 V_{\theta} + 2.79 V_{\varphi} + 1.65 V_{ij} \dots \text{Eq.3.11}$$

$$E_{\text{A}\beta\text{-Cu(II)-EDTA}} = -140.79 V_{\Sigma} = 3.63 V_b + 59.46 V_{\theta} + 16.30 V_{\varphi} - 31.30 V_{ij} - 4.27 V_{hb} - 184.61 V_{el} \dots \text{Eq.3.12}$$

$$\Delta E = -13.406 \text{kcal/mol}$$

$$E_{\text{A}\beta\text{-Zn(II)-EDTA}} = -135.42 V_{\Sigma} = 3.59 V_b + 59.87 V_{\theta} + 18.66 V_{\varphi} - 27.79 V_{ij} - 4.43 V_{hb} - 185.32 V_{el} \dots \text{Eq.3.13}$$

$$\Delta E = -4.476 \text{kcal/mol}$$

3.3.10. Formation of the nanoliposomal system

It is evident from the energy computations (Eqs. 3.3-3.7) that the nanoliposomal system was stabilized in terms of respective steric or potential energy factors. The preferred orientation of the polymers in the presence and absence of surfactant molecule is depicted in Figure 3.8. Starting with a DSPE-PEG/DSPC binary system, the miscibility behavior of PC and DSPE-PEGs are known to be controversial for the formation of spherical particles since they are completely immiscible at all relevant pressures and compositions (Lozano and Longo, 2009). In this Chapter, we used 1, 2 distearoyl-sn-glycero-3-phosphocholine with DSPE-PEG in order to form a

stoichiometric condensed complex, DSPE-PEG/DSPC that is miscible with an energy stabilization of $\Delta E_0 - 27.273$ kcal/mol (Eqs. 3-5). The energy was mainly stabilized in terms of bond angles and torsional contributions (bonding energies) as well as London dispersion forces and H-bonding (nonbonding interaction). Among these forces, H-bonding stabilization was 40 times (due to the presence of the glycerol functionality) greater than the combination, which led to a stabilized molecular entity. Although, the blend was miscible, the formation of a liposomal system was still a challenge. To further increase the stabilization of the system, cholesterol (in excess) was introduced to act as filler in the space lattice of the binary system as shown in Figure 3.8. This ternary system led to a super-stable molecular structure, with a further decrease in constituent energies (Eqs. 3.6-3.7; $\Delta E_0 - 79.786$ kcal/mol) mainly in the form of van der Waals forces compared to H-bonding. This change in stabilization from H-bonding to van der Waals forces was due to hydrophobic interactions arising from the inclusion of cholesterol (over powering the glycerol induced hydrophilic forces) leading to the formation of NLPs in excess of phosphate buffered saline.

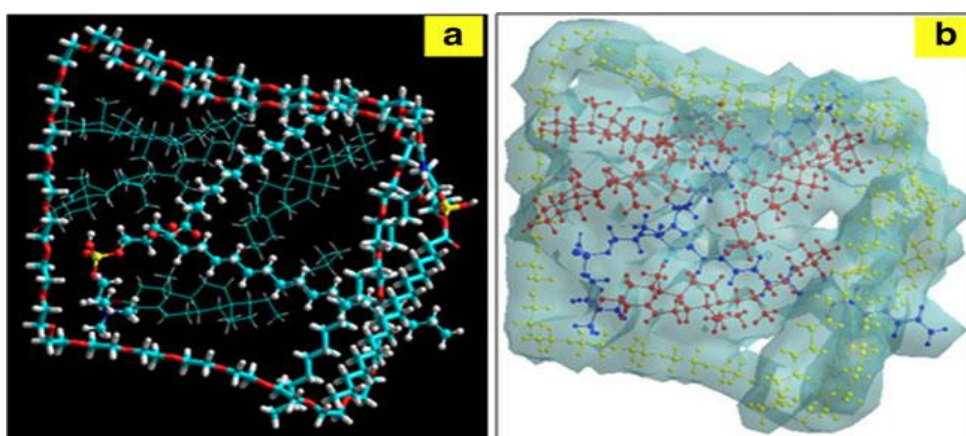


Figure 3.8: Visualization of (a) geometrical preferences (color codes: C (cyan), O (red), N (blue), P (yellow) and H (white)); and (b) Connolly molecular electrostatic potential surfaces (color codes: DSPE-PEG (yellow), DSPC (blue) and CHOL (red)) in translucent display mode showing the nanoliposomal after molecular simulation in vacuum

3.3.11. Energy transformations involving metal binding, aggregation and chelation

To study the effect of chelating agents, A β protein was individually modelled in conjugation with Cu(II) and Zn(II) followed by treating the energy minimized/stabilized molecular structures with EDTA (a metal chelator) as the prototype (Figures 3.9 and 3.10). To increase the efficiency and selectivity of the computational process, we employed A β 10-21 (YEVHHQ KLVFFA) containing the His13 and His14 residues as a theoretical model variant instead of A β 1-42 (Morgan et al., 2002). Systematic combination of the ligand atoms were studied in several possible binding sites and modes for evaluating the optimum metal/protein energy minimized configurations of Cu(II)/Zn(II) binding to A β 10-21. The metal ions form close van der Waals space interactions with the A β protein, as depicted in Figures 3.10a and 11a for Cu-A β and Zn-A β , respectively. The main region of interaction with minimized energy was His13-Cu(II)/His13-Zn(II) (with no H₂O molecules involved) which was in accordance with previously reported studies (Daxiong et al., 2008). Although Zn(II) displayed a more stable protein complexation (Eqs. 3.8-3.10), both metal ions/protein interactions resulted in near equivalent minimization in potential energy ($\Delta E_{\text{Cu-A}\beta}$ -2.122 kcal/mol; $\Delta E_{\text{Zn-A}\beta}$ -5.683 kcal/mol) which was due to the close proximity of these metals within the periodic table and similar van der Waals radius. This observation was supported by the MMER analysis (Eqs. 3.8-3.10), where it was evident that London dispersion/van der Waals forces (hydrophobic interactions) led the entire energy minimization process. The effect of adding a chelating agent on resolubilization of the aggregated A β protein (metal-induced aggregation) was modelled using EDTA as the prototype where a marked effect on the geometrical configuration of the metal/protein complex was observed.

As soon as the EDTA molecule was in proximity to the van der Waals radius of the metal ion, it engulfed the metal ion with the so called “acetic acid claws”. Interesting binding of the A β protein with EDTA in the case of A β -Cu (II)-EDTA confirmed the selectivity of A β towards the chelating agent in comparison to the metal ion, which led to resolubilization. The stabilization in energies was not comparable with ΔE_0 -13.406 kcal/mol and ΔE_0 -4.476 kcal/mol in the case of A β -Cu(II)-EDTA and A β -Zn(II)-EDTA, respectively (Eqs. 3.11-3.13), respectively. This difference in energy was attributed to a decrease in dispersion forces and increased non-bonding interaction in the case of A β -Cu (II)-EDTA with the formation of H-bonds. In addition, close examination of the geometrical conformations clearly depicted the preference of metal ions towards EDTA (i.e. the chelating agents successfully extracted the metal ions from the A β -Cu(II)/A β -Zn(II) complex). This corroborates well with the observed *in vitro* experimental results where chelating ligand-bound modified NLPs modulated CuA β (1-42)/ ZnA β (1-42) aggregates.

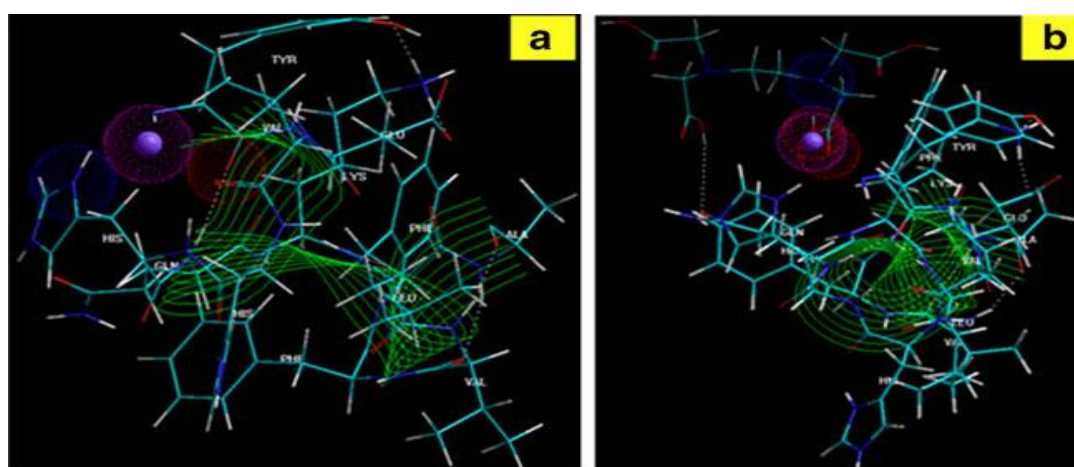


Figure 3.9: Visualization of geometrical preferences of (a) A β (10-21)-Cu (II) and (b) β (10-21)-Cu (II)-EDTA after molecular simulation in vacuum. Color codes: c (cyan), O (red), N (blue), P (yellow), H (white) and Cu (violet). Dots represent the overlapping van der Waals radii and the ribbon represents the secondary structure.

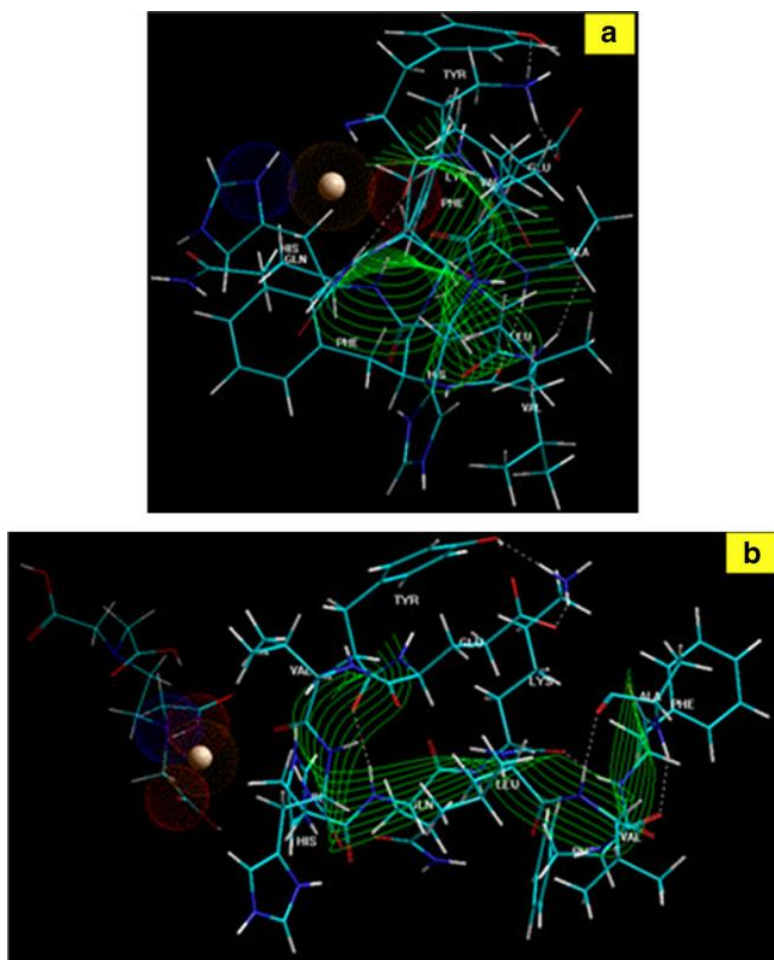


Figure 3.10: Visualization of geometrical preferences of (a) A β (10-21)-Zn(II) and (b) A β (10-21)-Zn(II)-EDTA after molecular simulation in vacuum. Color codes: C (cyan), O (red), N (blue), P (yellow), H (white) and Zn (brown). Dots represent the overlapping van der Waals radii and the ribbon represents the secondary structure.

3.4. Concluding Remarks

The outcome of this Chapter addressed the production of a novel NLPs surface engineered with chelating ligands. The chelating ligands were successfully conjugating onto the surface of NLPs using either covalent or non-covalent conjugation procedures (Chapter 3, Section 3.2.4, Figure 3.1; Table 3.2). Modification of the NLPs did not have a significant effect on the size of the NLPs when compared with unmodified NLPs, which renders them suitable for crossing the BBB. *In vitro* studies confirmed that the incubation of Cu(II) or Zn(II) with A β (1-42) peptide stimulated A β -aggregation. Modified NLPs (with EDTA, histidine and ZnAc)

were suitable for resolubilization of CuA β (1-42) and ZnA β (1-42) aggregates *in vitro*. Furthermore, the high survival of PC12 neuronal cells after treatment with modified NLPs was influenced by inhibition of A β (1-42) aggregates, thereby protecting the cells from A β (1-42) aggregate related toxicity. High fluorescence microscopy also revealed that the modified NLPs in the presence of Zn(II) or Cu(II) was influenced by an ionophore process or macropinocytosis, which is non-receptor mediated endocytosis or a biological metal ion pathway. The surface modified NLPs were able to protect PC12 neuronal cells from insoluble A β -peptides associated with neurotoxicity in AD. The *in vitro* studies (as discussed in Chapter 3, section 3.3.5) were well corroborated by the *in silico* molecular mechanistic studies (as discussed in Chapter 3, section 3.3.10) thus further confirming the potential of NLPs/chelation therapy for AD.

CHAPTER 4

FORMULATION OF THE LIGAND-FUNCTIONALIZED NANOLIPOSOMES FOR TARGETED DELIVERY OF GALANTAMINE IN ALZHEIMER'S DISEASE

4.1. Introduction

The development of novel targeted drug delivery systems that are capable of enhancing neuroprotectant efficacy for CNS disease management such as NDs has gained a lot of attention in recent years (Roney et al., 2005). AD is one of the fatal ND's, characterized by the aggregation of β -amyloid ($A\beta$) peptides that accumulate into plaques and neurofibrillary tangles comprising hyperphosphorylated tau proteins (Kowalska, 2004; Delacourte, 2005; Marino et al., 2010). Currently, most neuroactive drug therapies against AD are associated with several disadvantages such as: i) being beneficial only in higher doses; ii) having limited bioavailability; iii) possessing poor absorption following systemic delivery; iv) severe peripheral side-effects due to higher uptake by normal cells; and v) difficulty in penetrating the highly restrictive BBB (Rubin and Staddon, 1999; Roney et al., 2005). Studies have shown that the BBB restricts the entry of large molecules into the CNS, while smaller lipophilic molecules, peptides and nutrients satisfy BBB penetration via endogenous transporters (Kroll and Neuwelt, 1998; Pardridge, 2003). Galantamine (GAL) is a neuroactive drug that is currently approved by the USA Food and Drug Administration (FDA) and the European Medicines Agency (EMA) for the symptomatic treatment of AD due to its ability to moderate acetylcholinesterase inhibition in the CNS (Heinrich and Lee Teoh, 2004; Shytle et al., 2004). Its potentiating effects are derived from allosteric interaction with nicotinic acetylcholine

receptors (nAChRs) that enhance the sensitivity of the receptors to acetylcholine (Erkinjuntti, 2002). In a recent study, it has been demonstrated that GAL may also prevent A β aggregation and A β induction of neuronal apoptosis (Matharu et al., 2009; Liu et al., 2010). However, the clinical utility of the drug is hampered by its poor retention in the CNS and the intricacy of transporting it across the BBB (De Boer and Gaillard, 2007; Ying et al., 2010). Several strategies employing liposomes have been developed in order to enhance the CNS bioavailability of neuroactive drugs (Bangham et al., 1974). Liposomes are vesicles comprising concentric bilayer phospholipid-based membranes that can incorporate hydrophilic or hydrophobic drugs and achieve targeted drug delivery to the CNS (Woodle and Lasic, 1992; Gabizon and Papahadjopoulos, 1988; Veerareddy and Vobalaboina, 2004; Torchilin, 2005; Immordino et al., 2006; Drummond et al., 2008). However, liposomes have reduced blood circulation times due to high uptake by macrophage cells of the reticuloendothelial system (RES).

Surface-modified liposomes with either polyethylene glycol (PEG), chitosan (CHT), silk-fibroin or polyvinyl alcohol (PVA) have shown to enhance the blood circulation half-life of liposomes (Allen et al., 2002; Gobin et al., 2006; Immordino et al., 2006; Nakano et al., 2008; Yousefi et al., 2009; Wang et al., 2010; Ruizhen et al., 2011). In addition, liposomal formulations have been approved by the US FDA for clinical use (Veerareddy and Vobalaboina, 2004; Immordino et al., 2006). A study conducted by Rousseau and co-workers (1999) demonstrated the successful localization of liposomes within the CNS. Although liposomes can satisfy BBB penetrability, they are associated with the inability to access and penetrate targeted regions within the CNS. This results in intracellular uptake of drug by normal cells as

well (De Boer and Gaillard, 2007). Various types of targeted liposomes have been developed in order to evade drug uptake by normal cells using targeting moieties such as glucose, folic acid, polysaccharides, antibodies, glycoproteins and peptide ligands to further enhance the drug delivery specificity and increase the therapeutic efficacy (Scherphof et al., 1985, Schnyder and Huwyler, 2005; Suzuki et al., 2008; Torchilin et al., 2008; Yamada et al., 2008). Antibodies, peptides and glycoproteins have been largely reported as drug markers due to their molecular constituency of known amino acid sequences, ease of engineering onto liposome surfaces, and binding with high affinity to specific cell-surface receptors (Mufamadi et al., 2011). In addition, targeted liposomes (with ligands) can further improve the specificity and efficacy in tissues or cells via over expressed surface receptors such as Serpin Enzyme Complex-Receptor (SEC-R), antigens and unregulated selectin (Boland et al., 1995; Ziady et al., 1997; Hossen et al., 2010; Simonis et al., 2010, Yu et al., 2010). SEC-R has been reported to have a high affinity for binding with the α 1-antitrypsin domain (Perlmutter et al., 1990). A study by Boland and co-workers (1995) demonstrated SEC-R expressed on the surface of hepatoma and neuronal (PC12) cells and their interaction with soluble and non-toxic A β -peptides. Another study undertaken by Ziady and co-workers (1997) showed synthetic peptide CI315 was able to deliver genes to hepatoma cells via SEC-R. Furthermore, Patel and co-workers (2001) reported that two synthetic peptides, namely polylysine antitrypsin and antitrypsin delivered DNA to hepatocytes cells via SEC-R.

Therefore, the aim of this Chapter was to design optimized ligand-functionalized NLPs with maximum synthetic coupling of the peptide (Lys-Val-Leu-Phe-Leu-Ser-NH₂) onto the surface of the NLPs. In addition, the goal was also to achieve

maximum drug entrapment efficiency, desirable targeting, uptake and release of galantamine (GAL) specifically to neuronal cells. The optimized ligand-functionalized NLPs were further assessed for cytotoxicity and intracellular uptake on PC12 neuronal cells via SEC-R in a mediated manner. The energetic profile for the nanonization of the liposomal system and the peptide-DSPE reactional profile was generated and corroborated with experimental and analytical data using Molecular Mechanics Energy Relationships by exploring the spatial disposition of energy minimized molecular structures.

4.2. Materials and Methods

4.2.1. Materials

Phospholipids included distearoyl-sn-glycero-phosphatidylcholine (DSPC), cholesterol (CHOL), and 1,2-distearoyl-sn-glycero-3-phosphatidyl-ethanolamine-methoxypolyethyleneglycol-2000 (DSPE). Fluorescein isothiocyanate (FITC), N-hydroxysulfosuccinimide (NHS) and N,N'-dicyclohexylcarbodiimide (DCC) purchased from Sigma-Aldrich (St. Louise, MO, USA). Dimethylsulfoxide (DMSO), sodium hydroxide (NaOH) and potassium dihydrogen phosphate (KH_2PO_4) were purchased from Saarchem (Pty) Ltd. (Brakpan, South Africa). Membrane filters (0.22 μm) purchased from Millipore (Billerica, MA, USA). Liquid nitrogen was purchased from Afrox Ltd., (Industria West, Germiston, South Africa). RPMI-1640 media (with L-glutamine and sodium bicarbonate), fetal bovine serum (heat inactivated), horse serum (heat inactivated), 1% penicillin (100IU/mL) and streptomycin (100 $\mu\text{g}/\text{mL}$) were used for the cell culture studies and were purchased from Sigma-Aldrich (St. Louise, MO, USA). The CytoTox-Glo™ Assay Kit was purchased from Promega

Corporation (Madison, WI, USA). All other solvents and reagents were of analytical grade and were used as received.

4.2.2. Preparation of the nanoliposomes

NLPs were prepared as previously described in Chapter 3, section 3.2.2 employing adapted reverse-phase evaporation technique describes by Suzuki and co-workers (2007). For preparing the FITC-labeled NLPs, the lipid film was hydrated in 48mM of FITC at 65°C for 30-40 min, thereafter cooled to 4°C to form multilamellar vesicles (MLV). For the GAL-loaded NLPs, 30mg of the lipid film and 1.5mg/mL of GAL was hydrated in 130mM ammonium sulfate and 4mL PBS buffer at pH7.4 for 30 min at 65°C. Thereafter the mixture was cooled to 4°C and dialyzed against PBS buffer at pH7.4 or 5% w/v dextrose to remove the ammonia and residual drug (Haran et al., 1993; Song et al., 2008; Ke et al., 2011, Accardo et al., 2012). Alternatively, residual drug and fluorescence were separated by centrifugation (Optima[®] LE-80K, Beckman, USA) in PBS buffer at pH7.4 (1000rpm; 30 min). Unilamellar NLPs were obtained by a freeze-thawing technique. Briefly, NLPs solutions were firstly frozen at -80°C using liquid nitrogen followed by thawing on a waterbath set at 37°C (N=6) (Yagi et al., 2000). Thereafter samples were placed in an ultrasonic bath at 50kHz for 5 min before being stored at 4°C. Particle size obtained by gradual extrusion of the NLPs formulation through a 0.22µm pore size polycarbonate membrane filter (Millipore, Billerica, MA, USA) (Verma et al., 2003; Zhua et al., 2007).

4.2.3. Optimization of the ligand-functionalized nanoliposomes

A Box-Behnken experimental design was constructed to produce experimental NLPs formulations for optimization of the formulation variables. The design comprised 15

experimental runs. DSPC (mg), CHOL (mg), and DSPE (mg) were selected as the independent formulation variables (Table 4.1) followed by determining the effects of the dependent formulation variables such as the particle size, zeta potential, polydispersity index (Pdl), drug entrapment efficiency (DEE) and *in vitro* drug release. Optimization for the ligand-functionalized NLPs were subsequently undertaken on Minitab® V15 software (Minitab Inc., State College, PA, USA) (Table 4.2). The peptide coupling efficiency (PCE) and DEE were maximized to ensure that maximum GAL was entrapped within the NLPs and that the functionalized moieties of the ligands were sufficiently engineered onto the surface of the NLPs. Drug release (in terms of the Mean Dissolution Time - MDT) were minimized to ensure that there was maintenance of adequate GAL levels by the ligand-functionalized NLPs over a prolonged period of time.

Table 4.1. Box-Behnken experimental design template for producing the NLPs with quantity of DSPC, CHOL and DSPE used in each experimental formulation

F#	DSPC (mg)	CHOL (mg)	DSPE (mg)
1	10	100	12.5
2	100	62.5	20
3	10	62.5	20
4	55	62.5	12.5
5	55	100	5
6	100	100	12.5
7	10	62.5	5
8	55	62.5	12.5
9	55	25	5
10	100	25	12.5
11	55	25	20
12	55	62.5	12.5
13	55	100	20
14	10	25	12.5
15	100	62.5	5

Table 4.2. Independent formulation variables and measured responses employed.

Independent Variables	Level		
	High	Current	Low
DSPC	100	63.3284	10
CHOL	100	74.4749	25
DSPE	20	6.5801	5
	1	0	-1
Measured Responses	Objective		
Peptide Coupling Efficiency	Maximize		
Drug Entrapment Efficiency	Maximize		
Drug Release	Minimize		
Mean Dissolution Time	Minimize		

4.2.4. Surface-engineering of synthetic peptide ligands onto the nanoliposomes

Peptides were synthesized by SBS Genetech Co. (Pty) Ltd. (Shanghai, China) employing Fmoc-chemistry with an HPLC purity > 98%. In order to synthesize the ligand-functionalized NLPs, native NLPs were allowed to react with 46mg of NHS in the presence of 87mg of DCC after dissolving in 100 μ L of methanol or DMSO and 4mL of PBS buffer at pH 7.2. After maintenance at room temperature for 45 minutes, 10mg/mL of synthetic peptide was added to the treated NLPs suspension and allowed to react for another 6 hours at room temperature (Figure 4.1). For comparison purposes three different ligands were investigated as shown in Figure 4.1. Thereafter, solvents were removed by rotary evaporation, water bath with temperature maintained at 65°C for 2-3 hours. This was followed by dialyzing the ligand-functionalized NLPs against PBS buffer at pH 7.4 using SnakeSkin™ Pleated dialysis tubing of (10,000 MWCO; Sigma-Aldrich, St. Louise, MO, USA) for 24 hours to remove excess DCC, NHS and uncoupled synthetic peptide ligands. The ligand-

functionalized NLPs were further stabilized by a freeze-thawing technique and then stored at 4°C for further use. The peptide coupling efficiency (PCE) onto the surface of the NLPs was measured by a NanoPhotometer™ spectrophotometer (Implen GmbH, Munich, Germany). Briefly, 2mL of 0.5% v/v triton X-100 in methanol was added to 2mL of the ligand-functionalized NLPs suspension and allowed to react for 2 hours at 45°C in a laboratory oven. The absorbance of the final solution was measured at $\lambda_{max}=285nm$ against native (non-functionalized) nanoliposomes. The PCE value was used to confirm the total quantity of synthetic peptide ligands coupled onto the surface of the NLPs and was computed using Eq. 4.1.

$$PCE\% = \frac{Aq}{Tq} \times 100 \dots \dots \dots \text{Eq. 4.1}$$

Where Aq is the actual quantity of synthetic peptide ligand coupled onto the NLPs surface and Tq is the theoretical quantity of the synthetic peptide ligand utilized during the coupling reaction for synthesizing the ligand-functionalized NLPs.

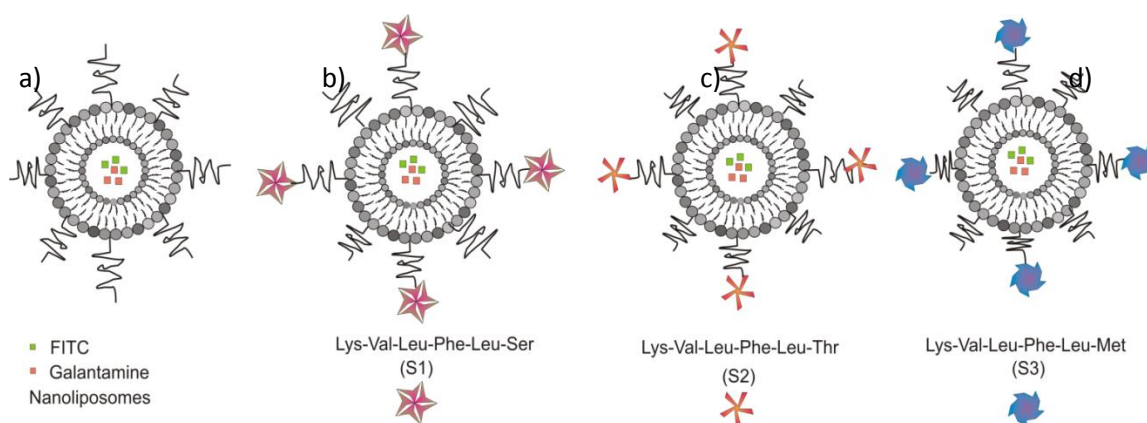


Figure 4.1: Schematic representation of FITC or GAL-loaded ligand-functionalized NLPs showing; a) drug-loaded NLPs, b) GAL-loaded functionalized NLPs with ligand 1, c) ligand 2 and d) ligand 3.

4.2.5. Determination of the drug entrapment efficiency of the ligand-functionalized nanoliposomes

In order to determine the entrapment efficiency of GAL within the ligand-functionalized NLPs, samples solubilized into a sufficient volume of 0.5% v/v triton X-100 in methanol solution. The drug content released from the ruptured NLPs was separated by centrifugation (Optima® LE-80K, Beckman, USA) at 10,000rpm for 20 minutes. Thereafter the supernatant was used for UV absorbance measurement at a fixed wavelength of $\lambda_{\max}=288\text{nm}$ and computed utilizing a standard linear curve of GAL in concentrations between 0.1-5.0 $\mu\text{g/mL}$ in PBS (pH 6.8; 37°C); $R^2=0.99$). The DEE value used to validate the total GAL content within the NLPs and computed using Eq. 4.2.

$$\text{DEE \%} = \frac{Aq}{Tq} \times 100 \dots\dots\dots \text{Eq 4.2}$$

Where Aq is the actual quantity of GAL measured by UV spectrophotometry and Tq is the theoretical quantity of GAL added in the NLPs formulation.

4.2.6. Physicochemical characterization of the ligand-functionalized nanoliposomes

Physicochemical characterizations of the ligand-functionalized NLPs were undertaken, which were analyzed either as samples suspended in PBS buffer at pH 7.4 or as a lyophilized powder (both GAL-loaded native and ligand-functionalized NLPs). A lyophilized powder of the formulation was pre-formed in the presence of a cryoprotectant (0.5% w/v sucrose) that protected the NLPs membranes from destruction or leakage of the entrapped GAL due to mechanical stress during freezing and dehydration (Chen et al., 2010). Briefly, 2.5mL of cryoprotectant (1.5%) in water was firstly mixed with 2.5mL of PBS buffer at pH 7.4 and thereafter added to

sample solutions (5mL) and subjected to both freeze-thaw and freeze-drying processes.

4.2.7. Analyses of the molecular structural variation due to nanoliposomes formulation

Fourier Transmission Infrared (FTIR) spectrophotometry of the ligand-functionalized NLPs was performed in order to characterize the potential molecular structural interactions of the synthetic peptide ligands and the NLPs comprising DSPE on the surface of the NLPs. Analyses was undertaken at high resolution with wavenumbers ranging from 400-4000 cm^{-1} on a FTIR Spectrophotometer using PerkinElmer® spectrum quant software (Perkin Elmer Inc. MA, USA).

4.2.8. Thermal characterization of the ligand-functionalized nanoliposomes

Temperature Modulated Differential Scanning Calorimetry (TMDSC) analysis of native NLPs, GAL-loaded NLPs and GAL-loaded ligand-functionalized NLPs was undertaken (Mettler Toledo DSC1 STARe System, Switzerland) in order to determine the multiple glass transition temperature (T_g), endothermic melting temperature (T_m) and crystallization temperature (T_c) peaks that were consequences of irreversible heat flow corresponding to the total heat flow. Indium was used to calibrate the instrument and samples (5.2-6.5mg) were weighed in standard DSC aluminum pans and analyzed within a temperature gradient of 20-240°C under an 8kPa nitrogen atmosphere. A bare pan served as a reference for all TMDSC scans. The instrument parameters and settings employed are shown in Table 4.3.

4.2.9. Particle size and distribution analysis of the ligand-functionalized nanoliposomes

The average particle size and polydispersity index (Pdl) of GAL-loaded ligand-functionalized NLPs measured by Dynamic Light Scattering (DLS) measurements using a Zetasizer NanoZS (Malvern Instruments, Worcestershire, UK) at a fixed angle of 90°C and 25°C. Prior to measurement, the NLPs were diluted 1:10 with filtered PBS buffer at pH 7.4. Disposable cuvettes were used for particle sizing and measurements were undertaken in triplicate with multiple iterations for each run in order to elute size intensity profiles over time. The average value of three measurements was recorded. The Pdl values measure of the distribution of the particulate population (Baek et al., 2009).

Table 4.3. Temperature Modulated Differential Scanning Calorimetry settings employed for thermal analysis of the NLPs

Segment Type	Parameter Setting
SINE PHASE^a	
Heat rate	20°C
Amplitude	1°C/min
Period	0.8°C
LOOP PHASE^b	
Segment	1
Increment	0.8°C
End	240°C
Count	436

^aSinusoidal oscillations, ^bOscillation period

4.2.10. Zeta potential analysis of the ligand-functionalized nanoliposomes

In order to confirm the physical stability and surface charge of the GAL-loaded ligand-functionalized NLPs, samples were analyzed for their zeta potential using a Zetasizer NanoZS (Malvern Instruments, Worcestershire, UK). Prior to measurement, GAL-loaded ligand-functionalized NLPs were produced in accordance with the Box-Behnken experimental design template and were diluted with deionized water in a 1:10 ratio and extruded through a polycarbonate filter (0.22 μ m, Millipore Corp., Bedford, MA, USA). Disposable quartz cuvettes were used for analyzing the GAL-loaded ligand-functionalized NLPs surface charge (N=3). High absolute zeta potential values indicate a high electric charge on the surface of the GAL-loaded ligand-functionalized NLPs that may cause repulsion between particles to prevent aggregation of the ligand-functionalized NLPs.

4.2.11. Morphological characterization of the nanoliposomes

The morphology of the native NLPs, GAL-loaded NLPs and ligand-functionalized NLPs (suspensions in PBS pH 7.4) were examined using transmission electron microscopy (TEM) (JEOL 1200EX, Tokyo, Japan). The NLPs suspensions were dropped onto a carbon-coated copper grid, which was used as a sample holder. Eradication of excess liquid was achieved by blotting with filter paper and air-drying at room temperature for 5-10 minutes. The films on the copper grid were examined at 50x magnification. The TEM was operated at a voltage of 80kV.

4.2.12. Evaluation of the *in vitro* release of GAL from the ligand-functionalized nanoliposomes

In vitro drug release studies of GAL-loaded ligand-functionalized NLPs were assessed in a shaking incubator set at 20,000rpm. The ligand-functionalized NLPs were immersed in 100mL PBS (pH 7.4) in a closed vessel and positioned in an orbital shaker bath maintained at 37°C. Samples were withdrawn (5mL) at specific time intervals, filtered through a 0.22µm membrane filter and the vessel was immediately replaced with an equal quantity of drug-free PBS medium. The samples were then centrifuged at 10,000 rpm for 30 minutes (Vaidya et al., 2011). Filtered supernatant was further analyzed for GAL release by UV spectrophotometry at $\lambda_{\text{max}}=288\text{nm}$.

The quantity of GAL released was assayed by the quantity of drug initially present in the NLPs compared to the quantity of drug retained in the NLPs at each sampling point and computed from a standard linear curve ($R^2=0.99$) of GAL in PBS (pH 7.4). Each experiment was performed in triplicate. The Mean Dissolution Time (MDT) values were computed for each sample employing Equation 4.3.

$$\text{MDT} = \sum_{i=1}^n t_i \left(\frac{M_t}{M_{\infty}} \right) \dots \dots \dots \text{Eq. 4.3}$$

Where, M_t is the fraction of dose released in time $t_i=(t_i+t_{i-1})/2$ and M_{∞} corresponds to the loading dose.

4.2.13. *Ex vivo* cytotoxicity and cell uptake studies

4.2.13.1. Neuronal cell culture and preservation

PC12 neuronal cells line was maintained and cultured according to the method previously described in Chapter 3, section 3.2.10.

4.2.13.2. *Ex vivo* cytotoxicity assay of the ligand-functionalized nanoliposomes

PC12 neuronal cells were seeded into 96-well culture plates at a density of 10,000 cells per well and grown at 37°C in the presence of 5% CO₂ for 24 hours. The optimized non-functionalized GAL-loaded NLPs as well as the optimized GAL-loaded ligand-functionalized NLPs were added into 96-well culture plates. Cell viability was determined at 0, 12 and 24 hours intervals using a CytoTox-Glo™ Cytotoxicity Assay (Cho et al., 2008). Briefly, 50µL CytoTox-Glo™ Cytotoxicity assay reagent was added to each sample per well plate. The plates were instantaneously incubated at room temperature for 15 minutes and the dead cell signal measured using a Victor™X3 Perkin Elmer 2030 Luminometer Filter (Wellesley, Minnesota, USA). For cell viability, additional lysis reagent (50µL) was added to each well to achieve complete cell lysis. Subsequently the plate was incubated at room temperature for another 15 minutes and then analyzed for live cell signal. The cell viability percentages were computed using Eq. 4.

$$\text{Cell viability \%} = \frac{A_q}{A_c} \times 100 \dots \dots \dots \text{Eq. 4.4}$$

Where A_q represent the average quantity of luminescence determined from PC12 neuronal cells (treated, but not lysed) with the various NLPs formulations, and A_c is

the average quantity of luminescence detected for control PC12 neuronal cells (not treated, but lysed) at each time point.

4.2.13.3. *Ex vivo* uptake of the ligand-functionalized nanoliposomes

PC12 neuronal cells were placed into 96-well cell culture plates at an initial density of 10,000 cells/well and grown for 48 hours under the conditions described earlier. For uptake studies, the PC12 neuronal cells were first exposed to native NLPs and ligand-functionalized NLPs labeled with fluorescent marker 28mM FTIC or GAL, which were maintained at 37°C in a CO₂ incubator (RS Biotech Galaxy, Irvine, UK). Briefly, the cells were first incubated in serum free (FBS and horse serum) RPMI 1640 medium (with L glutamine and sodium bicarbonate), and after 2 hours the cells were re-suspended in fresh RPMI 1640 media supplemented with 5% FBS and 10% horse serum. Samples were withdrawn at 0, 2, 4, 6, 8 and 24 hours and thereafter maintained at 37°C in a CO₂ incubator (RS Biotech Galaxy, Irvine, UK). For the GAL-load formulations, the uptake study by the PC12 neuronal cells was performed at the end of the incubation period (24 hours). At the end of incubation, the cells were washed thrice with ice-cold PBS (pH 7.4) and lysed in the lysis buffer (0.5% triton X-100 in NaOH solution). The lysate was vortexed and thereafter centrifuged (Optima[®] LE-80K, Beckman, USA) at 10,000 g for 15 minutes at room temperature. The supernatant was collected and the quantity associated with the FITC fluorescent was measured with a Victor[™]X3 2030 Fluorometer Filter (Perkin-Elmer, Inc. USA) at an excitation wavelength of 450nm and emission wavelength of 482nm. GAL equivalents were measured by UV spectrophotometry at $\lambda_{\max}=288\text{nm}$. Each experiment was performed in triplicate. The percent drug uptake by the PC12 neural cells was computed using Eq 4.5.

$$\text{Cell uptake Efficiency \%} = \frac{C_q}{T_c} \times 100 \dots \dots \dots \text{Eq 4.5}$$

Where C_q is the cumulative quantity of FITC or GAL in the supernatant eluted from the lysed PC12 neuronal cells and T_c is the total quantity of FITC or GAL added in the ligand-functionalized NLPs.

4.2.13.4. Cellular uptake and intracellular localization of the ligand-functionalized nanoliposomes

Confocal microscopy was employed to further accessed cellular uptake and intracellular localization of fluorescent-labeled native NLPs and the ligand-functionalized NLPs PC12 neuronal cells. Fluorescence activity was measured using Confocal Laser Scanning Microscopy (CLSM) (Zeiss LSM780, Oberkochen, Germany) at an excitation wavelength of 450nm and an emission wavelength of 482nm after 24 hours incubation at 37°C in a CO₂ incubator. The upper surface morphology of the PC12 neuronal cells were examined using Scanning Electron Microscopy (SEM) (Jeol JSM-120, Tokyo, Japan).

4.2.14. Static lattice atomistic simulations for polymer-peptide interaction analysis

All modelling procedures and computations, including energy minimizations in Molecular Mechanics (MM), were performed using HyperChem™ 8.0.8 Molecular Modelling (Hypercube Inc., Gainesville, FL, USA) and ChemBio3D Ultra 11.0 (CambridgeSoft Corp., Cambridge, UK) software. DSPC and DSPE (without the aliphatic chains) were constructed in their syndiotactic stereochemistry as 3D models whereas the structures of the peptides were built using the Sequence Editor Module

on HyperChem 8.0.8. The structure of CHOL was built with natural bond angles as defined by the software. The models were initially energy-minimized using the MM+ Force Field and the resulting structures were once again energy-minimized using the AMBER 3 (Assisted Model Building and Energy Refinements) Force Field. The conformer having the lowest energy was used to create the polymer-polymer and peptide-polymer complexes. A complex of one molecule with another was assembled by disposing the molecules in parallel to generate the final models (including all three ligand types): DSPE/DSPC/CHOL, DSPE-ligand 1, DSPE-ligand 2, and DSPE-ligand 3. Full geometry optimization was performed in vacuum employing the Polak-Ribiere conjugate gradient algorithm until an RMS gradient of 0.001kcal/mol was reached. Force Field options in the AMBER and MM+ methods were used as defaults. To generate the final models in a solvated system, the MM simulations were performed for cubic periodic spaces with the polymer-polymer complex at the centre of the cubic space and the remaining free space filled with approximately 200 H₂O molecules, and the same procedure of energy-minimization was repeated to generate the solvated models except that the Force Fields were utilized with a constant dielectric (epsilon) with no scaling. In addition, the Force Field options in the AMBER (with explicit solvent) were extended to incorporate limits to inner and outer options with the nearest-image periodic boundary conditions. The outer and inner limits ensured that there were no discontinuities in the potential surface. Furthermore, various molecular attributes involved in the molecular interactions between the polymer and peptides in the presence of water were computed.

4.3. Results and Discussion

4.3.1. Characterization of the peptide-based ligand coupled onto the nanoliposomes surface

The appropriate quantity of peptide coupled onto the surface of the NLPs was validated by a NanoPhotometer™. Table 4.4 lists the peptide coupling efficiency (PCE) values that ranged between 40-79% for the 15 Box-Behnken experimental design formulations after stirring the reaction mixtures at room temperature for 6 hours. Additional results in this Chapter also revealed that the content of DSPE that constituted PEG 2000 did not alter the interaction of DSPE with the peptide, nor did it elicit any significant effect on the PCE value. The high quantity of peptide coupled onto the surface of the NLPs was due to the greater degree of covalent bonding via the DSPE free carboxyl (-COOH) group and the free amine (-NH₂) group of the lysine residue within the peptide.

4.3.2. Assessment of structural variations in the ligand-functionalized nanoliposomes

FTIR spectra were employed to validate the covalent conjugation peptides onto the surface of the NLPs. Figure 4.2(a-c) shows a typical FTIR spectrogram of native NLPs, GAL-loaded NLPs and GA-loaded ligand-functionalized NLPs, respectively (Figure 4.2a). The FTIR spectrum for the native NLPs showed a broad band at wavenumber 3200-3600cm⁻¹ and an absorption band at 1234cm⁻¹ that indicated the presence of a free hydroxyl group. Two bands were visible at 2918cm⁻¹ and 2850cm⁻¹ that were ascribed to -CH₂ and -CH₃ stretching vibrations. Further two bands were

observed at 1234cm^{-1} and 1054cm^{-1} due to the presence of carboxyl groups, vibration and absorption.

After the embedded blending of GAL with the NLPs, the absorption bands at 2850cm^{-1} disappeared. This was due to GAL interaction with the NLPs during the drug entrapment process (Figure 4.2b). GAL-loaded ligand-functionalized NLPs showed an absorption band at 1647cm^{-1} and a slight shift in the peak position to a low frequency of 1590cm^{-1} . This indicated the formation of amide (-NH) bond which associated with bending vibrations during covalent attachment of the peptide (Figure 4.2c). These results also revealed that there was an interaction between the $-\text{NH}_2$ group on the peptide and the $-\text{OH}$ group of DSPE during formulation of the GAL-loaded ligand-functionalized NLPs. This was an added advantage to the developed formulation since it would be beneficial in terms of enhancing the site specific delivery of GAL.

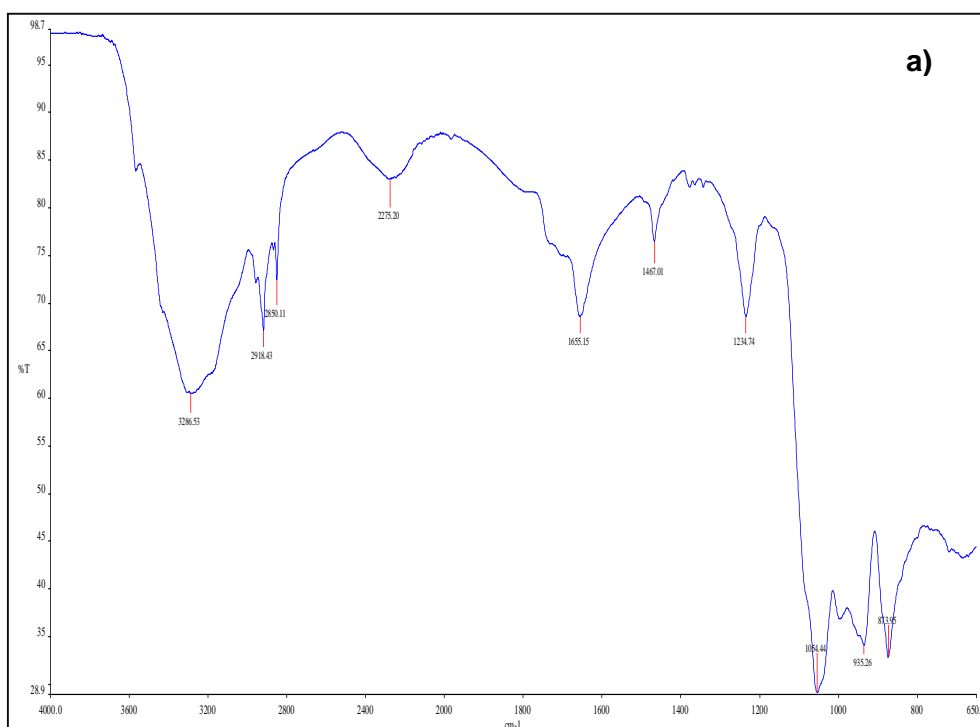


Figure 4.2: *Contd. on pg 101*

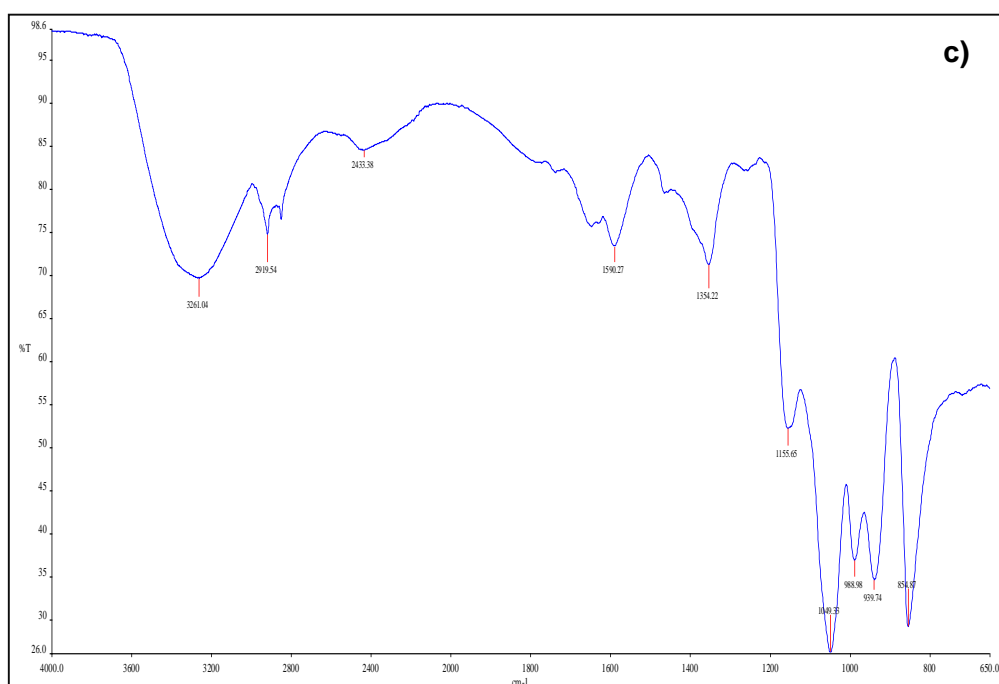
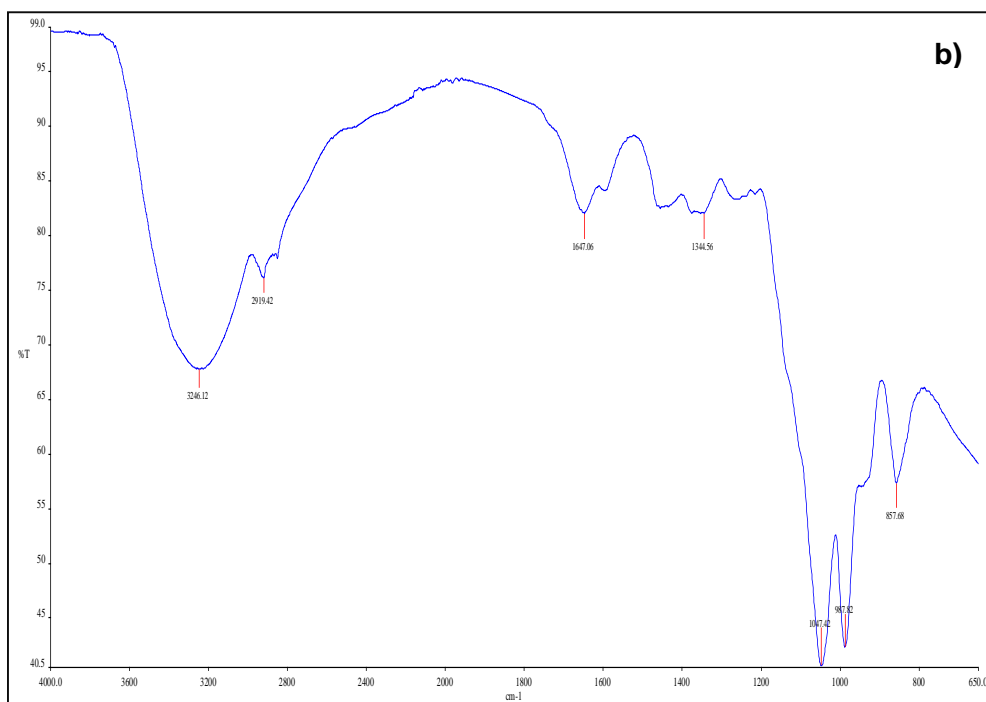


Figure 4.2: Typical FTIR profiles of the NLPs showing; a) native NLPs, b) GAL loaded NLPs and c) GAL-loaded ligand functionalized NLPs.

4.3.3. Drug entrapment efficiency within the ligand-functionalized nanoliposomes

The DEE (%) within the ligand-functionalized NLPs produced in accordance with the Box-Behnken experimental design is as shown in Table 4.4. The DEE values ranged between 42-79% as a result of the varying composition of the formulations based on the 3 independent formulation variables selected for the design. The results clearly indicated that formulations 4, 8 and 12 (centre points) produced from 55%^{w/w} DSPC, 65%^{w/w} CHOL and 12.5%^{w/w} DSPE resulted in stable ligand-functionalized NLPs with a desirable DEE% ranging between 75-79%. The results also showed that CHOL and DSPE had the same favorable effect during drug entrapment within the NLPs. CHOL is known to increase the stability and reduce the permeability of nanoliposomal bilayers (Kirby et al., 1980; Liang et al., 2004). DSPE has been confirmed to enhance NLPs stability to other components used for the formulation of NLPs (Yousefi et al., 2009). In another similar study, it was shown that remote loading with ammonium sulfate at 130mM could improve drug-loading (Ke et al., 2011). However, further increases in CHOL and DSPE concentration showed to have a potentially negative effect since it resulted in a decrease in the DEE value as well as NLPs membrane instability and an increase in drug leakage (Ali et al., 2010).

4.3.4. Determination of the particle size distribution and zeta potential

Table 4.5 shows the effect of the three (3) independent variables on the particle size, Pdl and zeta potential of the 15 experimental NLPs formulations. The average particle size was in the range of 118-153nm (Pdl=0.30-0.03; ZP= -18mV to -28mV) for the native NLPs; 124-163nm (Pdl=0.32-0.03; ZP= -23mV to -20mV) for the GAL-loaded non-functionalized NLPs and 127-165nm (Pdl=0.39-0.03; ZP= -28mV to -

36mV) for the ligand-functionalized NLPs. Figure 4.3 shows a typical size and zeta potential intensity profile generated for the GAL-loaded ligand-functionalized NLPs. Dynamic Light Scattering (DLS) measurements did not show any influence on zeta potential values because of GAL entrapment. However, the presence of peptide revealed an increase in zeta potential due to the negatively charged amino acid sequence. Overall, these results have shown that the presence of the peptide on the surface of the NLPs had a significant effect on their physical stability.

Table 4.4. Characterization of the 15 formulations generated by the Box-Behnken experimental design

Formulations Number	Peptide Coupling Efficiency (%)	DEE (%)	Drug Release (t_{8h})	MDT (t_{8h})
1	55	46	0.29	2.9
2	63	59	0.44	4.4
3	46	42	0.41	4.1
4	67	75	0.25	2.5
5	72	67	0.32	3.2
6	43	54	0.27	2.7
7	46	44	0.30	3.0
8	68	79	0.28	2.8
9	56	60	0.34	3.4
10	71	57	0.40	4.0
11	58	48	0.43	4.3
12	66	76	0.27	2.7
13	78	63	0.33	3.3
14	40	46	0.38	3.8
15	58	70	0.34	3.4

Table 4.5. Particle size distribution, polydispersity index, and zeta potential of the 15 Box-Behnken experimental design formulations evaluated.

F#	Native NLPs			GAL-loaded NLPs			GAL-loaded-functionalized NLPs		
	PSDa	Pdl	ZPc	PSD	Pdl	ZP	PSD	Pdl	ZP
1	140	0.02	-25	145	0.03	-28	149	0.24	-32
2	129	0.18	-23	134	0.28	-26	139	0.2	-30
3	139	0.23	-28	141	0.26	-29	143	0.3	-34
4	124	0.02	-27	126	0.21	-30	133	0.13	-36
5	137	0.17	-21	141	0.23	-29	144	0.29	-34
6	127	0.24	-26	132	0.17	-24	138	0.18	-30
7	153	0.12	-26	163	0.31	-23	165	0.39	-27
8	119	0.02	-25	124	0.22	-25	127	0.27	-35
10	152	0.3	-22	159	0.3	-23	163	0.21	-28
11	145	0.09	-21	159	0.34	-28	162	0.03	-29
12	123	0.12	-26	131	0.21	-25	135	0.32	-32
13	125	0.03	-26	132	0.13	-26	133	0.23	-34
14	132	0.22	-18	140	0.27	-26	143	0.13	-29
15	118	0.05	-21	127	0.13	-28	134	0.14	-28

F#: Formulation Number, ^aPSD: particle size distribution, ^bPdl: polydispersity index, ^cZP: zeta potential

4.3.5. Characterization of the surface morphology of the ligand- functionalized nanoliposomes

The surface morphology of the ligand-functionalized NLPs formulated as per the Box-Behnken design was characterized by TEM. Figure 4.4 shows typical TEM images of the native NLPs, GAL-loaded NLPs and the GAL-loaded ligand-functionalized NLPs. Results revealed that the morphology of the native NLPs, GAL-loaded NLPs and the GAL-loaded ligand-functionalized NLPs were uniformly spherical in shape with an intact/stable structure. Importantly, the morphology profile

of the GAL-loaded ligand-functionalized NLPs did not show any aggregation after GAL entrapment within the core and surface engineering of peptide onto the NLPs surface. The size distribution of the native NLPs, GAL-loaded NLPs, and GAL-loaded ligand functionalized NLPs were within the nanoscale. These results also displayed a desirable correlation with the data obtained by DLS measurement.

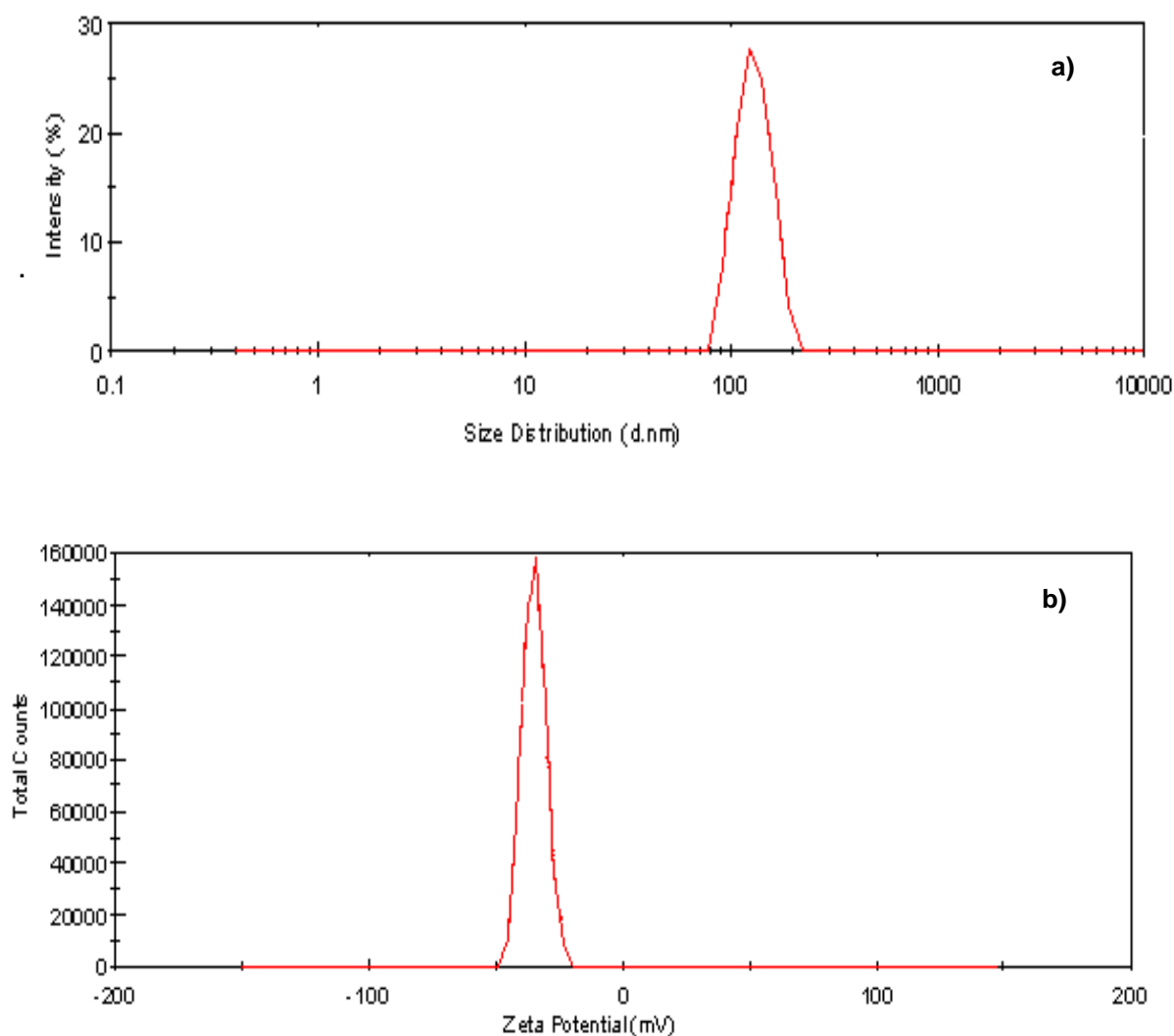


Figure 4.3: Typical physical profile distributions showing; a) average particle size and b) zeta potential distributions of the GAL-loaded ligand functionalized NLPs.

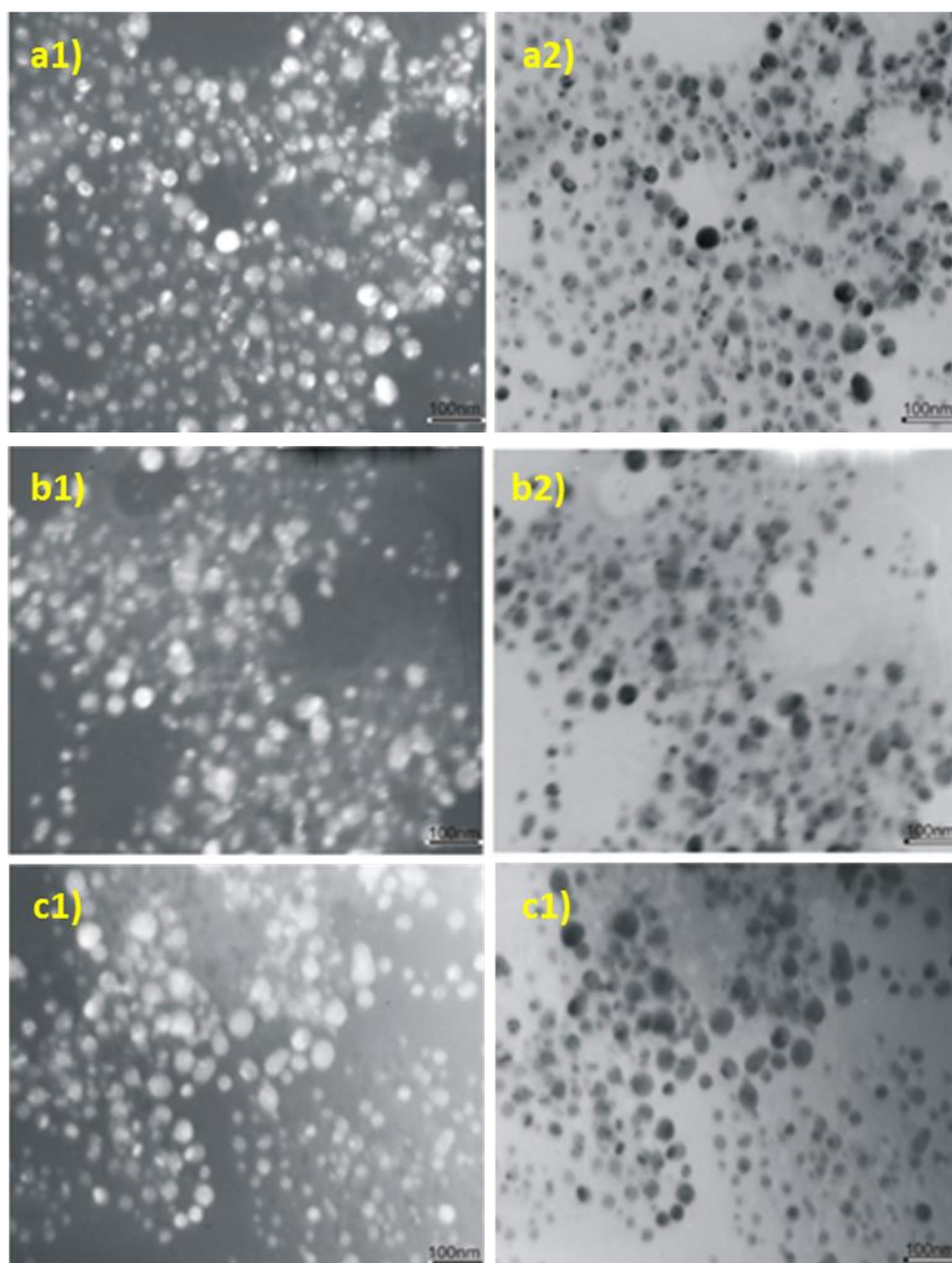


Figure 4.4: Darkfield (1) and brightfield (2) TEM micrographs of NLPs showing a1-a2) native NLPs, b1-b2) GAL-loaded NLPs and c1-c2) GAL-loaded ligand-functionalized NLPs.

4.3.6. Thermal behavior of the ligand-functionalized nanoliposomes

Thermal behavior of the native NLPs, GAL-loaded NLPs and the GAL-loaded ligand-functionalized NLPs were validated by TMDSC. The changes in glass transition temperature (T_g), endothermic melting temperature (T_m) and crystallization temperature (T_c) that occurred during formation of the NLPs are depicted in Figure

4.5a-c. Significantly large variation in the T_g , T_m and T_c peaks were observed between the native NLPs ($T_g=25-38^\circ\text{C}$; $T_m=55^\circ\text{C}$; $T_c=153-180^\circ\text{C}$), the GAL-loaded NLPs ($T_g=30-35^\circ\text{C}$; $T_m=62^\circ\text{C}$, $T_c=155-182^\circ\text{C}$) and the GAL-loaded ligand-functionalized NLPs ($T_m=80-95^\circ\text{C}$; $T_c=140-160^\circ\text{C}$). The thermal behavior of the GAL-loaded NLPs indicated that there was a strong hydrophobic interaction between GAL and the phospholipids during drug entrapment. The broadening T_m peak and the disappearing T_g in the GAL-loaded ligand-functionalized NLPs indicated a strong hydrophobic interaction between GAL and the ligand-functionalized NLPs (Ramana et al., 2010). The thermodynamic parameters also revealed an ideal transition enthalpy on both Fourier transform and non-reversing heat, which confirmed that the structure's phase transitions (with varying heat flow) enhanced the physical stability of the NLPs; or alternatively the structure remained intact due to the presence of cryoprotectant (0.5%) during lyophilization.

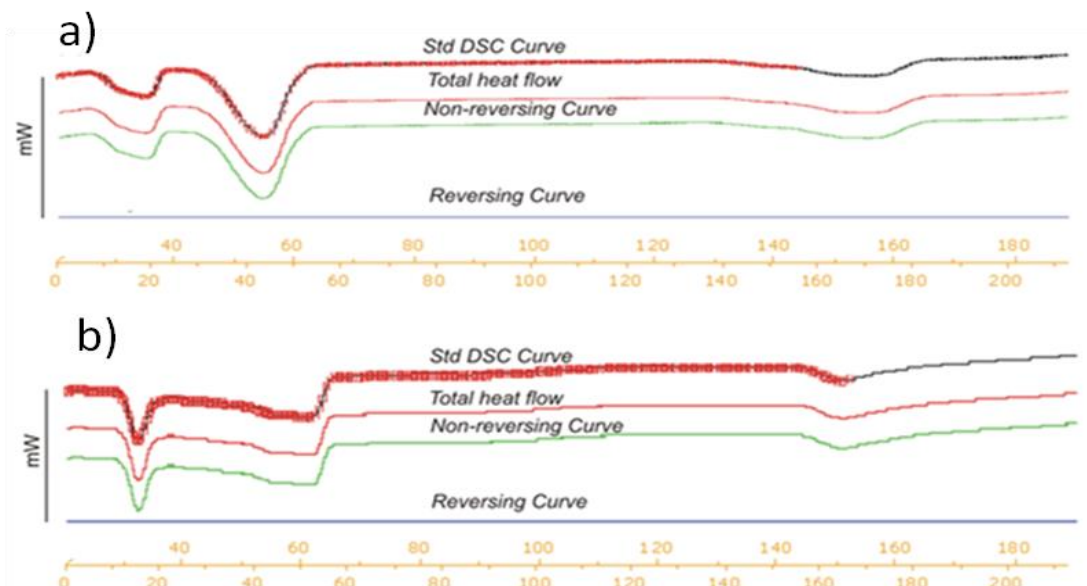


Figure 4.5: *Contd. on pg 108*

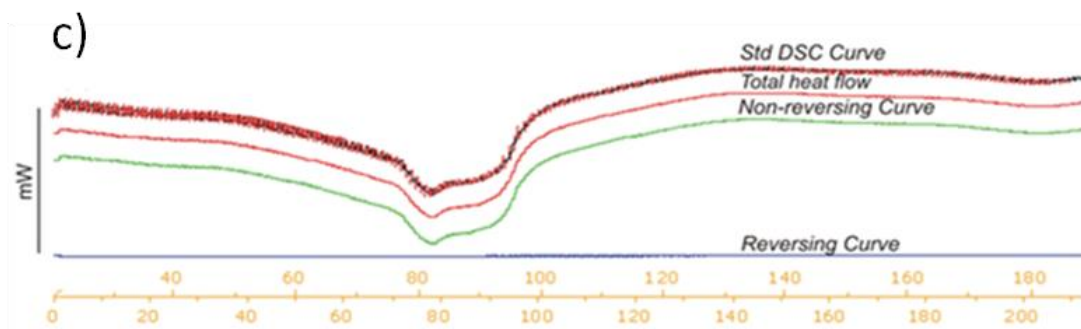


Figure 4.5: TMDSC profiles for the NLPs showing; a) native NLPs, b) GAL loaded NLPs and c) GAL-loaded ligand functionalized NLPs.

4.3.7. *In vitro* drug release from the ligand-functionalized nanoliposomes

In vitro release behavior of the GAL-loaded functionalized NLPs was investigated in PBS (pH7.4, 37°C) over 48 hours. PBS (pH7.4) was used to increase the sensitivity of the analytical method and create pH conditions pertinent to a CNS environment (Chesler et al., 2003). Figure 4.6(a-c) demonstrates the cumulative fractional release profiles of GAL from the 15 experimental formulations as per the Box-Behnken experimental design. Based on the experimental design, the 3 independent formulation variables resulted in different GAL release rates. Formulations 2, 3, 10, 11 and 14 exhibited similar release patterns of an initial burst at 8 hours followed by approximately 70-80% of GAL released within 48 hours. All other formulations (F1, F4, F5-F9, F12, F13 and F15) showed typical sustained release profiles, with less than 50% of GAL released from the ligand-functionalized NLPs over a period of 48 hours. The rapid release of GAL at the initial burst phase may have been influenced by the hydration process in formulations that contained higher concentrations of DSPE (>10mg) with PEG2000, which together modified the surface of the NLPs (Yousefi et al., 2009). Results also revealed that sustained release from the GAL-loaded ligand-functionalized NLPs was influenced by the CHOL concentration.

CHOL is well-known to stabilize lipid bilayers by reducing the membrane fluidity, thereby restricting the movement of drug across the nanoliposomal membrane (Betageri and Parsons, 1992; Karki et al., 2009). The MDT value at 8 hours ranged between 2.5-4.4 demonstrating slower drug release rates achieved from different ligand-functionalized NLPs formulations (F1-F15) as per the Box-Behnken experimental design.

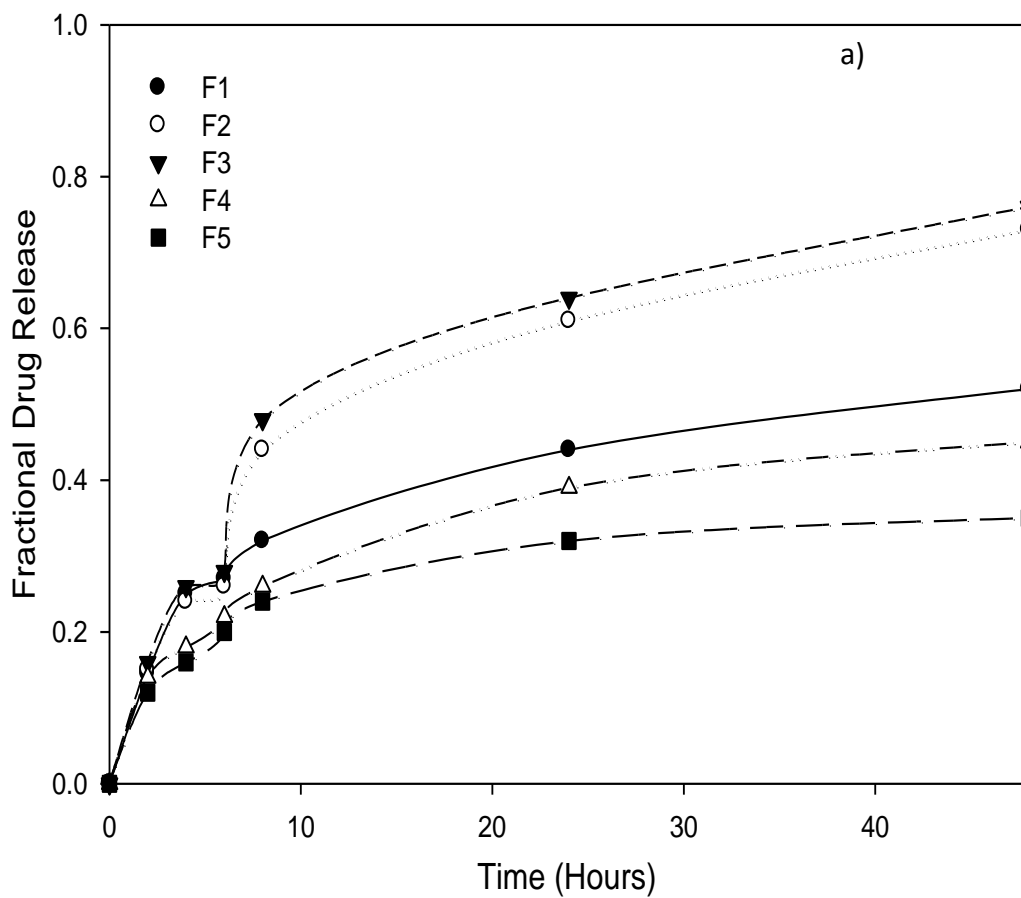


Figure 4.6: Contd. on pg 110

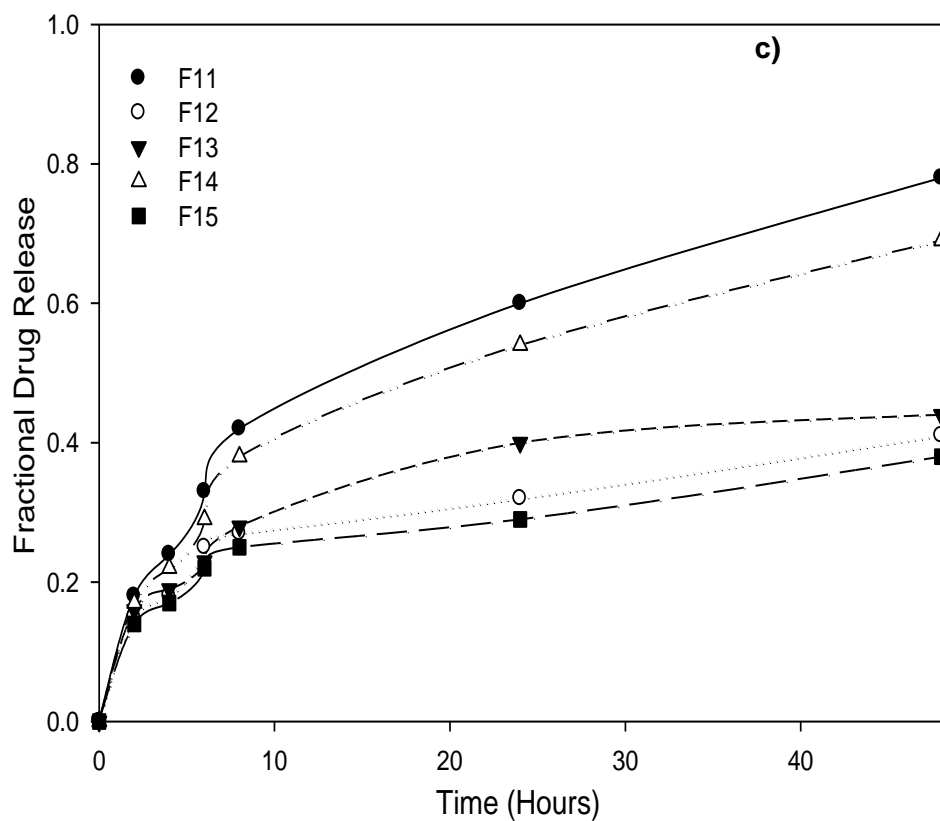
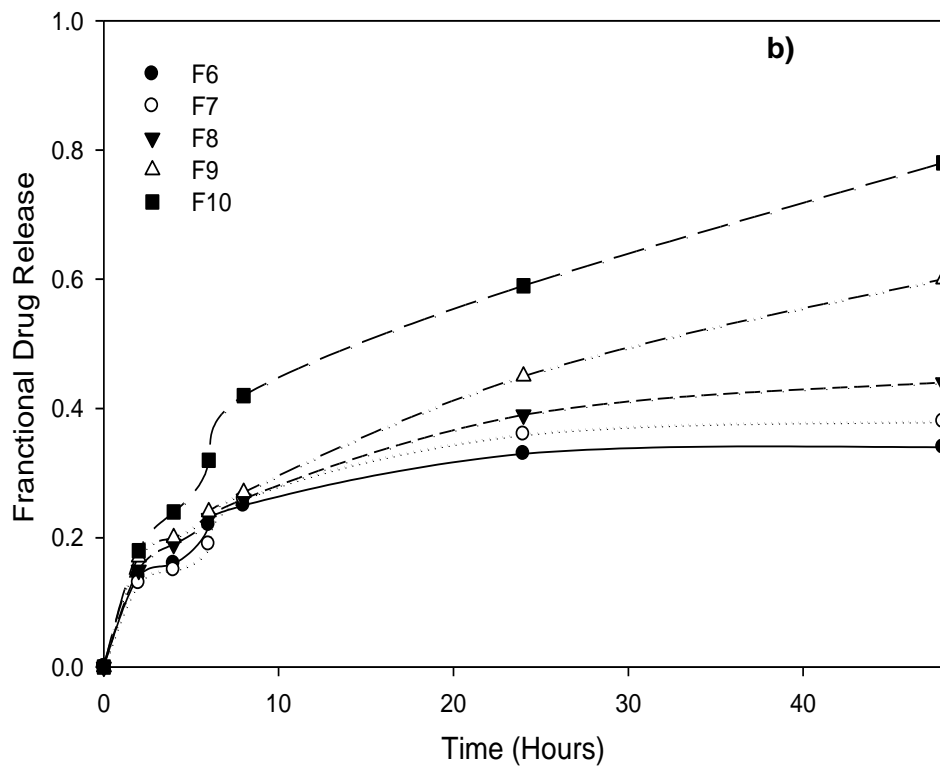


Figure 4.6: Drug release profiles obtained from the ligand-functionalized NLPs formulated as per the Box-Behnken design template showing a) formulation 1-5, b) formulations 6-10 and c) formulations 11-15 in PBS (pH7.4; 37°C) over 48 hours.

4.3.8. Response optimization of the GAL-loaded ligand-functionalized nanoliposomes

Statistical software (Minitab[®], V15, Minitab Inc., PA, USA) was used to obtain the optimized formulation pertaining to the following formulation responses: Peptide Coupling Efficiency (PCE), Drug Entrapment Efficiency (DEE), Drug Release (DR) and Mean Dissolution Time at 8 hours (MDT_{8h}). These responses were selected to attain maximum GAL-loaded ligand-functionalized NLPs desirability in terms of performance (Figure 4.7 and Table 4.6).

Table 4.6 shows the comparative experimental and predicted values of the optimized ligand-functionalized NLPs. PCE, DEE, DR and MDT_{8h} were computed to the converged desirability scores. The experimental values of PCE, DEE, DR and MDT_{8h} were 68.29%, 69.68%, 0.26 and 2.53 respectively. The experimental values obtained from each individual response had desirable correlation with the fitted values (Figure 4.7).

The release profile of the optimized formulation is shown in Figure 4.8. The desirability plot describes the influence of each independent variable for formulating the optimized ligand-functionalized NLPs with the desired targeted responses (PCE, DEE, DR and MDT).

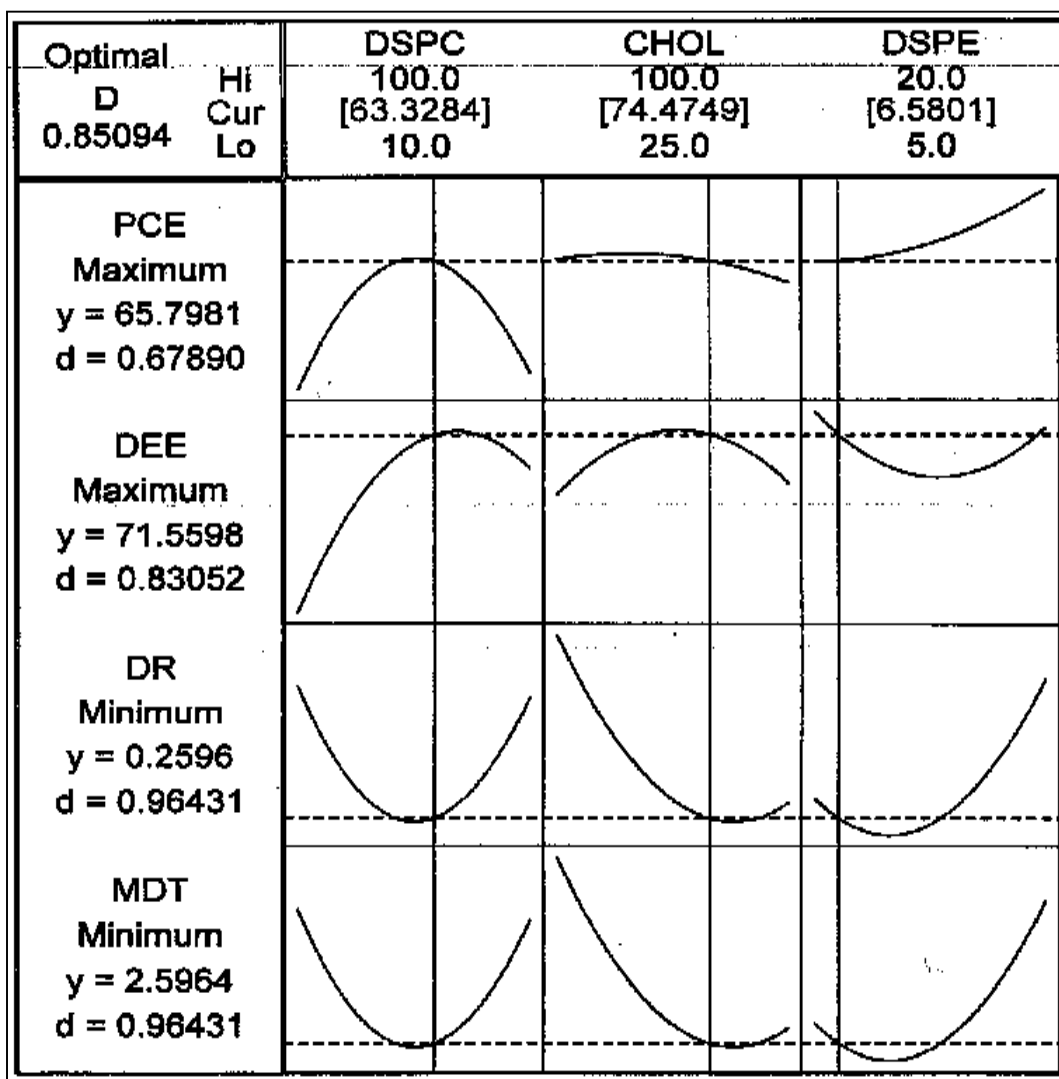


Figure 4.7: Desirability plots obtained for the optimized ligand-functionalized NLPs at each response.

Table 4.6. Comparative experimental and fitted values of the optimized ligand-functionalized NLPs

Measured Responses	Fitted	Experimental	% error
PCE	65.7981	68.2886	-3.3647
DEE	71.5598	69.675	2.70
DR	0.2596	0.2684	-3.2787
MDT	2.5964	2.5317	2.5556

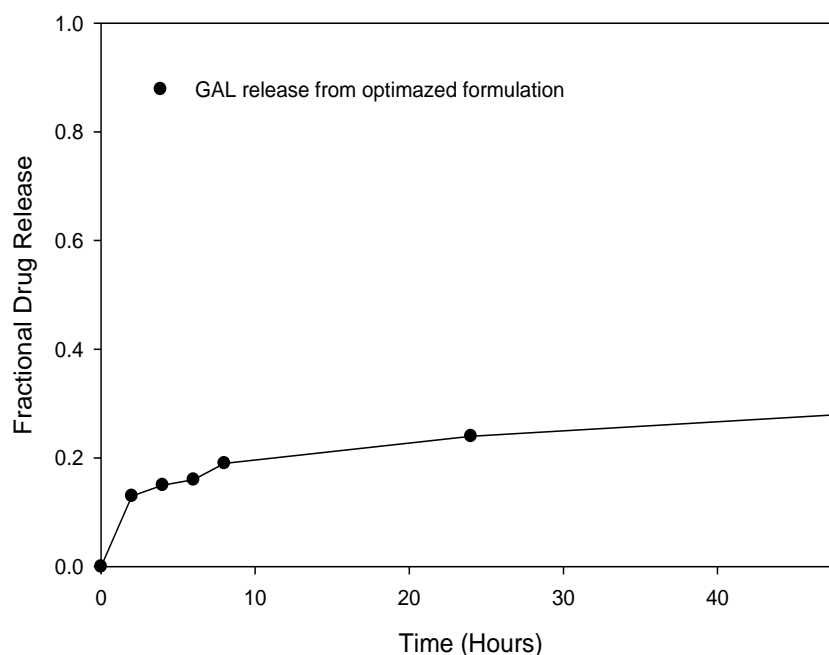


Figure 4.8: Drug release profile obtained for the optimized ligand-functionalized NLPs formulation in PBS (pH7.4; 37°C) over 48 hours.

4.3.9. *Ex vivo* analysis of the ligand-functionalized nanoliposomes

4.3.9.1. *Ex vivo* cytotoxicity assay of the ligand-functionalized nanoliposomes

The cytotoxicity of the native peptides at different concentrations (0.1mg/mL, 1mg/mL and 10mg/mL) as well as the optimized ligand-functionalized NLPs were compared employing PC12 neuronal cells. As shown in Figure 4.9, the effects of the peptides on PC12 neuronal cells were concentration dependent. When the ligand-functionalized NLPs formulations were exposed to the PC12 neuronal cells at concentrations of 1mg/mL or 10mg/mL, there was no significant difference between the cytotoxicity of the native peptides and the ligand-functionalized NLPs after 24 hours in a 5% CO₂ incubator at 37°C. However, when 10mg/mL of ligand 3 was coupled to the NLPs, results revealed 25% of cell loss occurred compared with ligands 1 and 2. These results suggested that pegylated NLPs may have effectively reduced the cytotoxicity associated with ligand 3 on PC12 neuronal cells. The overall

findings in this Chapter demonstrated that there were no significant differences between the native peptides (at 1mg/mL or 10mg/mL) or the non-functionalized and ligand-functionalized NLPs formulated when compared with untreated PC12 neuronal cells at the same conditions over a period of 24 hours.

4.3.9.2. *Ex vivo* uptake of labeled ligand-functionalized nanoliposomes

The *ex vivo* uptake of labeled ligand-functionalized NLPs was investigated to determine the intracellular fate of the NLPs. Figure 4.10 (a-b) show the quantification of fluorescence intensity measured at different times intervals in PC12 neuronal cells after being treated with NLPs formulations at different peptide concentrations (1mg/mL and 10mg/mL). The quantities of cellular uptake of the ligand-functionalized NLPs were higher compared with non-functionalized NLPs. The fluorescence intensity produced by ligand-functionalized NLPs was optimal and demonstrated that ligand-coupling led to increased cellular uptake of the NLPs. However, cellular uptake was increased with increasing time intervals over a period of 24 hours. Figure 4.10b depicts weak uptake of ligand-functionalized NLPs when 10mg/mL of ligand was used for functionalizing the NLPs, which revealed that higher peptide concentration during the coupling process led to a decreased, if not delayed, cellular uptake. Figure 4.10c exhibited significant GAL uptake by PC12 neuronal cells after 24 hours incubation. The intracellular uptake was 15% for free GAL, 23% for R1 and 83% for R2 with a peptide concentration of 1mg/mL. The results also indicated that the uptake of GAL into PC12 neuronal cells was evidently increased when GAL-loaded NLPs became ligand-functionalized. Figure 4.11 (a-b) depicts the confocal fluorescence microscopy images highlighting the difference between the intracellular uptake of the non-functionalized and ligand-functionalized NLPs. Figure 4.11 (a-b)

showed 2D histograms and 3D images representing the fluorescence intensity and distribution of the PC12 neuronal cells which had internalized with the ligand-functionalized NLPs. Figure 4.11 [a (1a-4b)] histograms depict the fluorescence intensity for PC12 neuronal cells treated with non-functionalized (A1b) and ligand-functionalized NLPs (A2b for R2, A3b for R3, A4b for R4). Figure 4.11b depicts a typical 3D profile that displayed a topographical image representing the fluorescence intensity and distribution in the z-direction of the PC12 neuronal cells internalizing with non-functionalized (B1) and ligand-functionalized NLPs (B2). In fact, confocal fluorescence microscopy images revealed that the ligand-functionalized NLPs were effectively localized within the PC12 neuronal cells. Non-functionalized NLPs showed weak or no FITC fluorescence activity, while PC12 neuronal cells treated with R2, R3 and R4 displayed intense and evident FITC fluorescence activity. These results suggested that the increase in fluorescence activity in PC12 neuronal cells may have been influenced by post-engineered peptides on the surface of the NLPs, which promoted intracellular uptake via SEC-R in a mediated manner. Furthermore, confocal microscopy imaging was well correlated with corresponding quantitative studies of fluorescence intensity measured. Figure 4.11c displays a typical SEM micrograph exhibiting the cell surface morphology.

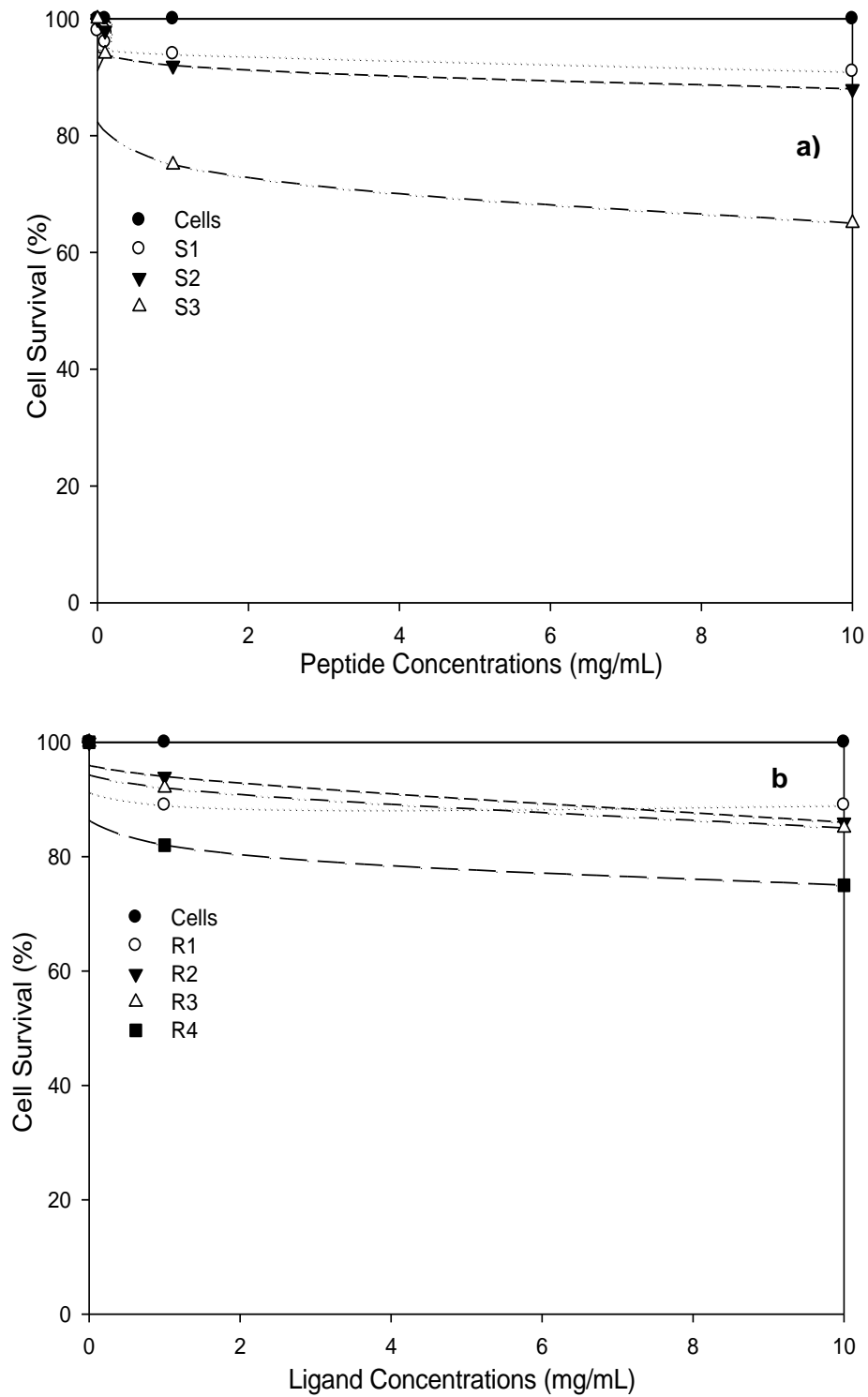


Figure 4.9: Cytotoxicity profiles showing a) native ligands (S1, S2 and S3) and b) non functionalized NLPs (R1), functionalized NLPs with S1 is R2; R3, functionalized with S2; and R4, functionalized with S3

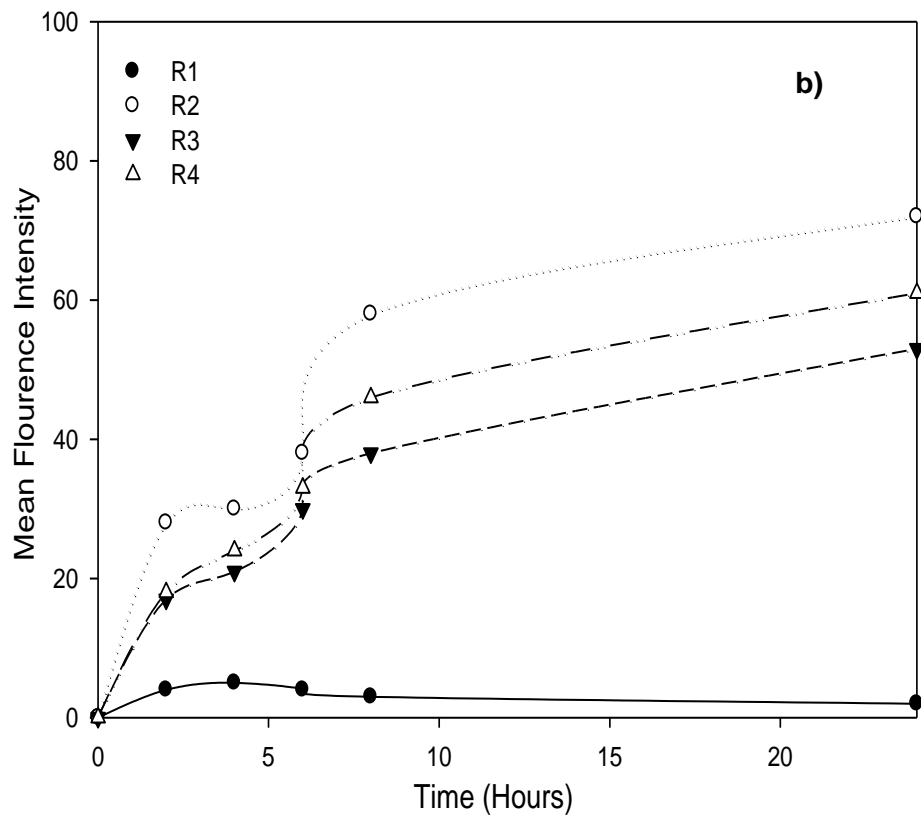
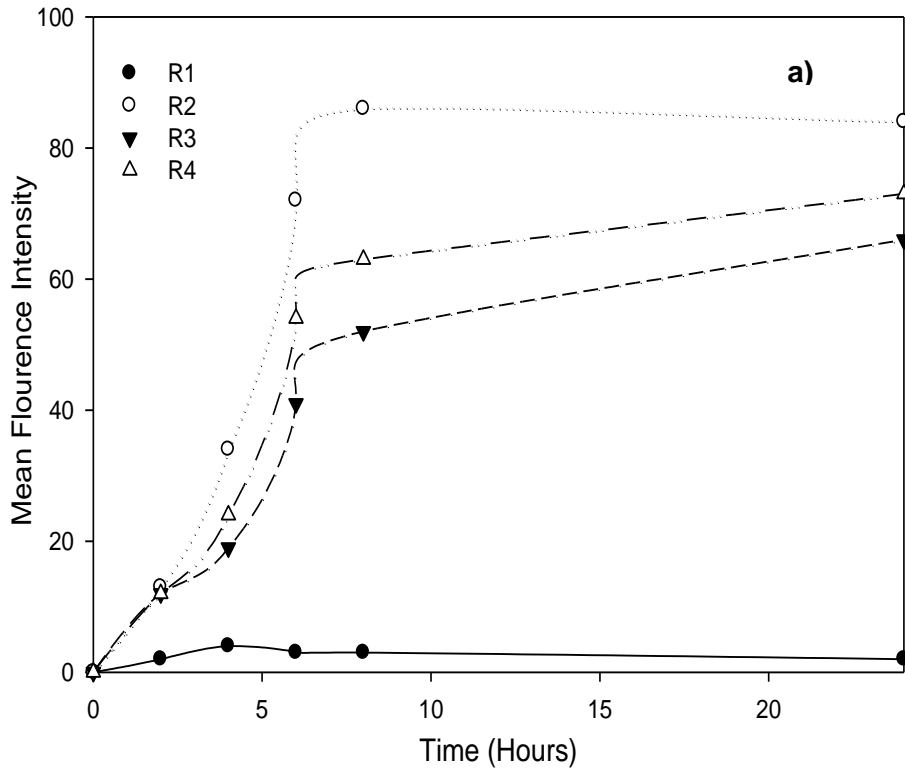


Figure 4.10: Contd. on pg 118

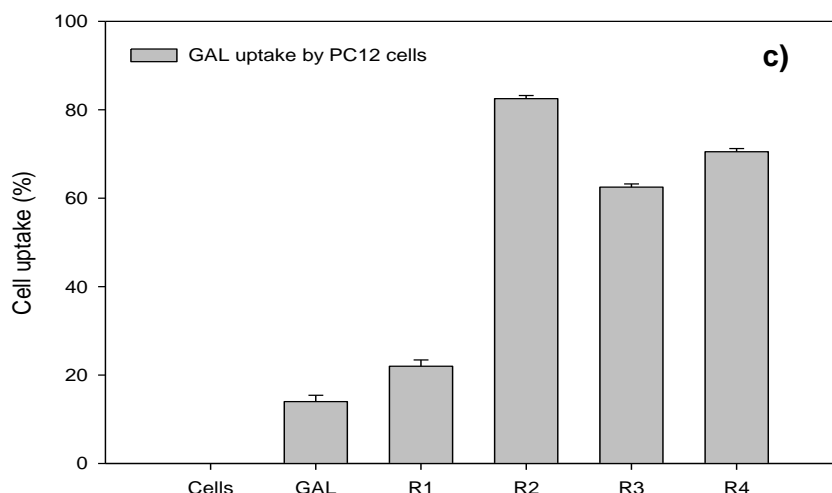
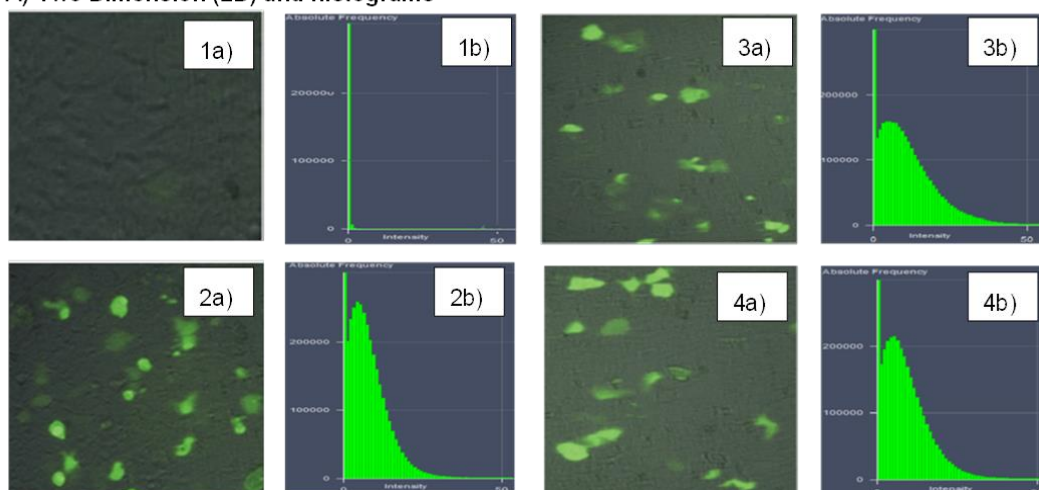
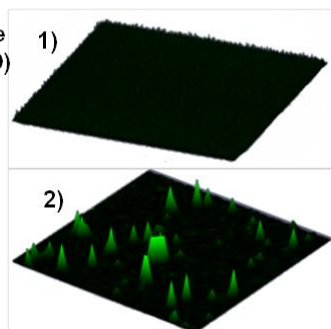


Figure 4.10: *Ex vivo* PC12 neuronal cells uptake of the ligand-functionalized NLPs with a) non-functionalized NLPs (R1) and R2-R4 coupled with 1mg/mL peptide, b) R2-R4 coupled with 10mg/mL peptide and c) GAL uptake by PC12 neuronal cells (R1-R4) after 24 hours of incubation.

A) Two Dimension (2D) and histograms



B) Pseudo Three Dimensional (3D)



C) Surface Morphology

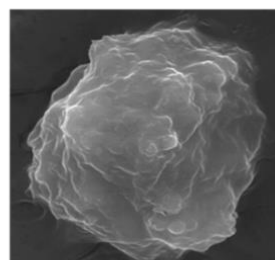


Figure 4.11: Confocal microscopy images representing the population of fluorescence PC12 neuronal cells associated with uptake of the NLPs with (A) 2D images: 1a) R1, 2a) R2, 3a) R3 and 4a) R4 and histograms 1b) R1, 2b) R2, 3c) R3, and 4d) R4; (B) Pseudo 3D images of the topographical view of cells and its fluorescence intensity and distribution after treatment with 1) non-functionalized NLPs and 2) ligand-functionalized NLPs and (C) SEM image exhibiting the cell surface morphology.

4.3.10. Molecular Mechanics Energy Relationship (MMER) analysis

MMER was employed as a method for analytical-mathematical representation of the potential energy surfaces and provided supportive data regarding the contributions of valence terms, non-covalent Coulombic terms and non-covalent van der Waals interactions for peptide-linkage and NLPs formation. The MMER model for potential energy in various molecular complexes is shown in Eq 4.6.

$$E_{\text{molecule/complex}} = V_{\Sigma} = V_b + V_{\theta} + V_{\varphi} + V_{ij} + V_{hb} + V_{el} \dots \text{Eq 4.6}$$

Where, V_{Σ} =total steric energy for an optimized structure, V_b = bond stretching contributions, V_{θ} =bond angle contributions, V_{φ} =torsional contribution arising from deviations from optimum dihedral angles, V_{ij} =van der Waals interactions due to non-bonded interatomic distances, V_{hb} =H-bond energy function and V_{el} =electrostatic energy (Choonara et al., 2011).

4.3.11. *In silico* formation of nanoliposomal system

In the present MM study, the global energy relationships for the various complexes derived after AMBER 3 are shown in Equations 7-13.

$$E_{\text{CHOL}} = 38.246 V_{\Sigma} = 1.890 V_b + 11.442 V_{\theta} + 14.170 V_{\varphi} + 10.7425 V_{ij} \dots \text{Eq 4.7}$$

$$E_{\text{DSPC}} = 30.243 V_{\Sigma} = 0.424 V_b + 27.475 V_{\theta} + 1.070 V_{\varphi} + 1.271 V_{ij} \dots \text{Eq 4.8}$$

$$E_{\text{DSPE}} = 7.661 V_{\Sigma} = 0.139 V_b + 2.677 V_{\theta} + 5.552 V_{\varphi} - 0.706 V_{ij} \dots \text{Eq 4.9}$$

$$E_{\text{CHOL/DSPC}} = 56.565 V_{\Sigma} = 2.200 V_b + 38.626 V_{\theta} + 16.457 V_{\varphi} - 0.718 V_{ij} - 0.002 V_{hb} \dots \text{Eq 4.10}$$

$$\Delta E = -11.924 \text{kcal/mol}$$

$$E_{\text{CHOL/DSPE}} = 41.886 V_{\Sigma} = 2.282 V_b + 18.539 V_{\theta} + 17.872 V_{\phi} + 3.337 V_{ij} - 0.145 V_{hb} \dots \text{Eq 4.11}$$

$\Delta E = -4.021 \text{kcal/mol}$

$$E_{\text{DSPC/DSPE}} = 25.023 V_{\Sigma} = 0.517 V_b + 30.372 V_{\theta} + 6.234 V_{\phi} - 12.099 V_{ij} - 0.001 V_{hb} \dots \text{Eq4.12}$$

$\Delta E = -12.881 \text{kcal/mol}$

$$E_{\text{CHOL/DSPC/DSPE}} = 59.964 V_{\Sigma} = 2.700 V_b + 46.572 V_{\theta} + 21.143 V_{\phi} - 9.948 V_{ij} - 0.503 V_{hb} \dots \text{Eq 4.13}$$

$\Delta E = -16.186 \text{kcal/mol}$

The energy Equations 4.7-4.13 demonstrated that the nanoliposomal system composed of CHOL, DSPC and DSPE were stabilized in terms of respective bonding and non-bonding energy factors. The preferred orientations of the polymers as binary and ternary polymeric systems are depicted in Figure 4.12. The binary system modeled using phosphatidyl-derivatives yielded energetically stabilized molecular complexes with energy of interactions equivalent to -12.881kcal/mol (DSPC/DSPE) suggesting desirable compatibility and miscibility. As reported by Lozano and co-worker (2009) and Mufamadi and co-workers (2012), the addition of a third lipophilic agent such as CHOL further enhanced the stability of the binary system composed of cholines and enolines. For proof of concept, CHOL was modelled with DSPE and DSPC to form CHOL/DSPE and CHOL/DSPC with interaction energies of -11.924kcal/mol and -4.021kcal/mol, respectively. In this Chapter, the ternary complex to quantify the final stoichiometric condensed complex, CHOL-DSPE-DSPC was modelled, where the components were miscible with an energy stabilization of $\Delta E = -16.186 \text{kcal/mol}$ (Equations 4.7-4.9, 4.13). The complexes were stabilized by generalized energy times in terms of bond angles and torsional contributions as well

as London dispersion forces and H-bonding. Interestingly, introduction of CHOL introduced H-bonding into the binary and ternary systems with energy values ranging from -0.002kcal/mol to -0.503kcal/mol that led to a stabilized molecular entity. The van der Waals interactions further contributed to the stabilization and retrieved high negative values due to CHOL (in excess) acting as a filler in the space lattice of the binary and ternary systems (Figure 4.13). These non-bonding interactions, from H-bonding to van der Waals forces, are due to the hydrophobic interactions arising from the inclusion of CHOL, which further led to the formation of NLPs in excess of PBS (pH7.4).

4.3.12. Investigation of the amphiphilic properties involving polymer-peptide aggregation

In order to investigate the cellular-internalization of peptide-conjugated systems, three ligands viz. (Ligand 1: Lys-Val-Leu-Phe-Leu-Ser), (Ligand 2: Lys-Val-Leu-Phen-Leu-Thr) and (Ligand 3: Lys-Val-Leu-Phe-Leu-Met), differing by one amino acid group, were individually modeled with DSPE, where the peptides displayed clear preference to DSPE over DSPC. The modeling was performed in the absence and presence of H₂O molecules corresponding to the lipophilic and hydrophilic phases, respectively. The more the complex was stabilized in vacuum the more lipophilic it was for penetrating the PC12 neuronal cells. Inversely, the more stabilized in H₂O, the more hydrophilic the complex. For cellular-internalization, the passing of a polymer-peptide conjugate through the cell membrane requires a hydrophilic-lipophilic-balance with lipophilicity on the higher side. Eq 4.9 and 4.14 - 4.19 display the energy profiles of individual molecules as well as of the conjugates and it is evident that DSPE-ligand 1, DSPE-ligand 2, and DSPE-ligand 3 were

stabilized at -17.299kcal/mol,-11.738kcal/mol, and-14.427kcal/mol energies of interaction, respectively. These energy stabilization values proved that ligand 1 provided more lipophilicity to DSPE followed by ligands 2 and 3. The changes in the conformational space lattice of the DSPE caused by the peptide chains also contributed to its lipid-soluble behavior as the London dispersion forces stabilized.

$$E_{\text{DSPE}} = 7.661 V_{\Sigma} = 0.139 V_b + 2.677 V_{\theta} + 5.552 V_{\varphi} - 0.706 V_{ij} \dots (4.9)$$

$$E_1 = -34.431 V_{\Sigma} = 1.653 V_b + 8.010 V_{\theta} + 5.206 V_{\varphi} + 3.119 V_{ij} - 1.301 V_{hb} - 51.119 V_{el} \dots \text{Eq 4.14}$$

$$E_2 = -24.391 V_{\Sigma} = 1.228 V_b + 6.775 V_{\theta} + 3.262 V_{\varphi} - 1.778 V_{ij} - 1.220 V_{hb} - 32.658 V_{el} \dots \text{Eq 4.15}$$

$$E_3 = -39.242 V_{\Sigma} = 1.529 V_b + 9.824 V_{\theta} + 5.799 V_{\varphi} + 0.814 V_{ij} - 2.235 V_{hb} - 54.975 V_{el} \dots \text{Eq 4.16}$$

$$E_{\text{DSPE-1}} = -44.069 V_{\Sigma} = 1.715 V_b + 11.218 V_{\theta} + 13.122 V_{\varphi} - 13.331 V_{ij} - 2.149 V_{hb} - 54.644 V_{el} \dots \text{Eq 4.17}$$

$\Delta E = -17.299\text{kcal/mol}$

$$E_{\text{DSPE-2}} = -28.468 V_{\Sigma} = 1.438 V_b + 9.288 V_{\theta} + 11.881 V_{\varphi} - 19.964 V_{ij} - 1.460 V_{hb} - 29.651 V_{el} \dots \text{Eq 4.18}$$

$\Delta E = -11.738\text{kcal/mol}$

$$E_{\text{DSPE-3}} = -46.008 V_{\Sigma} = 1.657 V_b + 12.204 V_{\theta} + 11.490 V_{\varphi} - 14.210 V_{ij} - 2.318 V_{hb} - 54.832 V_{el} \dots \text{Eq 4.19}$$

$\Delta E = -14.427\text{kcal/mol}$

$$E_{\text{DSPE}} = -2988.489 V_{\Sigma} = 28.296 V_b + 31.953 V_{\theta} + 8.961 V_{\varphi} + 106.105 V_{ij} - 4.06 V_{hb} - 3159.75 V_{el} \dots \text{Eq 4.20}$$

$$E_1 = -2687.829 V_{\Sigma} = 25.278 V_b + 36.626 V_{\theta} + 9.833 V_{\varphi} + 82.198 V_{ij} - 5.175 V_{hb} - 2836.59 V_{el} \dots \text{Eq 4.21}$$

$$E_2 = -2742.775 V_{\Sigma} = 26.298 V_b + 31.870 V_{\theta} + 11.748 V_{\varphi} + 63.083 V_{ij} - 7.719 V_{hb} - 2868.06 V_{el} \dots \text{Eq 4.22}$$

$$E_3 = -2679.527 V_{\Sigma} = 25.137 V_b + 30.802 V_{\theta} + 9.693 V_{\varphi} + 66.0426 V_{ij} - 5.776 V_{hb} - 2805.43 V_{el} \dots \text{Eq 4.23}$$

$$E_{\text{DSPE-1}} = -2441.783 V_{\Sigma} = 22.532 V_b + 33.053 V_{\theta} + 22.7071 V_{\varphi} + 23.378 V_{ij} - 7.377 V_{hb} - 2536.08 V_{el} \dots \text{Eq 4.24}$$

$\Delta E = 3234 \text{kcal/mol}$

$$E_{\text{DSPE-2}} = -2575.518 V_{\Sigma} = 25.944 V_b + 37.039 V_{\theta} + 18.886 V_{\varphi} + 24.375 V_{ij} - 7.058 V_{hb} - 2674.71 V_{el} \dots \text{Eq 4.25}$$

$\Delta E = 3155 \text{kcal/mol}$

$$E_{\text{DSPE-3}} = -2467.305 V_{\Sigma} = 24.8047 V_b + 37.451 V_{\theta} + 17.921 V_{\varphi} + 23.641 V_{ij} - 7.877 V_{hb} - 2563.25 V_{el} \dots \text{Eq 4.26}$$

$\Delta E = 3200 \text{kcal/mol}$

The effect of adding the solvated-phase to the reactional-profile and stabilization of the polymer-peptide aggregates was extracted via relative modeling of the peptide-polymer complex under the same conditions. Referring to Eq 4.24-4.26, the energetic profiles of bimolecular complexes revealed that the conjugated systems represented stable systems with negative potential energies. However, in comparison to the cumulative energy profile of the individual constituent molecules, the complexes were highly destabilized in the following order: DSPE-ligand 2 > DSPE-ligand 3 > DSPE-ligand 1 having energy of interactions ranging from ~3155 kcal/mol through ~3200 kcal/mol to ~3234 kcal/mol, respectively. These high energies of destabilization were mainly due to electrostatic interactions (V_{el}) and partially to torsional constraints (V_{φ}) and H-bonding (V_{hb}), as evident from Eq 4.20-4.26. With

reference to the results from the vacuum and solvated system simulations, it is concluded that DSPE-ligand 1 displayed superior hydrophilic-lipophilic-balance (HLB) producing desirable cellular internalization efficiency compared to ligands 2 and 3. These results are in corroboration with the *ex vivo* data discussed earlier.

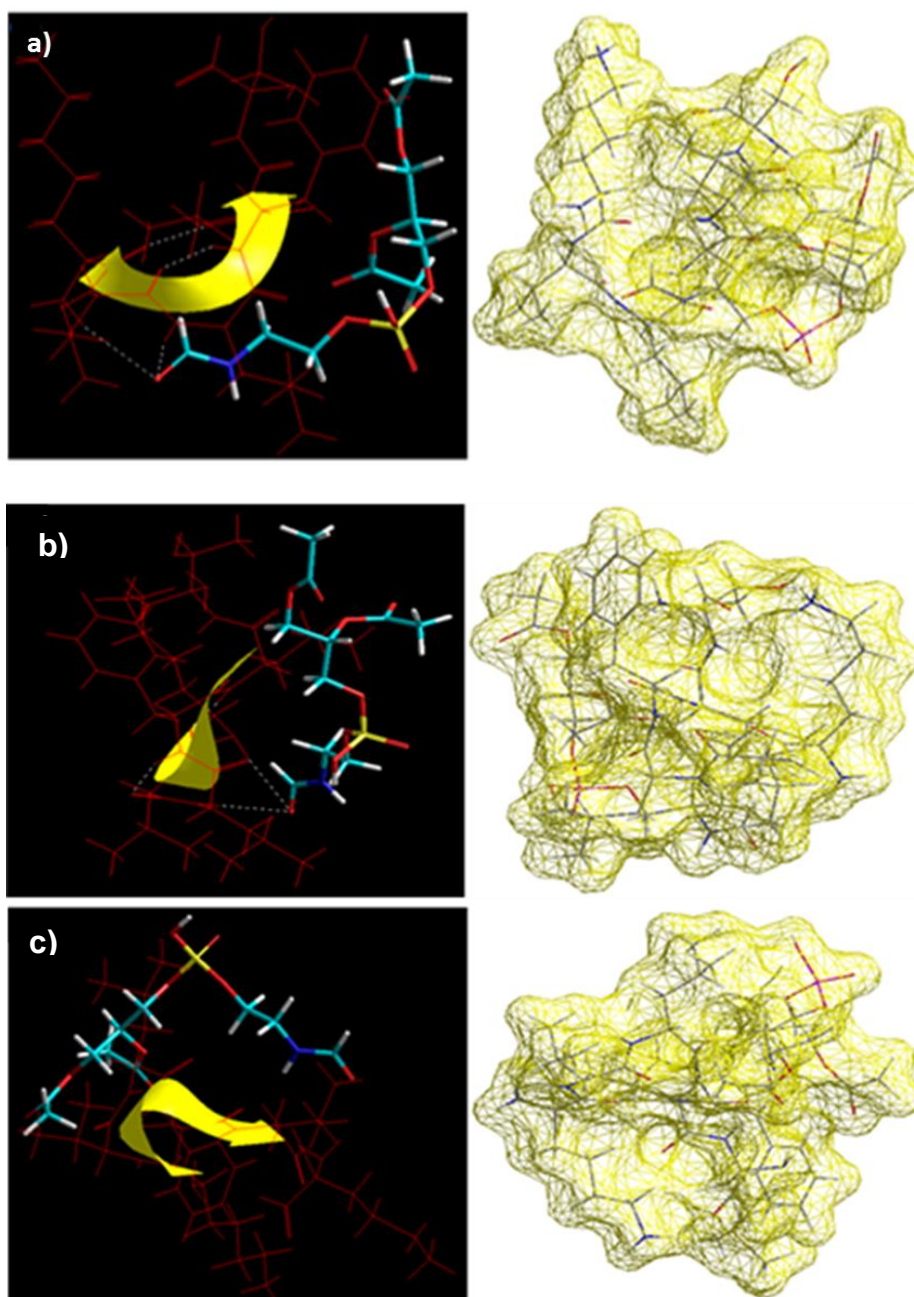


Figure 4.12: Visualization of geometrical preferences of a DSPE molecule in complexation with the ligands showing a) ligand 1, b) ligand 2 and c) ligand 3 after molecular simulations in vacuum. Color codes for DSPE tube rendering: C (cyan), O (red), H (white), and P (yellow). Peptide molecules are rendered in stick mode (red) and thin ribbon secondary structures (yellow). The respective Connolly molecular electrostatic potential surfaces are in wire-mesh display mode.

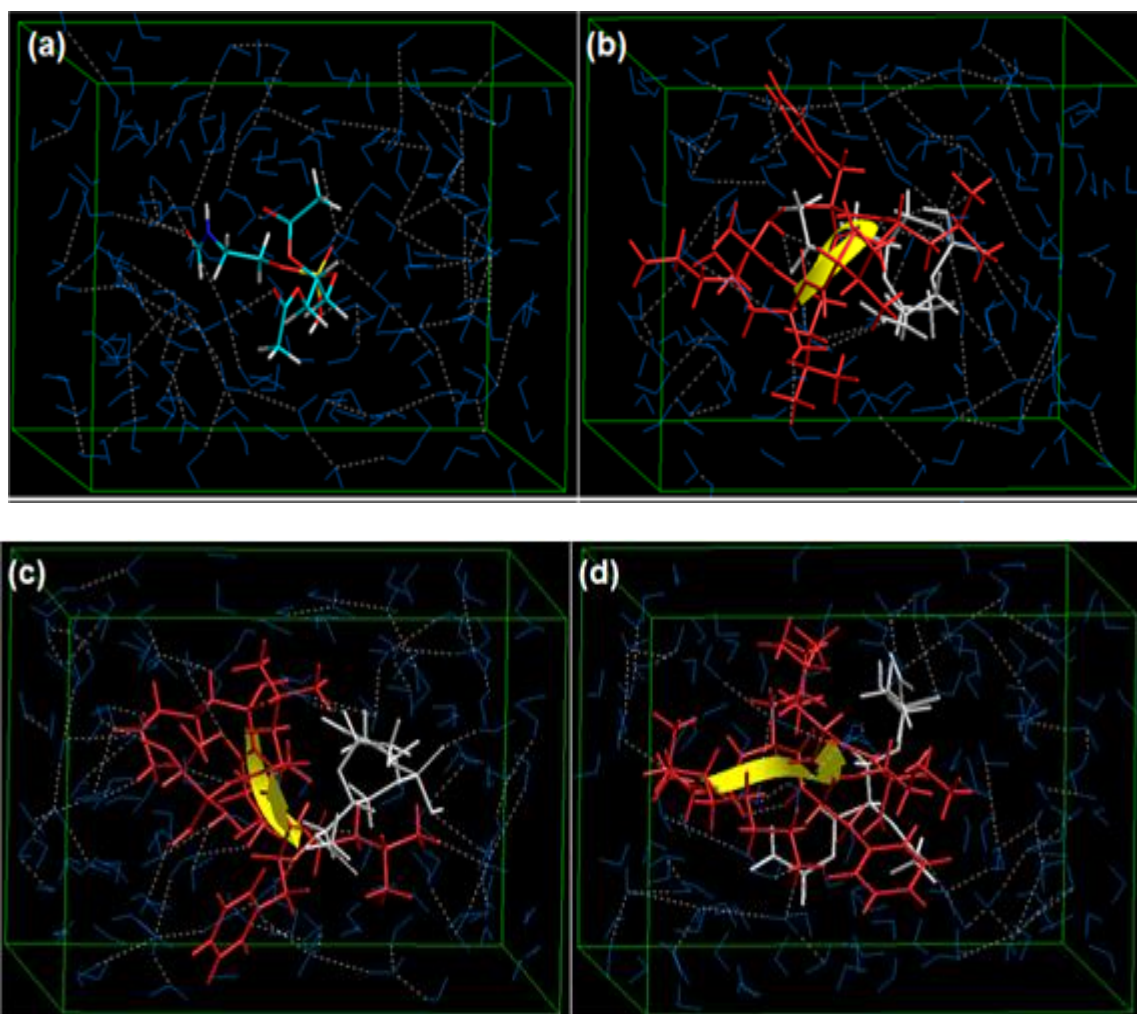


Figure 4.13: Visualization of geometrical preferences showing a) DSPE, b) DSPE-ligand 1, c) DSPE-ligand 2, and d) DSPE-ligand 3 after molecular simulation in a solvated system consisting of 200 H₂O molecules (blue). The peptides (red-yellow) and DSPE (white) are rendered in tube displays. Color codes for figure a): C (cyan), O (red), H (white), P (yellow).

4.4. Concluding remarks

The data obtained in this Chapter showed that the ligand-functionalized NLPs enhance the delivery of the neuroactive drug GAL into PC12 neuronal cells as a model for AD. PC12 neuronal cells exhibit high surface SEC-R expression that mediated internalization of the ligand-functionalized NLPs (Perlmutter et al., 1990; Boland et al., 1995; Ziady et al., 1997; Patel et al., 2001). The results of the FTIR and TMDSC analysis revealed a change in molecular structure due to the presence of GAL entrapped within the NLPs and peptide conjugated to the NLPs surface.

Particle size analysis confirmed that the ligand-functionalized NLPs were spherical and within the nanoscale size range. TEM studies revealed that all formulations, namely native NLPs, GAL-loaded NLPs and the ligand-functionalized NLPs were stable with no aggregation observed (Kirby et al., 1980; Kim and Park, 1987). The Box-Behnken experimental design template and subsequent optimization process revealed the ideal concentrations of the 3 independent formulation variables selected and can be used successfully for producing the ligand-functionalized NLPs with desirable PCE, DEE and drug release properties. DEE and drug release behavior were dependent on the presence of DSPE and CHOL in the NLPs formulations (Ali et al., 2002). The optimized formulation comprised 63.32mg DSPC, 74.47mg CHOL and 6.6mg DSPE. The experimental data was well correlated with the fitted values generated by the experimental design. Post-engineering of peptides onto the surface of GAL-loaded NLPs proved to provide targeted delivery of GAL directly into PC12 neuronal cells. Native GAL and non-functionalized NLPs showed no significant accumulation into PC12 neuronal cells after 24 hours of incubation due to non-specific drug delivery. Overall, *in vitro* and *ex vivo* results revealed that the ligand-functionalized NLPs produced in this Chapter have the potential of trapping GAL and are suitable for targeted drug delivery to neuronal cells in response to treating AD. Furthermore, this Chapter may serve as proof-of-concept that the ligand-functionalized NLPs can offer an ingenious scientific solution for the current limitations in the neuropharmaceutical management of AD.

CHAPTER 5

***IN VITRO* SYNTHESIS AND CHARACTERIZATION OF THE CROSS-LINKED CHITOSAN-EUDRAGIT RSPO-POLYVINYL ALCOHOL HYDROGEL FOR THE PREPARATION OF THE NANO-ENABLED BIO-ROBOTIC INTRACRANIAL DEVICE**

5.1. Introduction

The development of a hydrogel that may enhance the mechanical stability and/or act as temporal polymeric depots of a liposomal drug delivery system has revolutionized the current state of formulation design in the pharmaceutical field (Stenekes et al., 2000; Chung et al., 2006; Muluk et al., 2009; Mufamadi et al., 2011). Liposomes are well researched because of their excellent capability to accommodate both hydrophilic and hydrophobic drugs (Yu et al., 2008; Deligkaris et al., 2010; Kulkarni et al., 2010). Liposomal drug delivery approaches, particularly in nanotechnologies, such as targeted nanoliposomes (NLPs) and nanobubbles (gas-filled) have gained attention in recent years (Ying et al., 2010; Du Toit et al., 2011).

In addition, micro/nanocomposite liposomal devices have been developed by loading drug-loaded liposomes into hydrogel networks (Schexnailder et al., 2009; Epstein-Barash et al., 2010; Mufamadi et al., 2011). *In vitro* studies of a microcomposite hydrogel seemed to influence the hydrogel strength *in vivo* (Martina et al., 2007; Van Raaij et al., 2011). As a depot, hydrogel networks possess essential physical properties that are equivalent to those of human tissue and can protect liposomal

drug delivery systems from surrounding inflammatory cells (Soppirnath and Aminabhavi, 2002; Epstein-Barash et al., 2010). A study conducted by Hennik and Van Nostrum (2002) reported that hydrogel structures are embraced by three-dimensional cross-linked networks with hydrophilic domains comprised of high water adsorption properties. Furthermore, studies have shown that networks in hydrogel formulations are essentially attained through cross-linked structures from one or more natural and/or synthetic polymers employing either chemical or physical interactions post-reaction.

Natural polymers, including chitosan (CHT), collagen, fibrin and dextran and synthetic polymers, including Eugradit[®] RSPO and polyvinyl alcohol (PVA), have been reported as the structural materials used in hydrogel networks (Hartwell et al., 2011; Mufamadi et al., 2011; Li et al., 2012). Different cross-linking agents such as formaldehyde, glutaraldehyde (GA) and genipin have been reported to be successful for enhanced stability and suitability of hydrogel in drug delivery applications (Bhattarai et al., 2010). In numerous investigations, the hydrogel networks for pharmaceutical applications were selected based on their fundamental properties such as biodegradability, biocompatibility, non-toxicity and non-inflammatory tendency (Mufamadi et al., 2011). In addition, the advantage of injectable hydrogel networks is that they can deliver the drug directly or indirectly to the targeted sites through subcutaneous and intratumoral injections (Ta et al., 2008). Despite the many advantages, clinical limitations of hydrogels used in pharmaceutical applications are their poor mechanical and rheological properties (Gauvin and Berthod, 2010). In drug delivery systems, a poor structure may result in abnormal homogeneity on drug loading into the polymeric hydrogel/depot (Hoare and Kohane, 2008). These

shortcomings may be governed by mechanical or rheological dynamics of CEP hydrogel such as viscoelastic-like behavior [elastic modulus (G') and viscous loss moduli (G'')], and Newtonian or non-Newtonian behaviors (such as viscosity, shear thinning and thixotropic behaviors) (Arguelles-Monal et al., 1998; Horn et al., 2011). Several attempts to evade these limitations have been made, including manipulation of the hydrogel viscosity or viscoelastic-like behaviors (Albu et al., 2009; Matricardi et al., 2009). However, the mechanical or rheological dynamics of CEP hydrogels have been shown to be governed by the temperature, pH, cross-linking agents and polymers used during the fabrication process (Weng et al., 2007; Karazhiyan et al., 2009). A permanent covalent hydrogel network was reported to be associated with restricted gel mobility and low deformation (Armoškaitė et al., 2012). As a depot, this may result in undesirable drug dispersion during the embedding process and may lead to an early burst and release phase (Hoare et al., 2008).

CHT is a natural linear biopolyaminosaccharide polymer obtained by N-deacetylation of chitin (Berger et al., 2004; Pillai et al., 2009). PVA is a highly hydrophilic polymer with a molecular mass of 80kDa and containing numerous reactive hydroxyl groups (DeMerlis and Schoneker et al., 2003). A study by De Souza and co-workers (2009) demonstrated the presence of enhanced mechanical properties such as tensile strength and electrostatic interaction in cross-linked CHT and PVA. In a similar study, Mansur and co-workers (2008) reported that the hydrolysis degree of PVA decrease as GA concentration increased. In yet another study by Jin and co-workers (Jin and Song, 2006), it was reported that cross-linking between CHT and polyethylene oxide (PEO) affected drug release behavior, whereby the drug release rate was decreased by increasing the cross-linking density. Eudragit® RSPO (EU) is

a copolymer containing acrylic and methacrylic acid esters (Lehman, 2001; Wittayaarekul et al., 2006). Ghaffari and co-workers (2006) have reported that blends of EU with natural polymers, such as CHT, can enhance and/or control the drug release rate.

The novel technique of developing liposomes containing gaseous perfluorocarbons or sulfur hexafluoride into the cores of the lipid monolayers has revolutionized the current state of drug delivery technology (Unger et al., 2004). The presence of perfluoropropane gas has shown to induce cavitations in liposomes (Prentice et al., 2005). Furthermore, the formulation of liposome gas-filled/loaded microbubbles and ultrasound has been reported to facilitate a fast uptake of both gene and drug (Liu et al., 2006; Suzuki et al., 2007; Willmann et al., 2010). In diagnostic applications, it has shown to facilitate the tracking of the development of cancer, AD and diabetes via an ultrasonic imaging system (Hernot et al., 2008). In addition, gas-filled liposomes can be used to visualize subcutaneous body structures and ultrasound contrast in a medium via traditional medical sonography (Van Raaij et al., 2011). Progressive bio-imaging techniques such as micro-ultrasound imaging and fibered fluorescence microscopy have been currently initiated for further advanced tracking, employing both ultrasound contrast agents and co-localized bio-labeled markers such as Fluorescein Isothiocyanate (FITC), trypan blue and rhodamine (Ducongé et al., 2004; Bharali., et al., 2005; Al-Gubory and Houdebine, 2006; Martina et al., 2007; Mufamadi, 2011; Van Raaij et al., 2011).

Therefore the aim of this Chapter was to synthesize cross-linked CHT-EU-PVA or PEO (CEP) hydrogel for the preparation of a nano-enabled Bio-Robotic Intracrainal

Device (BICD). BICD was fabricated by embedding fluorescence-labeled functionalized NLPs or gas-filled functionalized NLPs within non-fluorescence or fluorescence-labeled CEP hydrogel. Functionalized NLPs were modified from previously constructed liposomal nanostructures presented in Chapter 4, section 4.2.4 of this thesis (Mufamadi et al., 2013), via incorporating sulfur hexafluoride (SF₆) gas into the core of the NLPs. The CEP hydrogels were fabricated by cross-linking CHT, EU and PVA or PEO solutions using GA as a cross-linking agent. The CEP hydrogels were characterized of their biomechanical strength; such as non-Newtonian viscosity and viscoelastic properties. The stability, morphology and distribution of gas-filled functionalized NLPs post-embedded within CEP hydrogel of the BICD were tracked employing real-time ultrasound imaging, whereas fluorescence-labeled functionalized NLPs were visualized employing real-time fibered fluorescence microscopy and optical Immunofluorescence Microscopy.

5.2. Materials and Method

5.2.1. Materials

Natural and synthetic polymers that are commercially available such chitosan (CHT) [Medium Molecular Weight (Mw), viscosity 200,000cps] and poly(vinyl alcohol) (PVA, Mw=146-186kDa) were purchased from Sigma-Aldrich® (Steinheim, Germany). Polyethylene oxide (PEO) (POLYOX™WSR 303 NF, Mw=7000kDa) from Dow Chemical Co. (Dow, New Jersey, USA). The co-polymer Eugradit® RSPO (EU) was purchased from Rohn Pharm (GmbH, Darmstadt, Germany). Fluorescein isothiocyanate (FITC), 4,6-Diamidino-2-phenylindole (DAPI) stain (blue) and trypan blue solution (0.4%) were purchased from Fluka Biochemika (St. Louis, MS, USA).

Membrane filter with 0.22 μ m was purchased from Millipore (Millipore, Billerica, MA, USA). Nitrogen (N₂) and CO₂ medical gases were purchased from African Oxygen (Afrox) Ltd, (Industrial West, Germiston, RSA). Sulfur hexafluoride (SF₆, 99.75%) was purchased from Sigma-Aldrich® (St. Louise, MS, USA). EcoGel100™ ultrasonic imaging gel (low viscosity, 35000-45000cps) was purchased from Eco-Med Pharmaceuticals Inc (Mississauga, Ontario, Canada). All other chemicals used in the experiments were of analytical grade and were employed as purchased.

5.2.2. Fabrication of the gas-filled or fluorescence-labeled functionalized nanoliposomes

Gas-filled or fluorescence-labeled functionalized nanoliposomes (NLPs) were fabricated with multi-components (i.e. synthetic phospholipids, FITC, SF₆ gas and site-directing ligand) via multiple steps. In brief, multilamellar vesicles (MLVs) were formed employing the previously described protocol in Chapter 4, Sections 4.2.2 and 4.2.3 with appropriate amounts of DSPC, CHOL and DSPE-mPEG conjugate in the presence of FITC-labeled markers detailed in Tables 4.1 and 4.2 of this thesis. Small unilamellar vesicles (SUVs) of appropriate size distribution were obtained by gradually extruding (repeated 6 times) through a 0.22 μ m pore size polycarbonate membrane filter. Gas-filled functionalized NLPs are attained by SF₆ gas entrapment in the core of liposomes. Briefly, 1mL of the NLPs in a 15mL tube was exposed to various gases (SF₆, N₂ and CO₂) at a pressure of 100kPa for 30-45 seconds prior to analysis.

5.2.2.1. Particle size analysis of gas-filled functionalized nanoliposomes

Particle size analysis and polydispersity index (Pdi) of the native functionalized NLPs and gas-filled functionalized NLPs were analyzed as described in Chapter 4, Section 4.2.9 employing a Zetasizer NanoZS instrument (Malvern Instruments (Pty) Ltd., Worcestershire, UK).

5.2.2.2. Morphological characterization of the gas-filled functionalized nanoliposomes

The morphology of the native functionalized NLPs and gas-filled functionalized NLPs were examined as previous described in Chapter 4, Section 4.2.11 employing transmission electron microscopy (TEM) (JEOL1200EX, Tokyo, Japan).

5.2.2.3. *In vitro* investigation of the stability of the gas-filled functionalized nanoliposomes

In vitro investigations of the stability of the native functionalized NLPs and gas-filled functionalized NLPs were analyzed employing a Turbiscan Lab® Expert (Formulacion Co., Eunion, France). In short, NLPs suspensions were transferred into a glass cylindrical cell, and thereafter analyzed via a light beam that is emitted from a near-infrared light source. Two synchronous detectors, namely a transmission (T) detector and a backscattering (BS) detector were scanned at 880nm every 5 minutes over 1 hour, at room temperature.

5.2.3. Synthesis of the cross-linked Chitosan-Eudragit RSPO-Polyvinyl alcohol hydrogel

CEP hydrogel was synthesized by reacting different ratios of CHT, EU and PVA or control PEO solutions, which were exposed to a cross-linking solution of GA 5% (v/v). In brief, a CHT solution was prepared by dissolving CHT in 0.2M of acetic acid. EU solution was obtained by mixing different organic solvents such as acetone, methanol and isopropanol at a ratio of 2:1:1 v/v. PVA solution was obtained by dissolving PVA in deionized water (Milli-DI® Systems, Bedford, MA, USA) at 80°C. PEO solution was prepared by dissolving PEO in deionized water at room temperature. Six formulations consisting of various combinations of the polymers solution (CHT, EU, PVA and/or PEO) were blended together at different ratios; 3:3:1, 3:2:2 and 3:1:3 (Table 5.1). The reaction mixtures were allowed to agitate until a homogenous mixture was obtained in the presence of a cross-linking solution of GA 5% (v/v). Solvents used for synthesis of the CEP hydrogel were eliminated through rotary evaporation (Rotavapor® R11, BüchiLabortechnik AG, Switzerland) maintained at 60°C.

Table 5.1. Compositions of CEP hydrogel cross-linked with 5% GA

Formulation	CHT %w/v	EU %w/v	PVA %w/v	PEO %w/v
F1	3	3	1	0
F2	3	2	2	0
F3	3	1	3	0
F4	3	3	0	1
F5	3	2	0	2
F6	3	1	0	3

5.2.3.1. Molecular structural transition of the cross-linked Chitosan-Eudragit RSPO-Polyvinyl alcohol hydrogel

Fourier Transform Infra-Red (FTIR) spectroscopy was analyzed on native polymers (CHT, EU, PVA or PEO), the non-cross-linked, and cross-linked CEP hydrogel. FTIR spectra were generated to elucidate potential chemical interactions as a result of polymers blending and cross-linking process using Nicolet Impact 400D FTIR Spectrophotometer coupled with Omnic FTIR research grade software (Nicolet Instrument Corp., Madison, WI, USA).

5.2.3.2. Rheological properties of the cross-linked Chitosan-Eudragit RSPO-Polyvinyl alcohol hydrogel

Rheological properties such as viscosity and viscoelasticity of the CEP hydrogel (F1-6) were evaluated employing a Haake Modular Advanced Rheometer System (ThermoFisher Scientific, Karlsruhe, Germany). Yield stress and dynamic oscillatory frequency sweep tests were done on a CEP hydrogel. All tests were carried out with the following parameters: temperature of 37°C, a test time of 200s and a shear stress of 200Pa. The temperature was maintained by a recirculating bath connected to the cone-plate with a diameter of 35mm and a cone angle of 1°. The yield stress test was performed to determine the deformation or shear thinning behavior that may allow the evaluation of the shear stress (Pa) as a function of shear rate (1/s). On the other hand, the dynamic oscillatory frequency sweep test was to determine the viscoelastic properties (storage and loss moduli). The storage modulus G' test was essentially for measuring the CEP hydrogel elastic behavior, which is associated with energy storage. The loss modulus G'' test was conducted to measure the CEP hydrogel viscous behavior, which is associated with energy dissipation. The

oscillatory shear responses were determined at a single frequency of 10Hz (0-300 rad/s).

5.2.4. Fabrication of the Bio-Robotic Intracranial Device

The BICD was engineered by embedding gas-filled or fluorescence-labeled functionalized NLPs into the CEP hydrogel. Gas-filled functionalized NLPs were fabricated as per protocol described in Chapter 5, section 5.2.2, while FITC/fluorescence-labeled functionalized NLPs as previously described protocol in Chapter 4, section 4.2.2. In addition, CEP hydrogel was synthesized as previously described protocol in Chapter 5, section 5.2.3. In brief, gas-filled or FITC-labeled functionalized NLPs were loaded into the CEP hydrogel at a ratio of 1:5 (functionalized NLPs: CEP hydrogel). The gas-filled or FITC-labeled functionalized NLPs in suspension were added via drop-wise to the CEP hydrogel, and mixtures were also allowed to agitate until a homogenous mixture was attained under mechanical stirring at 37°C in the presence of a 5%^{v/v} of the cross-linking solution of GA. Particle distribution within the BICD was characterized using real-time ultrasound, real-time fluorescence imaging (cell-viZio, Mauna Kea Technologies, Paris, France) and optical immunofluorescence imaging (Olympus IX71 Immunofluorescence, Olympus Co., Tokyo, Japan).

5.2.4.1. Real-time ultrasound imaging of the gas-filled functionalized nanoliposomes embedded within the Bio-Robotic Intracranial Device

Real-time ultrasound imaging of the gas-filled functionalized NLPs embedded within a BICD was visualized using a high-frequency ultrasound scanner (Vevo[®] 2100, Visualsonics, Toronto, Ontario, Canada) with an MS-250 transducer. Native CEP hydrogel and intra-bubbles CEP hydrogel (bubbles induced by dynamic magnetic

stirring) were used as controls. The effect of different loading techniques for the gas-filled functionalized NLPs into CEP hydrogel such as i) loading into the CEP hydrogel prior to cross-linking; ii) loading post cross-linking; and iii) loading using 1mL syringe injection were also characterized. In addition, the effect of PVA or control PEO as part of the hydrogel component was also characterized. EcoGel 100™ imaging ultrasonic gel was applied onto the surface of all samples prior to it being visualized. Real-time imaging was executed via an ultrasound transducer (Figure 5.1) (Foster et al., 2011).

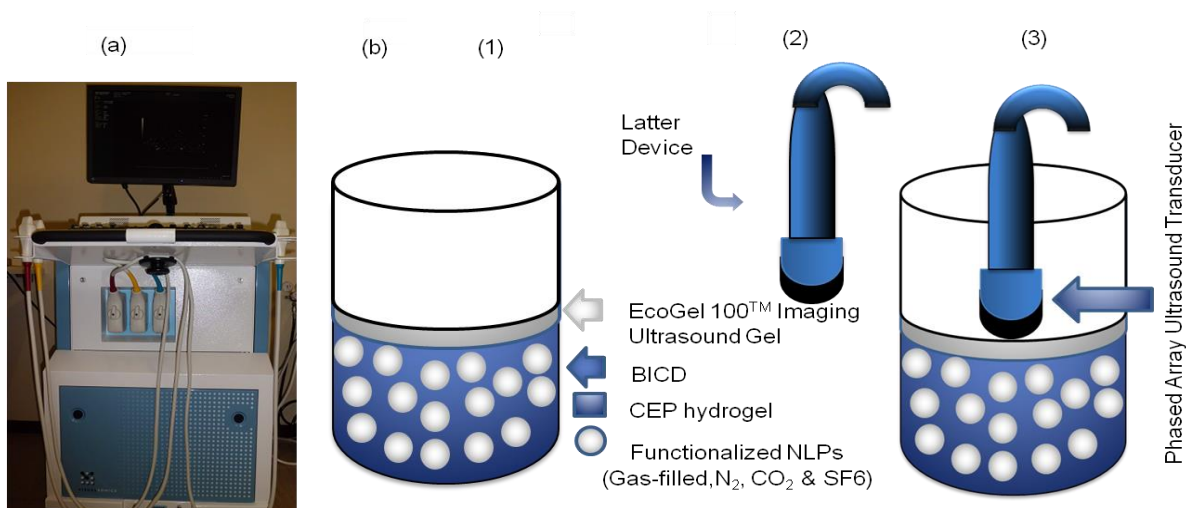


Figure 5.1: Schematic demonstrating ultrasound imaging analysis of the BICD, a) Vevo® 2100 Visual Sonics instrument; b1) EcoGel 100™, b2) lateral device (ultrasound transducer); and b3) transducer array on top of EcoGel 100™ and BICD.

5.2.4.2. Real-time fluorescence imaging of fluorescence-labeled functionalized nanoliposomes embedded within a Bio-Robotic Intracranial Device

Real-time fluorescence imaging of FITC-labeled functionalized NLPs embedded within a BICD was visualized using Cell-viZio fluorescence microscopy (Mauna Kea Technologies, Paris, France). CEP hydrogel was stained with DAPI or trypan blue in order to elucidate its network-like structure and to visualize FITC-labeled

functionalized NLPs embedded within the polymeric-based depot. Proflex™ fibered imaging optic probe with a wavelength of 488nm was used for either topographical or interior region visualization imaging of the FITC-labeled functionalized NLPs, the CEP hydrogel stained with DAPI or trypan blue stain, and double-labeled BICD (Figure 5.2).

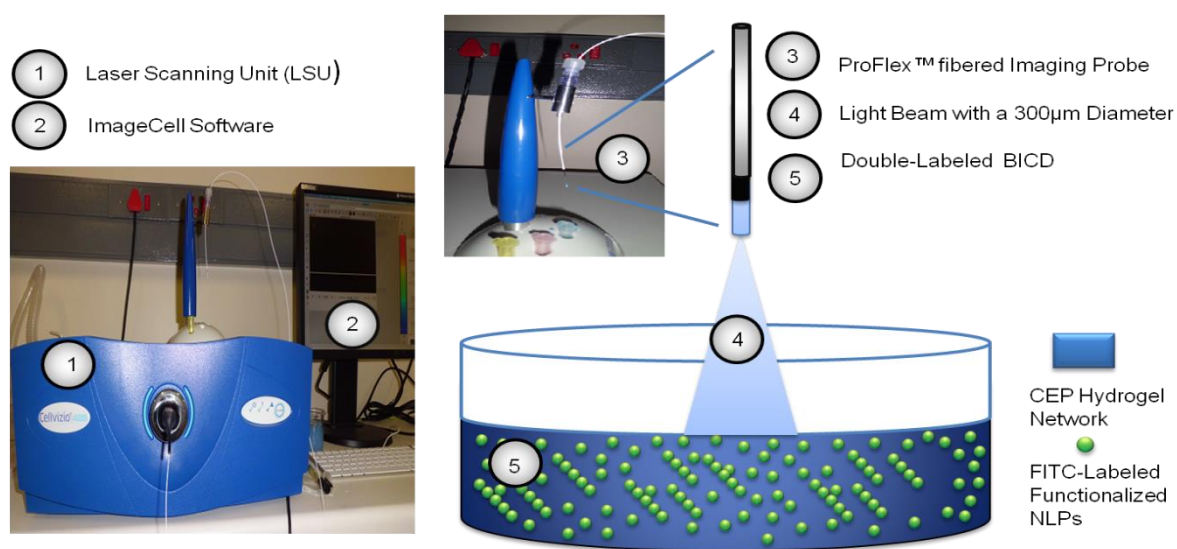


Figure 5.2: Schematic demonstrating detection of the labeled-BICD employing Cell-viZio™ imaging analysis via the optical proflex™ fiber probe.

5.2.4.3. Optical fluorescence imaging of fluorescence-labeled functionalized nanoliposomes embedded within the Bio-Robotic Intracranial Device

Fluorescence activities of the FITC or rhodamine-labeled functionalized NLPs embedded within the BICD, CEP hydrogel stained with DAPI or trypan blue and double-labeled BICD were further visualized using Olympus IX71 Immunofluorescence Microscopy (Olympus Co., Tokyo, Japan). All samples were mounted directly on a glass slide and thereafter dried under a fume hood prior to examination. Fluorescence measurements were executed at a different excitation and emission spectrum; 450/525nm for FITC, 540-625nm for rhodamine, 540/585nm

for trypan blue stain and 350/470nm for DAPI stain. The images for all samples were viewed at 10X magnifications.

5.3. Results and Discussion

5.3.1. *In vitro* characterization of the gas-filled functionalized nanoliposomes

5.3.1.1. Determination of the particle size distribution of the gas-filled functionalized nanoliposomes

Table 5.2 shows the effect of SF₆, CO₂ and N₂-filled functionalized NLPs on the particle size and PDI employing Dynamic Light Scattering (Zetasizer NanoZS, Malvern Instrument, UK). The average particle size was in range of 135-150nm with a PDI from 0.17-0.13 for the native functionalized NLPs, 154-165nm (PDI = 0.19-0.18) for the N₂-filled functionalized NLPs, 152-154nm (PDI = 0.18-0.14) for the CO₂-filled functionalized NLPs, and 158-168nm (PDI = 0.17-0.12) for the SF₆-filled NLPs. The particle size values validate that the presence of gases such SF₆ or control N₂ or CO₂ may have induced vesicle cavitations resulting in a larger particle size (Prentice et al., 2005, Liu et al., 2006, Suzuki et al., 2007). Figure 5.3 shows a typical particle size and zeta potential were, and TEM micrograph of gas-filled functionalized NLPs. The micrographs depicted uniformity within the nanosize range and spherical shape of the gas-filled functionalized NLPs in suspension.

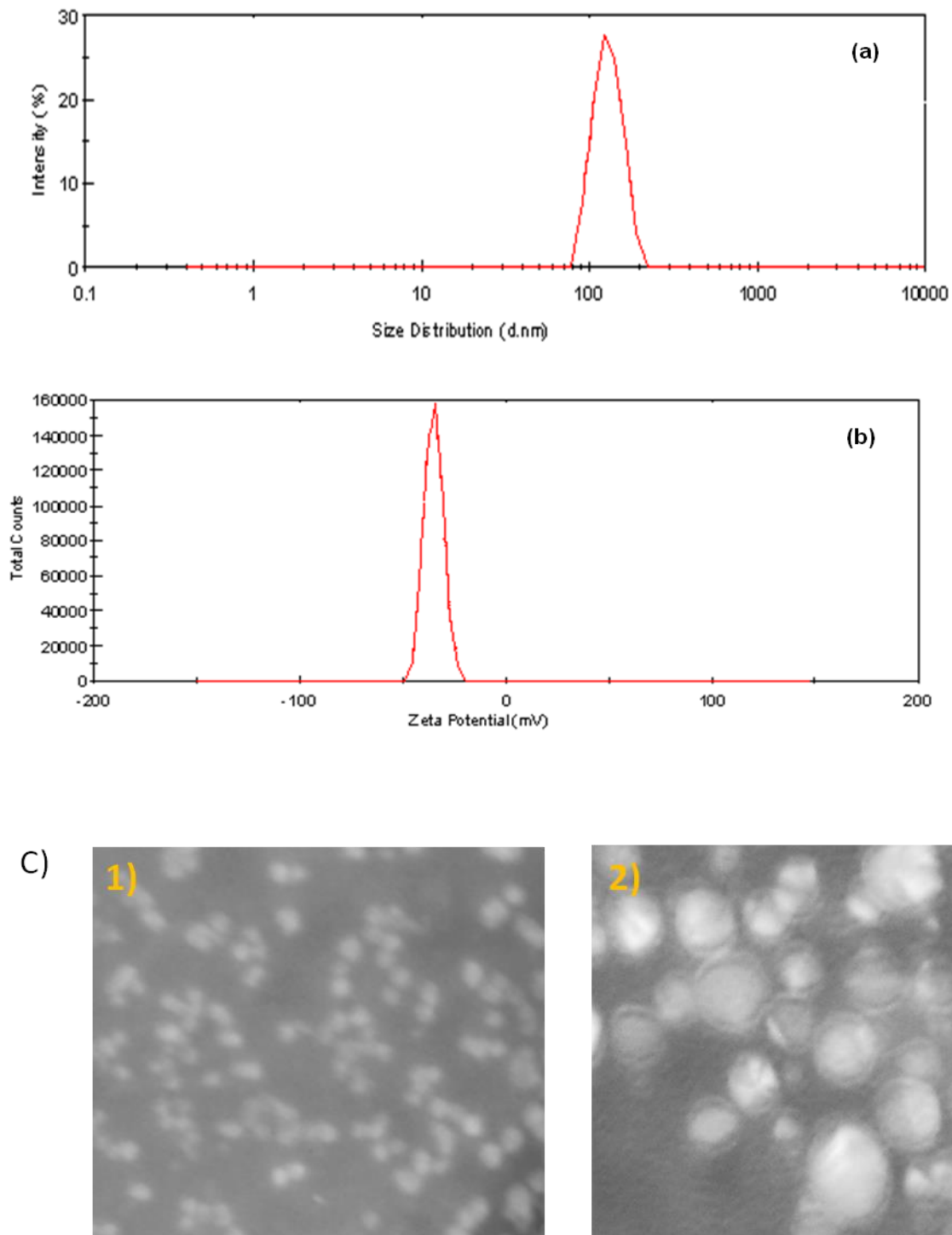


Figure 5.3: Physicochemical characterization of the functionalized NLPs, a typical a) particle size, b) zeta potential, and c) TEM micrographs, c1) 50x, c2) 100x magnification.

Table 5.2. The alteration in particle size of the functionalized NLPs following incorporation of various gases

F#	Functionalized Nanoliposomes		Particle Size (nm)	Polydispersity Index
	DSPC/CHOL/DSPE/Peptide			
	(mg)			
1	63.3/74.5/6.5/1		135±15	0.174-0.130
	Gas-filled Functionalized Nanoliposomes		Particles Size	Polydispersity Index
	(mg/mg/mg/mg)		(nm)	
		Gas		
2	63.3/74.5/6.5/1	N ₂	154±11	0.190-0.185
3	63.3/74.5/6.5/1	CO ₂	152±04	0.188-0.149
4	63.3/74.5/6.5/1	SF ₆	158±10	0.170-0.129

5.3.1.2. *In vitro* stability of the gas-filled functionalized nanoliposomes

In vitro stability of the native (MLVs and SUVs) and gas-filled functionalized NLPs was analyzed using Turbiscan Lab® Expert (Formulacrion Co., Eunion, France). Figures 5.4a-c show typical transmission and backscattering profiles of the native and gas-filled NLPs. The y-axis in the diagram represents the percentage variations of transmitted light or backscattering behaviors, while the x-axis represents the height of the sample cell at different time intervals. Figure 5.4a depicts a poor transmission which appropriately corroborated with the digital image of the milky white suspension of the MLVs in glass cylindrical vials. Although a low percentage of transmission was reported, the suspension demonstrated a homogeneous state and stable system with a single backscattering variation along the entire hour of scanning the sample as previously reported by Mengual and co-workers (1999). The higher percentage of backscattering light may have been attributed to the bigger particle size and the density between organic solvent (such as chloroform and methanol at ratio 9:1) and phosphate buffer at a pH7.4 phase that is employed for the adapted reverse-phase evaporation technique for MLVs fabrication. A high transmission was

exhibited for the SUVs samples, native and gas-filled functionalized NLPs. The increase of the transmission (%) for native and gas-filled functionalized NLPs may be influenced by the size of the particles that allows a light beam to pass through easily. These results validate that SUVs, native and gas-filled functionalized NLPs were stable *in vitro* in the dispersion phase with low and/or poor sedimentation post scanning at $\lambda=880\text{nm}$ over 1 hour at room temperature.

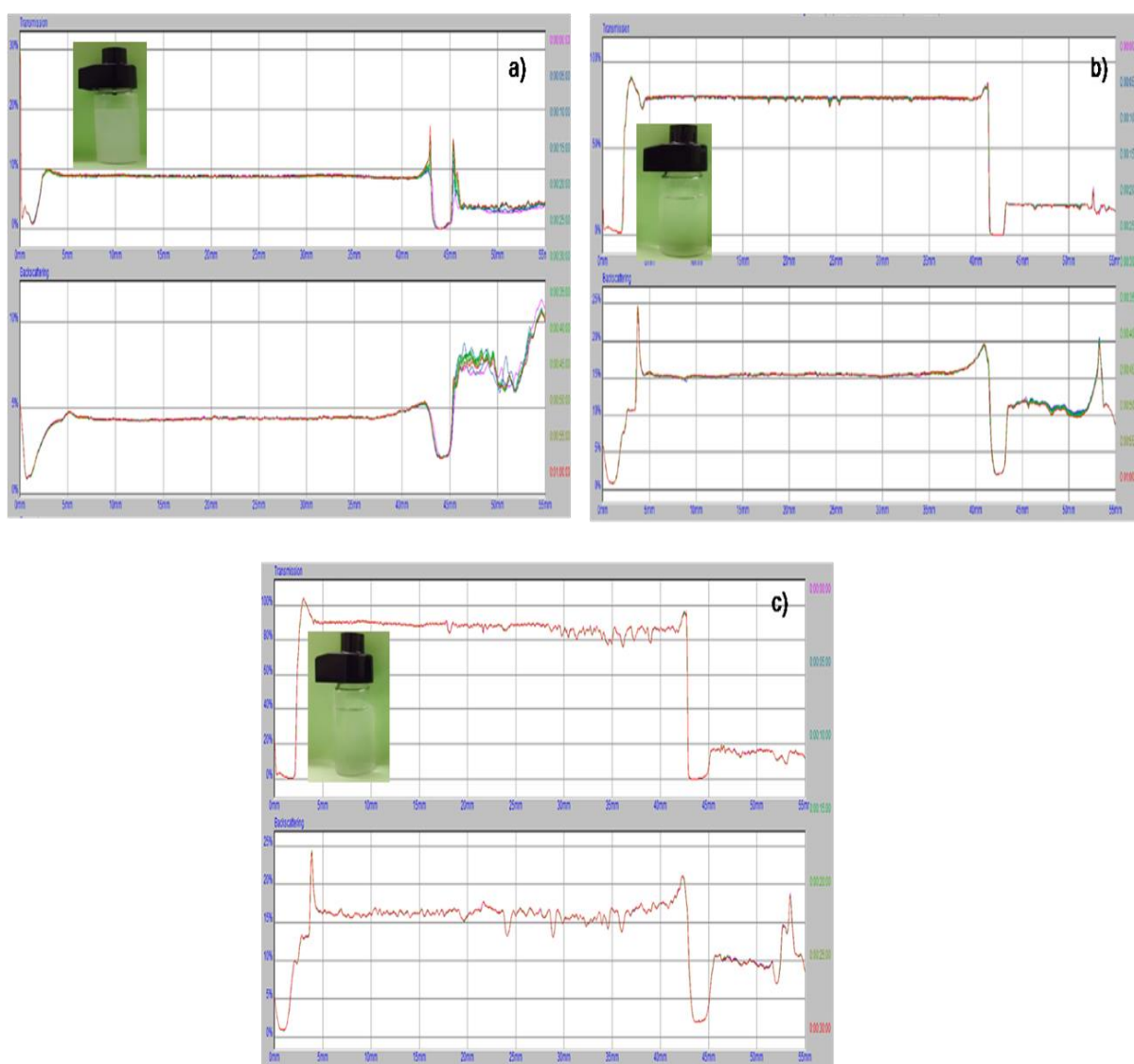


Figure 5.4: Transmission and backscattering images of the functionalized NLPs obtained using Turbiscan LAB spectra. Samples scanned at $\lambda=880\text{nm}$ every 5 minutes for an hour, a) MLVs b), native NLPs and c) gas-filled functionalized NLPs.

5.3.2. Physicochemical characterization of the cross-linked Chitosan-Eudragit RSPO-Polyvinyl alcohol hydrogel

5.3.2.1. Molecular structural transition of the cross-linked Chitosan-Eudragit RSPO-Polyvinyl alcohol hydrogel

FTIR analysis revealed molecular structural transition during synthesis of the cross-linked CEP hydrogel as depicted in Figure 5.5. Figure 5.5a-b shows the FTIR spectra for native CHT, EU, PVA and PEO, cross-linked CEP hydrogels (CHT-EU-PVA-GA and CHT-EU-PEO-GA). Figure 5.5a1 and b1, revealed that all major bands that were essentially associated with native CHT at about $3500\text{-}3200\text{cm}^{-1}$, correspond to the hydroxyl group (OH) stretch vibration and amine group (NH) symmetrical vibration. The band of 2870cm^{-1} corresponded to CH stretch vibration, 1649cm^{-1} to an amide I stretch vibration (acetylated amine), 1588cm^{-1} band to an amide II deformation (deacetylated amine), 1375 and 1317cm^{-1} to CH_2 and CH_3 deformation, and the 1059 and 1024cm^{-1} band O-C stretch vibration (Yang et al., 2004; Kim et al., 2007). Figure 5.5a2 and b2 displays the native EU characteristic band at 3445cm^{-1} for the OH stretch vibration; 2989 , 2970 and 2950cm^{-1} were attributed to the stretching vibration of CH_3 , CH_2 and CH, while the bands at 1724 and $1000\text{-}1300\text{cm}^{-1}$ mainly corresponded to the C-O stretching vibration. The band lending from $1350\text{-}1470\text{cm}^{-1}$ and corresponded to CH_2 and CH_3 deformation while the 986cm^{-1} corresponded to -CH and - CH_2 bend vibrations (Ammar et al., 2009).

As depicted in Figure 5.5a3, native PVA characteristic bands appear at 3290cm^{-1} (for OH stretch vibration); bands at 2970 and 2042cm^{-1} are associated with C-H stretching vibration; 1738 , 1229 and 1085cm^{-1} bands are assigned to C-O stretching

vibration; while 1423 and 1366 cm^{-1} bands correspond to CH_2 and CH_3 deformation (Dos Reis et al., 2006). The native PEO characteristic bands at 2877 and 1466 cm^{-1} are attributed to the $-\text{CH}_2-$ stretching and bending vibrations respectively. The band at 1413 cm^{-1} is assigned to C-H bending vibrations, while 1059 and 960 cm^{-1} bands are associated with an ether C-O stretch vibration, O-C stretch vibration, -CH and - CH_2 bend vibration (Figure 5b3). Figure 5.5a4, displays the FTIR spectra of the cross-linked CEP hydrogel (CHT-EU-PVA-GA). The disappearance of the major vibration band at around 3400 cm^{-1} may have indicated that there were no free -OH groups. This is possibly due to hydrogen bonding that occurred during polymer interactions. The shifting of amide (I and II) bands of the native CHT in cross-linked CEP hydrogel (CHT-EU-PVA-GA) from 1649 cm^{-1} to 1655 cm^{-1} (increase) and 1588 cm^{-1} to 1555 cm^{-1} (decrease) indicates that there was a polymeric interaction at the position of the amino groups. In addition, the interaction may be enhanced by the presence of GA during the cross-linking reaction between the amine group of CHT and OH group of PVA or EU and aldehyde group of GA.

Figure 5.5b4 showed the FTIR spectra of the cross-linked CEP hydrogel incorporating PEO (CHT-EU-PEO-GA). This spectrum showed almost an identical trend as cross-linked CEP hydrogel incorporating PVA (CHT-EU-PVA-GA). The following bands of the native CHT in cross-linked CEP (CHT-EU-PEO-GA) shifted: Amine bands were shifted from 1649 cm^{-1} to 1650 cm^{-1} (slightly), and 1588 cm^{-1} to 1560 cm^{-1} ; C-H showed some stretching vibrations at a wavelength of around 2949 cm^{-1} , while free OH disappeared. The appearance of these signals signifies that strong intermolecular and/or intermolecular hydrogen bonds occurred between the

polymers. In addition, the band shift in the amine position during formulation of CEP hydrogel confirmed that GA was successful cross-linking polymers.

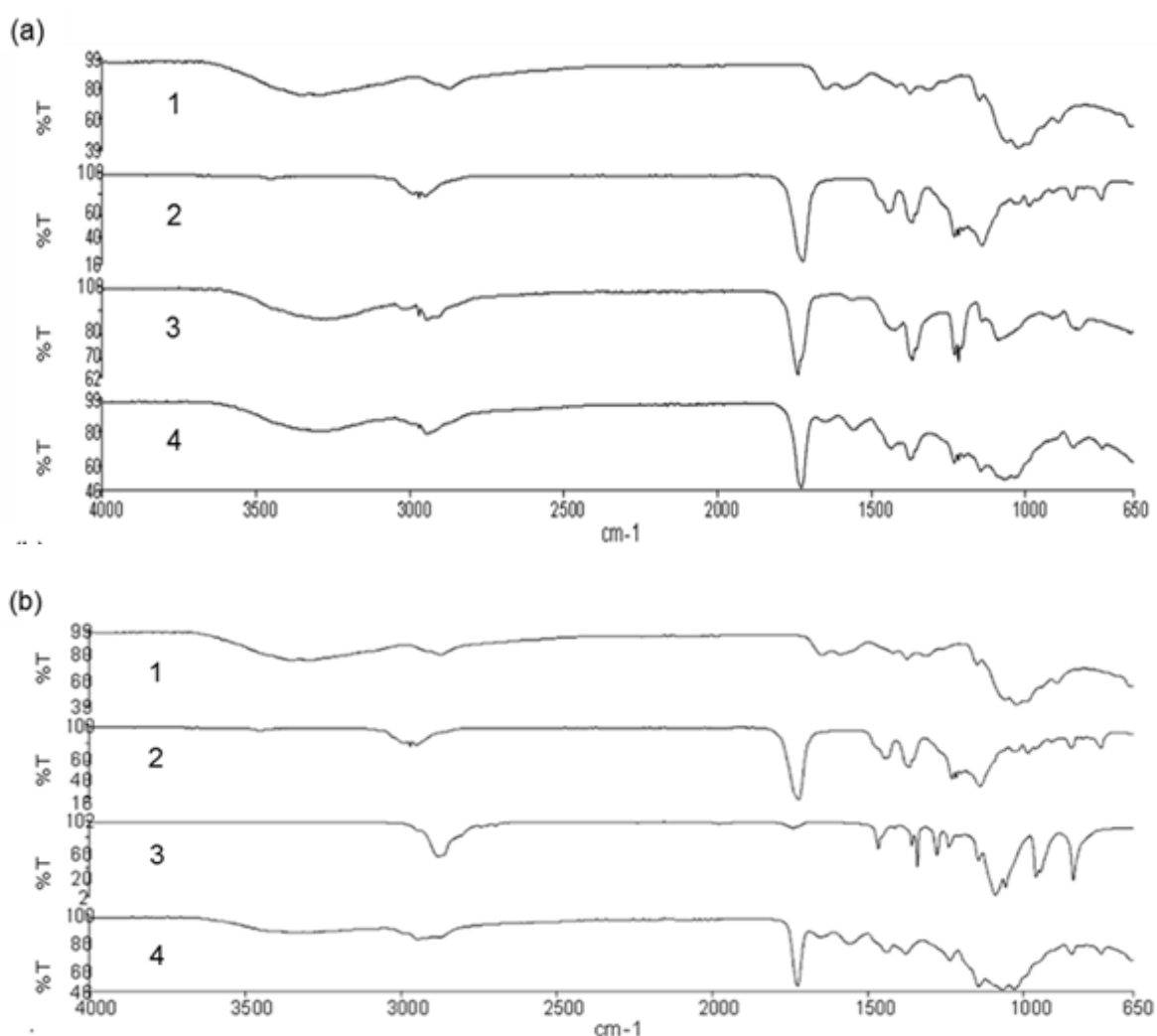


Figure 5.5: FTIR spectra of the cross-linked CEP hydrogels; a) cross-linked CEP hydrogel fabricated from, native polymers; 1) CHT, 2) EU, 3) PVA and 4) CHT-EU-PVA-GA, b) cross-linked CEP hydrogel fabricated from native polymers: 1) CHT, 2) EU, 3) PEO and (4) CHT-EU-PEO-GA

5.3.2.2. Rheological properties of the cross-linked Chitosan-Eudragit RSPO-Polyvinyl alcohol hydrogel

Fluid behaviors and/or viscosity of polymers appeared to be governed by many factors such as temperature, pH and polymer concentrations. As the concentration of viscous polymers increased, a high resistance to flow is created from Newtonian behavior to non-Newtonian behavior, which is known as shear thinning (Mohamed,

2004). The viscosity (slope of the curve) of shear thinning has been reported in many studies where it decreases with an increased shearing rate (Mohamed, 2004; Chacko et al., 2010). The viscosity and viscoelasticity of the CEP hydrogel (F1-6) are depicted in Figures 5.6 and 5.7. F1-2 and F4-5 showed a great transition of hydrogel flow behaviors from low resistance to high resistance when EU concentration decreased from 3% to 1%^{w/v}, and while PVA or PEO concentration increased from 1% to 3% ^{w/v}, at a constant CHT concentration of 3% ^{w/v}. F3 and F6 showed the highest viscosity with low deformation as compared to the above formulations. For low deformation, a higher force is required for the sample to attain properties of a running fluid (Albu et al., 2009; Karazhiyan et al., 2009). These results may be influenced by an increase in the intermolecular interaction and/or entanglements between polymer chains (Karazhiyan et al., 2009). The flow curves of the typical cross-linked and non-cross-linked CEP hydrogels further highlighted strong shear-thinning behavior due to GA being a constituent for enhanced intermolecular interaction between polymers (Figure 5.6c). Furthermore, upon diluting CEP hydrogel with functionalized NLPs (at liquid state), results showed a decreased viscosity slope or lower shear thinning behavior and high deformation (Figure 5.6d). Overall, results suggest that the flow capability and/or deformation of the CEP hydrogel may have been governed by either polymer concentration or an entanglement between polymer chains in the presence of the GA as a cross-linking agent.

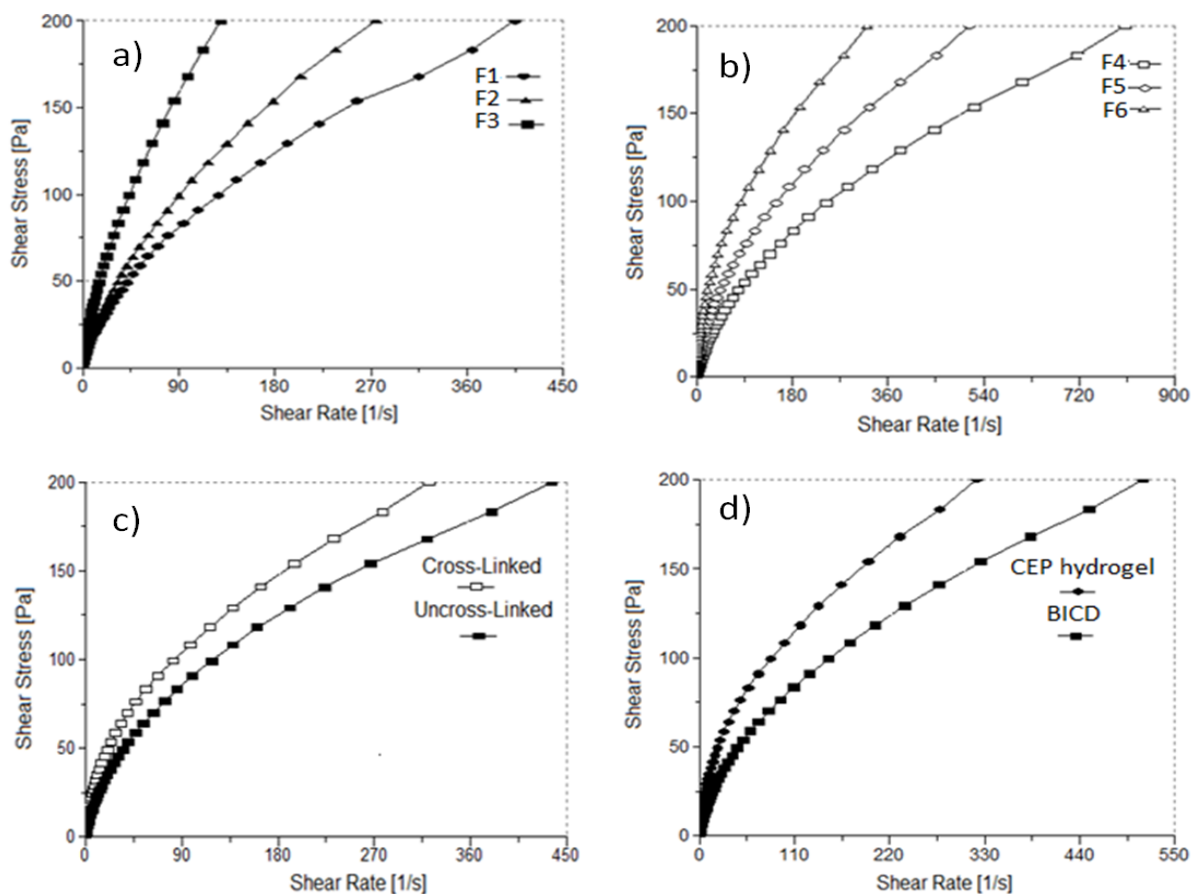


Figure 5.6: Flow behaviour of CEP hydrogels (F1-6) and the BICD. a) F1-3, b) F4-6, c) non-cross-linked and cross-linked CEP hydrogel, d) typical cross-linked CEP hydrogel and BICD.

CEP hydrogels were further investigated on their elastic storage moduli (G') and viscous loss moduli (G'') responses. The viscoelastic properties (liquid-like to solid-like state) of the hydrogel networks (F1-6) were shown to be guided by the angular frequency and different polymer concentrations in the presence of a cross-linking agent (Figure 5.7). F1-2 and F4-5 demonstrated viscoelastic transition/behaviors as the EU concentration decreased from 3% to 2% w/v, while PVA concentration increased from 1% to 2% w/v, or PEO concentration increase from 1% to 2% w/v at a CHT concentration of 3% w/v. In addition, the increase in angular frequency (ω) seemed to cause a significant transition in G' and G'' . Furthermore, the nano-enabled embedment of these CEP hydrogel also showed a slight increase in rigidity, thus highlighting an entangled network of the polymer chains with the NLPs. A slight

increase in PVA concentration from 1-2% w/v or PEO concentration of 1-2% w/v resulted in the transition of the CEP hydrogel from a liquid state toward a gel-like or solid-like state. The G' and G'' crossover is an indication of relaxation time of the CEP hydrogel (Arguelles-Monal et al., 1998; Weng et al., 2007). F2 resulted in a relaxation time at $\omega \approx 3$ rad/s (G' and G''), while for F5 this occurred at $\omega \approx 10-40$ rad/s. These results may be attributed to the decrease in CEP hydrogel mobility as entangled network forms. Additionally, early relaxation time after the increase in PVA concentration increase from 1-2% w/v depicted early gelation time, indicating a quick reaction or gel-like formation at the early phase of the oscillation process (Arguelles-Monal et al., 1998). PEO showed gel-like formation at the late phase of the oscillation process, which depended solely on the angular frequency.

F3 and F6 evidently demonstrated that a higher PVA concentration of 3% w/v or PEO concentration of 3% w/v exhibited a complete transition from liquid state to solid-like state. Furthermore, G' and G'' hardly show any alteration as angular frequency increases. These results may be due to stronger mechanical properties that increased the interconnection of the hydrogel such as covalent bonding and molecular entanglements interactions (Weng et al., 2007). Furthermore, this may also be attributed to the enhanced nano-enabled structural rigidity, molecular mobility, retardation and long life span of the CEP hydrogel networks structure. The complex viscosity for all formulations was of the same trend and decreased as the oscillation frequency increased. These results depicted that there was an occurrence of a strong intermolecular, cross-linking reaction in the presence of GA and covalent bonds as previously described (in Chapter 5, section 5.3.2.1) confirmed by FTIR. These results showed a significant transition in the viscoelastic properties due to

polymer concentrations and the presence of GA as a cross-linking agent. Overall, these studies demonstrated that transformation from liquid state to solid state behavior occurred, and cross-linked CEP hydrogel were predominantly elastic with $G' > G''$.

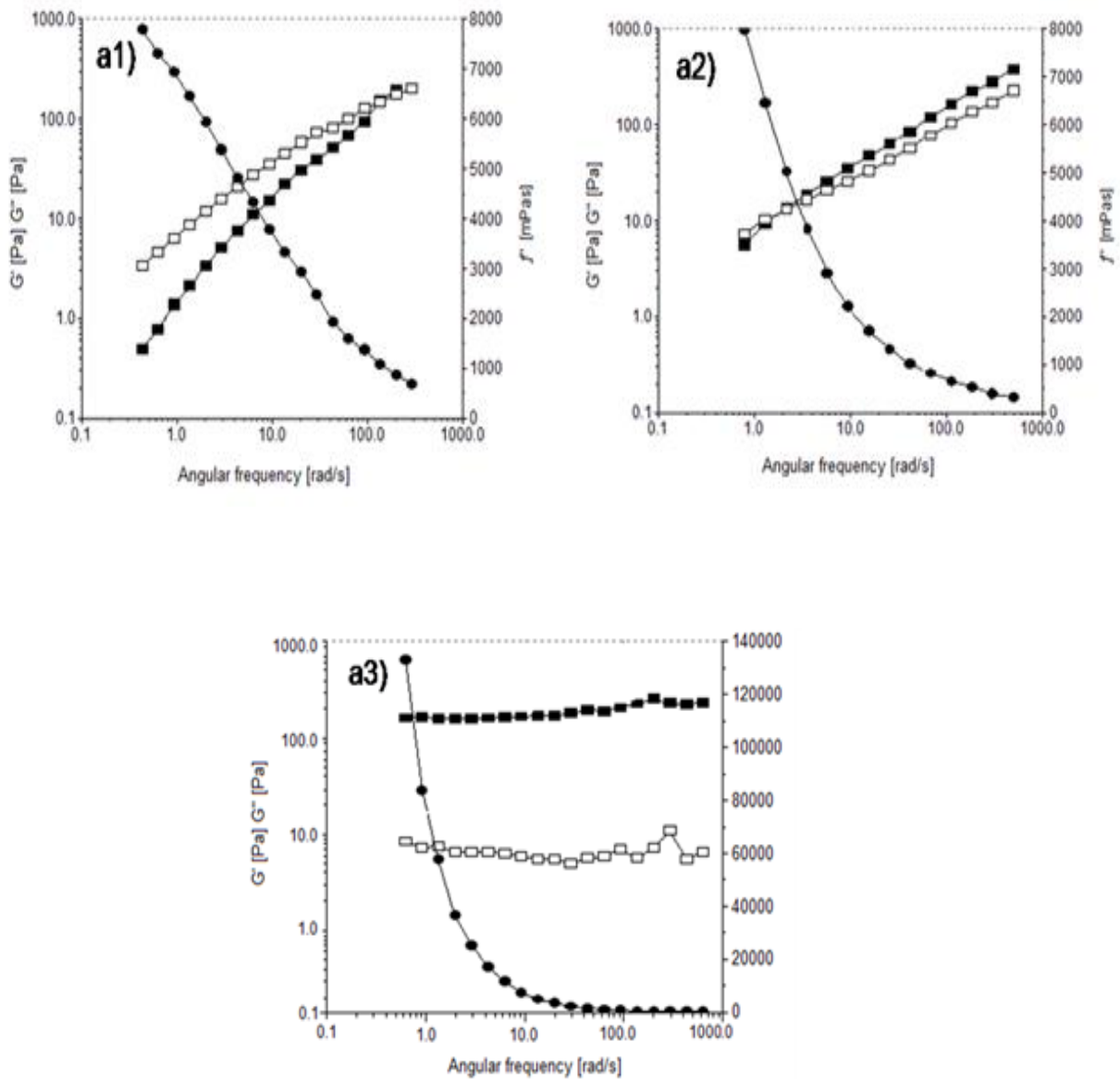


Figure 5.7: Contd. on pg 150

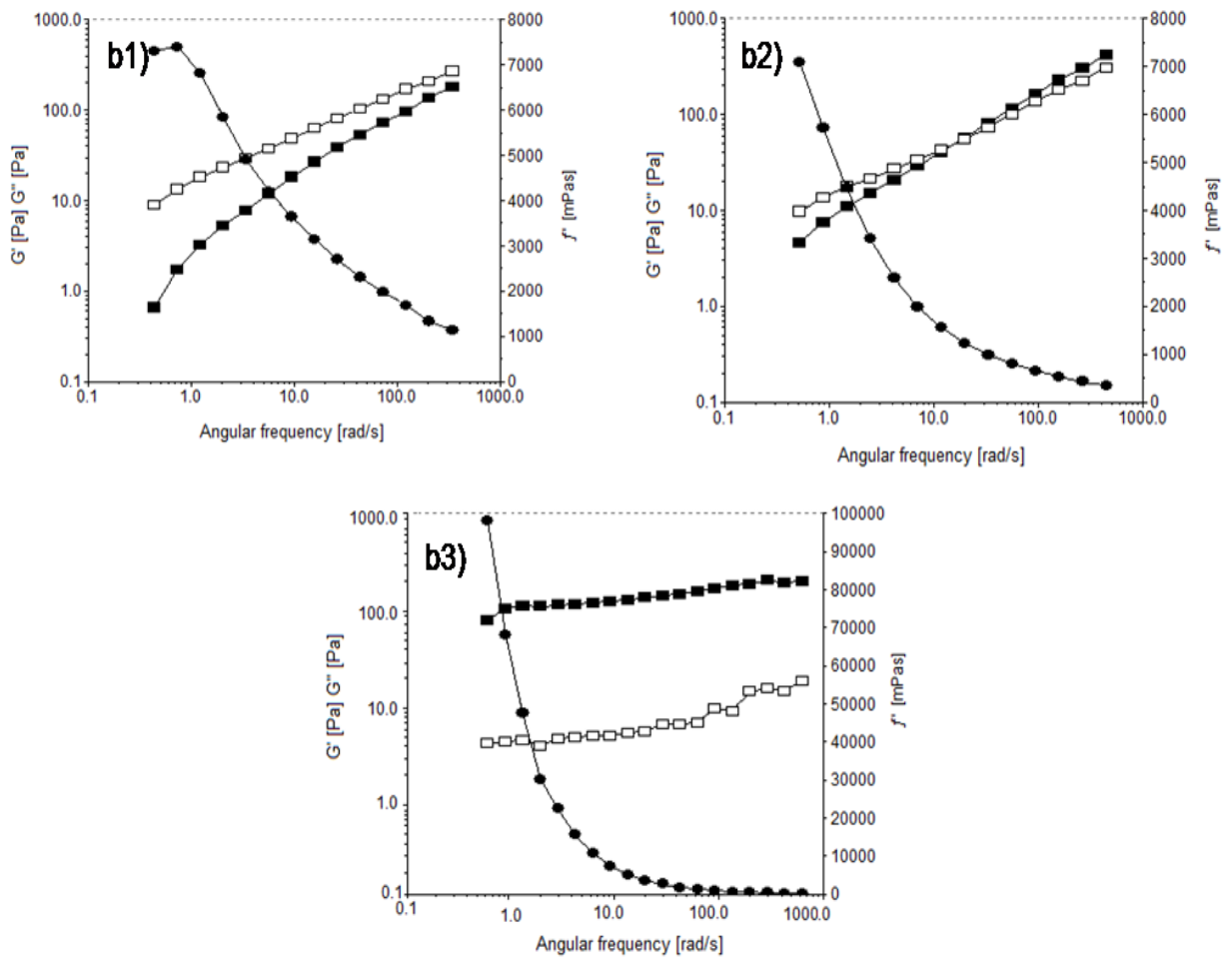


Figure 5.7: Viscoelastic moduli [G' (■), G'' (□)] and complex viscosity (●) of a) F(a1-3), and F(b4-6) at 37°C.

5.3.3. Characterization of the Bio-Robotic Intracranial Device using imaging system

5.3.3.1. Real-time ultrasound imaging of gas-filled functionalized nanoliposomes embedded within the Bio-Robotic Intracranial Device

The use of real-time ultrasound imaging for the investigation of drug, gene transportation and organ imaging *in vivo* has continued to grow in recent years (Hernot and Klivanov, 2008; Mancini et al., 2009; Wanga et al., 2010, Tabakovi et

al., 2012). In this chapter, real-time ultrasound imaging was used to visualize the particle distribution and morphological architecture of gas-filled functionalized NLPs post-embedded in the BICD; results are presented in Figure 5.8a-d. Figure 5.8a show no sphere-like structure distribution within the CEP hydrogel. Figure 5.8b depict a larger sphere-like structure in the control (intra-bubbles) CEP hydrogel in which bubbles were induced through prolonged stirring or gas-filled within the CEP hydrogel. Figures 5.8c-d, shows homogeneity distribution, uniformity and small sphere-like structure of the gas-filled native and functionalized NLPs distribution within the BICD. The presence of the functional moiety did not show any effect on particle distribution post-embedded within CEP hydrogel.

Figure 5.9 shows effect on particle distribution when different loading techniques used for embedded of gas-filled functionalized NLPs into CEP hydrogel of the BICD: a) loading into CEP hydrogel prior to cross-linking; b) loading post cross-linking; and c) loading using 1mL syringe injection. As shown in Figures 5.9a-c, homogeneity in particle distribution within the internal of the CEP hydrogel was achieved by loading prior to cross-linking, surface distribution occurred with loading post cross-linking, and regional distribution for loading through syringe injection.

Figures 5.10a-b shows, the appearance of gas-filled functionalized NLPs distribution within CEP hydrogels composed of different polymeric components; a) cross-linked CEP hydrogels (CHT-EU-PVA-GA) and b) (CHT-EU-PEO-GA). Results showed no significant differences in particle distribution when either PVA or PEO was used as a component of the CEP hydrogel network. Overall, results showed that the BICD has a greater capability to act as a depot for gas-filled functionalized NLPs. In addition,

the study also demonstrated that gas-filled functionalized NLPs were still intact or stable post-embedding into the BICD. Ultrasound imaging technology, which is currently used for *in vivo* imaging, has also demonstrated to be a good qualitative technique for BICD visualization *in vitro*.

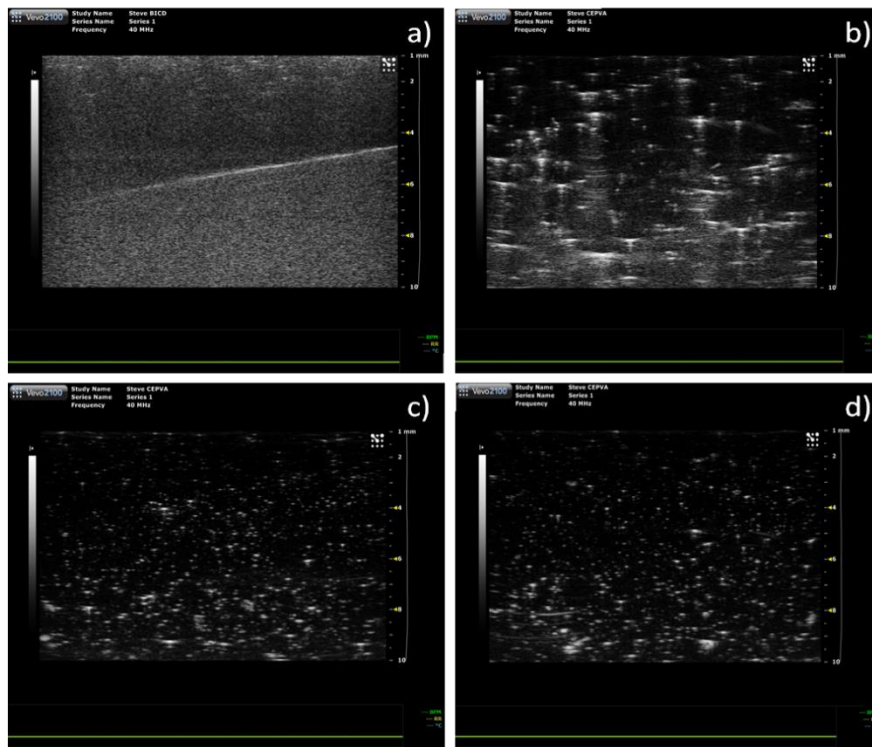


Figure 5.8: Ultrasound images of the gas-filled functionalized NLPs embedded within the BICD, a) native CEP hydrogel; b) CEP hydrogel induced inter-bubbles, c) SF6-filled native NLPs d) SF6-filled functionalized NLPs.

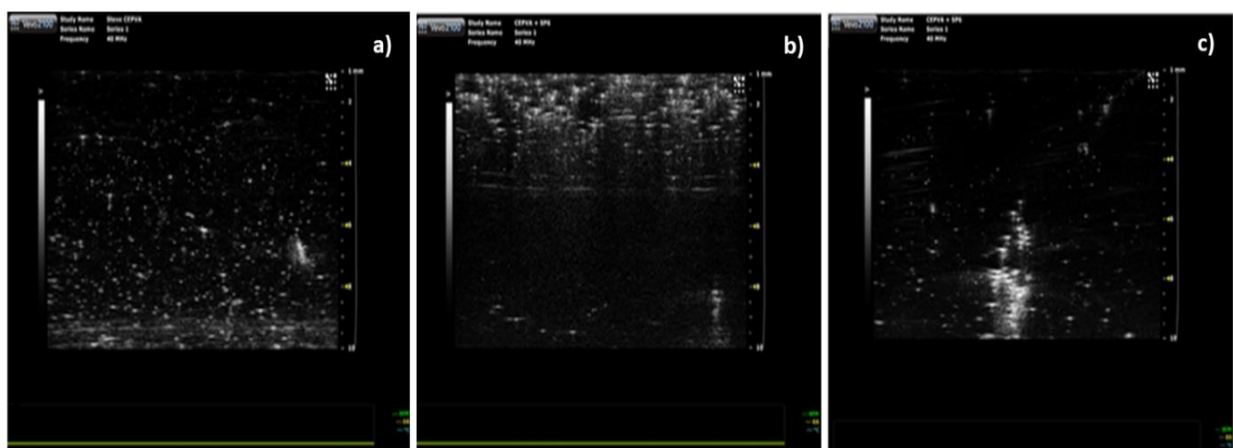


Figure 5.9: Ultrasound images of the gas-filled functionalized NLPs embedded within the BICD employing different loading techniques: a) loading into CEP hydrogel prior to cross-linking; b) loading post cross-linked and c) loading using 1mL syringe injection.

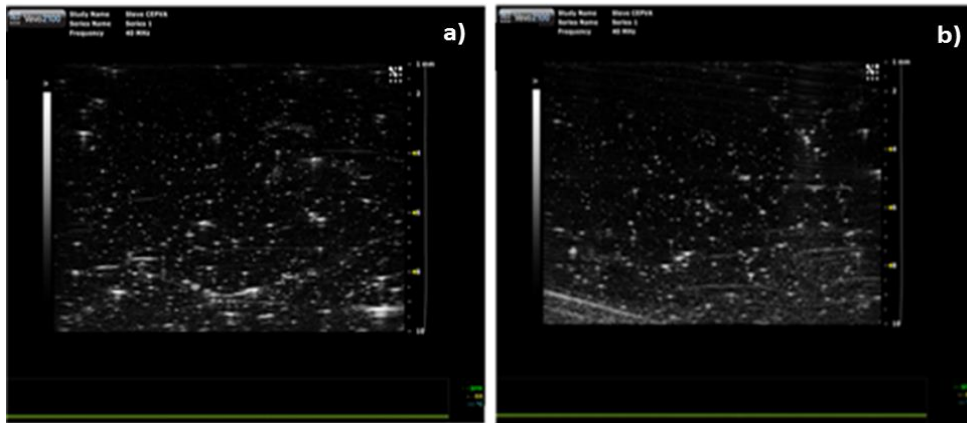


Figure 5.10: Typical ultrasound images of SF6-functionalized NLPs embedded within CEP hydrogels fabricated out of different polymeric components. CEP hydrogels a) CHT-EU-PVA-GA and b) CHT-EU-PEO-GA

5.3.3.2. Fluorescence imaging of the fluorescence-labeled Bio-Robotic Intracranial Device

Fluorescence imaging technology in pharmaceuticals has been the most-often-used technology for validating the capability of targeting of the gene or drug delivery system into a disease site (Martina et al., 2007; Wanga et al., 2010). In this chapter, fluorescence imaging was used for further validating BICD formation. Figures 5.11a-c, shows two-dimensional (2D) fluorescence profiles of FITC-labeled functionalized NLPs embedded within the BICD, visualized using a Cell-viZio fluorescence microscopy (Mauna Kea Technologies, Paris, France). Figure 5.11a-c, shows the following: a) FITC-labeled, b) gas-filled FITC-labeled functionalized NLPs embedded within cross-linked CEP hydrogel (CHT-EU-PVA-GA), c) FITC-labeled, and d) gas-filled FITC-labeled functionalized NLPs embedded within cross-linked CEP hydrogel (CHT-EU-PEO-GA).

CEP hydrogel was stained with DAPI or trypan blue in order to elucidate its network-like structure and to visualize the FITC-labeled functionalized NLPs embedded within the polymeric-based depot. In a simultaneously conducted fluorescence study on the

same formulation, it was evidently observed that surface topography fluorescence spikes correlated with those of the 2D fluorescence profile. The surface topography imaging illuminated the fluorescence intensity per fluorescent spot.

Figure 5.12 depicts typical fluorescence profiles of the control native CEP hydrogel (unlabeled), CEP hydrogel stained with DAPI or trypan blue and double-labeled BICD. Figure 5.12a shows no fluorescence activity in the control CEP hydrogel (unlabeled). Figure 5.12b shows high fluorescence-labeled activity in 2D of the CEP hydrogel with network-like structure post-labeled or stained with DAPI or trypan blue. Figure 5.12c shows a typical doubled-labeled BICD. In addition, the co-existence of two fluorescence markers may indicate effectively co-localized gas-filled FITC-labeled NLPs inside the CEP hydrogel. Furthermore, FITC-labeled functionalized NLPs exhibited an intact (arrows) or slight burst (spherical shape into smear-like morphology, see circles) of FITC-labeled functionalized NLPs post-embedded within the CEP hydrogel during BICD fabrication. This outcome could have been influenced by the structure disruption of the gas-filled functionalized NLPs during fabrication of the BICD. The surface topography fluorescence spikes were further matched to those of the 2D fluorescence image, where either fluorescence activity or surface topography activities were detected.

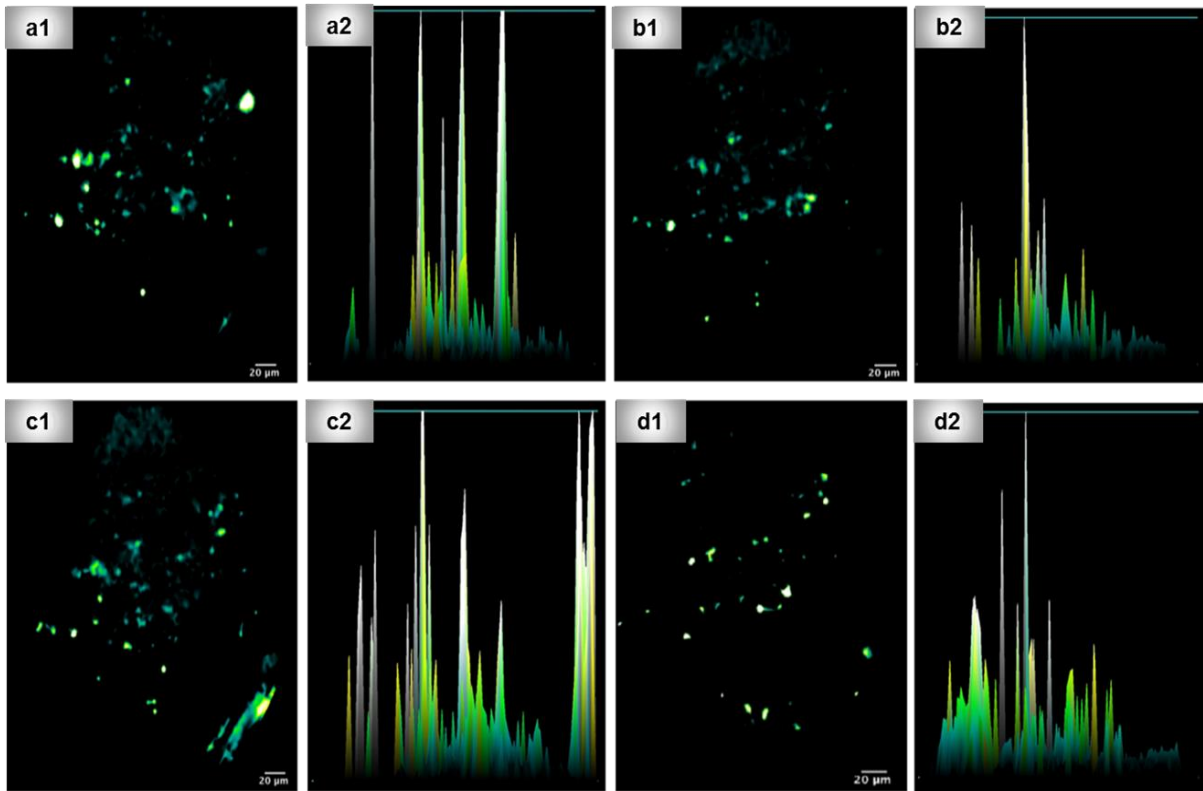


Figure 5.11: Cell-viZio images of FITC-labeled functionalized NLPs distribution within the CEP hydrogels of the BICD. a) FITC-labeled functionalized NLPs b) FITC-labeled and gas-filled functionalized NLPs within the cross-linked CEP hydrogel (CHT-EU-PVA-GA), and c) FITC-labeled functionalized NLPs, d) FITC-labeled and gas-filled functionalized NLPs within the cross-linked CEP scaffold (CHT-EU-PEO-GA).

Figures 5.13a-c show typical fluorescence profiles of the rhodamine, FITC-labeled functionalized NLPs and CEP hydrogel stained with trypan-blue or DAPI examined employing the Olympus IX71 Immunofluorescence Microscopy (Yin et al., 2012). Figures 5.13a1-3 and b confirm the morphology of the rhodamine or FITC-labeled functionalized NLPs with a spherical shape, uniform and inertial cavitations with a shell-like structure throughout the surface structure, and a single hollow core. Figure 5.13c further validates that the CEP hydrogel stained DAPI or Trypan blue depicts a network-like structure. Overall, results or fluorescence profiles exhibited a study correlated with the data obtained employing TEM, ultrasound and cell-viZio imaging

systems in particles distribution and morphology of FITC-labeled or gas-filled functionalized NLPs.

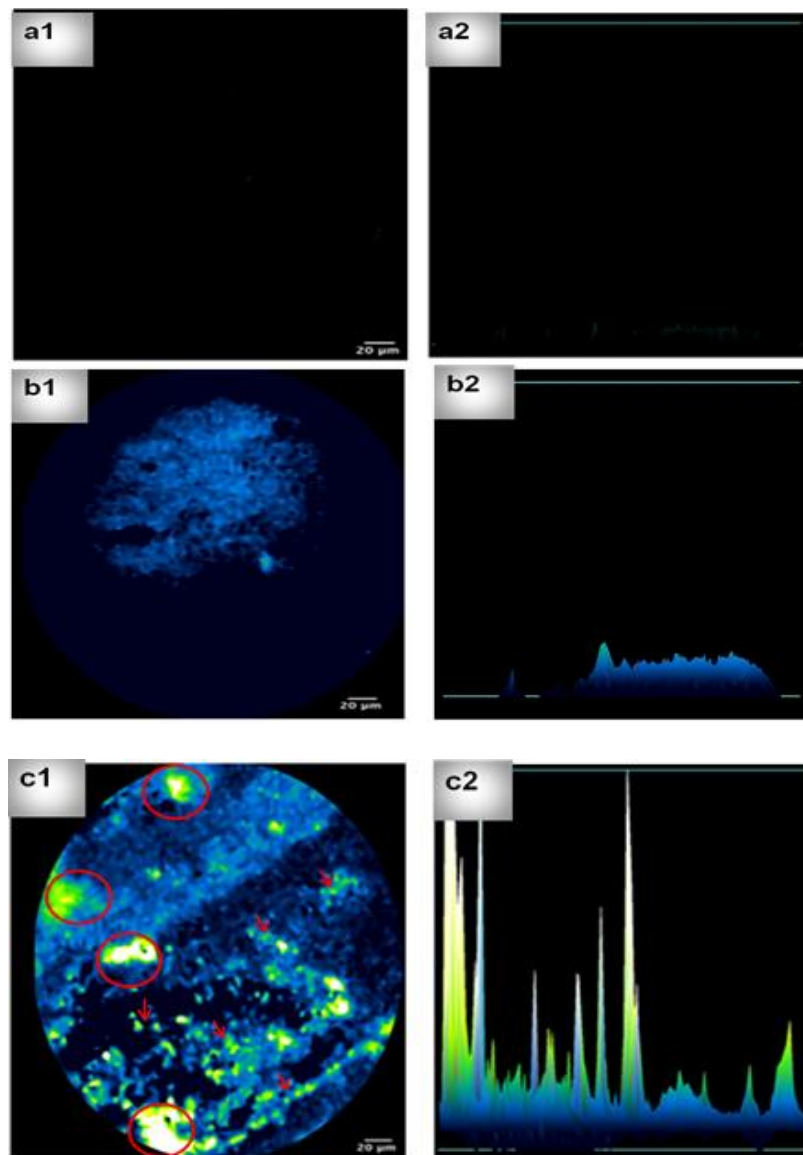


Figure 5.12: Typical Cell-viZio profiles of the double fluorescence-labeled BICD. a) Control CEP hydrogel (unlabeled), b) CEP hydrogel stained with DAPI or trypan blue, and c) double fluorescence-labeled BICD.

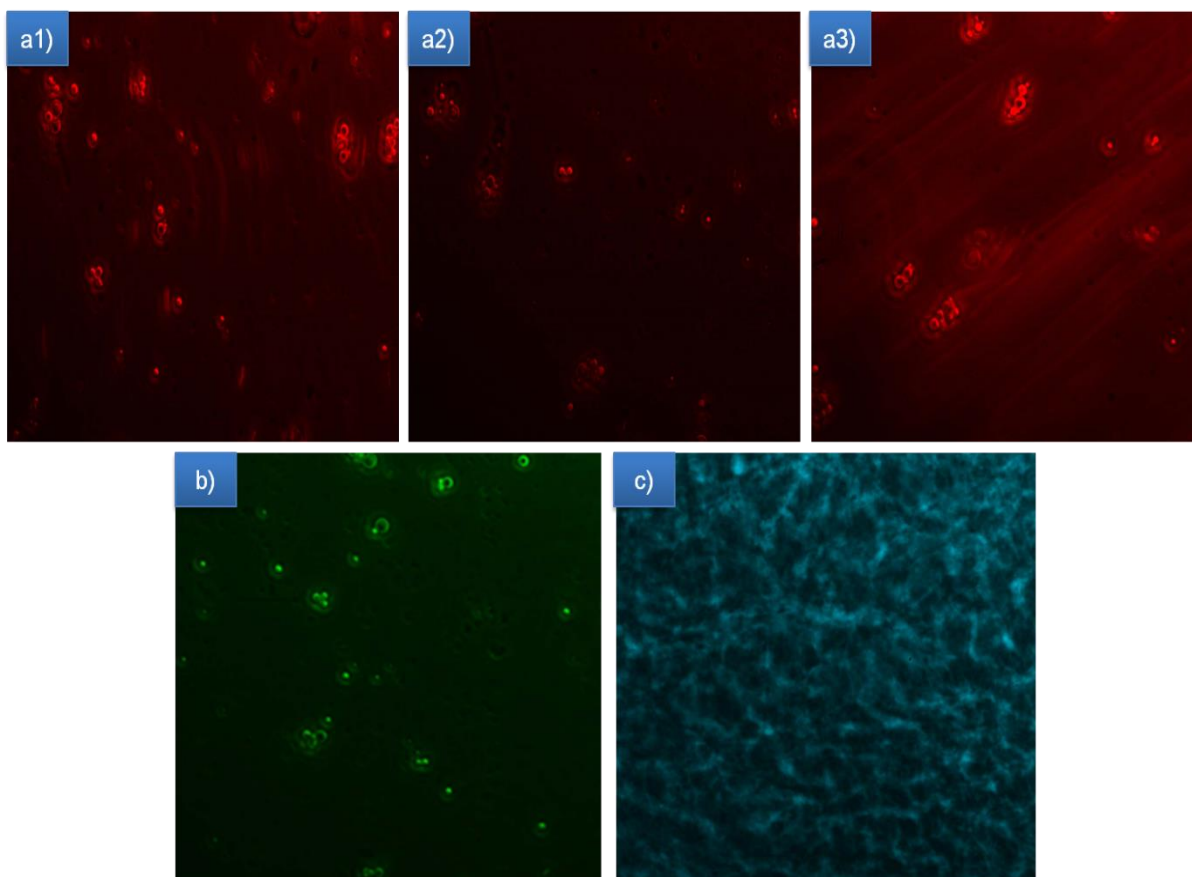


Figure 5.13: Typical fluorescence images of the BICD. a1-3) rhodamine, b) FITC-labeled functionalized NLPs and c) CEP hydrogel stained with DAPI or trypan blue.

5.4. Concluding Remarks

The results obtained in this chapter evidently validate the development of the BICD fabricated by embedding fluorescence-labeled or gas-filled functionalized NLPs within cross-linked CEP hydrogel. Modified functionalized NLPs showed a slight effect on the particle size distributions of post gas-filled; SF₆, control N₂ and CO₂ within the core of the lipid bilayers. FTIR analysis revealed the presence of bands produced during molecular structural interactions or cross-linking of the polymers during the design of the CEP hydrogel. Furthermore, these results postulate that biomechanical properties must also be considered when designing the BICD drug delivery system. The non-Newtonian (shear thinning) behavior and viscoelastic

properties (G' and G'') were both shown to be governed by polymer concentrations and GA.

The results obtained in this chapter evidently validate the development of the BICD fabricated by embedding fluorescence-labeled or gas-filled functionalized NLPs within cross-linked CEP hydrogel. Modified functionalized NLPs showed a slight effect on the particle size distributions following filling with gas (SF_6 , control N_2 and CO_2 within the core of the lipid bilayers). FTIR analysis revealed the presence of bands produced during molecular structural interactions or cross-linking of the polymers during the design of the CEP hydrogel. Furthermore, these results postulate that biomechanical properties must also be considered when designing the BICD drug delivery system. The non-Newtonian (shear thinning) behavior and viscoelastic properties (G' and G'') were both shown to be governed by polymer concentrations and cross-linker. The mechanical properties of the permanent CEP hydrogel were shown to be influenced by gel flow which was observed in solid state rather than liquid state. In this case, G' was greater than G'' , indicating that strong intermolecular interactions were obtained during CEP hydrogel fabrication. TEM and imaging systems validated that the morphological architecture of the gas-filled functionalized NLPs were uniform and spherical in shape pre- or post-embedding into the BICD, respectively. In addition, gas-filled functionalized NLPs distribution within the internal core of the CEP hydrogel were shown to be associated with hydrogel flow behaviors and loading techniques used during generation of the BICD. Moreover, homogeneity and particle distribution within CEP hydrogel may have been influenced by NLPs stability in suspension with low sedimentation prior to embedding into the BICD. The presence of the functionalized moieties did not show any

significant effect on the gas-filled functionalized NLPs distribution post-embedding into the BICD. Fluorescence imaging studies exhibited a co-localization and burst-like of the FITC-labeled NLPs post-embedding within the double-labeled BICD. Further studies are necessary to identify the BICD's potential for diagnosis and/or targeted treatment for afflictions such as AD, since attached functionalized moieties have previously been shown to have the potential for guiding NLPs to targeted sites of AD (see Chapter 4, section 4.3.9.2). The findings in this chapter also validated that biomechanical dynamics and imaging techniques could be used as appropriate future techniques for characterization of track-labeled or gas-filled drug delivery vehicles post-embedded into a BICD.

CHAPTER 6

EX VIVO CYTOTOXICITY ANALYSIS OF THE NANO-ENABLED BIO-ROBOTIC INTRACRANIAL DEVICE FOR PROLONGED GALANTAMINE RELEASE

6.1 Introduction

The bio-construction of potential neuropharmaceutical devices that have capability to extend neuroprotectant drug efficacy over a prolonged period, particularly to Alzheimer's disease (AD) has gained attention over the past few decades (Nowacek et al., 2009; Sahni et al., 2011). Liposomal-based systems are among other nanotechnologies that have showed potential in transporting drugs into the central nervous system (CNS) (Schnyder and Huwyler, 2005; Torchilin, 2005; Nowacek et al., 2009).

Liposomes are fabricated using both natural and synthetic phospholipids (Johnsson and Edwards, 2003). The advantages of employing liposomal-based drug delivery systems for neuropharmaceutical applications includes the capability to incorporate hydrophilic and hydrophobic drugs, good biocompatibility and low toxicity, the ability to bypass BBB and target drug delivery (Abbot and Romero, 1996; Schnyder and Huwyler, 2005; Ying et al. 2010). However, liposomal-based systems are ineffective on clinical neuropharmaceutical applications because of the poor absorption following systemic delivery, which is associated with a rapid clearance in the presence of the reticuloendothelial system (RES) and short plasma half-life (Krown et al., 2004; Immordino et al., 2006; Li et al., 2009). To overcome or bypass these challenges associated with liposomal-based systems, the following studies were

done: liposomes were surface engineered with polymers that have good mechanical stability and/or liposomal-based system were amalgamated with polymeric-based systems/ temporal depots (Frank, 1993; Torchilin, 2005; Immordino et al., 2006; Nakano et al., 2008; Wang et al., 2010; Ruizhen et al., 2011).

In addition, the temporal depots that are made up of polymeric-based systems such as hydrogels and pre-fabricated polymeric scaffolds have also been reported to be suitable for prolonged drug release and/or cell seeding (Stenekes et al., 2000; Hara and Miyake, 2001; Chung et al., 2006; Mulik et al., 2009; Mufamadi et al., 2011). Both natural and synthetic polymers have been used as building block materials to create an ideal structure of the temporal depot of the pre-fabricated polymeric scaffold (Young et al., 2005; Kojima et al., 2009; Bhattarai et al., 2010). In neuropharmaceutics, an “ideal” temporal depot would exhibit the following desirable elements: ability to enhance local drug retention, mechanical stability, sustained/or prolonged drug release, ease of manipulation *in vitro* (particularly the shape of the structure and pore capacity), and having the capability for cell seeding on the surface of a bio-structure (Cheng et al., 2008; Wang et al., 2008; Bhattari et al., 2010). In addition, since temporal depots are fabricated with biodegradable polymers, the developed devices will not need further surgical removal post-implantation (Chung and Park, 2007). However, the development of the polymeric-based depot systems have been associated with poor biocompatibility due to organic solvents or sonication process that are used during fabrication (Hara and Miyake, 2001; Sandor et al., 2002; Chung et al., 2006). Therefore, the development of a bio-structure that can surmount the impediments posed by either nanoliposomal or polymeric scaffold systems is highly desirable.

A study conducted by Stenekes and co-workers (2000) demonstrated the success of employing a temporal depot fabricated with polymeric materials. In the same study, both storage and prolonged release of drug-loaded liposomes post-embedded within dextran-based microspheres over 25 days has been reported. The prolonged release kinetics was shown to be influenced by different factors such as degradation, size of liposomes and diffusion through pores on the surface structure. Another study by Budai and co-workers (2007) demonstrated the success of embedding liposomes into a pre-fabricated polymeric scaffold by using the hydration temperatures above the glass transition temperature of Polyvinyl alcohol (PVA). Furthermore, a study by Chung and co-workers (2006) also reported the success on an encapsulation of the drug-loaded liposomes into a chitosan (CHT) matrix by injection of drug-loaded liposomes into the porous surface structure of the CHT matrix followed by freeze-drying.

Many tissues engineering studies have demonstrated success of the various types of cell growth and proliferation on the surface of the three-dimensional scaffolds (Klapperich and Bertozzi, 2004; Budai et al., 2007; Autissier et al., 2010; Chatterjee et al., 2012). In the case of a drug delivery study, cell growth and proliferation on the scaffold could also be used to postulate the state of the functionalized liposomes ensuing their escape of the polymeric depot. The following could also be validated: 1) an intact structure of liposomes and 2) ability of ligand/targeted moieties for targeting drug delivery.

This Chapter aims to further investigate the potential of the constructed BICD for prolonged release of galantamine (GAL)-loaded functionalized NLPs (NLPs) over a

period of 50 days in simulated cerebrospinal fluid (sCSF) condition and PC12 neuronal cell environment. The BICD was further characterized for the following attribute: the capability of the device to act as a platform for the bio-robotic marker for the precise delivery of GAL into the brain in response to AD. The surface morphology and porosity of the polymeric scaffold/depot (CEP scaffold) were also analysed using the scanning electron microscopy (SEM) and micromeritics. SEM micrographs further validated the surface morphology of the CEP scaffold and/or drug-loaded functionalized NLPs after embedding within the CEP scaffold, with subsequent freeze-drying for 48 hours at 25mTorr (Virtis[®], Gardiner, NY, USA). The Karl Fisher titrator (Metrohm, Herisau, Switzerland) validated the residual amounts of water present post-lyophilization of the CEP scaffold.

Mechanical properties of the CEP scaffold such as Matrix hardness, resilience, hydration and the swelling mechanism were assessed in a sCSF condition (0.1M PBS; pH7.4, 37°C). The *in vitro* study evaluated drug-loaded functionalized NLPs release kinetics from the BICD at sCSF conditions (in the form of pellet or supernatant samples). A pellet sample was used to quantify the intact drug-loaded functionalized NLPs, whereas the supernatant was used to quantify drug release occurring prior to drug-loaded functionalized NLPs escaping the BICD. *Ex vivo* studies were carried out to assess the viability of the PC12 neuronal cells seeded on the surface of the BICD. The cytotoxicity induced by the functionalized NLPs, CEP scaffold, and BICD was also assessed. In addition, *ex vivo* studies were further used to validate the uptake of FITC-labeled and/or drug-loaded functionalized NLPs post-escape from the BICD.

6.2. Materials and Methods

6.2.1. Materials

The materials used for fabrication of the fluorescent-labeled or drug-loaded functionalized NLPs, CEP scaffold (Table 6.1) and BICD (Table 6.2) were identical to those used to fabricate cross-linked CEP hydrogel of the nano-enabled BICD, and can be found in Chapter 5, Section 5.2.1 of this thesis.

6.2.2. Bio-construction of a nano-enabled Bio-Robotic Intracranial Device

A BICD was constructed as previously described in Chapter 5, section 5.2.4. In brief, rhodamine or FITC labeled-functionalized or GAL-loaded functionalized NLPs (as described in Chapter 4, section 4.2.2) in an aqueous dispersion was loaded drop-wise into the CEP scaffold prior to freeze-drying at a ratio of 1:5 v/v (NLPs: CEP scaffold) (Table 6.1 and 6.2). The functionalized NLPs were pre-treated with 0.5%^{w/v} sucrose as a cryoprotectant prior to entrapment within the core of the CEP scaffold and thereafter freeze-dried employing a 25mTorr (Virtis®, Gardiner, NY, USA) for 48 hours.

The particle size and zeta potential of the GAL-loaded functionalized NLPs prior embedded within CEP scaffold (cross-linked or non-cross-linked CEP scaffold) of the BICD were analyzed employing a Zetasizer NanoZS instrument (Malvern Instruments (Pty) Ltd., Worcestershire, UK) as previously described in Chapter 3, section 3.2.5.

Table 6.1. Composition of the cross-linked CEP scaffolds formulations employing CHT, EU, PVA and GA as cross-linker.

F#	*CHT (% ^W /V)	^a EU (% ^W /V)	^b PVA (% ^W /V)	Cross-linker GA (% ^V /V)	Frozen at -80°C / hours	Lyophilized hours
1	3	1	3	0	48	48
	3	1	3	5	48	48
2	3	2	2	0	48	48
	3	2	2	5	48	48
3	3	3	1	0	48	48
	3	3	1	5	48	48

#F: CEP scaffold formulation, *CHT: Chitosan, ^aEU: Eugradit[®] RSPO and ^bPVA: Poly (Vinyl alcohol).

Table 6.2. Composition of the different BICD formulations (D1-D3)

F#	GAL-loaded Functionalized NLPs (% ^V /V)	CEP Scaffold (% ^V /V)		Frozen at -80C/ hours	Lyophilized hours
D1	1	5	F1 (Non-cross-linked)	48	48
	1	5	F1 (Cross-linked)	48	48
D2	1	5	F2 (Non-cross-linked)	48	48
	1	5	F2 (Cross-linked)	48	48
D3	1	5	F3 (Non-cross-linked)	48	48
	1	5	F3 (Cross-linked)	48	48

#F: BICD Formulation

6.2.3. Thermal analysis of the cross-linked Chitosan-Eudragit RSPO-Polyvinyl alcohol scaffold

6.2.3.1. Differential Scanning Calorimetry of the cross-linked Chitosan-Eudragit RSPO-Polyvinyl alcohol scaffold

Thermal analysis of the native CHT, EU and PVA, non-cross-linked, and cross-linked lyophilized CEP scaffold were evaluated using differential scanning calorimetry (DSC) (Mettler Toledo DSC1 STARe System, Switzerland). The samples were weighed (5-8mg) and sealed in perforated aluminum pans. The samples were further scanned at a temperature gradient of 10-260°C, at a rate of 10°C/min under an 8kPa N₂ atmosphere. An empty aluminum pan served as a reference for all DSC scans.

6.2.3.2. Thermogravimetric analysis of the cross-linked Chitosan-Eudragit RSPO-Polyvinyl alcohol scaffold

Thermogravimetric analysis (TGA) of the native CHT, EU and PVA and the CEP scaffold was carried out by connecting the TGA software (PerkinElmer STA 6000, Beaconsfield, United Kingdom) to a Fourier transmission infrared (FTIR) spectrophotometer (PerkinElmer Spectrum 100, Beaconsfield, United Kingdom) to elucidate the chemical reactions and/or temperature changes that occurred when native polymeric components were blended together in the presence of GA as a cross-linking agent. The following parameters were employed for the analysis: heat from 30-450/500°C at a rate of 10°C/min and nitrogen gas (N₂). The percentage mass loss was calculated using delta Y software against maximum decomposition temperature-initial decomposition temperature.

6.2.4. Surface morphological characterization of the cross-linked Chitosan-Eudragit RSPO-Polyvinyl alcohol scaffold

Surface morphology, surface area and porosity of the CEP scaffold post-lyophilization was evaluated by employing SEM (JEOL JSM-Japanese Electronic Optical Laboratories, Tokyo, Japan) and a porosimetry analyzer (ASAP 2020 Micrometrics, Georgia, USA). Microscopic analysis of the surface of the nano-enabled structure of the CEP scaffold was undertaken, by first lyophilizing the scaffold at 25mTorr (Virtis™, Gardiner, New York, USA). The sample was mounted onto double-sided tape attached to a metallic sample stand and sputter-coated with a layer of gold. Each sample was viewed under varying magnifications at an accelerating voltage of 20keV. Surface properties of the CEP scaffold structure were validated using a porosimetry analyzer (ASAP 2020, Micrometrics Georgia, USA).

Each CEP scaffold sample was weighed (75-90 mg), inserted into the glass holding tube and closed with a glass filler rod in order to decrease the total free space within the tube. The samples were first degassed prior to analysis in order to eliminate surface moisture and gas particles. Degassing conditions included an evacuation and heating phase. Table 6.3 indicates the parameters employed for the porositometric analysis.

Table 6.3. Evacuation and heating phase parameters employed during porositometric analysis of the CEP scaffold

Parameter	Rate/target
Evacuation Phase	
Temperature ramp rate	10°C/min
Target temperature	40°C
Evacuation rate	50.0mmHgs/s
Unrestricted evacuation from	30mmHg
Vacuum set point	500µmHg
Evacuation rate	60min
Heating phase	
Temperature ramp rate	10°C/min
Hold temperature	30°C
Hold time	900min

6.2.5. Physicomechanical characterization of the cross-linked Chitosan-Eudragit RSPO-Polyvinyl alcohol scaffold

The physicochemical and physicomechanical properties of cross-linked CEP scaffold were validated for description of the following: thermal properties (see Section 6.2.3), textural properties (Section 6.2.5.1), rate of dehydration (Section 6.2.5.3), swelling (see Section 6.2.5.4) and rate of erosion (Section 6.2.5.5).

6.2.5.1 Textural analysis of the cross-linked Chitosan-Eudragit RSPO-Polyvinyl alcohol scaffold

Textural analysis was validated to elucidate the physicochemical properties of the cross-linked CEP scaffold in terms of scaffold matrix resilience (MR), matrix hardness (MH), and deformation energy (DE). An analysis was conducted on the dehydrated and hydrated samples. A calibrated Texture Analyzer (TA XTplus; Stable Micro Systems, Surrey, UK) fitted with a cylindrical steel probe (50mm diameter for MR) and a flat-tipped steel probe (2mm diameter for matrix hardness and deformation energy) was employed. Data was captured at a rate of 200 points per second through Texture Exponent Software (Version 3.2). The parameter settings employed for the analysis are outlined in Table 6.4. Samples were analyzed for variations in MH (N/mm²), DE (J) and MR (%).

Table 6.4. Textural parameters employed for determination of CEP scaffold matrix hardness, deformation energy and matrix resilience

Parameters	MH ^a (N/mm ²)	DE ^b (J)	MR ^c (%)
Pre-test speed	1.00 mm/s	1.00 mm/s	1.00 mm/s
Test speed	2.00 mm/s	2.00 mm/s	2.00 mm/s
Post-test speed	10.0 mm/s	10.0 mm/s	10.0 mm/s
Target mode	Force	Force	10 % strain
Target force	0.98067 N	0.98067 N	-
Trigger type	Auto (force)	Auto (force)	Auto (force)
Trigger force	0.04903 N	0.04903 N	0.04903 N
Load cell	5 kg	5 kg	5 kg

^aMH: Matrix hardness, ^bDE: Deformation energy, ^cMR: Matrix resilience

6.2.5.2. Determination of the water content in cross-linked Chitosan-Eudragit RSPO-Polyvinyl alcohol scaffold

The water content in the lyophilized cross-linked CEP scaffold (F1-F3) was determined using a Karl Fisher titrator (Metrohm, Herisau, Switzerland). Parameter settings and sampling procedures were instituted using an adapted protocol by Bruttell and co-worker (2003). All samples were weighed (~0.005g/sample) and measured in triplicate.

6.2.5.3. Hydration study of the cross-linked Chitosan-Eudragit RSPO-Polyvinyl alcohol scaffold

Hydration study of the CEP scaffold in a sCSF condition was characterized employing protocol a previously described by Ngwuluka and co-workers (2012). The lyophilized CEP scaffold was placed in the probe-tuning cell containing glass beads and images acquired over 24 hours with a Bench Top magnetic resonance digital MARAN-i system (Oxford Instruments Magnetic Resonance, Oxon, UK).

6.2.5.4. Swelling characteristics of cross-linked Chitosan-Eudragit RSPO-Polyvinyl alcohol scaffold

Swelling characteristics of non-cross-linked and cross-linked CEP scaffolds (F1-F3) in a sCSF were expressed in terms of weight gain. The CEP scaffolds were weighed before and after immersion in 100mL of sCSF (0.1M PBS, pH7.4; 37°C) in a shaking incubator set to 20rpm (Harilall et al., 2013). The enlarged samples were removed at different time intervals and weighed, over 24 hours of incubation. Prior to weight measurements, excess media was removed by blotting the CEP scaffold with a filter

paper for 30 seconds. Swelling characteristics or mass gain of the CEP scaffold in sCSF was calculated using Eq. 6.1

$$\text{Swelling hydration (\%)} = \frac{\text{Swollen CEP scaffold weight} - \text{Dry CEP scaffold weight}}{\text{Swollen CEP scaffold weight}} \times 100$$

6.2.5.5. Matrix erosion of the cross-linked Chitosan-Eudragit RSPO-Polyvinyl alcohol scaffold

Matrix erosion (ME) of the non-cross-linked and cross-linked CEP scaffold was assessed in a sCSF condition over 50 days. In brief, CEP scaffold samples were added to 100mL of sCSF (0.1M PBS, pH7.4; 37°C) in a shaking incubator set to 20rpm. At different immersion times (day 0, 5, 10, 15, 20, 25, 30, 35, 40 and 50), the samples were dried in a digital oven and weighed. The weight loss data of the CEP scaffold was a means of three determinations. The mass or weight loss percentage of the CEP scaffold in sCSF was calculated using Eq. 6.2.

$$\text{Weight Loss (\%)} = \frac{i\text{CEP}w - e\text{CEP}w}{i\text{CEP}w} \times 100 \dots \dots \dots \text{Eq 6.2}$$

Where iCEPw is initial CEP scaffold weight and eCEPw is the eroding CEP scaffold weight.

6.2.6. Morphology and structure characterization of the Bio-Robotic Intracranial Device

The morphology and structure characterization of the BICD, engineered by embedding drug-loaded or rhodamine-labeled functionalized NLPs into the CEP scaffold, were examined using SEM (See Section 6.2.4) and confocal laser scanning microscopy (CLSM) (Zeiss LSM 780, Oberkochen, Germany). Confocal microscopy was employed to further characterized fluorescence activity or visualized localization

of rhodamine-labeled functionalized NLPs post-embedded within the BICD, at an excitation wavelength of 540nm and an emission wavelength of 625nm.

6.2.7. *In vitro* release of drug-loaded functionalized nanoliposomes from Bio-Robotic Intracranial Device

In vitro release of drug-loaded functionalized NLPs from non-cross-linked and cross-linked CEP of the BICD were validated in sCSF (0.1M PBS; pH7.4; 37°C). In brief, each BICD (D1-D3) was immersed in 100mL of the sCSF condition (0.1M PBS; pH7.4; 37°C), and thereafter closed in vials and placed in an orbital shaking incubator (Labex, Stuart SBS40®, South Africa) at 20rpm. At predetermined time intervals, 5mL samples were collected for analysis. An equal volume of the drug free sCSF medium was added to replace the quantity removed. The samples (NLPs) were centrifuged at 20,000rpm, and both supernatant and pellet were collected. The supernatant was collected to quantify the amount of GAL released prior to liposomal release from the nano-enabled structure, while the pellets were used to hypothesize the drug-loaded functionalized NLPs release in their intact state post-escape the BICD structure. The pellets were first lysed with 0.5-1%_v Triton X-100 in methanol solution prior to quantifying the amount of GAL associated with the loaded-NLPs that escaped in their intact form from the BICD. The amount of GAL was analyzed by UV spectroscopy at a maximum wavelength (λ_{max}) of 288nm. The quantity of GAL released was computed from a standard linear curve ($R^2 = 0.98$). Each experiment (F1-F3) was performed in triplicate. The amount of GAL released at day 10 was measured by the mean dissolution time (MDT) values using the Eq. 6.3.

$$\text{MDT} = \sum_{i=1}^n t_i \left(\frac{M_t}{M^\infty} \right) \dots \dots \dots \text{Eq 6.3}$$

Where M_t is the fraction of dose released in time $t_i = (t_i + t_{i-1})/2$ and M^∞ corresponds to the loading dose.

6.2.8. *Ex vivo* characterization of the Bio-Robotic Intracranial Device

6.2.8.1 Cell seeding on the Bio-Robotic Intracranial Device

The PC12 neuronal cells were maintained and cultured in an identical condition as described in Chapter 3, section 3.2.10 (Mufamadi et al., 2013). Prior to seeding cells on the surface of the BICD (D1-D3), D1-D3 samples were sterilized with either 75% ethanol or under UV light for ± 6 hours. To eliminate excess ethanol employed during sterilization, the BICD was washed twice with sterile RPMI media and thereafter rinsed in cell culture media (see Chapter 3, section 3.2.10). The D1-D3 samples were then added to 96 well-culture plates, PC12 neuronal cell seeded at a density of 10,000 cells, and cells cultured for 28 days. At different time intervals (3, 7, 14, 21 and 28), media (50 μ L) was collected for assessment of anti-proliferation and/or cytotoxicity, cell uptake and cell growth observed on the surface of the BICD.

6.2.8.2. Morphological characterization of the Bio-Robotic Intracranial Device seeded with PC12 neuronal cells

The surface morphology of the BICD seeded with PC12 neuronal cell was visualized using SEM (Jeol JSM-120, Tokyo, Japan). In brief, the BICD was removed from the growth media and air-dried, for 24 hours prior to the examination. Air-dried BICD was mounted onto a double-sided tape attached to a metallic sample stand thereafter

sputter-coated with a layer of gold and viewed using the protocol previous described in Section 6.2.4 of this thesis.

6.2.8.3. Cytocompatibility of the Bio-Robotic Intracranial Device in the PC12 neuronal cells

Cytocompatibility was determined using a cytoTox 96® non-radioactive cytotoxicity assay (Madison, WI, USA). Briefly, drug-loaded functionalized NLPs, CEP scaffold and BICD were incubated within 100µL of PC12 neuronal cells at a density of 10,000 cells/wells and grown as described previously in Section 6.2.8.1, over 28 days. The lactate dehydrogenase (LDH) release was quantified on 50µL of treated cells (drug-loaded functionalized NLPs, CEP scaffold and BICD) and control untreated. LDH release activity hypothesized to be associated with membrane damage/injury and cytotoxicity (Cho et al., 2008). In addition, 50µL of the reconstituted substrate mix (Promega reagents) was added to each well, and the enzymatic reaction allowed occurring at room temperature for 30 minutes as per the promega protocol. Since the substrate is light sensitive, all experiments in this section were conducted under dark conditions in order to avoid substrate degradation as per promega protocol description. The enzymatic reaction stopped when stop solution (50µL/well, Promega reagent) was introduced to the reaction. The untreated control PC12 neuronal cells were lysed with the lysis buffer (0.5% triton X-100 in ethanol/NaOH solution) in order to attain LDH background and/or maximum release. At the wavelength of 490nm, the LDH activity was quantified employing a Victor™X3 Perkin Elmer microplate reader (Wellesley, MS, USA). The LDH release percentages were calculated using Eq 6.4.

$$\text{LDH release \%} = \frac{\text{A490nm of treated PC12 neuronal cells}}{\text{A490nm of untreated PC12 neuronal cells}} \times 100 \dots \dots \dots \text{Eq 6.4}$$

Where treated PC12 neuronal cells with drug-loaded functionalized NLPs, CEP scaffold and BICD.

6.2.8.4. Cell uptake of the FITC-labeled functionalized nanoliposomes post release from the Bio-Robotic Intracranial Device

Ex vivo release and uptake of GAL-loaded or FITC-labeled functionalized NLPs embedded into the BICD were characterized by UV spectrophotometry and CLSM. At different time intervals, 50 μ L of growth media was aspirated. The aspirated cells were then washed twice with sterile PBS (pH7.4), and thereafter lysed with the lysis buffer (0.5% triton X-100 in ethanol/NaOH solution). The lysate was vortexed and subsequently centrifuged at 10,000 \times g for 15-20 minutes at room temperature. The supernatant was collected, and GAL quantity analyzed by UV spectrophotometry at λ_{max} =288nm (N=3). The percentage drug uptake by the PC12 neuronal cells was calculated as previously described in Chapter 4, Section 4.2.13.3. Confocal microscopy was employed to provide evidence of cellular uptake and active FITC-labeled functionalized NLPs released from the BICD into the cellular environment. Cell uptake of FITC-labeled functionalized NLPs post-release from the BICD was visualized as pseudo 3D images at day 3, 7, 14, 21 and 28 using CLSM. The topographical view of the fluorescence PC12 neuronal cells characterized the cell uptake intensity and intra-cellular localization. The results of the confocal microscopy were field dependent as previously addressed in Chapter 3, Section 3.3.8.

6.3. Results and Discussion

6.3.1. Thermal properties of the cross-linked Chitosan-Eudragit RSPO-Polyvinyl alcohol scaffold

6.3.1.1. Differential Scanning Calorimetry analysis of the cross-linked Chitosan-Eudragit RSPO-Polyvinyl alcohol scaffold

Figure 6.1 depicts DSC, glass transition (T_g), melt (T_m) and crystallization (T_c) temperature of native polymeric components (CHT, EU and PVA), the non-cross-linked, and cross-linked CEP scaffold. In Figure 6.1a, native CHT exhibited endothermic peaks at 90°C and 125°C, which may be associated with the dissociation process of interchain hydrogen bonding of CHT as previously reported by Chuang and co-workers (1999). Native EU exhibited exothermic peaks at 70°C, melting peak of 182°C, and a temperature onset (T_0) and the completion of melt (T_c) at a range between 175-185°C (Figure 6.1b). In Figure 6.1c, native PVA exhibited a T_g of 40°C and T_m peak of 223°C. When all native polymeric components (CHT, EU and PVA) were blended collectively in the absence of a cross-linking agent, a T_g was observed at 55°C, and T_m at 85°C (Figure 6.1d). The thermal shifting of the non-cross-linked post-lyophilized CEP scaffold may have been influenced by polymer interaction (covalently and non-covalent interaction). In Figure 6.1e, the cross-linked CEP scaffold exhibit a broadening T_m peak temperature at 100°C, temperature onset (T_0) and the completion of melt (T_c) at a range between 60-140°C, and a crystallization temperature (T_c) of 240°C. The results depicted that thermal dynamics of the lyophilized cross-linked CEP scaffold over 48 hours was still stable or covalent

bonds were attained as previously reported in FTIR (see Chapter 5, section 5.3.2.1) and rheological studies (see Chapter 5, section 5.3.2.2).

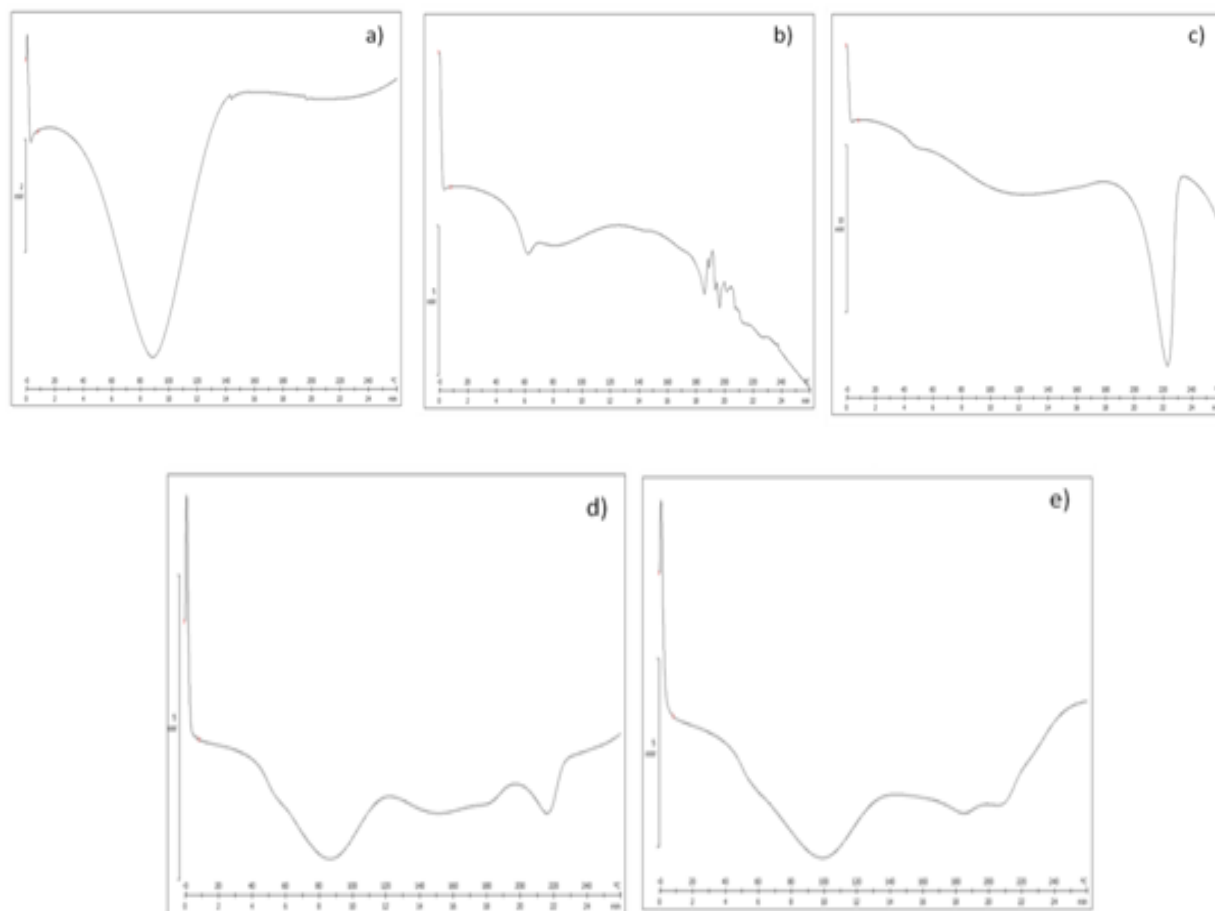


Figure 6.1: DSC profiles of the CEP scaffold; native a) CHT, b) EU, and c) PVA, d) non-cross-liked CEP scaffold and e) cross-linked CEP scaffold.

6.3.1.2. Thermogravimetric analysis of the cross-linked Chitosan-Eudragit RSPO-Polyvinyl alcohol scaffold

The stability and decomposition temperatures of native polymeric components (CHT, EU and PVA) and lyophilized cross-linked CEP scaffold were validated by TGA (see Figure 6.2). Each sample was analyzed for both the initial and maximum decomposition program temperature at 30-450/500°C at a rate of 10°C/minute and in the nitrogen gas (N₂) atmosphere.

Figure 6.2a and Table 6.5 shows the highest thermal stability point of the native CHT at 230°C, with less than 2% weight loss. At 279.41°C, the CHT starts to decompose and its mass starts to deplete as it vaporized, and the maximum decomposition temperature was obtained at 350°C. Figure 6.2b and Table 6.5 represents thermal stability and decomposition temperature of native EU. The results exhibited the highest thermal stability of EU at 270°C. Initial decomposition temperature of EU was at about 293.88°C, and the maximum decomposition temperature was 374.29°C. About 66.31% of the mass was lost between the onset and offset range temperatures. Figure 6.2c and Table 6.5 also represent thermal stability and decomposition temperature of native PVA. The results exhibited the highest mass loss of about 95% at an initial temperature of 281.27°C and maximum temperature of 318.70°C. The quick depletion of mass may have been influenced by loss of water and full decomposition or polymer degradation, which influenced the high evaporation state. Figure 6.2d and Table 6.5 depict a thermograph of the post-lyophilized cross-linked CEP scaffold (weight loss curve is the solid line, and its first derivative is the dashed curve).

The results also showed a remarkable stability when all native polymeric components (CHT, EU and PVA) were blended simultaneously in the presence of GA as a cross-linking agent to form the cross-linked scaffold. Decomposition and mass depletion only occurred at around 350°C. This may have been manipulated by the following: amalgamated physicommechanical properties of each native polymer, and strong intermolecular and intramolecular hydrogen bonds occurring between the polymers in the presence of GA as a cross-linking agent. The results also showed only single (slope)-stage decomposition which indicates high mass loss when the

degradation temperature is reached. The cross-linked CEP scaffold demonstrated a derivative temperature peak (T_p) at around 417.32°C; this observation could be attributed to a decomposition pattern associated with the highest amount of weight loss.

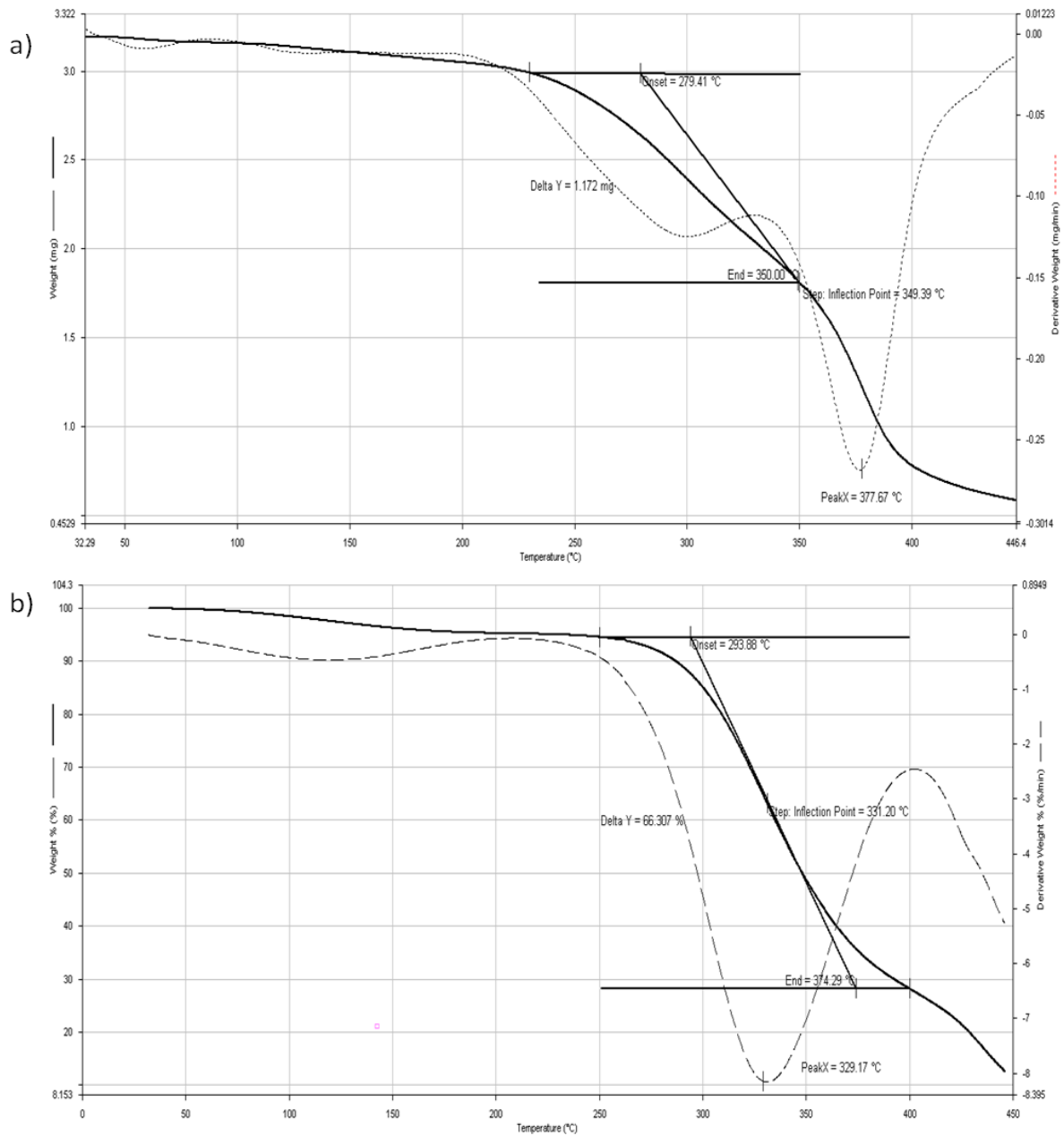


Figure 6.2: Contd. on pg 179

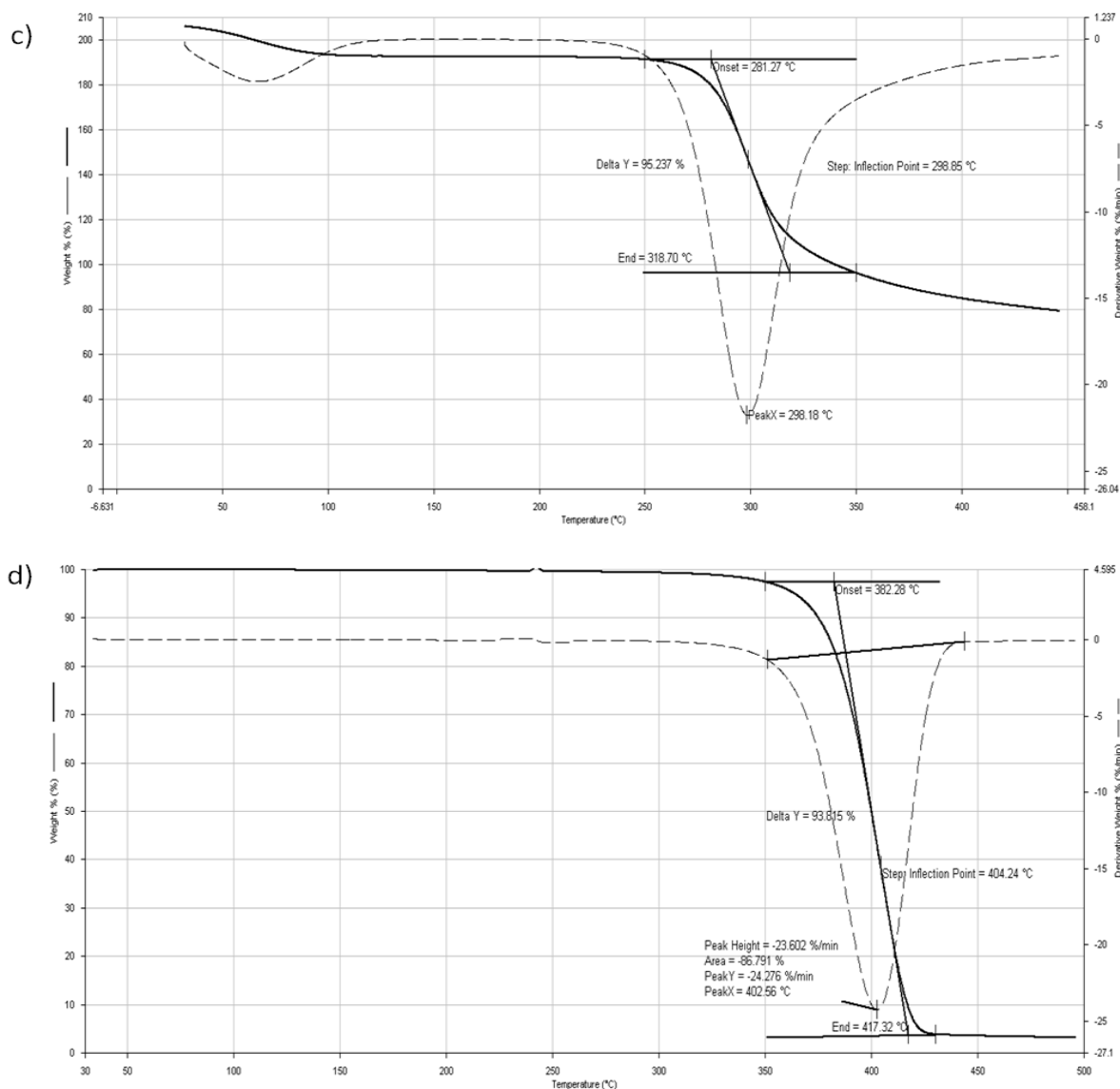


Figure 6.2: TGA thermographs of the cross-linked CEP scaffold; native a) CHT, b) EU and c) PVA, and d) cross-linked CEP scaffold.

Table 6.5. Decomposition temperature of native polymers (CHT, EU and PVA) components and cross-linked CEP scaffold.

Components	Decomposition points		Derivative temperature		
	Onset point *DT °C	^a Delta Wieght Loss (%)	Offset point DT °C	Peak #Tp °C	Inflection point °C
Chitosan	279.41	54.28	350.00	377.67	349.39
Eudragit RSPO	293.88	66.31	374.29	329.17	331.20
PVA	281.27	95.24	318.71	298.18	298.85
Cross-linked CEP scaffold	382.28	93.82	417.27	402.56	404.24

*DT= Decomposition temperature, ^aDelta Y= percentage weight loss from onset point until end point, [#]Peak Tp = First derivative peak temperature associated with highest rate of change on the weight loss

6.3.2. Surface morphology of the cross-linked Chitosan-Eudragit RSPO-Polyvinyl alcohol scaffold

The morphology and bio-architecture of the CEP scaffold were examined employing SEM (Jeol JSM-120, Tokyo, Japan) (Figure 6.3). Figure 6a-c (1-2) depicts the porous morphology of the CEP scaffold formulations (F1-F3). The images reveal that developed structures have spherical interconnected pores with a random size distribution. The pore structures and size may have been manipulated by different parameters such as a hydrophilic polymer or cross-linking agents. In addition, the pore structure and size may be influenced by the diffusion of water molecules during evaporation or lyophilization procedures.

Figures d1-2 and e1-2 show micrographs of the CEP scaffold at its edge and of its pore at high magnification. Porosity data accumulated by employing a micrometrics Analyzer displayed linear isothermal adsorption and desorption indicative of highly porous CEP scaffolds. Different percentages of porosity were obtained from F1-F3. The percentage porosity showed a decrease with increased EU concentration, being 90% for CEP scaffold (F1), 85% for CEP scaffold (F2) and 80% for CEP scaffold (F3). Typical CEP scaffold formulation exhibited a type IV isotherm, which indicates microporosity (Figure 6.4). The isotherm was near $P/P_0=1$, which indicates the presence of macropores. In addition, SEM micrographs further reveal a pore structure with a spherical shape, an interconnected pore system and random

distribution. Porosity distribution of the CEP scaffolds may have been influenced by the fabrication procedure, concentration of hydrophilic polymers (PVA and CHT), freezing temperature (-80°C, 48 hours) and freeze-drying (48 hours). The structure and architecture of developed porous CEP scaffold exhibited essential parameters that may add advantages to prolonged release when drug-loaded functionalized NLPs escape through diffusion post-embedded into the BICD. Furthermore, an interconnecting pore network of the CEP scaffold is even more important for cultivation and proliferation studies following PC12 neuronal cells being seeded on the surface of the CEP scaffold.

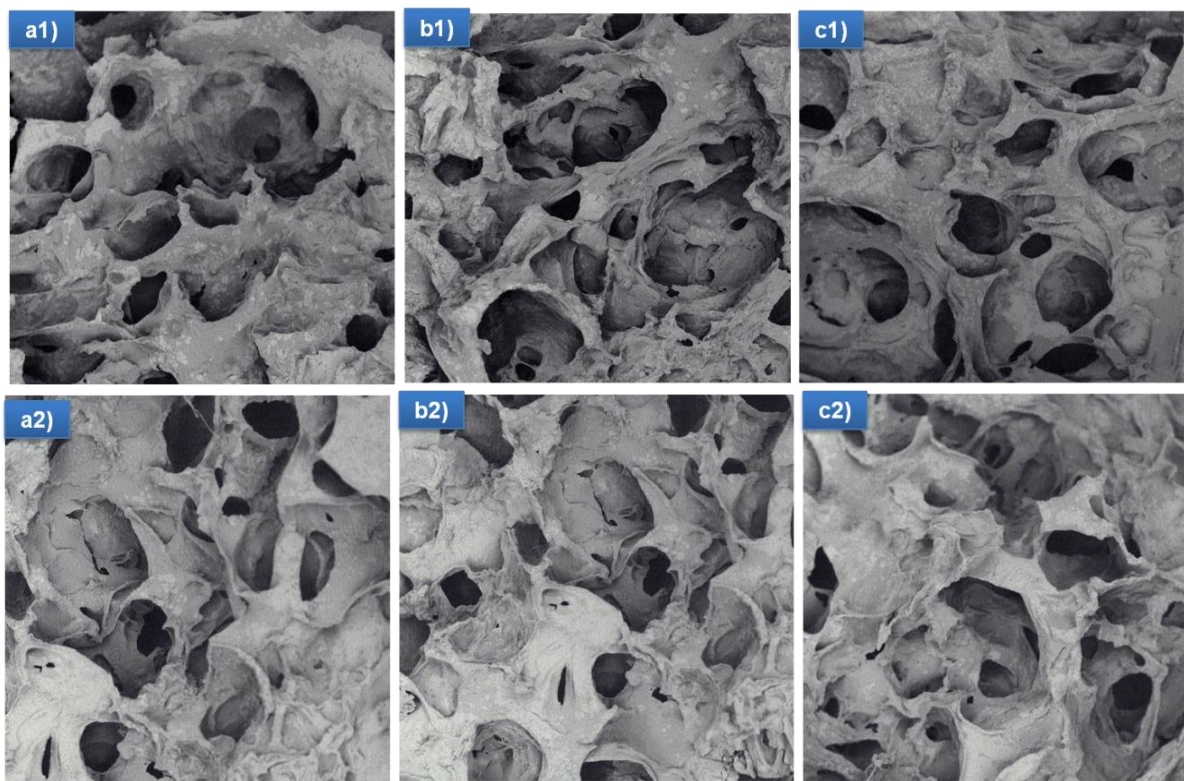


Figure 6.3: *Contd.on pg 182*

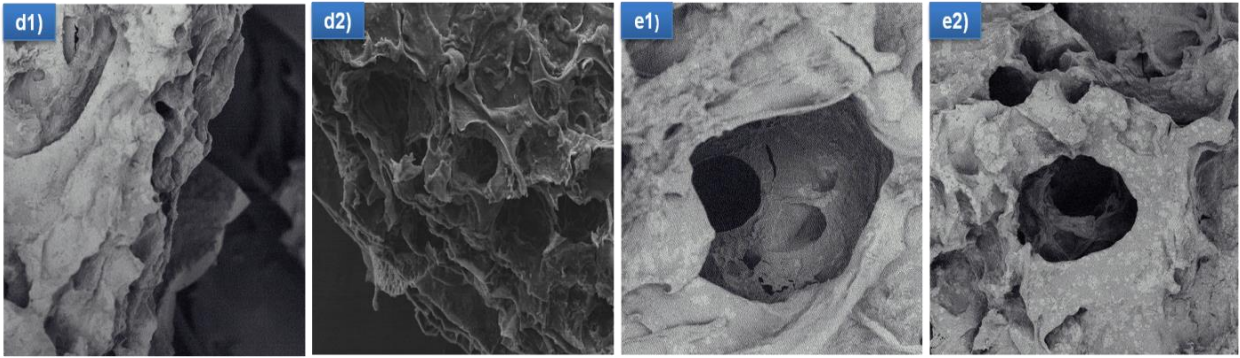


Figure 6.3: SEM micrograph of the CEP scaffolds, a1-2) (F1), b1-2) F2, c1-2) F3, d1-2) scaffold edge and e1-2) magnified view of a pore of the CEP scaffold magnification 450-1000x.

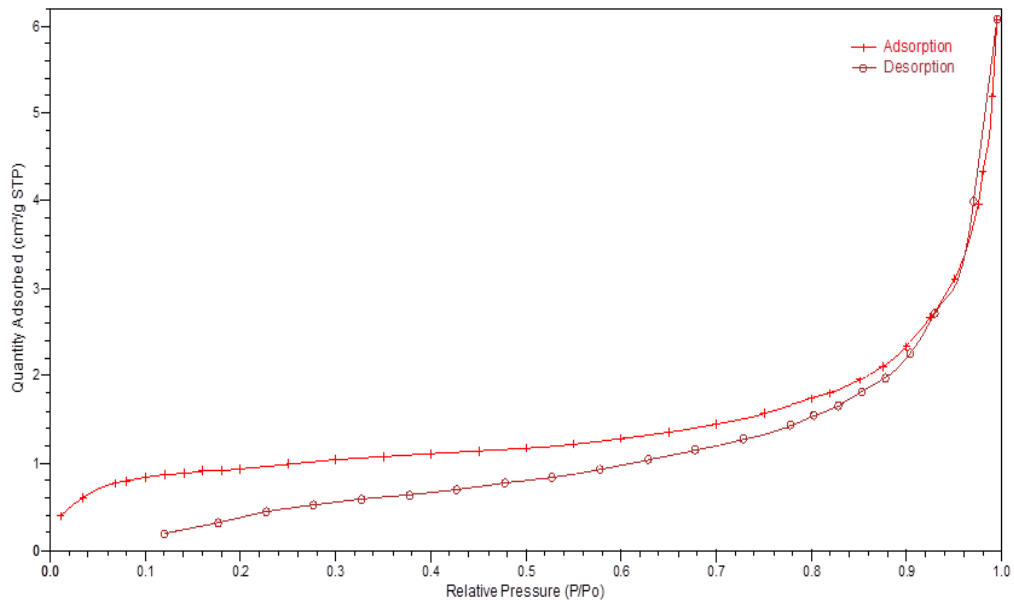


Figure 6.4: Typical Isothermal linear plot of the CEP scaffold

6.3.3. Physicochemical and physicommechanical characterization of the cross-linked Chitosan-Eudragit RSPO-Polyvinyl alcohol scaffold

The textural properties, water contents, hydration, swelling characteristics and rate of erosion were characterized on the lyophilized cross-linked CEP scaffold post-exposure to sCSF condition.

6.3.3.1. Textural properties of the cross-linked Chitosan-Eudragit RSPO-Polyvinyl alcohol scaffold

Textural properties of the cross-linked CEP scaffold such as MH, MR and energy absorbed were measured in the unhydrated and hydrated state in sCSF using a calibrated Texture Analyzer. Figure 6.5 and Table 6.6 indicate the force-time and force-distance profiles of the cross-linked CEP scaffold for determining a) deformation energy, b) MR and c) MH. The unhydrated cross-linked CEP scaffold showed high resilience at a range of 11.53-14.42%, F1-F3 respectively. However, when the cross-linked CEP scaffold was exposed to sCSF, the resilience force decreased, and ranged between 8.87-13.37%, for F1-F3 respectively. In the case of the hardness and deformation energy, the unhydrated showed high hardness (10.67-12.76N/mm) and deformation energy (0.031-0.049J). However, the hydrated cross-linked CEP scaffold showed a slight decline in hardness (7.97-9.65N/mm) and deformation energy (0.029-0.049J). This outcome could have influenced by hydrolysis or swelling behaviour of network structure in sCSF that resulting in a chain relaxation of the CEP scaffold.

Table 6.6. Textural profile of the unhydrated and hydrated cross-linked CEP scaffold

Unhydrated CEP scaffold			
F#	Hardness	Resilience (%)	Deformation Energy (J)
F1	10.67	11.53	0.031
F2	12.07	12.81	0.039
F3	12.76	14.42	0.049

Table 6.6. *Contd. on pg 184*

Hydrated CEP scaffold

	Hardness (N/mm)	Resilience (%)	Deformation Energy (J)
F1	7.97	8.87	0.029
F2	8.87	10.38	0.036
F3	9.65	13.37	0.040

F#: Formulation

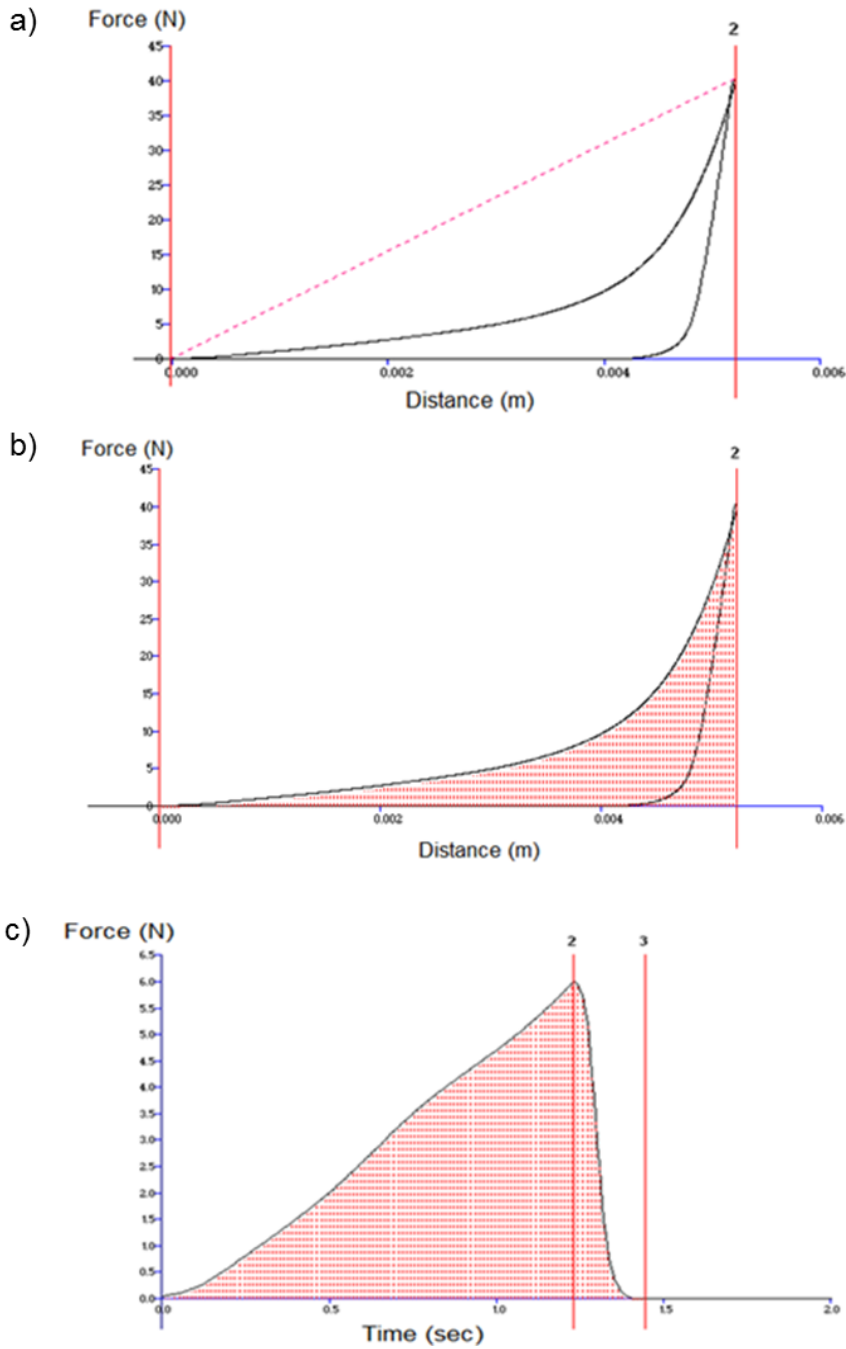


Figure 6.5: Typical textual profiles of the cross-linked CEP scaffold, deformation energy, matrix resilience and matrix hardness.

6.3.3.2. Water content of the cross-linked Chitosan-Eudragit RSPO-Polyvinyl alcohol scaffold

The water contents of the lyophilized cross-linked CEP scaffolds (F1, F2 and F3) were determined by the Karl-Fisher titrator (Metrohm, Herisau, Switzerland). Different percentage water volumes or residual moisture/solvents in the post-lyophilized cross-linked CEP scaffolds were observed, being 10% water content for F1, 9% for F2 and 7% for F3. A high amount of residual moisture/solvents in the lyophilized CEP scaffold may have been influenced by the concentration of the hydrophilic polymers or residual organic solvent. In the case of the BICD, it could also be influenced by cryoprotectant employed to preserve drug-loaded functionalized NLPs during the embedding process (Hashem et al., 2007; Chen et al., 2010).

6.3.3.3. Magnetic Resonance Imaging and swelling characteristics of the cross-linked Chitosan-Eudragit RSPO-Polyvinyl alcohol scaffold

Magnetic Resonance Imaging and swelling characteristics of the CEP scaffold were assessed using benchtop-Magnetic Resonance Imaging (MRI) and following exposure to drug release conditions in an orbital shaking incubator (20rpm, 37°C), respectively, and are presented in Figure 6.6. Figures 6.6a-b depicts the swelling characteristics of the non-cross-linked CEP scaffold and cross-linked CEP scaffold. Figure 6.6c shows the three-dimensional network structure of the unhydrated cross-linked CEP scaffold. Figures 6.6c-f shows the images of the cross-linked CEP scaffold post-hydration, outside the hydration medium, and at 30 minutes, 12 and 24 hours. The three-dimensional matrix and/or network structure of the hydrated cross-linked CEP scaffold was preserved post-hydration; however, the CEP scaffold size

increased as hydration increased. The arrows designate CEP scaffold erosion. The top arrow indicates possible erosion on the post-hydrated CEP scaffold, and the bottom arrow indicates eroded CEP scaffold residuals. The size of the CEP scaffold increase by one-third at equilibrium state. Uptake of the medium in both hydration and swelling studies may have been influenced by the surface architecture of the non-cross-linked CEP scaffold (Figure 6.6a) and cross-linked CEP scaffold (Figure 6.6b), which are highly porous and sponge-like structures. Furthermore, the behavior of the CEP scaffold may have also been influenced by hydrolysis of the polymers in dissolution medium. Overall findings confirmed the changing physicochemical and mechanical dynamics of the CEP scaffold that may ensue on release of the post-embedded drug-loaded functionalized NLPs *in vitro*, *ex vivo* and *in vivo*.

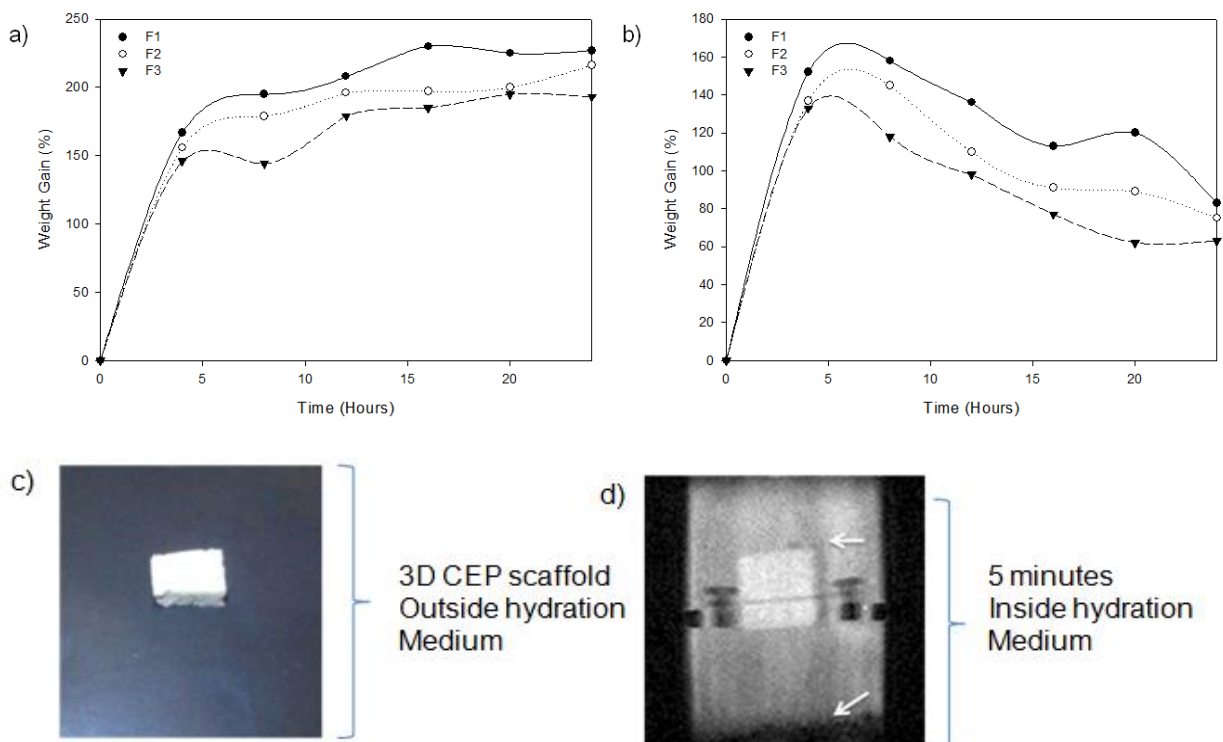


Figure 6.6: Contd.on pg 187

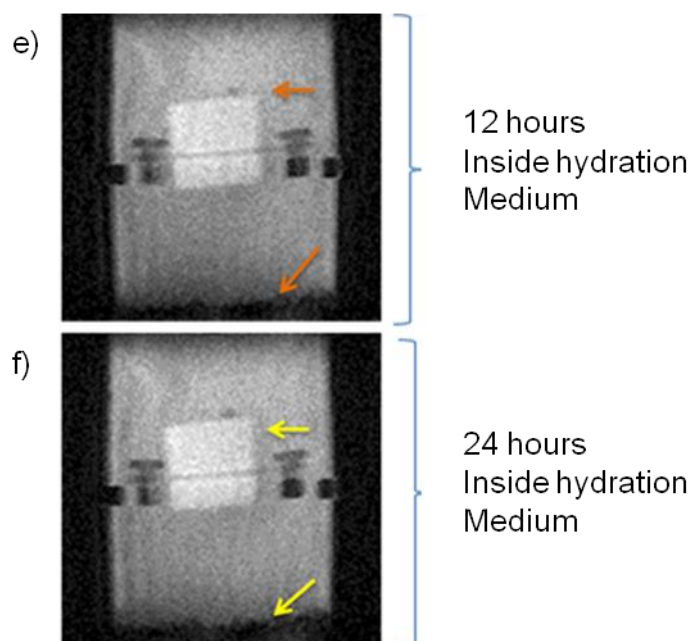


Figure 6.6: Swelling profiles of the CEP scaffold (F1-F3) in sCSF condition over 24 hours; a) non-cross-linked CEP scaffold, b) cross-linked CEP scaffold, c) CEP scaffold outside hydration medium, d) 30 minutes, e) 12 and f) 24 hours inside hydration medium.

6.3.3.4. Matrix erosion of the cross-linked Chitosan-Eudragit RSPO-Polyvinyl alcohol scaffold

ME of the CEP scaffold in a sCSF was investigated using an orbital shaking incubator (at 20rpm, 37°C) over 50 days. Figures 6.7a-b depicts the ME of the non-cross-linked and cross-linked CEP scaffold. Figure 6.7a exhibits high ME on the non-cross-linked CEP scaffold at about 65-80% weight loss over 50 days, for F1-F3 respectively. On the other hand, Figure 6.7b exhibits low ME on the cross-linked CEP scaffold at about 41-59% weight loss over 50 days, for F1-F3 respectively. The low ME is due to crosslinking decreasing hydrolytic cleavage. In addition, the presence of the biodegradable polymers such as CHT and PVA as building components of the CEP scaffold may have added significant influence in erosion behaviors (Kean and Thanou, 2010).

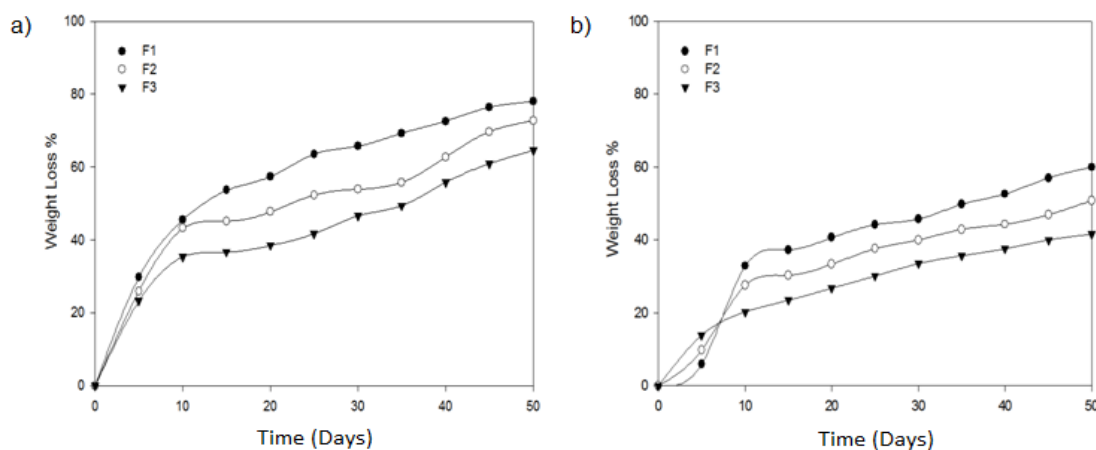


Figure 6.7: Weight loss profiles of the CEP scaffolds (F1-F3) in sCSF condition over 50 days; a) non-cross-linked CEP scaffold and b) cross-linked CEP scaffold.

6.3.4. Morphology characterization of the Bio-Robotic Intracranial Device

Morphology of the BICD was characterized by confocal microscopy and SEM. Figure 6.8 evidently depicts the morphology of the rhodamine-labeled and drug-loaded functionalized NLPs post-embedded into the CEP scaffold of the BICD. Figures 6.8a1-2 and b shows the surface morphology of the BICD with intact drug-loaded functionalized NLPs. Drug-loaded functionalized NLPs evidently possessed a uniform spherical shape previously demonstrated in Chapter 5, Section 5.3.3.1 and Figure 5.8. Confocal microscopy further validates distribution of the labeled functionalized NLPs in the temporal polymeric-based depot systems as previously discussed in Chapter 5, Section 5.3.3.2. control native or unlabeled CEP scaffold depicts no rhodamine activities. Figure 6.8c depicts high distribution of rhodamine-labeled functionalized NLPs on the surface and within the core region of the BICD. The overall data substantiates that drug-loaded functionalized NLPs remain intact post-lyophilization for 48 hours. The outcomes of these findings advise that 0.5% sucrose (see Chapter 4, section 4.2.6) as a cryoprotectant was adequate for liposomal nanostructure protection during freeze-drying.

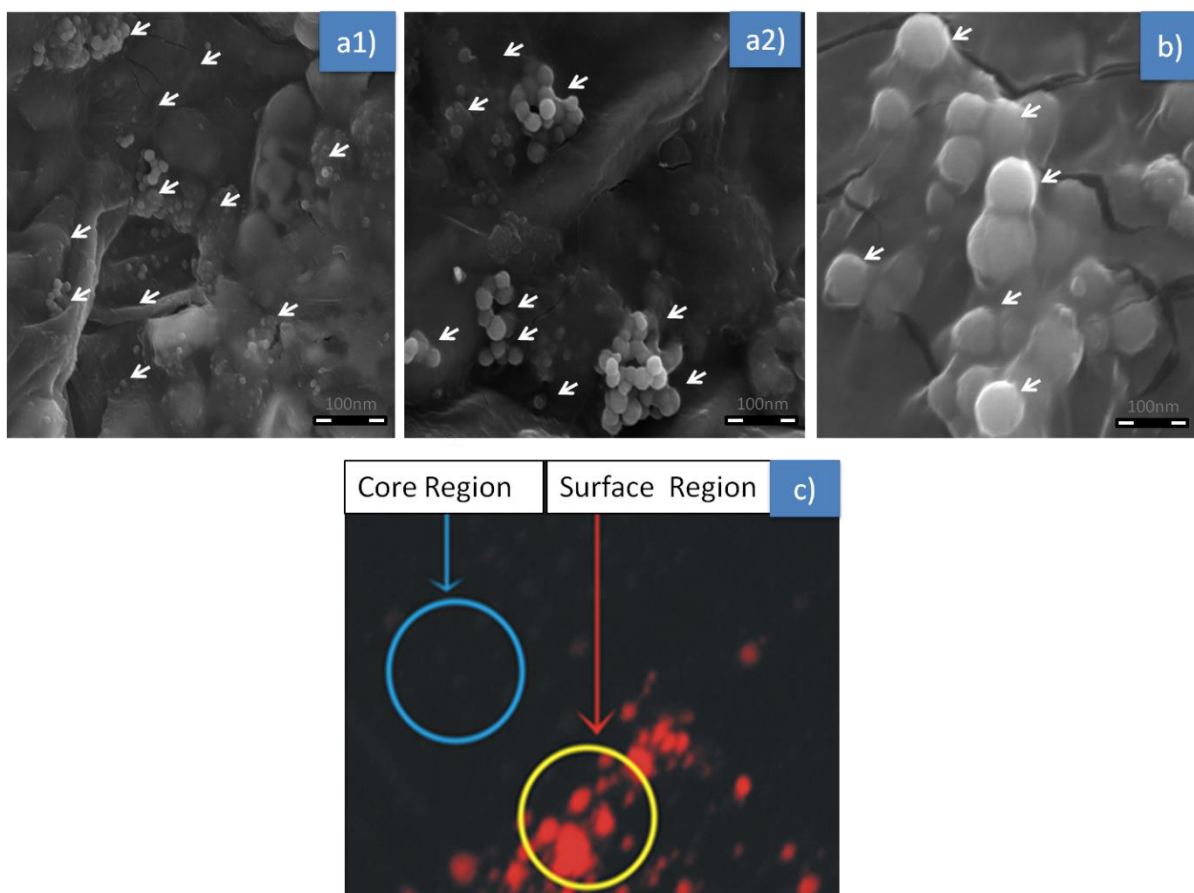


Figure 6.8: Typical SEM micrographs and fluorescence images of the BICD a1-2) drug-loaded functionalized NLPs post embedded within the BICD at 50x magnification, b) high magnification 100x and c) fluorescence images of the control unlabeled CEP scaffold and d) rhodamine-labeled functionalized NLPs within the surface and core region of the BICD.

6.3.5. *In vitro* drug release from functionalized nanoliposomes post-embedded from the Bio-Robotic Intracranial Device

Accumulative release of the drug-loaded functionalized NLPs from temporal non-cross-linked or cross-linked CEP scaffolds of the BICD (D1-D3) was investigated in a sCSF (0.1M PBS; pH7.4; 37°C) over 50 days.

Figure 6.9 depicts the release profiles of the drug-loaded functionalized NLPs from 6 different experimental formulations of the BICD (D1-D3, consist of either non-cross-linked or cross-linked CEP scaffolds). Figures 6.9a-c exhibited the release profiles of

the drug-loaded functionalized NLPs from the BICD over 50 days. Figures 6.9a-b shows a release profile of drug-loaded functionalized NLPs from cross-linked CEP scaffolds of the BICD (D1-D2) with a percentage ranged from 60-70% over 50 days respectively, while cross-linked CEP scaffolds of the BICD (D3) reached only 50% at day 50. However, in case of the BICD formulations (D1-D3) consist of the non-cross-linked CEP, about 70-90% drug-loaded functionalized NPLs were obtained at day 50 in sCSF medium. The quantity of GAL released was detected in either supernatant or pellet (sample centrifuged at 20,000rpm thereafter lysed with 0.5-1% v/v Triton X-100 in methanol) employing UV spectropotometry at $\lambda_{max}=288nm$ (Table 6.7). The quantity of GAL in a pellet hypothesize that the released drug-loaded functionalized NLPs were still in their intact form post-escaping the BICD, whereas GAL in supernatant might be the result of ruptured of the functionalized NLPs prior escape from scaffold structure of BICD. $MDT_{5-10day}$ ranged from 0.330-0.366 were obtained from the BICD (D1-D3, consist of non-cross-linked CEP scaffold) representing rapid release period. The $MDT_{5-10day}$ of the BICD (D1-D3, consist of cross-linked CEP scaffold) ranged from 0.107-0.174 representing prolongs release period. The rapid release of GAL-loaded functionalized NLPs from the BICD may have influenced by the properties of the non-cross-linked CEP scaffold such as structure chain relaxation state in sCSF medium. Other factors that may have influenced rapid release behavior could be by diffusion of the nanosize liposomal particles, porosity, hydration, erosion and swelling properties of the non-cross-linked CEP scaffold. Figure 6.10 shows a typical structure profile of drug-loaded functionalized NLPs with $\pm 100nm$ particles size and zeta potential of 34mV. The results also validate that the physicochemical properties of the liposomal structure, particularly the size distribution ($\pm 100nm$), could also have added an influence on drug-loaded

functionalized NLPs release via a diffusion process of the porous structure of the CEP scaffold of the BICD possessing a pore size $\sim 100\mu\text{m}$.

Overall, the results elucidate that the presence of cross-linking agent in the CEP scaffold contributed toward prolong release of the drug-loaded functionalized NLPs from the BICD. A high release of the drug-loaded functionalized NLPs was observed on a non-cross-linked CEP scaffold of the BICD; this may have been influenced by poor mechanical properties or weak interaction between polymers (CHT, PVA and EU). The presences of GA as a cross-linker add robustness to the developed CEP scaffold, extending the duration of drug-loaded functionalized NLPs release. In addition, D3 formulation further hypothesize that EU concentration could have contributed toward CEP scaffold stability or mechanical properties (Ghaffari et al., 2006). The quantity of GAL in sCSF medium (pellet sample) further validated that released drug-loaded functionalized NLPs were still in their intact form post-escaping the BICD.

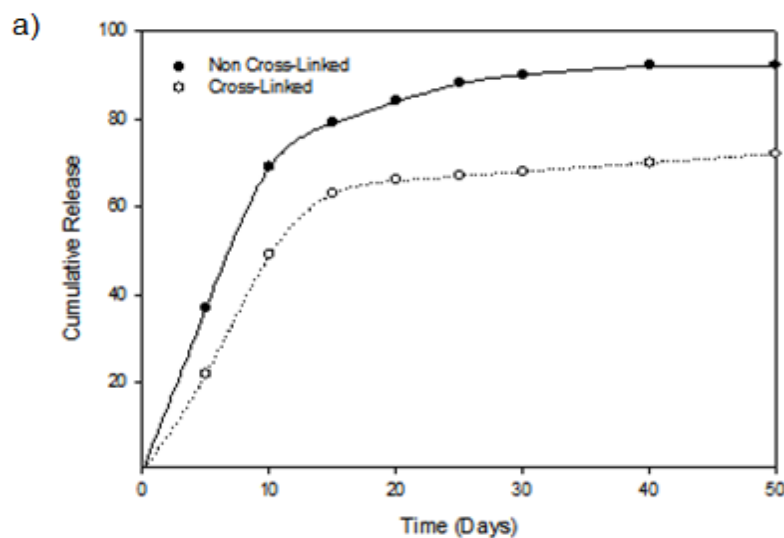


Figure 6.9: *Contd.on pg 192*

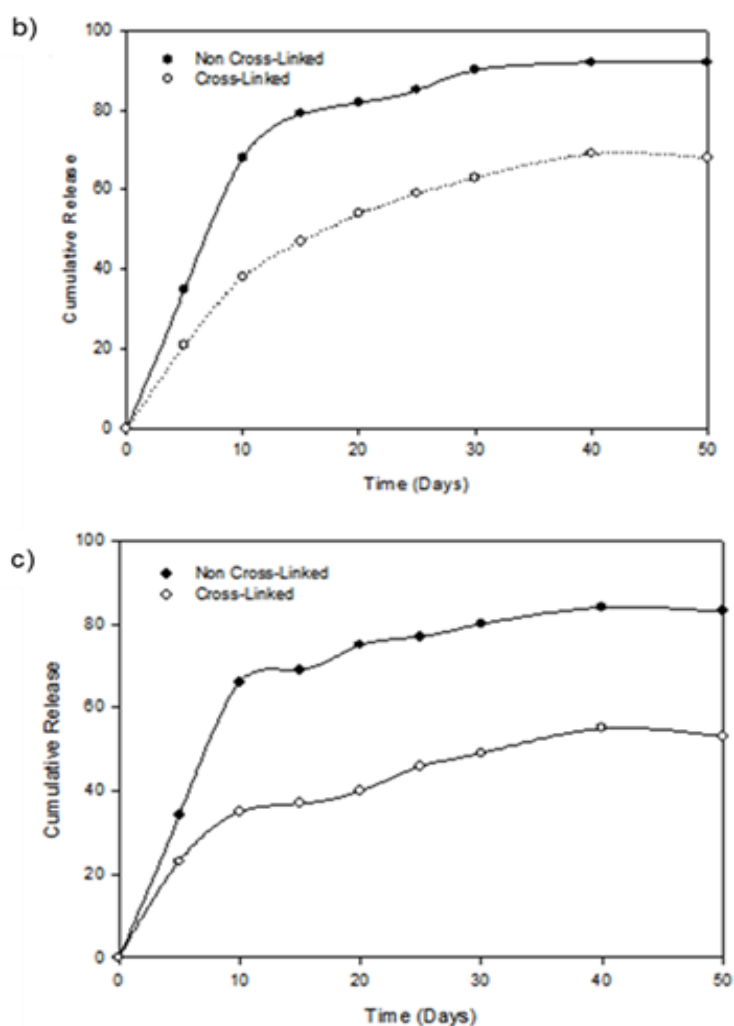


Figure 6.9: *In vitro* drug release from the functionalized NLPs post-embedded within the CEP scaffold of the BICD over 50 days in a sCSF condition a) D1, b) D2) and c) D3 (with non-cross-linked and cross-linked CEP).

Table 6.7. *In vitro* drug release characterization of three BICD formulations

F#		Drug release from BICD		MDT (t ₅₋₁₀ days)
		Collected from supernatant t ₁₀ day (%)	Collected from Pellet t ₁₀ days(%)	
D1	Non-cross-linked	16	69	0.37
	Cross-Linked	06	49	0.17
D2	Non-cross-linked	10	68	0.35
	Cross-linked	06	38	0.11
D3	Non-cross-linked	10	66	0.33
	Cross-linked	05	35	0.10

*MDT: Mean dissolution time

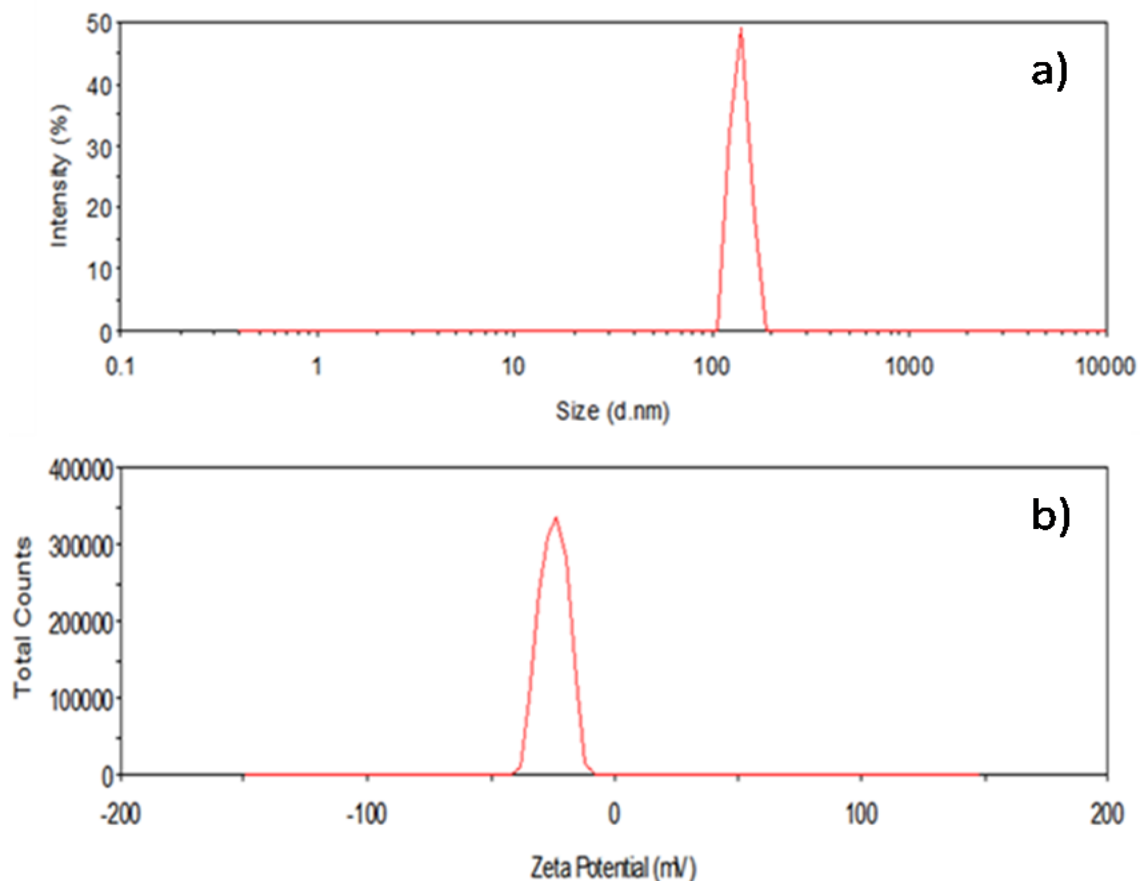


Figure 6.10: Typical drug-loaded functionalized NLPs profile showing (a) particle size (nm) and b) zeta potential (mV).

6.3.6. *Ex vivo* characterization of the Bio-Robotic Intracranial Device

6.3.6.1. Morphological characterization of the PC12 neuronal cells seeded on the surface of Chitosan-Eudragit RSPO-Polyvinyl alcohol scaffold

Morphological characterization of the PC12 neuronal cells seeded on the surface of the cross-linked CEP scaffold of the BICD was examined using SEM and a stereomicrograph imaging system. PC12 neuronal cell attachment and proliferation on the surface of the cross-linked CEP scaffold over 28 days are visualized in Figure 6.11. Figures 6.11a1, b1 and c1 depict micrographs of the control porous cross-linked CEP scaffold that exhibit no activity on the PC12 neuronal cells. Figures

6.11a2-a3, b2-b3 and c2-c3 exhibit typical micrographs of PC12 neuronal cells seeded on the surface of the cross-linked CEP scaffold using SEM and a stereomicrograph imaging system. Figure 6.11a2 displays a typical SEM micrograph (insert image) of the PC12 neuronal cell surface morphology following the seeding process.

Overall, the micrographs evidently validate that the cross-linked CEP scaffold and its architecture were suitable for promoting PC12 neuronal cell growth and proliferation post-seeding and cultivation in the *ex vivo* culture medium. In previous studies, it has been demonstrated that surface properties of natural polymers, particularly CHT, promote cell adhesion and proliferation (Li et al., 2012; Seonwoo et al., 2013). In addition, a study by Álvarez and co-workers (2012) exhibited satisfying cell growth on the surface of a CHT-PVA hydrogel; the following factors were hypothesized as enabling such dynamics: cross-linking, zeta potential (surface charges) and the presence of amide groups on the surface of CHT.

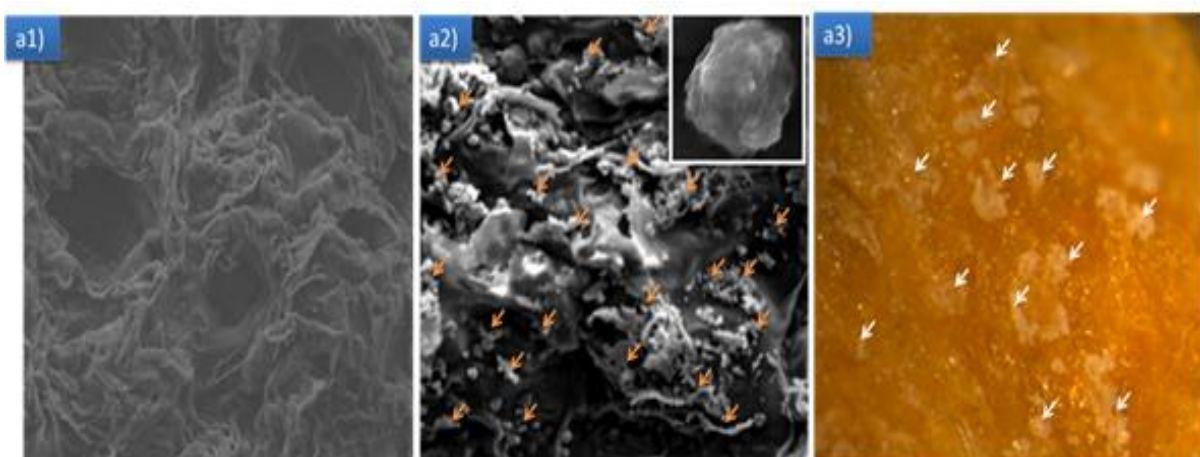


Figure 6.11: *Contd.on pg 195*

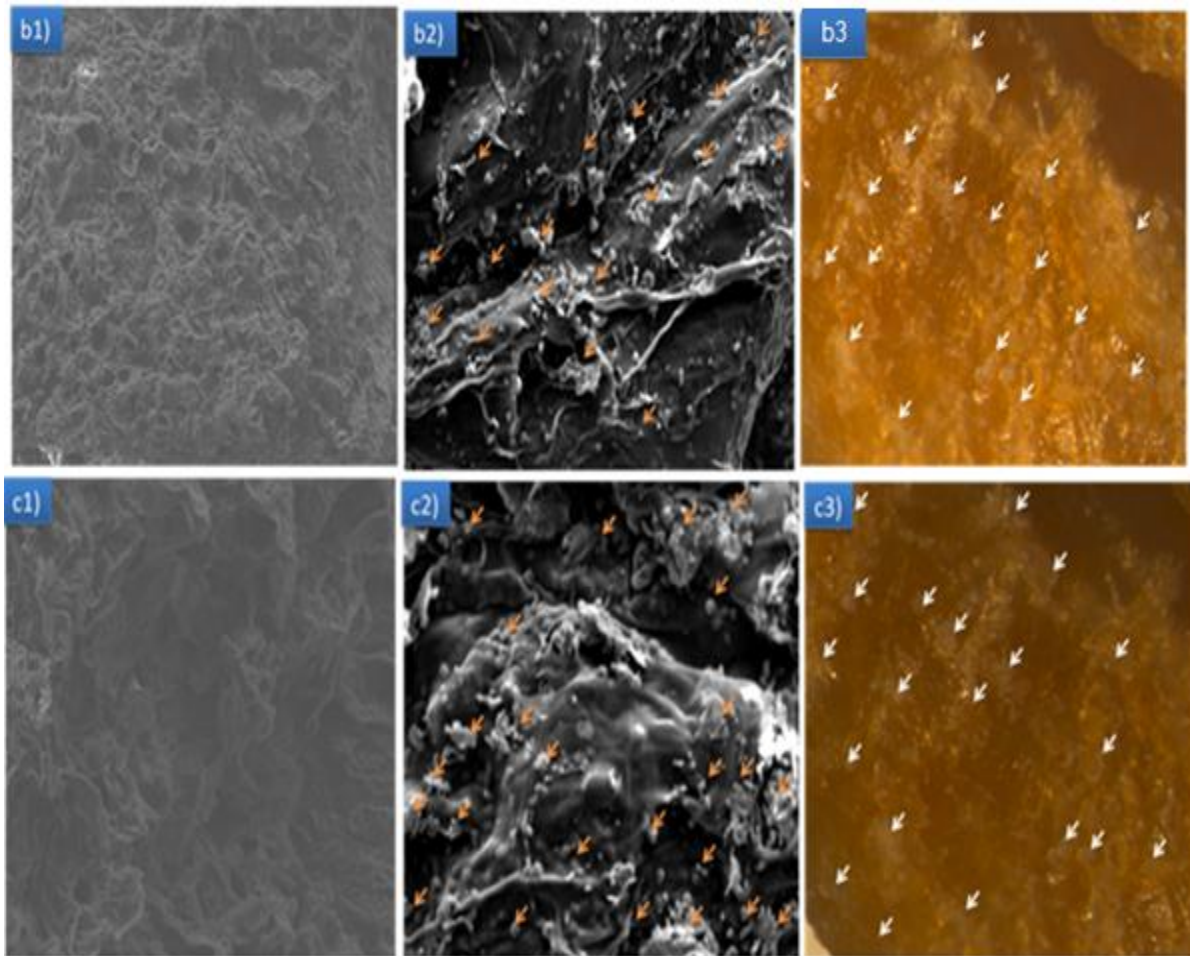


Figure 6.11: SEM and stereomicrographs of *ex vivo* incubation of the BICD seeded with PC12 neuronal cells at day 28. SEM micrographs of a1) F1, a2) D1, b1) F2, b2) D2, c1) F3, c2) D3 and Stereomicrographs of a3) D1, b3) D2) c3) D3.

6.3.6.2. Cytocompatibility of the Bio-Robotic Intracranial Device in the PC12 neuronal cells

The cytocompatibility and/or cytotoxicity of the functionalized NLPs, CEP scaffold and BICD in the presence of PC12 neuronal cells was evaluated using LDH leakage assay associated with cell membrane damage (Figure 6.12). An untreated PC12 neuronal cell was used as a negative control and for indirect measurements of the LDH activity. Maximum LDH percentage (100%) from the cytoplasm was achieved in the intracellular medium after untreated PC12 cells were lysed with lysis buffer (9% ν/ν Triton[®] X-100 in sterile water/ethanol). Functionalized NLPs showed a low effect

on cell membrane damage or cytotoxicity (15-22% LDH) when compared to untreated PC12 neuronal cells, while the effect on the CEP scaffold (31%) and BICD (30-32%) were slightly higher. These results validate that functionalized NLPs, CEP scaffold and BICD have low effect on extracellular LDH release post-cultivation in a cellular environment (37°C in a CO₂ condition) over 28 days. Slightly lower LDH levels in the presence of the functionalized NLPs may have been influenced by PEG engineered on the surface of the NLPs. A previous study conducted by Cho and co-workers (2008) reported the success of PEG on reversing membrane injury/damage while reducing LDH leaking. In addition, the presence of CHT also demonstrated a significant effect on sealing cell membrane damage or restraining the large endogenous LDH enzyme through maintaining membrane integrity (Bhattarai et al., 2005; Heinemann et al., 2009).

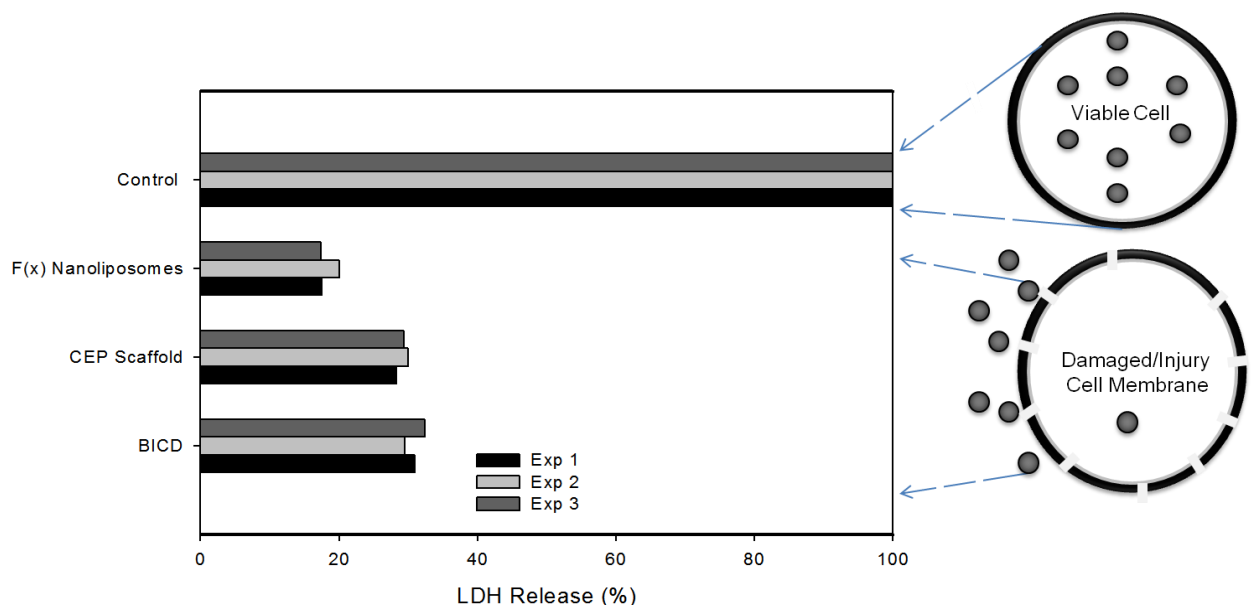


Figure 6.12: LDH release profiles measured from PC12 neuronal cells treatment with functionalized drug-loaded NLPs, CEP scaffold and BICD.

6.3.6.3. *Ex vivo* uptake of the drug-loaded functionalized nanoliposomes post-embedded within Bio-Robotic Intracranial Device

Ex vivo uptake of the drug-loaded functionalized NLPs, previously discussed in Chapter 4, Section 4.3.9.2, have demonstrated the high GAL accumulation into PC12 neuronal cells. Additionally, the study further validates the bioactivity of the targeting moiety (synthetic peptide) on facilitating cell uptake as previously demonstrated in Chapter 4, Section 4.3.9.2.

Figure 6.13 shows the cumulative activity of GAL at different time intervals in PC12 neuronal cells post-exposure to three BICD formulations (D1-D3) over 28 days. Figure 6.13 shows high GAL accumulation in PC12 neuronal cells post-exposure to D1, D2 and D3. D1 showed the most efficacy, which may have been influenced by mechanical and physicochemical dynamics of the CEP scaffold of the BICD, such as high diffusion, high porosity and swelling kinetics. Over and above that, the high GAL uptake exhibited for D1 may be associated with high drug-loaded functionalized NLPs released post-embedment in the CEP scaffold as reported in the *in vitro* study in Section 6.3.5. On the other hand, a slightly lower GAL uptake was exhibited for both D2 and D3. This may have been influenced by the physicochemical properties of the liposomal structure (particularly particle size, $\pm 100\text{nm}$) and/or mechanical structure of cross-linked CEP scaffold of the BICD (particularly low porosity, intermediate hydration, low erosion and swelling properties). The *in vitro* study also demonstrated that the D1 had a rapid release of drug-loaded functionalized NLPs post-exposure to dissolution medium over 50 days in a sCSF (see Section 6.3.5). Therefore, high GAL uptake exhibited for D1 could have been influenced by a high quantity of intact drug-loaded functionalized NLPs outside culture medium *ex vivo*.

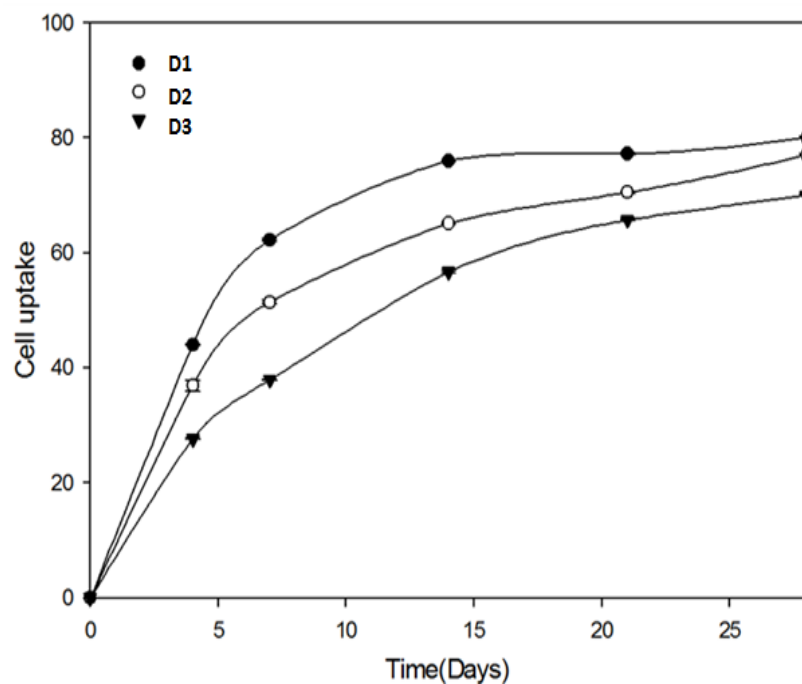


Figure 6.13: PC12 neuronal uptake of the post-embedded drug-loaded functionalized NLPs from within the BICD (D1, D2 and D3) over 28 days.

Confocal microscopy imaging further validated intracellular localization of the FITC-labeled functionalized NLPs post-release from the BICD *ex vivo*. Figure 6.14 depicts a topographical view of the fluorescence pseudo three-dimensional images of the PC12 neuronal cells. Confocal micrographs of the BICD post-seeding with PC12 neuronal cells demonstrated an apt corroboration with GAL uptake over 28 days *ex vivo*. Both GAL and FITC intracellular activity confirm that the molecular structure of the synthetic peptide surface engineered on the surface of the NLPs was still intact post-lyophilization ensuring potency for targeted delivery post-escaping the BICD *ex vivo*.

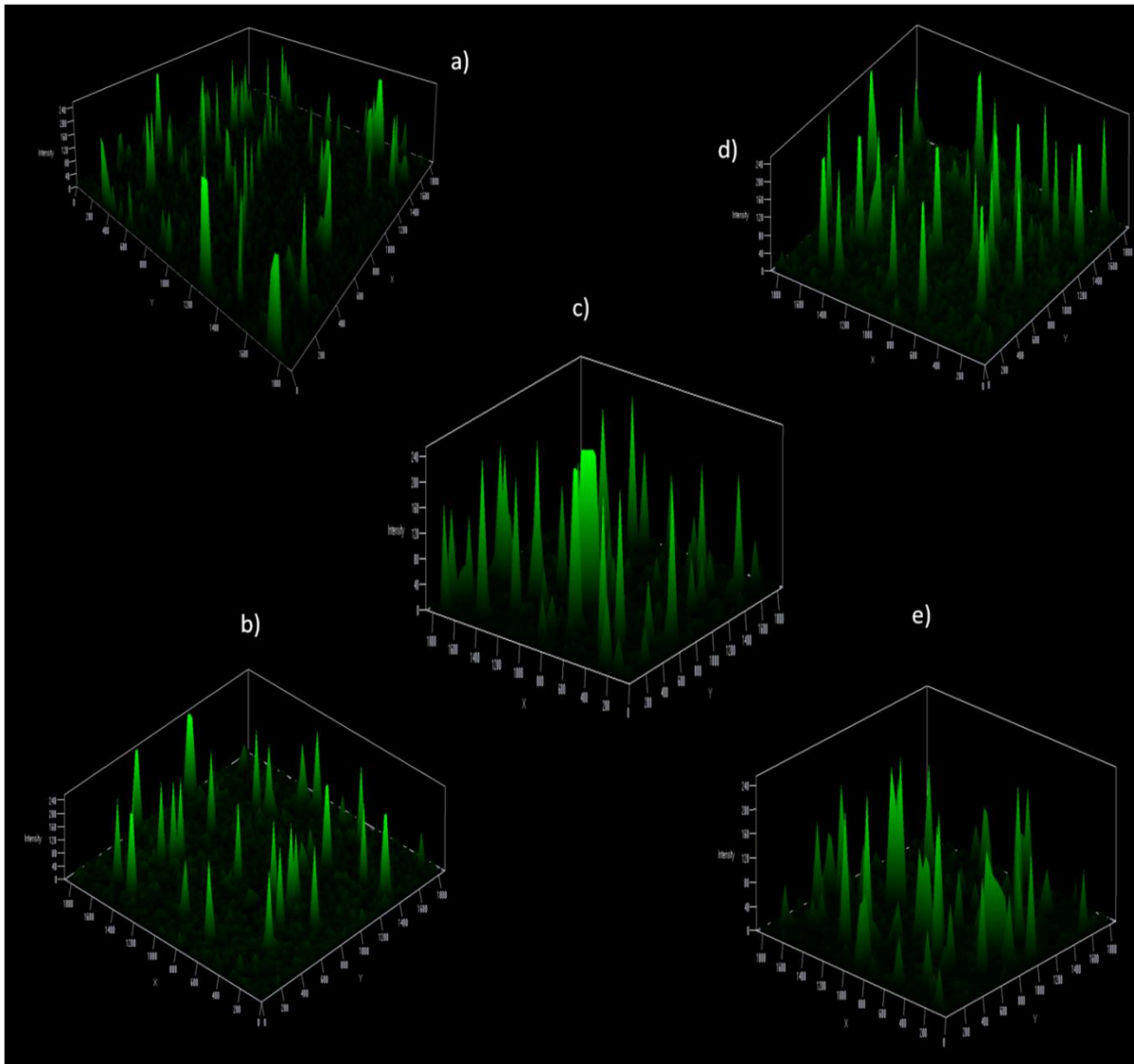


Figure 6.14: Topographical view of fluorescence Pseudo 3D images of the PC12 neuronal cells exposed to the BICD. Images were acquired at day a) 3, b) 7, c) 14, d) 21 and e) 28 using confocal microscopy.

6.4. Concluding remarks

The fabricated BICD may provide an improvement to existing drug delivery systems and may render satisfactory management of AD in terms of neuroprotectant efficacy, long-term pharmaceutical stability, targeted drug delivery and less frequent drug dosing intervals. The morphology of drug-loaded functionalized NLPs post-embedding into the CEP scaffold of the BICD evidently validated that the cryoprotectant agent was sufficient to preserve the nanoliposomal structure post-

lyophilization. The polymeric materials and/or cross-linking agent used during the fabrication of the CEP scaffold seemed to facilitate the physical stability and/or mechanical properties of a nano-enabled structure under sCSF conditions. *In vitro* studies also showed that the BICD was suitable for prolonged release of drug-loaded functionalized NLPs in their intact form. Comparability release studies demonstrate that drug-loaded functionalized NLPs from the non-cross-linked CEP scaffold promoted a rapid release rate and high quantity of the free drug release prior to the functionalized NLPs escaping from the BICD, whereas cross-linked CEP scaffold promoted prolonged release behavior and a lower quantity of the free drug being released prior to the functionalized NLPs escaping from the BICD over 50 days. In addition, this study also validates that cumulative release of drug-loaded functionalized NLPs may have been influenced by both physicochemical and physicochemical dynamics; these include the size of NLPs, institution of a cross-linking agent, porosity, swelling and erosion properties of the CEP scaffold. *Ex vivo* studies further provided a clear indication that the CEP scaffold and BICD were suitable for PC12 neuronal cell growth and proliferation. High accumulation of GAL and low LDH level in the PC12 neuronal cells post-exposure to the BICD suggest that the device had superior cytocompatibility *ex vivo*. Overall findings in this chapter indicated that the BICD may be suitable for prolonged release of the GAL-loaded functionalized NLPs, and thus capable of acting as bio-robotic markers for the precise delivery of GAL into the brain cells to treat AD.

CHAPTER 7

IN VIVO DEVELOPMENT OF THE PRE-CLINICAL MODEL FOR ALZHEIMER'S DISEASE USING NON-TRANSGENIC SPRAGUE DAWLEY RATS FOR THE ASSESSMENT OF THE BICD PERFORMANCE

7.1. Introduction

Amyloid β peptides ($A\beta$) are well researched and proven to be primary constituents that play a crucial role in the pathogenesis of Alzheimer's disease (AD) (Miller et al., 1993; Selkoe., 1999; Kowalska, A., 2004). Although the full-length $A\beta$ peptide contains 1-42 amino acid residues, small fragments contain 1-28, 25-35 and 36-42 amino acid residues and both share similarities such as biochemical and biophysical dynamics (Delobette et al., 1997, De Strooper, 2000). Numerous *in vitro* studies have exhibited the ability of soluble $A\beta$ peptides (fragments 25-35 and 1-42) to undergo a process of self-assembly or aggregation when reacted with biological ions, particularly zinc and copper ions. Thereafter these form insoluble $A\beta$ peptides that induce neurotoxicity (Pike et al., 1991; Pike et al., 1993; Lublin and Gandy, 2010). Despite the success on the stimulation of neurotoxicity *in vitro* and in cell culture by employing aggregated $A\beta$ peptides, *in vivo* or pre-clinical outcomes after administration of these aggregated $A\beta$ peptides in rats or mice models are still challenges when one seeks to develop an appropriate model for AD (Delobette et al., 1997; Dong et al., 2010; Mufamadi et al., 2012). Previous reports had validated that intracerebroventricular (ICV) administration of aggregated $A\beta(25-35)$ peptides induced amnesia in the rats and mitochondrial dysfunction (Delobette et al., 1997; Nakamura et al., 2001; Stephan et al., 2001; Lecanu et al., 2006). A study conducted

by Frautschy and co-workers (1992) is among the first studies to pave the way for a new non-transgenic animal model of AD. This study showed success in plaque formation into the cortex and hippocampus following administration of the purified amyloid plaques from human AD brains. Another study conducted by Delobette and co-workers (1997) demonstrated significant memory deficit 14 days after ICV administration of the aggregated A β (25-35) peptides. A study conducted by Nakamura and co-workers (2001) demonstrated the progressive brain dysfunction following ICV infusion of full A β (1-42) peptides.

Despite the possibility of employing A β peptides when developing a new model of the AD, the CNS is associated with difficulties when administering peptides into the brain through the Blood Brain Barrier (BBB). A recent study conducted by Frank and co-workers (2012) demonstrated how single dose of protein (IL-1RA) was administered employing intra-cisternamagna (ICM) injection, which resulted into a prolonged protein expression and detection in hippocampus post-ICM treatment. The outcome of the study opened a new door when one seeks to develop a new animal model or bypass the BBB, which was previously considered as one of the major setback. The histochemical stains such as thioflavin T and S and congo red are the among stains used to mark amyloid-like deposits or disease pathologies in AD brain tissues post-administration of the A β (25-35 and 1-42) peptides (Klunk et al., 2002; Bussie`re et al., 2004). In this chapter, an attempt on generation of the pre-clinical AD animal model using of non-transgenic Sprague Dawley rats was undertaken for the evaluation of *in vivo* performance of the BICD. The first attempt was to employ a novel ICM injection for a single dose of A β (25-35) peptides that effectively bypasses barriers posed by the BBB. Experimental animals were grouped into three groups,

(1) animals administered with 1µg/µL of the aggregated Aβ(25-35) peptides, (2) animals administered with 3µg/µL of the aggregated Aβ(25-35) peptides and (3) the control group where no aggregated Aβ(25-35) peptides were administered. The second attempt was the morphological characterization of positive amyloid-like deposits into brain tissues by employing traditional histochemical stains such as thioflavin T (ThT) and congo red.

7.2. Materials and Methods

7.2.1. Sprague Dawley rats and husbandry

Adult female Sprague Dawley rats (300-350 grams, n=15) were obtained from University of the Witwatersrand Central Animal Services (CAS). Animals were housed in groups of five (5) per cage, with free access to food and water at all times. All animals were maintained in a temperature and humidity-controlled environment in a 12 h light/12 h dark cycle. They were weighed once a day to indicate their general state of well-being. All the animal procedures described in this chapter were in accordance with the guide for the care and use of laboratory animals of the University of the Witwatersrand CAS, prepared by qualified neurosurgeons and veterinarians.

7.2.2. Preparation of aggregated Aβ(25-35) peptides and microscopy characterization

Acetyl beta amyloid (25-35) peptide was purchased from Sigma-Aldrich (Sigma-Aldrich Ltd., St. Louis, MO, USA). Self-aggregation Aβ(25-35)peptide (1mg) of was induced by dissolving in 0.2mL saline purchased from Sigma-Aldrich (Sigma-Aldrich

Ltd., St. Louis, MO, USA) and thereafter gently stirring at 37°C for 4 days (Delobette et al., 1996). TEM examination was conducted as previously described in Chapter 3, Section 3.2.7.2 of this thesis. The Confocal microscopy examination was conducted as previously described in Chapter 3, Section 3.2.10.3 of this thesis.

7.2.3. Experimental design of non-transgenic rat model of Alzheimers disease

Fifteen (15) adult female Sprague Dawley rats were randomly assigned into to the three groups. The first group of 5 rats each received 5-10µl of 1µg/µL of the Aβ(25-35) peptides. The second group of 5 rats each received 5µl of 3µg/µL of the Aβ(25-35) peptides and third group of 5 rats was the control group that did not receive the Aβ(25-35) peptide treatment.

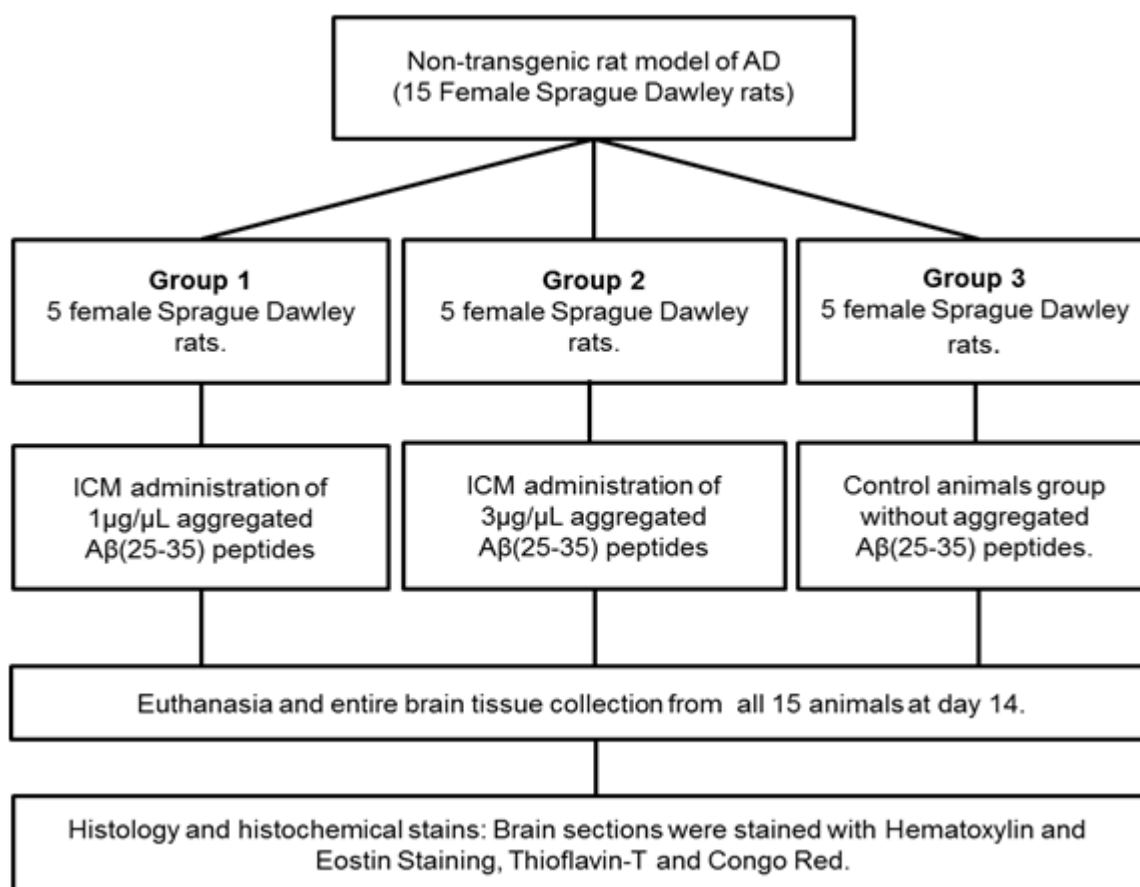


Figure 7.1: Schematic diagram representing the study design and number of Sprague Dawley rats used for the development of a model for AD for pre-clinical studies.

7.2.3.1. Intra-Cisterna Magna administration of aggregated A β (25-35) peptides

The aggregated A β (25-35) peptides were delivered into the hippocampus after a single ICM administration using a 26-gauge needle (inserted into the cisterna magna) attached through a 58cm PE50 tubing (containing samples) to a 50 μ L Hamilton syringe. All instruments were disinfected prior to injection using 70% ethanol for 30 min thereafter flushed with distilled water or sterile saline. All experimental rats were briefly anesthetized with halothane. The heads of all 10 experimental rats were shaved and swabbed with 70% ethanol. Five microliters (5 μ L) of the aggregated A β (25-35) peptides were delivered into cisterna magna through ICM injection as described by Frank and co-workers (2012).

7.2.3.2 Euthanasia and brain tissue collection

The amyloid deposits formation was validated at day 14 post-ICM treatment with aggregated A β (25-35) peptides. Both control and experimental animals were sacrificed by euthanasia for the study termination and the brain tissues were removed. The brains were then immediately stored in 50mL of 10% paraformaldehyde for further investigation.

7.2.3.3. Histopathology of brain tissues

Histopathology of brain tissues of the Sprague Dawley rats was conducted by hematoxylin and eosin stain in a reference laboratory (IDEXX Laboratories Inc., Pretoria, South Africa). The brain specimens were trimmed and cross sections from two levels in the cerebrum and one from the cerebellum were placed in a tissue

cassette and processed in an automated histological tissue processor (Pathcentre Enclosed Tissue Processor, Thermo Scientific, Johannesburg, South Africa). After overnight automated tissue processing, wax blocks were prepared and 6µm sections were cut on a HM450 Sliding Microtome (Thermo Scientific, Johannesburg, South Africa). The tissues were then stained with hematoxylin and eosin staining using a Shandon Varistain Gemini ES automatic slide stainer (Thermo Scientific, Johannesburg, South Africa). The following were evaluated: neuroparenchyma, blood vessels, and leptomeninges appearing on the brain tissues. The morphological findings on the brain sections stained with hematoxylin and eosin were graded and photographed with light microscopy.

7.2.3.5. Histochemical stains on the brain section

Histochemical stains on the brain sections of the Sprague Dawley rats were conducted in order to validate the formation of the amyloid deposits post-ICM treatment with aggregated A β (25-35) peptides by employing traditional Thioflavin T and Congo red staining (Sigma-Aldrich Ltd., St. Louis, MO, USA), with the assistance of a reference laboratory (IDEXX Laboratories Inc., Pretoria, South Africa). The morphological evaluation in the Congo Red stained section was observed under a light microscope (Olympus Co., Tokyo, Japan). The fluorescence images post-Thioflavin T staining were executed at fluorescence excitation (450nm) and emission wavelengths (480nm). Possible Thioflavin fluorescence associated with amyloid-like deposits were visualized employing Olympus IX71 Immunofluorescence Microscope (Olympus Co., Tokyo, Japan).

7.3. Results and Discussion

7.3.1. *In vitro* characterization of aggregation and fibril morphology of the Peptide

7.3.1.1. Morphological examination by Transmission Electron Microscopy

TEM micrographs of A β (25-35) peptide fragment and aggregated A β (25-35) peptides are shown in Figure 7.2. TEM images revealed the physical state of A β (25-35) peptide, self-assembled and aggregated A β (25-35) peptides following *in vitro* incubation. Figure 7.2a1-2 depicts the monomer structure with a less compact A β (25-35) fragment. Figure 7.2b1-2-c1-2 depicts the irregularly shaped, dense, compact, and stable aggregates of the A β (25-35) peptides at concentrations of 1 μ g/ μ L and 3 μ g/ μ L. Results also validated that the increased proportion of β -sheet structure was facilitated by the formation of aggregated A β (25-35) peptides.

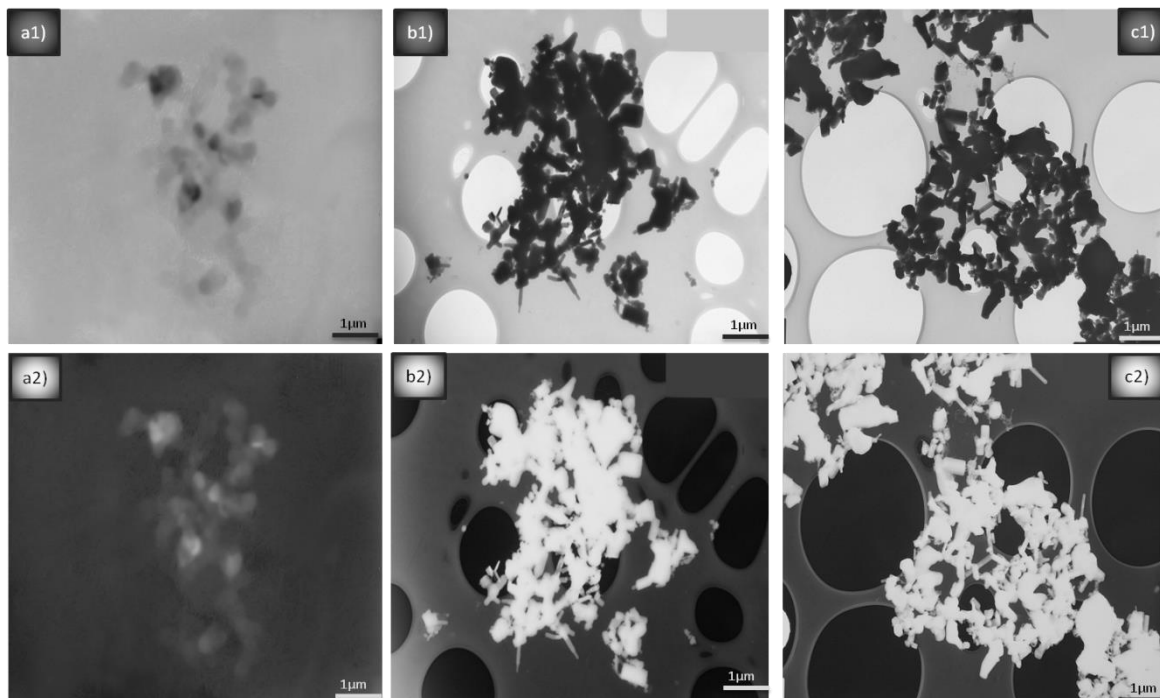


Figure 7.2: Darkfield and brightfield TEM micrographs of a1-2) A β (25-35) peptides, b1-2) aggregated A β (25-35) peptides at 1 μ g/ μ l concentration and c1-2) at 3 μ g/ μ l concentration.

7.3.1.2. Morphological examination by fluorescence microscopy

Figure 7.3 depicts the morphology images of the ThT labeled-A β (25-35) peptides and aggregated A β (25-35) peptides visualized employing Immunofluorescence microscopy. Figure 7.3a shows a monomeric A β (25-35) peptide structure with low yield of ThT fluorescence. Figure 7.3b-c exhibits a high quantum yield of the polymeric β -sheet-like structure and fibril-associated ThT fluorescence which appeared to be facilitated by aggregated A β (25-35) peptides. The fibril-associated ThT fluorescence was observed at all concentrations (1 μ g/ μ L and 3 μ g/ μ L) of the aggregated A β (25-35) peptides after 4 days of incubation at 37°C *in vitro*. The structure also showed strong interconnection which could have been influenced by monovalency between ThT upon binding A β (25-35) peptides. The outcome of this study postulates a clear observation of the morphological structure of induced aggregated A β (25-35) peptide post-incubation *in vitro* employing a histochemical confirmation study and fluorescence microscopy examination.

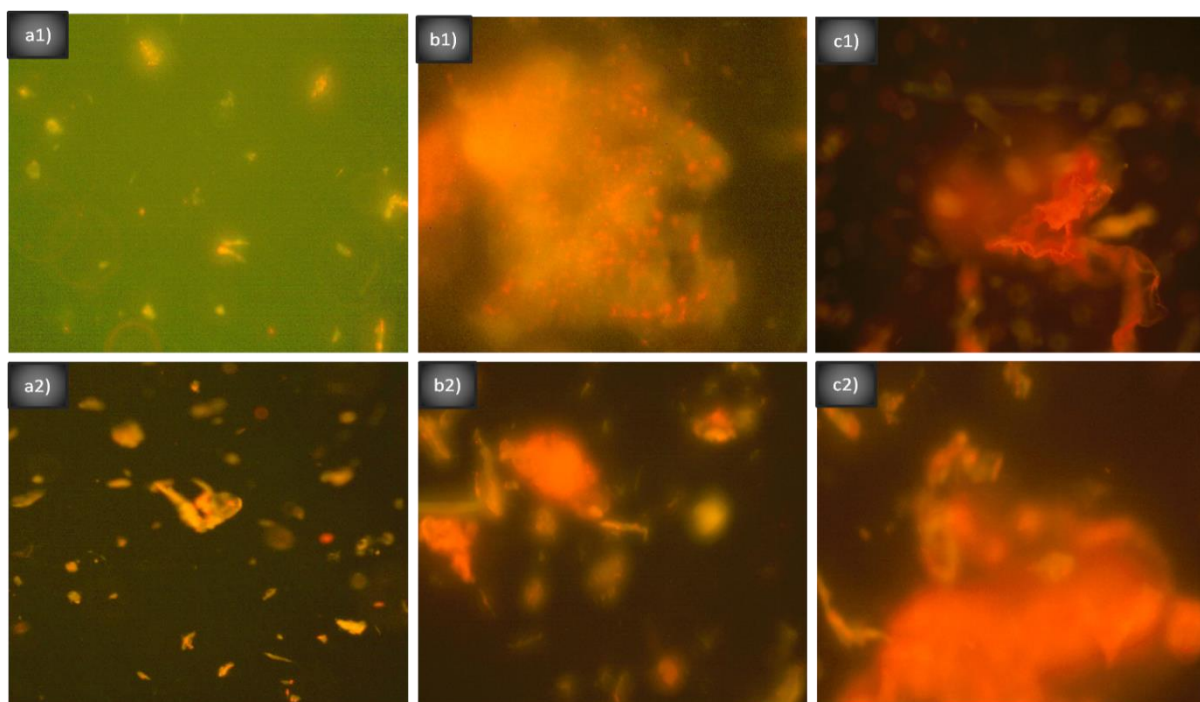


Figure 7.3: Fluorescent microscopy analysis of a) A β (25-35) peptides, b) aggregated A β (25-35) peptides at 1 μ g/ μ L concentration and c) at 3 μ g/ μ L concentration.

7.3.2. Brain tissues for paraffin wax embedding and mounting

The brain tissues of the Sprague Dawley rats were harvested from the skulls, then processed with paraffin wax for tissue embedment. Thereafter they were mounted onto the glass slide for pathological characterization. Figure 7.4 depicts the brain tissues' treatment post-embedment in the paraffin wax for all the different animal groups 1, 2 and 3. All brain tissues were sectioned using a HM450 Sliding Microtome and thereafter stained with hematoxylin and eosin, Congo red and ThT stain. A hematoxylin and eosin-stained slide was visualized with a red background, a ThT-stained slide was visualized with a gray background, and congo red-stained slide presented with a blue background. Histopathological effects and validation on the formations of amyloid deposits were further investigated by employing light microscopy and fluorescence microscopy.

7.3.3. Histopathology examinations

The histopathology was evaluated on fifteen (15) brain sections at day 14 post-ICM treatment with aggregated A β (25-35) peptides. Table 7.1 exhibits the effects to the aggregated A β (25-35) peptides in experimental groups and the control group (no treatment) on the morphological pathology of the neuroparenchyma, blood vessels and leptomeninges. The histological evaluation on brain sections was assessed by employing hematoxylin and eosin stains. The histological examination showed no foreign material on the neuroparenchyma, blood vessels and leptomeninges morphology. All presented with morphological normality. This outcome postulates that aggregated A β (25-35) peptides with intra-cerebral ICM injection did not induce any inflammatory responses post-administration.

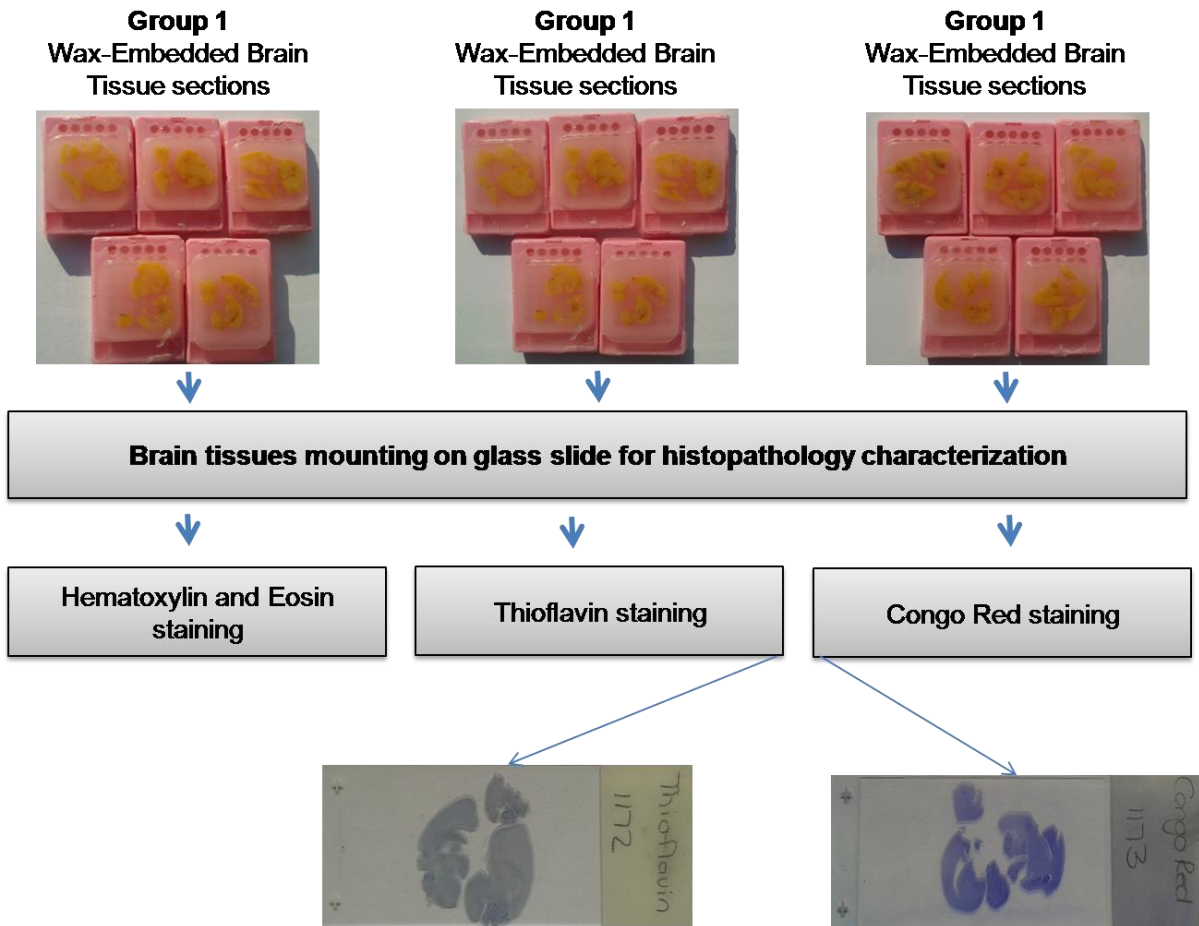


Figure 7.4: Digital images displayed wax embedded brain tissues sections and mounted section on the glass slide and stained (hematoxylin and eosin, ThT and congo red stain).

Figure 7.5 showed detailed histological examination of the brain sections of the experimental animals post-ICM injection with aggregated $A\beta(25-35)$ peptides, with normal morphology of the Cortex, Hippocampus, Cerebral white matter, Pia mater on cerebrum, Lateral ventricle, Coroid in ventricle, White matter cerebrum, peduncle cerebel, Medulla oblongata, Cerebellum and Cerebel white matter.

Table 7.1. Morphological pathology of the brain tissues of the Sprague Dawley rats post-ICM injection with aggregated A β (25-35) peptides

GROUP 1	β -AMYLOID PEPTIDE DOSAGE (25-35)	MORPHOLOGICAL APPEARANCE		
		NP ^a	BV ^b	LM ^c
Rat 1	1 μ g/ μ L	Normal (-)	Normal (-)	Normal (-)
Rat 2	1 μ g/ μ L	Normal (-)	Normal (-)	Normal (-)
Rat 3	1 μ g/ μ L	Normal (-)	Normal (-)	Normal (-)
Rat 4	1 μ g/ μ L	Normal (-)	Normal (-)	Normal (-)
Rat 5	1 μ g/ μ L	Normal (-)	Normal (-)	Normal (-)
GROUP 2				
Rat 6	3 μ g/ μ L	Normal (-)	Normal (-)	Normal (-)
Rat 7	3 μ g/ μ L	Normal (-)	Normal (-)	Normal (-)
Rat 8	3 μ g/ μ L	Normal (-)	Normal (-)	Normal (-)
Rat 9	3 μ g/ μ L	Normal (-)	Normal (-)	Normal (-)
Rat 10	3 μ g/ μ L	Normal (-)	Normal (-)	Normal (-)
GROUP 3				
Rat 11	0 μ g/ μ L	Normal (-)	Normal (-)	Normal (-)
Rat 12	0 μ g/ μ L	Normal (-)	Normal (-)	Normal (-)
Rat 13	0 μ g/ μ L	Normal (-)	Normal (-)	Normal (-)
Rat 14	0 μ g/ μ L	Normal (-)	Normal (-)	Normal (-)
Rat 15	0 μ g/ μ L	Normal (-)	Normal (-)	Normal (-)

^aNP: Neuroparenchyma, ^bBV: blood vessels and ^cLM: leptomeninges. All histological evaluation demonstrated normal morphology and no foreign body reaction [(-) (negative/none grade)] post-ICM treatment with aggregated A β (25-35) peptides.

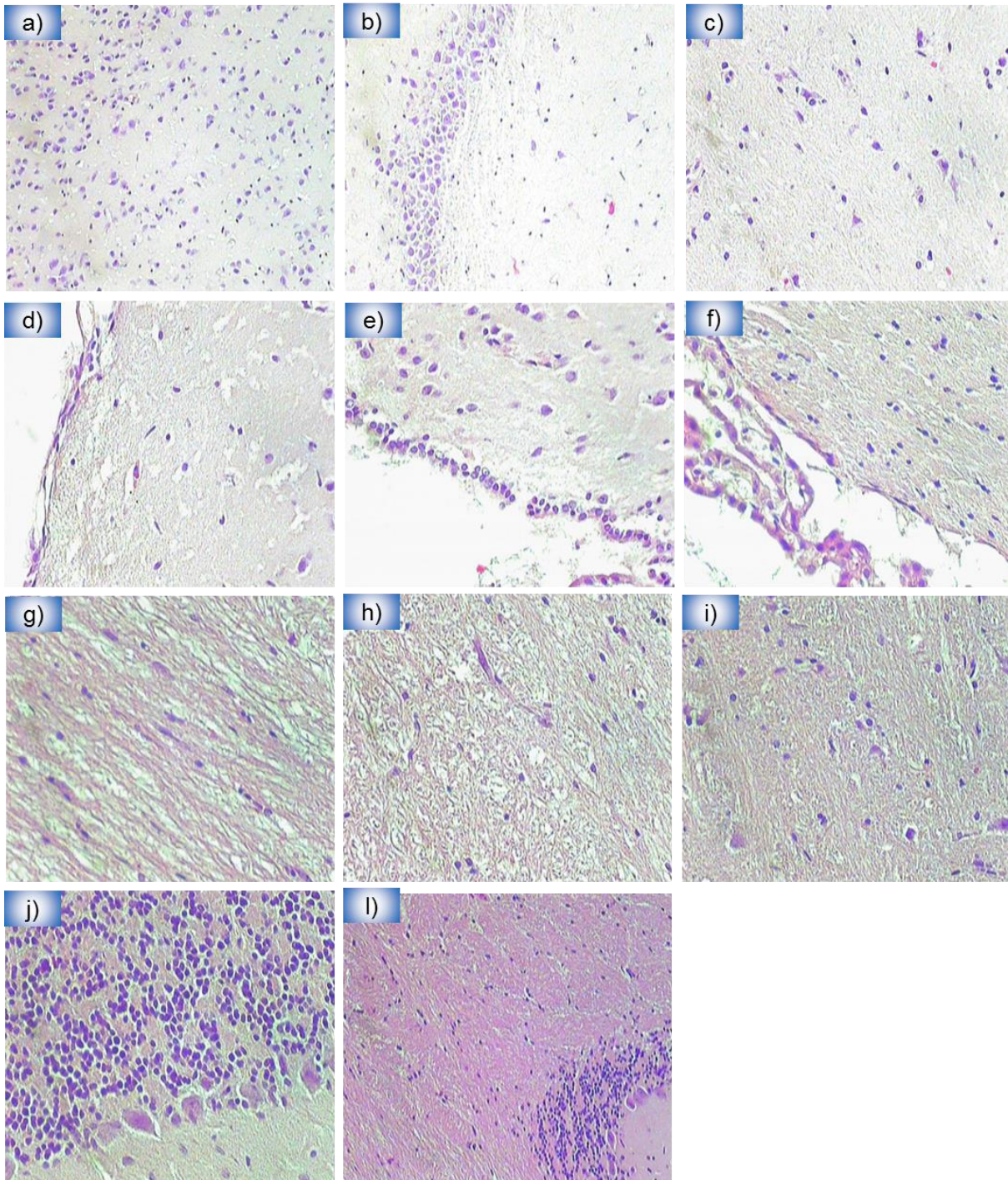


Figure 7.5: Histological slides of the brain sections of the experimental animals post-ICM injection with aggregated $A\beta(25-35)$ peptides, a) Cortex, b) Hypocampus, c) Cerebral white matter, d) Pia mater on cerebrum, e) Lateral ventricle, f) Coroid in ventricle, g) White matter cerebrum, h) peduncle cerebel, i) Medulla oblongata, j) Cerebellum and l) Cerebel white matter.

7.3.4. Amyloid deposits formations

7.3.4.1. Thioflavin Stain

To validate the outcome of the aggregated A β (25-35) peptides on inducing amyloid-like deposits post-ICM injection into the brain of the Sprague Dawley rats, traditional ThT stain was used. Figure 7.6 depicts possible thioflavin positive amyloid-like deposits in the animal group that received ICM injection with either 1 μ g/ μ L (Group 1) or 3 μ g/ μ L (Group 2) of the aggregated A β (25-35) peptides. Figures 7.6a1-3 show little or no fluorescence intensity after being treated with 1 μ g/ μ L of the aggregated A β (25-35) peptides. Figures 7.6b1-3 did not exhibit any significant effect when a high concentration of 3 μ g/ μ L of the aggregated A β (25-35) peptides was delivered through the ICM injection into the brain of the Sprague Dawley rats. However, the amyloid-like deposits, visualized in images for Group 1 and Group 2, depict amorphous plaque morphology. This outcome could be associated with the presence of different types of plaques as previously described by Bussière and co-workers (2004). The plaques that exhibited a spherical shape were claimed to be immature plaques. The amyloid-like deposits that displayed as a mesh-like stain were grouped as plaque type 1. This plaque type was associated with weak plaques of irregular shape and variable diameter; while those with strong and compressed fluorescence, a central dense core and homogenous amyloid-like deposits were identified as plaque type 2. Control group (3) of animals without ICM injection of the aggregated A β (25-35) peptides did not show any fluorescence activities following staining with thioflavin (Figure 7.6c1-3). To determine whether these fluorescence activities validated the formation of the amyloid-like deposits that mimicked the pathology observed in the brain of AD, additional pathological examinations have to be undertaken. A major

setback associated with thioflavin is that it is not perfectly specific for amyloid, which elicits the possibility of displaying false negative findings.

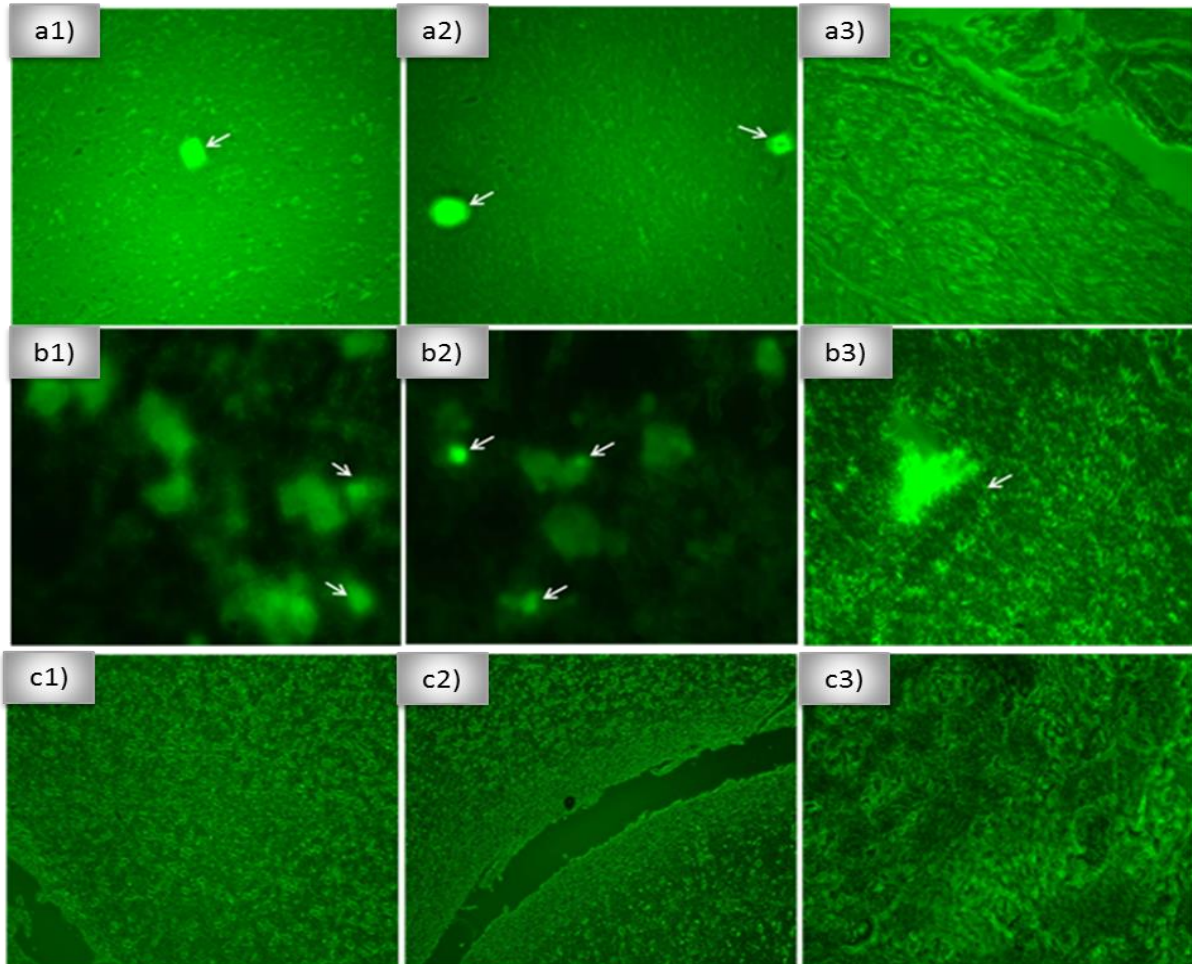


Figure 7.6: Sprague Dawley rat brain sections representing the morphology of the amyloid-like deposits post ThT staining, a1-3) Group 1: animals received ICM treatment with 1µg/µL of the aggregated Aβ(25-35) peptides, b1-3) Group 2: animals received ICM treatment with 3µg/µL of the aggregated Aβ(25-35) peptides, and c1-3) Control group (3): animals without ICM injection (40x magnification).

7.3.4.2. Congo Red Stain

Although the ThT stain demonstrated the formation of the amyloid-like deposits, additional pathological examination is still essential in order to postulate success on development of an animal model for AD. A histochemical examination was further conducted on the brain sections by employing Congo red stain. Microscopic

examination of the brain sections stained with Congo red for the presence of amyloid-like deposits and related proteinaceous material did not demonstrate any Congo red positivity on light microscopy as per the pathology report (reference IDEXX Laboratories Inc., Pretoria, South Africa). Fluorescence visualized by employing Immunofluorescence microscopy also showed low intensity of congophilic-like material activity post-ICM injection with aggregated A β (25-35) peptides into the brain of the Sprague Dawley rats (Figure 7.7). Figures 7.7a1-3 depict experimental group 1. This group showed only one (1) congophilic-like material post-ICM injection with 1 μ g/ μ L of the aggregated A β (25-35) peptides. Figures 7.7b1-3 depict experimental group 2. This group displayed few congophilic like materials post-ICM injection with 3 μ g/ μ L of the aggregated A β (25-35) peptides. Figures 7.7c1-3 depict the control group (3). This group did not show any congophilic-like materials on the brain sections post-staining with the Congo red stain.

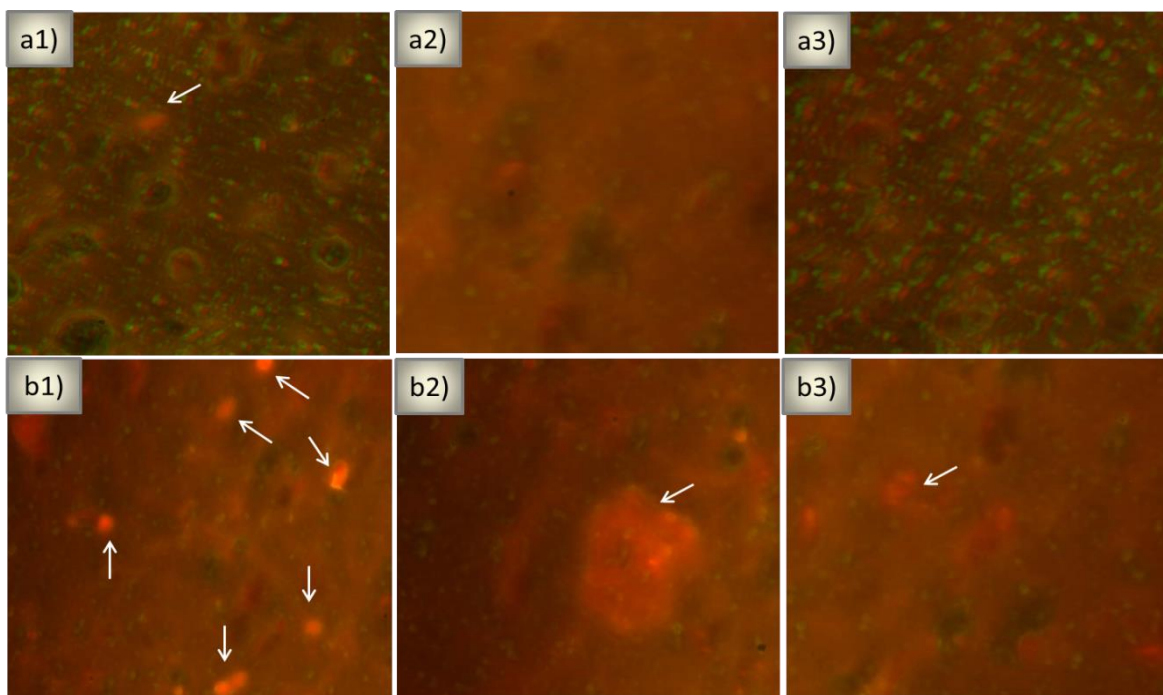


Figure 7.7: *Contd. on pg 216*



Figure 7.7: Sprague Dawley rats brain sections representing the morphology of the amyloid-like deposits post ThT staining, a1-3) group 1, animals received ICM treatment with 1µg/µl of the aggregated Aβ(25-35) peptides, b1-3) group 2, animals received ICM treatment with 3µg/µl of the aggregated Aβ(25-35) peptides and c1-3) control group (3), animals without ICM injection.

7.4. Concluding Remarks

The data in this Chapter postulates that the single dose of Aβ(25-35) peptides administered intra-cerebrally may not be sufficient enough for the generation of a pre-clinical AD animal model on non-transgenic Sprague Dawley rats. *In vitro* results depict a basic structural morphology, and modality of the Aβ(25-35) peptide self-assembly and aggregation. Both TEM and fluorescence images exhibit a fraction of the Aβ(25-35) peptides, with aggregation proceeding more as the concentration of peptide increases and after 4 days incubation at 37°C *in vitro*. The Aβ(25-35) peptide spherical aggregates labeled with thioflavin demonstrated the morphological transformation from non-coiled (monomers) into complex morphologies with twisted pairs and coiled structures, visualized employing fluorescence microscopy (Norlin et al., 2012). The histopathological examination portrayed that ICM injection/administration of aggregated Aβ(25-35) peptides intra-cerebrally did not alter the morphological pathology of the neuroparenchyma, blood vessels and leptomeninges, as observed in hematoxylin and eosin-stained brain sections. The concentration of aggregated Aβ(25-35) peptides (1µg/µL and 3µg/µL) did not exhibit

any significant effect on the formation of amyloid-like deposits, confirmed via both ThT and congo red staining. This outcome hypothesizes that neither dosage nor concentration of aggregates may be adequate for development of an animal model that mimics the pathology observed in the brain of AD.

Although *in vitro* β -amyloid peptide (25-35) aggregation can be used to develop of the pre-clinical model or non-transgenic Rat model of AD, the outcomes is still associated with low level of the A β expression, no senile plaque formation and show very few congophilic-like materials deposition. To develop an effective model that can express all biological markers associated with AD such as SEC-R and that can be used for the assessment of the BICD performance *in vivo*, transgenic Rat Model of AD is recommended. Hogan and co-worker (1986) demonstrated how to development of the transgenic Sprague Dawley rat model of AD via manipulating microinjection of DNA from trangene plasmid into rat/mouse embryo.

CHAPTER 8

CONCLUSION AND RECOMMENDATIONS

8.1. Conclusions

Although alkaloid drugs have the potential to inhibit pathological activation while metal chelators are also capable for prevention of the β -amyloid aggregation in AD patients, the global brain drug market is still considered under-developed due to impediments associated with current systemic drug administration such as poor drug retention and the difficulty in bypassing the highly restrictive BBB of the CNS. The aim of the research was the design and development of a novel drug delivery system that is capable of improving or bridging the gap between the drug therapies that are available and the improvement in the mode of drug delivery to ensure minimal drug toxicity, improved efficacy and a superior quality of life for patients challenged with AD. Three unique drug delivery modalities that could potentially overcome current AD impediments were developed, being NLPs surface engineered with a chelating ligand, a synthetic peptide targeting ligand, and an implantable hydrogel for the ultimate design of a nano-enabled bio-robotic intracranial device (BICD).

The *in vitro* reaction between biological metal ions and $A\beta(25-35)$ peptide as one of the prerequisite conditions that promote development $A\beta$ -aggregation in AD was elucidated. The presence of chelating ligands on the surface of NLPs was desirable for resolubilization of $CuA\beta(1-42)$ and $ZnA\beta(1-42)$ aggregates *in vitro*. In a cellular environment, the presence of chelating ligands on the surface of NLPs enabled

protection of PC12 neuronal cells post-exposure to CuA β (1-42) and ZnA β (1-42) aggregates, which is associated with neurotoxicity in AD.

FTIR, DSC, TEM and SEM studies on the surface engineered NLPs with either chelating or synthetic peptide ligands were extensively validated in order to elucidate their chemical structure variations, nano-morphology and physicochemical characteristics. *Ex vivo* uptake studies revealed that the presence of the NLPs post-engineering of ligands may have influenced restoration of intracellular zinc and copper ion levels through an ionophore process or macropinocytosis in the presence of biological metals. When synthetic peptide was employed for targeted delivery, high accumulation of GAL was exhibited. Low intracellular activities in PC12 neuronal cells post-exposure to native GAL and non-functionalized NLPs further validated that the uptake was mediated through high surface SEC receptor expression. In addition, the results indicate that functionalized NLPs may act as a bio-robotic marker for the delivery of GAL into the neuronal cells in response to AD.

The novel BICDs were subjected to vigorous physicochemical, physicochemical, and biocompatibility for ascertainment of prolonged drug release in a simulated CSF and neuronal cellular environment. Physicochemical and physicochemical dynamics, including; size and zeta potential of the nanoliposomes, porosity, hydration rate, swelling properties and degradation of the BICD, were evidently validated to be responsible for prolonged release of GAL-loaded functionalized NLPs post- embedding into the CEP scaffold over 28-50 days in both a simulated CSF and neuronal cellular environment. The intracellular activities of the functionalized NLPs with synthetic peptide following escape from the BICD validated that the

nanostructure was still intact post-lyophilization while maintained their potency for targeted delivery.

Overall results obtained in this study indicated that novel BICD may provide an improvement to current impediment associated with existing systemic GAL administration or brain drug delivery systems. *In vitro* study provide clear evidence that the BICD may render satisfactory management of AD in terms of therapeutic efficacy and long-term pharmaceutical stability over 50 days in sCSF condition, while *ex vivo* further validated that BICD may be used on targeted drug delivery of GAL into the PC12 neuronal cells in response to AD. In addition, high accumulation of GAL and low LDH level in the PC12 neuronal cells post-exposure to the BICD suggest that the device had superior cytocompatibility *ex vivo*. Furthermore, if implantated *in vivo*, BICD may render less frequent drug dosing, may maintain drug concentrations above therapeutic level and may deliver drugs to a specific site of the brain and neurons in response to AD condition.

However, the amyloid-like deposits associated with ThT and Congo red fluorescence did not provide substantial indication that could validate effective development of an animal model that could mimic the pathology observed in the brain of AD patients. In addition, this outcome made it difficult to further pre-clinical studies for the assessment of the BICD efficacy following implantation *in vivo*.

8.2. Recommendations

Despite the fact that the developed BICD posed notable benefits toward overcoming impediments associated with current drugs for the management of AD such as

prolonged half-life of GAL, localization and targeted delivery, scientific obstacles still have to be overcome to establish a suitable pre-clinical animal model of AD prior to progression to human clinical trials.

Since the BICD was fabricated from natural and synthetic polymers (all of which are biodegradable), it is still important to further investigate post-implantation activities such as degradability, and the requirement for surgical removal. In addition, since the BICD exhibited a degree of hydration response in a simulated CSF environment, it is therefore important to further investigate the possibility of inducing an immune response post-implantation.

When the BICD was exposed to PC12 neuronal cells, the data exhibited a low LDH activity, which is associated with a low degree of cytotoxicity, cell membrane damaged, and/or injury. Future *in vivo* studies in a suitable animal model would be important for conducting a histological examination of brain tissue samples in order to further confirm any toxicity or an inflammatory response that could be induced by the BICD following implantation.

Although AD is a disease at cellular level and our study significantly elucidated the potential to suppress a major causative factor associated with AD, it is still necessary to validate pharmacodynamics in an appropriate animal model of AD in order to maximize the BICD biocompatibility prior to clinical evaluation. A transgenic mouse model of AD is ideal since it can express all other biological markers associated with AD such as surface receptors that can facilitate uptake when the drug-loaded functionalized NLPs are employed. However, the transgenic mouse model of AD

requires a special laboratory facility, with an elevated level of maintenance, which is only available at a high cost.

In addition, due to an overlap in the neuropathological symptoms of common neurodegenerative disorders the BICD may also have the potential to incorporate multiple drugs for the combinatory management of NDs. Since HIV/AIDS is a leading cause of death in South Africa, the BICD has been recommended for the design of future polytherapy for the management of patients that have HIV-associated AD and NDs.

REFERENCES

1. Abdelwahed W, Degobert G, Fessi H. Freeze-drying of nanocapsules: impact of annealing on the drying process. *Int J Pharm.* 2006; 324: 74-82.
2. Abbott NJ, Romero IA. Transporting therapeutics across the blood brain barrier. *Mol Med Today.* 1996; 2: 106-13.
3. Abra RM, Bankert RB, Chen F, *et al.* The next generation of liposome delivery systems: recent experience with tumor targeted, sterically-stabilized immunoliposomes and active loading gradients. *J Liposome Res.* 2002; 12:1-3.
4. Albu MG, Ghica MV, Popa L, *et al.* Kinetic of *in vivo* release of doxycycline hyclate from collagen hydrogels. *Rev Roumaine de chim.* 2009; 54: 373-9.
5. Accardo A, Salsano G, Morisco A, *et al.* Peptide-modified liposomes for selective targeting of bombesin receptors overexpressed by cancer cells: a potential theranostic agent. *Int J Nanomed.* 2012; 7: 2007-17.
6. Agnihotri SA, Aminabhavi TM. Novel interpenetrating network chitosan-poly(ethylene oxide-g-acrylamide) hydrogel microspheres for the controlled release of capecitabine. *Int J Pharm.* 2006; 324:103-15.
7. Alavijeh MS, Chishty M, *et al.* Drug metabolism and pharmacokinetics, the blood-brain barrier, and central nervous system drug discovery. *NeuroRx.* 2005; 2: 554-71.
8. Al-Gubory K, Houdebine L. In vivo imaging of green fluorescent protein-expressing cells in transgenic animals using fibred confocal fluorescence microscopy. *Eur J Cell Biol.* 2006; 85: 837-45.

9. Ali HM, Daniel J, Kirby DJ, *et al.* Solubilisation of drugs within liposomal bilayers: alternatives to cholesterol as a membrane stabilising agent. *J Pharm Pharmacol.* 2002; 62: 1646-55.
10. Allen C, Dos Santos N, Gallagher R, *et al.* Controlling the physical behavior and biological performance of liposome formulations through use of surface grafted poly(ethylene glycol). *Biosci Rep.* 2002; 22: 225-50.
11. Allen TM, Martin FJ. Advantages of liposomal delivery systems for anthracyclines. *Seminars Oncol.* 2004; 31: 5-15.
12. Álvarez AL, García EB, Callejas FG, *et al.* *In vitro* evaluation of the suppressive effect of chitosan/poly (vinyl alcohol) microspheres on attachment of *C. parvum* to enterocytic cells. *Euro J Pharm Sci.* 2012; 47: 215-27.
13. Ammar HO, Ghorab M, El-Nahhas SA, *et al.* Polymeric matrix system for prolonged delivery of tramadol hydrochloride, part I: physicochemical evaluation. *AAPS PharmSciTech.* 2009; 10: 7-20.
14. Anabousi S, Bakowsky U, Schneider M, *et al.* *In vitro* assessment of transferrin conjugated liposomes as drug delivery systems for inhalation therapy of lung cancer. *Eur J Pharm Biopharm.* 2006; 29: 367-74.
15. Appelbaum PC, Hunter PA. The fluoroquinolone antibacterials: past, present and future perspectives. *Int J Antimicrobial Agents.* 2000; 16: 5-15.
16. Arguelles-Monal W, Goycoolea FM, Peniche C, *et al.* Rheological study of the chitosan and glutaraldehyde chemical gel system. *Polym Gels Netw.* 1998; 6: 429-40.
17. Armoškaitė* V, Ramanauskienė K, Briedis V. Evaluation of base for optimal drug delivery for iontophoretic therapy: Investigation of quality and stability. *African J Pharm Pharmacol.* 2012; 6: 685-95.

18. Arti A, Molinuevo JL, Lemming O, *et al.* Mamantine in patients with Alzheimer's disease receiving donepezil: new analysis of efficacy and safety for combination therapy. *Alzheimers Res Ther.* 2013; 5: 1-11.
19. Atyabi F, Farkhondehfa A, Esmaeili F, *et al.* Preparation of pegylated nano-liposomal formulation containing SN-38: *in vitro* characterization and *in vivo* biodistribution in mice. *Acta Pharm.* 2009; 59: 133-44.
20. Autissier A, Le Visage C, Pouzet C, *et al.* Fabrication of porous polysaccharide-based scaffolds using a combined freeze-drying/cross-linking process. *Acta Biomaterialia.* 2010; 6: 3640-8.
21. Bachelder EM, Beaudette TT, Broaders KE, *et al.* *In vitro* analysis of acetalated dextran microparticles as a potent delivery platform for vaccine adjuvants. *Mol Pharm.* 2010; 7: 826-35.
22. Baek SH, Park SJ, Jin SE, *et al.* Subconjunctivally injected, liposome-encapsulated streptokinase enhances the absorption rate of subconjunctival hemorrhages in rabbits. *Eur J Pharm Biopharm.* 2009; 72: 546-51.
23. Bangham AD, Hill MW, Miller NGA. Preparation and use of liposomes as models of biological membranes. *Methods Membr Biol.* 1974;1: 61-8.
24. Benoit JP, Faisant N *et al.* Development of microspheres for neurological disorders: from basics to clinical applications. *J Control Release.* 2000; 65: 285-96
25. Bellavance MA, Poirier MB, Fortin D. Uptake and intracellular release kinetics of liposome formulations in glioma cells. *Int J Pharm.* 2010; 395: 251-9.
26. Berger J, Reist M, Mayer JM, *et al.* Structure and interactions in covalently and ionically crosslinked chitosan hydrogels for biomedical applications. *Eur J Pharm Biopharm.* 2004; 57:19-34.

27. Betageri GV, Parsons DL. Drug encapsulation and release from multilamellar and unilamellar liposomes. *Int J Pharm.* 1992. 81: 235-41.
28. Bharali DJ, Khalil M, Gurbuz M, *et al.* Nanoparticles and cancer therapy: a concise review with emphasis on dendrimers. *Int J Nanomedicine.* 2009; 4: 1-7.
29. Bharali DJ, Klejbor I, Stachowiak EK, *et al.* Organically modified silica nanoparticles: A nonviral vector for *in vivo* gene delivery and expression in the brain. *PNAS USA.* 2005; 102:11539-44.
30. Bhattarai N, Edmondson D, Veiseh O, *et al.* Electrospun chitosan-based nanofibers and their cellular compatibility. *Biomaterials.* 2005; 26:6176-84.
31. Bhardwaj N, Kundu SC. Electrospinning: a fascinating fiber fabrication technique. *Biotechnol Adv.* 2010; 28: 325-47.
32. Bhattarai N, Gunn J, Zhang M. Chitosan-based hydrogels for controlled, localized drug delivery. *Adv Drug Deliv Rev.* 2010; 62:83-99.
33. Briganti E, Spiller D, Mirtelli C, *et al.* A composite fibrin-based scaffold for controlled delivery of bioactive proangiogenic growth factors. *J Control Release.* 2010; 142:14-21.
34. Boland K, Manias K, Perlmutter H. Specificity in recognition of amyloid beta peptide by the serpin-enzyme complex receptor in hepatoma cells and neuronal cells. *J Biol Chem.* 1992; 270: 2802-28.
35. Bourke SL, Al-Khalili M, Briggs T, *et al.* A photo-crosslinked poly(vinyl alcohol) hydrogel growth factor release vehicle for wound healing applications. *AAPS PharmSciTech.* 2003; 5:1-11.
36. Brookmeyer R, Johnson E, Ziegler-Graham K, *et al.* Forecasting the global burden of Alzheimer's disease. *Alzheimer dementia.* 2007; 3: 186-91.

37. Brookmeyer R, Evans DA, Hebert L, *et al.* National estimates of the prevalence of Alzheimer's disease in the United States. *Alzheimer's Dementia*. 2011; 7: 61-73.
38. Bruttel P, Schlink R. Water determination by KF titration. *Metrohm Monography*. 2003: 4-11.
39. Budai L, Hajdu M, Budai M, *et al.* Gels and liposomes in optimized ocular drug delivery: studies on ciprofloxacin formulations. *Int J Pharm*. 2007; 343: 34-40.
40. Burke SA, Ritter-Jones M, Lee BP, *et al.* Thermal gelation and tissue adhesion of biomimetic hydrogels. *Biomed Mater*. 2007; 2: 203-10.
41. Bush AI. Metal complexing agents as therapies for Alzheimer's disease. *Neurobiol Aging*. 2002; 23: 1031-8.
42. Bush AI, Tanzi RE. Therapeutics for Alzheimer's disease based on the metal hypothesis. *Neurotherapeutics*. 2008; 5: 421-32.
43. Bussière T, Bard F, Barbour R, *et al.* Morphological characterization of thioflavin-s positive amyloid plaques in transgenic Alzheimer mice and effect of passive A β immunotherapy on their clearance. *Am J Pathol*. 2004; 165:987-95.
44. Campoli-Richards DM, Monk JP, Price A, *et al.* Ciprofloxacin. A review of its antibacterial activity, pharmacokinetic properties and therapeutic use. *Drugs*. 1988; 35: 373-447.
45. Cattell L, Ceruti M, Dosio F. From conventional to stealth liposomes: a new frontier in cancer chemotherapy. *J Chemotherapy*. 2004; 16: 94-6.
46. Chaudhry NA, Flynn HW, Murray TG, *et al.* Emerging ciprofloxacin-resistant *Pseudomonas aeruginosa*. *American J Ophthalmol*. 1999; 128: 509-10.

47. Chatterjee K, Hung S, Kumar G, *et al.* Time-dependent effects of pre-aging 3D polymer scaffolds in cell culture medium on cell proliferation. *J Functional Biomater.* 2012; 3: 372-8.
48. Chen C, Han D, Cai C, *et al.* An overview of liposome lyophilization and its future potential. *J Control Release.* 2010; 142: 299-311.
49. Chen H, Shana ZH. Stabilization of collagen by crosslinking with oxazolidine E-resorcinol. *Int J Bio Macromol.* 2010; 46: 535-9.
50. Cheng F, Choy YB, Choi H, *et al.* Modeling of small-molecule release from crosslinked hydrogel microspheres: effect of crosslinking and enzymatic degradation of hydrogel matrix. *Int J Pharm.* 2011; 403: 90-5.
51. Cheng K, Lai Y, Kisaalita WS. Three-dimensional polymer scaffolds for high through put cell-based assay systems. *Biomater.* 2008, 29: 2802-12.
52. Chesler M. Regulation and modulation of pH in the brain. *Physiol Rev.* 2003. 83; 1183-1221.
53. Chikha GG, Li WM, Schutze-Redelmeier MP, *et al.* Attaching histidine-tagged peptides and proteins to lipid-based carriers through use of metal-ion-chelating lipids. *Biochim Biophys Acta.* 2002; 1567: 204-12.
54. Christman KL, Vardanian AJ, Fang Q, *et al.* Injectable fibrin scaffold improves cell transplant survival, reduces infarct expansion, and induces neovasculature formation in ischemic myocardium. *J Am Coll Cardiol.* 2004; 44: 654-60.
55. Cho M, Niles A, Huang R, *et al.* A bioluminescent cytotoxicity assay for assessment of membrane integrity using a proteolytic biomarker. *Toxicol In vitro.* 2008. 22, 1099-106.

56. Choonara YE, Pillay V, Ndesendo VMK, *et al.* Polymeric emulsion and crosslink-mediated synthesis of super-stable nanoparticles as sustained-release anti-tuberculosis drug carriers. *Colloids Surf B: Biointerfaces*. 2011; 87: 243-54.
57. Chung HJ, Kim GW, Kim CH. Fabrication of porous chitosan scaffold in order to improve biocompatibility. *J Physics Chem Solids*. 2008; 69: 1573-6.
58. Chung HJ, Park TG. Surface engineered and drug releasing pre-fabricated scaffolds for tissue engineering. *Adv Drug Deliv Rev*. 2007; 59: 249-62.
59. Chung TW, Huang YY, Tsai YL, *et al.* Effects of solvent evaporation rate on the properties of protein-loaded PLLA and PDLLA microspheres fabricated by emulsion-solvent evaporation process. *J Microencapsulate*. 2002; 19: 463-71.
60. Chung TW, Yang MC, Tsai WJ. A fibrin encapsulated liposomes-in-chitosan matrix (FLCM) for delivering water-soluble drugs: influences of the surface properties of liposomes and the crosslinked fibrin network. *Int J Pharm*. 2006; 311: 122-9.
61. Citron M. Beta-secretase as a target for the treatment of Alzheimer's disease. *J Neurosci Res*. 2002; 70: 373-9.
62. Conway M, Holoman S, Jones L, *et al.* Selecting and using chelating agents. *J Chem Eng*. 1999; 106: 86-90.
63. Cui Z, Lockman PR, Atwood CS, *et al.* Novel d-penicillamine carrying nanoparticles for metal chelation therapy in Alzheimer's and other CNS diseases. *Eur J Pharm Biopharm*. 2005; 59: 263-72.
64. Cummings JL. Alzheimer's disease. *N Engl J Med*, 2004; 351:56-67.

65. Dai C, Wang B, Zhao H, *et al.* Preparation and characterization of liposomes-in-alginate (LIA) for protein delivery system. *Colloids and Surfaces B.* 2006; 47: 205-10.
66. Damen J, Regts J, Scherphof G. Transfer and exchange of phospholipid between small unilamellar liposomes and rat plasma high density lipoproteins. Dependence on cholesterol content and phospholipid composition. *Biochim Biophys Acta.* 1981; 665: 538-45.
67. Danysz W, Parsons CG. The NMDA receptor antagonist memantine as a symptomatic and neuroprotective treatment for Alzheimer's disease: preclinical evidence. *Int J Geriatr Psychiatry.* 2003; 18:S23-S32.
68. Dass CR, Choong PFM. Selective gene delivery for cancer therapy using cationic liposomes: *in vivo* proof of applicability. *J Control Release.* 2006; 113: 155-63.
69. Davidenko N, Campbell JJ, Thian ES, *et al.* Collagen-hyaluronic acid scaffolds for adipose tissue engineering. *Acta Biomaterialia.* 2010; 6: 3957-68.
70. Daxiong H, Haiyan W, Yang Y. Molecular modeling of zinc and copper binding with Alzheimer's amyloid b-peptide. *Biometals.* 2008; 21: 189-96.
71. De Boer AG, Gaillard PJ. Drug targeting to the brain. *Ann Rev Pharmacol Toxicol.* 2007; 47: 323-55.
72. De Felice FG, Vieira MN, Saraiva LM, *et al.* Targeting the neurotoxic species in Alzheimer's disease: inhibitors of A β oligomerization. *FASEB J.* 2004; 18: 1366-72.
73. De Groot CJ, Cadée JA, Koten JW, *et al.* Therapeutic efficacy of IL-2-loaded hydrogels in a mouse tumor model. *Int J Cancer.* 2002; 98: 134-40.

74. Delacourte A. Tauopathies: recent insights into old diseases. *Folia Neuropathol.* 2005; 43: 244-57.
75. Delobette S, Privat A, Maurice T. *In vitro* aggregation facilitates β -amyloid peptide (25–35) induced amnesia in the rat. *Eur J Pharmacol* 1997;319:1-4.
76. DeMerlis CC, Schoneker DR. Review of the oral toxicity of polyvinyl alcohol (PVA). *Food Chem Toxicol.* 2003; 41:319-326.
77. Deligkaris K, Tadele TS, Olthuis W, *et al.* Hydrogel-based devices for biomedical applications. *Sens Actuators B Chem.* 2010; 147:765-74.
78. Des Rieux A, Shikanov A, Shea LD. Fibrin hydrogels for non-viral vector delivery *in vitro*. *J Control Release.* 2009; 136: 148-54.
79. De Souza Costa-Júnior E, Pereira MM, Mansur HS. Properties and biocompatibility of chitosan films modified by blending with PVA and chemically crosslinked. *J Mater Sci Mater Med.* 2009; 20: 553-61.
80. De Strooper B, Annaert W. Proteolytic processing and cell biological functions of the amyloid precursor protein. *J Cell Sci.* 2000; 113: 1857-70.
81. Dhoot NO, Wheatley MA. Microencapsulated liposomes in controlled drug delivery: strategies to modulate drug release and eliminate the burst effect. *J Pharm Sci.* 2003; 92: 679-89.
82. DiTizio V, Ferguson GW, Mittelman MW, *et al.* A liposomal hydrogel for the prevention of bacterial adhesion to catheters. *Biomater.* 1998; 19: 1877-84.
83. Drummond DC, Noble CO, Hayes ME, *et al.* Pharmacokinetics and *in vivo* drug release rates in liposomal nanocarrier development. *J Pharm Sci.* 2008; 97: 4696-740.

84. Dong J, Atwood CS, Anderson VE, *et al.* Metal binding and oxidation of amyloid-beta within isolated senile plaque cores: Raman microscopic evidence. *Biochem J.* 2003; 42: 2768-73.
85. Dong W, Haung F, Fan W, *et al.* Differential effects of melatonin on amyloid- β peptide 25-35 induced mitochondrial dysfunction in hippocampal neurons at different stages of culture. *J. Pineal Res.* 2010; 48:117-25.
86. Dos Reis EF, Campos FS, Lage AP, *et al.* Synthesis and characterization of poly (vinyl alcohol) hydrogels and hybrids for rMPB70 protein adsorption. *Mater Res.* 2006; 9:185-91.
87. Duarte ARC, Mano JF, Reis RL. Preparation of chitosan scaffolds for tissue engineering using supercritical fluid technology. *Mater Sci Forum.* 2010; 636-7.
88. Duce JA, Bush AI. Biological metals and Alzheimer's disease: implications for therapeutics and diagnostics. *Prog Neurobiol.* 2010; 92: 1-18.
89. Ducongé F, Pons T, Pestourie C, *et al.* Fluorine-18-labeled phospholipid quantum dot micelles for *in vivo* multimodal imaging from whole body to cellular scales. *Bioconjug Chem.* 2004; 19: 1921-6.
90. Durrani AM, Davies NM, Thomas M, *et al.* Pilocarpine bioavailability from a mucoadhesive liposomal ophthalmic drug delivery system. *Int J Pharm.* 1992; 88: 409-15.
91. Du toit LC, Govender T, Pillay V, *et al.* Investigating the effect of polymeric approaches on circulation time and physical properties of nanobubbles. *Pharm Res.* 2011; 28(3): 494-504.
92. Eglin D, Alini M. Degradable polymeric materials for osteosynthesis: tutorial. *Eur Cells & Mater.* 2008; 16:80-91.

93. Eniola AO, Hammer DA. Characterization of biodegradable drug delivery vehicles with the adhesive properties of leukocytes II: effect of degradation on targeting activity. *Biomaterials*. 2005; 26: 661-70.
94. Epstein-Barash H, Orbey G, Polat BE, *et al.* A microcomposite hydrogel for repeated on-demand ultrasound-triggered drug delivery. *Biomater*. 2010; 31: 5208-17.
95. Erkinjuntti T. Treatment options: the latest evidence with galantamine (ReminylR). *J Neurol Sci*. 2002; 203: 125-30.
96. Exner AA, Saidel GM. Drug-eluting polymer implants in cancer therapy. *Expert Opinion on Drug Del*. 2008; 5: 775-88.
97. Fang JY, Hwang TL, Huang YL. Liposomes as vehicles for enhancing drug delivery via skin routes. *Cur Nanosci*. 2006; 2: 55-70.
98. Feaga HA, Maduka RC, Foster MN, *et al.* Affinity of cup for the copper-binding domain of the amyloid- β peptide of Alzheimer's disease. *Inorg Chem*. 2011; 50: 1614-8.
99. Feldman LJ, Steg G. Optimal techniques for arterial gene transfer. *Cardiovascul Res*. 1997; 35: 391-404.
100. Felgner PL, Gadek TR, Holm M, *et al.* Lipofection: a highly efficient, lipid-mediated DNA-transfection procedure. *PNAS USA*. 1987; 84: 7413-17.
101. Fernandes SP, Edwards TM, *et al.* HIV-1 protein gp120 rapidly impairs memory in chicks by interrupting the glutamate-glutamine cycle. *Neurobiol Learn Mem*; 2007; 87: 1-8.
102. Frank MG, Barrientos RM, Thompson BM, *et al.* IL-1RA injected intra-cisterna magna confers extended prophylaxis against lipopolysaccharide-induced

- neuroinflammatory and sickness responses. *J Neuroimmunol.* 2012; 252: 33-9.
103. Frank MM. The reticuloendothelial system and blood stream clearance. *J Lab Clin Med.* 1993; 122: 487-8.
104. Frautschy SA, Cole GM, Baird A. Phagocytosis and deposition of vascular beta-amyloid in rat brains injected with Alzheimer beta-amyloid. *Am J Pathol.* 1992; 140:1389-99.
105. Frei B. Reactive oxygen species and antioxidant vitamins, mechanisms of action. *AM J Med.* 1994; 26: 5S -13
106. Foster FS, Hossack J, Adamson SL. Micro-ultrasound for preclinical imaging. *Interface Focus.* 2011; 1: 576-601.
107. Gabizon A, Papahadjopoulos D. Liposome formulations with prolonged circulation time in blood and enhanced uptake by tumors. *PNAS USA.* 1988; 85: 6949-53.
108. Gao C, Liu M, Chen S, *et al.* Preparation of oxidized sodium alginate-graft-poly((2-dimethylamino) ethyl methacrylate) gel beads and *in vitro* controlled release behavior of BSA. *Int J Pharm.* 2009; 371: 16-24.
109. Gao HM, Hong JS. Why neurodegenerative diseases are progressive: uncontrolled inflammation drives disease progression. *Trends Immunol.* 2008; 29: 357-65.
110. Gella A, Durany N. Oxidative stress in Alzheimer disease, *Cell Adh Migr.* 2009; 13: 88-93.
111. George M, Abraham TE. Polyionic hydrocolloids for the intestinal delivery of protein drugs: alginate and chitosan-a review. *J Control Release.* 2006; 114: 1-14.

112. Ghaffari A, Oskoui M, Helali K, *et al.* Pectin/chitosan/Eudragit RS mixed-film coating for bimodal drug delivery from theophylline pellets: preparation and evaluation. *Acta Pharmaceutica*. 2006; 56: 299-310.
113. Greene LA, Tischler AS. Establishment of a noradrenergic clonal line of rat adrenal pheochromocytoma cells which respond to nerve growth factor. *PNAS USA*. 1974; 73: 2424-8.
114. Griesenbach U, Chonn A, Cassady R, *et al.* Comparison between intratracheal and intravenous administration of liposome-DNA complexes for cystic fibrosis lung. *Gene Therapy*. 1998; 5: 181-8.
115. Gobin AS, Rhea R, Newman RA, *et al.* Silk fibroin-coated liposomes for long-term and targeted drug delivery. *Int J Nanomedicine*. 2006; 1: 81-7.
116. Gombotz WR, Wee SF. Protein release from alginate matrices. *Adv Drug Deliv Rev*. 1998; 31: 267-85.
117. Goyal P, Goyal K, Kumar SGV, *et al.* Liposomal drug delivery systems-clinical applications. *Acta Pharmaceutica*. 2005; 55: 1-25.
118. Haesslein A, Ueda H, *et al.* Long-term release of fluocinolone acetonide using biodegradable fumarate-based polymers. *J Control Release*. 2006; 114: 251-60.
119. Hafeman AE, Zienkiewicz KJ, Carney E, *et al.* Local delivery of tobramycin from injectable biodegradable polyurethane scaffolds. *J Biomater Sci*. 2010; 21: 95-112.
120. Hang L, Lee PL, Yiannoussos CT, *et al.* A multicenter *in vivo* proton-MRS study of HIV-associated dementia and its relationship to age. *Neuroimage*. 2004; 23: 1336-47.

121. Hara M, Miyake J. Calcium alginate gel-entrapped liposomes. *Mater Sci Eng C*. 2001; 17: 101-5.
122. Haran G, Cohen R, Bar LK, *et al*. Transmembrane ammonium sulfate gradients in liposomes produce efficient and stable entrapment of amphipathic weak bases. *Biochim Biophys Acta*. 1993. 1151, 201-15.
123. Harashima H, Sakata K, Funato K, *et al*. Enhanced hepatic uptake of liposomes through complement activation depending on the size of liposomes. *Pharm Res*. 1994; 11: 402-6.
124. Harilall S, Choonara YE, Modi G, *et al*. Design and pharmaceutical evaluation of a nano-enabled crosslinked multipolymeric scaffold for prolonged intracranial release of zidovudine. *J Pharm Sci*. 2013; 16: 470-85.
125. Hartwell R, Leung V, Chavez-Munoz C, *et al*. A novel hydrogel-collagen composite improves functionality of an injectable extracellular matrix. *Acta Biomater*. 2011; 7: 3060-9.
126. Hao S, Li L, Yang X, *et al*. The characteristics of gelatin extracted from sturgeon (*Acipenser baeri*) skin using various pretreatments. *Food Chem*. 2009; 115: 124-8.
127. Hauptmann S, Keil U, Scherping I, *et al*. Mitochondrial dysfunction in sporadic and generic Alzheimer's disease. *Exp Gerontol*. 2004; 41, 668-73.
128. Heinemann C, Heinemann S, Lode A, *et al*. *In vitro* evaluation of textile chitosan scaffolds for tissue engineering using human bone marrow stromal cells. *Biomacromol*. 2009; 10: 1305-10.
129. Heinrich M, Teoh LH. Galanthamine from snowdrop-the development of a modern drug against Alzheimer's disease from local Caucasian knowledge. *J Ethnopharmacol*. 2004; 92, 147-62.

130. Hejazi R, Amiji M. Chitosan-based gastrointestinal delivery systems. *J Control Release*. 2003; 89:151-65.
131. Hennik WE, van Nostrum CF. Novel crosslinking methods to design hydrogels. *Adv Drug Deliv Rev*. 2002; 54:13-36.
132. Hernot S, Klibanov AL. Microbubbles in ultrasound-triggered drug and gene delivery. *Adv Drug Deliv Rev*. 2008; 60: 1153-66.
133. Hoare TR, Kohane DS. Hydrogels in drug delivery: progress and challenges. *Polym*. 2008; 49:1993-2007.
134. Hogan B, Constantini F, Lacy E. *Manipulating the Mouse Embryo: A Laboratory Manual*. Cold Spring Harbor Laboratory, Cold Spring Harbor (NY), 1986.
135. Holladay C, Keeney M, Greiser U, *et al*. A matrix reservoir for improved control of non-viral gene delivery. *J Control Release*. 2009; 136: 220-5.
136. Holland TA, Tabata Y, Mikos AG. Dual growth factor delivery from degradable oligo(poly(ethylene glycol) fumarate) hydrogel scaffolds for cartilage tissue engineering. *J Control Release*. 2005; 101: 111-25.
137. Horiike S, Matsuzawa S, Yamaura K. Preparation of chemically crosslinked gels with maleate-denatured poly(vinyl alcohol) and its application to drug release. *J Applied Polym Sci*. 2002; 84: 1178-84.
138. Horn MM, Martins VCA, Plepis AMG. Effects of starch gelatinization and oxidation on the rheological behavior of chitosan and starch blends. *Polym Int*. 2011; 60: 920-3.

139. Hornig S, Bunjes H, Heinze H. Preparation and characterization of nanoparticles based on dextran-drug conjugates. *J Colloid Interface Sci.* 2009; 338: 56-62.
140. Hosny KM. Ciprofloxacin as ocular liposomal hydrogel. *AAPS PharmSciTech.* 2010; 11: 241-6.
141. Hosny KM. Optimization of gatifloxacin liposomal hydrogel for enhanced transcorneal permeation. *J Liposome Res.* 2010; 20: 31-7.
142. Hossen MN, Kajimoto K, Akita H, *et al.* Ligand-based targeted delivery of a peptide modified nanocarrier to endothelial cells in adipose tissue. *J Control Release.* 2010; 147: 261-8.
143. Huang NF, Chu J, Lee RJ, *et al.* Biophysical and chemical effects of fibrin on mesenchymal stromal cell gene expression. *Acta Biomaterialia.* 2010; 6: 3947-56.
144. Tsai HG, Lee J, Tseng S, *et al.* Folding and membrane insertion of amyloid-beta (25-35) peptide and its mutants: Implications for aggregation and neurotoxicity. *Proteins*, 2010, 1-17.
145. Hynes RO. A re-evaluation of integrins as regulators of angiogenesis. *Nature Med.* 2002; 8: 918-21.
146. Illum L. Nasal drug delivery-possibilities, problems and solutions. *J Control Release.* 2003; 87: 187-98.
147. Immordino ML, Dosio F, Cattel L. Stealth liposomes: review of the basic science, rationale, and clinical applications, existing and potential. *Int J Nanomed.* 2006; 1: 297-315.
148. Iversen LL, Mortishire-Smith RJ, Pollack SJ, *et al.* The toxicity *in vitro* of beta-amyloid protein. *Biochem J.* 1995; 311: 1-16.

149. Janssen AP, Schiffelers RM, Hagen TL, *et al.* Peptide-targeted PEG-liposome in anti-angiogenic therapy. *Int J Pharm Pharm Sci.* 2003; 254: 55-8.
150. Jauch A, Fsadni M, Gamba G. Meta-analysis of six clinical phase III studies comparing lomefloxacin 0.3% eye drops twice daily to five standard antibiotics in patients with acute bacterial conjunctivitis. *Clin Exp Ophthalmol.* 1999; 237: 705-13
151. Jeon O, Bouhadir KH, Mansour JM, *et al.* Photocrosslinked alginate hydrogels with tunable biodegradation rates and mechanical properties. *Biomater;* 30: 2724-34.
152. Ji C, Barrett A, Poole-Warren LA, *et al.* The development of a dense gas solvent exchange process for the impregnation of pharmaceuticals into porous chitosan. *Int J Pharm.* 2010; 391: 187-96.
153. Jin J, Song M. Chitosan and chitosan-PEO blend membranes crosslinked by genipin for drug release. *J Appl Polym Sci.* 2006; 102: 436-44.
154. Jin T, Zhu J, Wu F, *et al.* Preparing polymer-based sustained-release systems without exposing proteins to water-oil or water-air interfaces and cross-linking reagents. *J Control Release.* 2008; 128: 50-9.
155. Johnsson M, Edwards K. Liposomes, disks, and spherical micelles: aggregate structure in mixtures of gel phase phosphatidylcholines and poly(ethylene glycol)-phospholipids. *Biophysical J.* 2003; 85: 3839-47.
156. Joslin G, Fallon RJ, Bullock J, *et al.* The Sec receptor recognizes a pentapeptide neodomain of alpha 1-antitrypsin-proteas complexes. *J Bio Chem.* 1991; 266: 11282-8.
157. Junginger HE, Verhoef JC. Macromolecules as safe penetration enhancers for hydrophilic drugs-a fiction. *Pharm Sci Technol.* 1998; 1: 370-6.

158. Kamidate T, Hashimoto Y, Tani H, *et al.* Uptake of transition metal ions using liposome containing dicetylphosphate as a ligand. *Anal Sci.* 2002; 18: 273-6.
159. Kaneda Y. Virosomes: evolution of the liposome as a targeted drug delivery system. *Adv Drug Deliv Rev.* 2000; 43: 197-205.
160. Kang H, O'Donoghue MB, Liu H, *et al.* A liposome-based nanostructure for aptamer directed delivery. *Chem Commun.* 2010; 46: 249-51.
161. Karazhiyan H, Razavi SMA, Phillips GO, *et al.* Rheological properties of *Lepidium sativum* seed extract as a function of concentration, temperature and time. *Food Hydrocolloids*, 2009; 23: 2062-8.
162. Kas HS. Chitosan: properties, preparations and application to microparticulate systems. *J Microencapsul.* 1997; 14: 689-711.
163. Kawakami K, Nishihara Y, Hirano K. Effect of hydrophilic polymers on physical stability of liposome dispersions. *J Physical Chem B.* 2001; 105: 2374-85.
164. Kean T, Thanou M. Biodegradation, biodistribution and toxicity of chitosan. *Adv Drug Deliv Rev.* 2010; 62: 3-11.
165. Ke X, Bei JH, Zhang Y, *et al.* *In vitro* and *in vivo* evaluation of sanguinarine liposomes prepared by a remote loading method with three different ammonium salts. *Pharmazie.* 2011; 66: 258-63.
166. Khanna O, Moya ML, Opara EC, *et al.* Synthesis of multilayered alginate microcapsules for the sustained release of fibroblast growth factor-1. *J Biomedical Mater Res Part A.* 2010; 95: 632-40.
167. Kibat PG, Igari Y, Wheatley MA, *et al.* Enzymatically activated microencapsulated liposomes can provide pulsatile drug release. *FASEB J.* 1990; 4: 2533-9.

168. Kikuchi M, Matsumoto HN, Yamada Y, *et al.* Glutaraldehyde cross-linked hydroxyapatite and collagen self-organized nanocomposites. *Biomater.* 2004; 25: 63-9.
169. Kim ES, Lu C, Khuri FR, *et al.* A phase II study of STEALTH cisplatin (SPI-77) in patients with advanced non small cell lung cancer. *Lung Cancer.* 2001; 34: 427-32.
170. Kim BK, Doh KO, Nam JH, *et al.* Synthesis of novel cholesterol-based cationic lipids for gene delivery. *Bioorganic Medicinal Chem Lett.* 2009; 19: 2986-9
171. Kim MS, Choi YJ, Noh I, *et al.* Synthesis and characterization of in situ chitosan-based hydrogel via grafting of carboxyethyl acrylate. *J Biomed Mater Res A.* 2007; 83: 674-82.
172. Kirby C, Clarke J, Gregoriadis G. Effect of the cholesterol content of small unilamellar liposomes on their stability *in vivo* and *in vitro*. *Biochem J.* 1980; 186: 591-8.
173. Kizelsztejn P, Ovadia H, Garbuzenko O, *et al.* Pegylated nanoliposomes remote-loaded with the antioxidant tempamine ameliorate experimental autoimmune encephalomyelitis. *J Neuroimmunol.* 2009; 213: 20-5.
174. Klapperich CM, Bertozzi CR. Global gene expression of cells attached to a tissue engineering scaffold. *Biomater.* 2004; 25: 5631-41.
175. Klunk WE, Bacskai BJ, Mathis CA, *et al.* Imaging A β plaques in living transgenic mice with multiphoton microscopy and methoxy-X04, a systemically administered Congo red derivative. *J Neuropathol Exp Neurol.* 2002 61:797-805.
176. Krebs MD, Salter E, Chen E, *et al.* Calcium phosphate-DNA nanoparticle gene delivery from alginate hydrogels induces *in vivo* osteogenesis. *J Biomed Mater Res Part A.* 2010; 92: 1131-8.

177. Kroll RA, Neuwelt EA. Outwitting the blood brain barrier for therapeutic purposes: osmotic opening and other means. *Neurosurgery*. 1998; 42: 1083-99.
178. Krown SE, Northfelt DW, Osoba D, *et al.* Use of liposomal anthracyclines in Kaposi's sarcoma. *Seminars in Oncol*. 2004; 31: 36-52.
179. Kojima C, Tsumura S, Harada A, *et al.* A collagen mimics dendrimer capable of controlled release. *J AM Chem Soc*. 2009; 131: 6052-3
180. Kong HJ, Kim ES, Huang YC, *et al.* Design of biodegradable hydrogel for the local and sustained delivery of angiogenic plasmid DNA. *Pharm Res*. 2008; 25: 1230-8.
181. Kong J, Yu S. Fourier transforms infrared spectroscopic analysis of protein secondary structures. *Acta Biochim Biophys Sin*. 2007; 39:549-59.
182. Kowalska A. The beta-amyloid cascade hypothesis: a sequence of events leading to neurodegeneration in Alzheimer's disease. *Neurol Neurochir Pol*. 2004; 38: 405-11.
183. Kulkarni M, Breen A, Greiser U, *et al.* Fibrin-lipoplex system for controlled topical delivery of multiple genes. *Biomacromol*. 2009; 10: 1650-4.
184. Kulkarni M, Greiser U, O'Brien T, *et al.* Liposomal gene delivery mediated by tissue-engineered scaffolds. *Trends Biotechnol*. 2010; 28: 28-36
185. Kumar CC, Armstrong L, Yin Z, *et al.* Targeting integrins $\alpha\beta$ and $\alpha\beta$ for blocking tumor-induced angiogenesis. *Adv Exp Med Bio*. 2000; 476: 169-80.
186. Kumar P, Pillay V, Choonara YE, *et al.* In silico theoretical molecular modeling for Alzheimer's disease: the nicotinecurcumin paradigm in neuroprotection and neurotherapy. *Int J Mol Sci*. 2011; 12: 694-724.

187. Kuwahara K, Yang Z, Slack GC, *et al.* Cell delivery using an injectable and adhesive transglutaminase-gelatin gel. *Tissue Eng Part C.* 2010; 16: 609-18.
188. Lecanu L, Greeson J, Papadopoulos V: Beta-amyloid and oxidative stress jointly induce neuronal death, amyloid deposits, gliosis, and memory impairment in the rat brain. *Pharmacol.* 2006; 76:19-33.
189. Lee VM, Goedert M, Trojanowski JQ. Neurodegenerative tauopathies. *Annu Rev Neurosci.* 2001; 24: 1121-59.
190. Lee WY, Chang YH, Yeh YC, *et al.* The use of injectable spherically symmetric cell aggregates self-assembled in a thermo-responsive hydrogel for enhanced cell transplantation. *Biomater.* 2009; 30: 5505-13.
191. Lehman KM. Practical course in film coating of pharmaceutical dosage forms with eudragit. Darmstadt, *Pharm Polym.* 2001: 8-15.
192. Lentacker I, Wang N, Vandenbroucke RE, *et al.* Ultrasound exposure of lipoplex loaded microbubbles facilitates direct Cytoplasmic entry of the Lipoplexes. *Mol Pharm.* 2009; 6: 457-67.
193. Lei P, Padmashali RM, Andreadis ST. Cell controlled and spatially arrayed gene delivery from fibrin hydrogels. *Biomater.* 2009; 30: 3790-9.
194. Liang X, Mao G, Ng KY. Mechanical properties and stability measurement of cholesterol containing liposome on mica by atomic force microscopy. *J Colloid Interface Sci.* 2004; 278: 53-62.
195. Lin HH, Ko SM, Hsu LR, *et al.* The preparation of norfloxacin-loaded liposomes and their invitro evaluation in pig's eye. *J Pharma Pharmacol.* 1996; 48: 801-5.

196. Lipton SA. The molecular basis of memantine action in Alzheimer's disease and other neurologic disorders: low-affinity, uncompetitive antagonism. *Curr Alzheimer Res.* 2005; 2: 155-65.
197. Liptay S, Weidenbach H, Adler G, Schmid RM. Colon epithelium can be transiently transfected with liposomes, calcium phosphate precipitation and DEAE dextran *in vivo*. *Digestion.* 1998; 59: 142-7.
198. Li SD, Huang L. Stealth nanoparticles: high density but sheddable PEG is a key for tumor targeting. *J Control Release.* 2010; 145: 178-81.
199. Li X, Ding L, Xu Y, et al. Targeted delivery of doxorubicin using stealth liposomes modified with transferrin. *Int J Pharm.* 2009; 373: 116-23.
200. Li X, Li Y, Zhanga S, et al. Preparation and characterization of new foam adsorbents of poly(vinyl alcohol), chitosan composites and their removal for dye and heavy metal from aqueous solution. *Chem Eng J.* 2012; 183: 88-97.
201. Li T, Shi XW, Du YM, et al. Quaternized chitosan/alginate nanoparticles for protein delivery. *J Biomed Mater Res Part A.* 2007; 83: 383-90.
202. Litvinchuk S, Lu Z, Rigler P, et al. Calcein release from polymeric vesicles in blood plasma and PVA hydrogel. *Pharm Res.* 2009; 26: 1711-7.
203. Liu G, Men P, Kudo W, et al. Nanoparticle-chelator conjugates as inhibitors of Amyloid- β aggregation and neurotoxicity: a novel therapeutic approach for Alzheimer's disease. *Neurosci Lett.* 2009; 455: 187-90.
204. Liu GP, Men P, Harris PL, et al. Nanoparticle iron chelators: a new therapeutic approach in Alzheimer disease and other neurologic disorders associated with trace metal imbalance. *Neurosci Lett.* 2006; 406: 189-93.

205. Liu X, Xu K, Yan M, *et al.* Protective effects of galantamine against A β induced PC12 cell apoptosis by preventing mitochondrial dysfunction and endoplasmic stress. *Neurochem Int.* 2010; 57: 588-99.
206. Liu Y, Miyoshi H, Nakamura M. Encapsulated ultrasound microbubbles: therapeutic application in drug/gene delivery. *J Control Release.* 2006; 114: 89-99.
207. Lovell MA, Robertson JD, Teesdale WJ, *et al.* Copper, iron and zinc in Alzheimer's disease senile plaques. *J Neurol Sci.* 1998; 158:47-52.
208. Lozano MM, Longo ML. Microbubbles coated with disaturated lipids and DSPE-PEG2000: phase behaviour, collapse transitions, and permeability. *Langmuir.* 2009; 25: 3705-12.
209. Lublin AL, Gandy S. Amyloid β oligomers: possible roles as key neurotoxicin in Alzheimer's disease. *Mt Sinai J Med.* 2010; 77: 43-9.
210. Lu Q, Hu K, Feng Q, *et al.* Growth of fibroblast and vascular smooth muscle cells in fibroin/collagen scaffold. *Mater Sci Eng C.* 2009; 29: 2239-45.
211. Lukyanov AN, Elbayoumi TA, Chakilam AR, *et al.* Tumor-targeted liposomes: doxorubicin loaded long-circulating liposomes modified with anti-cancer antibody. *J Control Release.* 2004; 100: 135-44.
212. Ma Q, Hu J, Wu W, *et al.* Characterization of copper binding to the peptide amyloid-b(1-16) associated with Alzheimer's Disease. *Biopolymers.* 2006; 83: 20-31.
213. Machluf M, Regev O, Peled Y, *et al.* Characterization of microencapsulated liposome systems for the controlled delivery of liposome-associated macromolecules. *J Control Release.* 1997; 43: 35-45.

214. Macquarrie DJ, Hardy JE. Applications of functionalized chitosan in catalysis. *Industrial Eng Chem Res.* 2005; 44: 8499-8520.
215. Magdesian MH, Giordano R, Ulrich H, *et al.* Infection by *Trypanosoma cruzi* identification of a parasite ligand and its host cell receptor. *J Biol Chem* 2001; 276: 19382-9.
216. Mahato RI. Water insoluble and soluble lipids for gene delivery. *Adv Drug Deliv Rev.* 2005; 57: 699-712.
217. Maia J, Ferreira L, Carvalho R, *et al.* Synthesis and characterization of new injectable and degradable dextran-based hydrogels. *Polym.* 2005; 46: 9604-14.
218. Mancini M, Vergara E, Salvatore G, *et al.* Morphological Ultrasound Micro-imaging of Thyroid in Living Mice. *Endocrinol.* 2009; 150:4810-15.
219. Manconi M, Sinico C, Valenti D, *et al.* Niosomes as carriers for tretinoin. I. Preparation and properties. *Int J Pharm.* 2002; 234: 237-48.
220. Mansur HS, Sadahira CM, Souza AN, *et al.* FTIR spectroscopy characterization of poly (vinyl alcohol) hydrogel with different hydrolysis degree and chemically cross-linked with glutaraldehyde. *Mater Sci Eng C.* 2008; 28: 539-48.
221. Marcellini M, Di Ciommo V, Callea F, *et al.* Treatment of Wilson's disease with zinc from the time of diagnosis in pediatric patients: a single-hospital, 10-year follow-up study. *J Lab Clin Med.* 2005;145: 139-43.
222. Marino T, Russo N, Toscano N, *et al.* On the metal ion (Zn(II), Cu (II)) coordination with beta-amyloid peptide: DFT computational study. *Interdiscipl Sci.* 2010; 2: 57-69.

223. Marston WA, Isala A, Hill RS, *et al.* Initial report of the use of an injectable porcine collagen-derived matrix to stimulate healing of diabetic foot wounds in humans. *Wound Repair Regen.* 2005; 13: 243-7.
224. Mastrobattista E, Koning GA, van Bloois L, *et al.* Functional characterization of an endosome-disruptive peptide and its application in cytosolic delivery of immunoliposome-entrapped proteins. *J Biol Chem.* 2002; 277 (30): 27135-43.
225. Martina M, Fortin J, Fournier L, *et al.* Magnetic targeting of rhodamine-labeled Superparamagnetic liposomes to Solid Tumors: *In vivo* Tracking by Fibered Confocal Fluorescence Microscopy. *Mol Imaging.* 2007; 6:140-6.
226. Mao S, Sun W, Kissel T. Chitosan-based formulations for delivery of DNA and siRNA. *Adv Drug Deliv Rev.* 2010; 62 12-27.
227. Matharu B, Gibson G, Parsons R, *et al.* Galantamine inhibits beta amyloid aggregation and cytotoxicity. *J Neurol Sci.* 2009; 280: 49-58.
228. Matricardi P, Cencetti C, Ria R, *et al.* Preparation and characterization of novel gellan gum hydrogels suitable for modified drug release. *Molecules.* 2009; 14: 3376-91.
229. McHugh AJ. The role of polymer membrane formation in sustained release drug delivery systems. *J Control Release.* 2005; 109: 211-21.
230. Medina OP, Zhu Y, Kairamo K. Targeted liposomal drug delivery in cancer. *Cur Pharm Design.* 2004; 10: 2981-9.
231. Mehvar R. Dextran for targeted and sustained delivery of therapeutic and imaging agents. *J Control Release.* 2000; 69: 1-25.

232. Mengual O, Meunier G, Cayre I, *et al.* Characterization of instability of concentrated dispersions by a new optical analyzer: the Turbiscan MA 1000. *Colloids Surf A: Physicochem Eng Aspects.* 1999; 152:111-23.
233. Meyenburg S, Lillie H, Panzner S, *et al.* Fibrin encapsulated liposomes as protein delivery system Studies on the *in vitro* release behavior. *J Control Release.* 2000; 69: 159-68.
234. Miller DL, Papayannopoulos IA, Styles J, *et al.* Peptide compositions of the cerebrovascular and senile plaque core amyloid deposits of Alzheimer's disease. *Arch Biochem Biophys.* 1993; 301: 41-52.
235. Modi G, Pillay V, Choonara YE. Advances in the treatment of neurodegenerative disorders employing nanotechnology. *Ann N Y Acad Sci.* 2010; 1184: 154-72.
236. Mohamed MI. Optimization of chlorphenesine mulgel formulation. *AAPS J.* 2004; 6: 1-7.
237. Mohan N, Nair PD. Novel porous, polysaccharide scaffolds for tissue engineering applications. *Trends Biomater Artific Organs.* 2005; 18: 219-24.
238. Mondal S, Bhattacharya P, Rahaman M, *et al.* A curative immune profile one week after treatment of Indian Kala-Azar patients predicts success with a short-course liposomal amphotericin B therapy. *PLoS Trop Dis.* 2010; 4.
239. Monshipouri M, Rudolph AS. Liposome encapsulated alginate: controlled hydrogel particle formation and release. *J Microencapsul.* 1995; 12: 117-27.
240. Morgan DM, Dong JJ, Jacob J, *et al.* Metal switch for amyloid formation: insight into the structure of the nucleus. *J Am Chem Soc.* 2002; 124: 12644-5.

241. Mourtas S, Fotopoulou S, Duraj S, *et al.* Liposomal drugs dispersed in hydrogels. Effect of liposome, drug and gel properties on drug release kinetics. *Colloids Surfaces B.* 2007; 55: 212-21.
242. Mufamadi MS, Pillay V, Choonara YE, *et al.* Review on composite liposomal technologies for specialized drug delivery. *J Drug Deliv.* 2011; 3: 1-19.
243. Mufamadi MS, Choonara YE, Kumar P, *et al.* Surface-engineered nanoliposomes by chelating ligands for modulating the neurotoxicity associated with amyloid aggregates of Alzheimer's disease. *Pharm Res.* 2012; 29: 3075-89.
244. Mufamadi MS, Choonara YE, Kumar P, *et al.* Ligand-functionalized nanoliposomes for targeted delivery of Galantamine. *Int J Pharm.* 2013; 448:267-81.
245. Mulik R, Kulkarni V, Murthy SR. Chitosan-based thermosensitive hydrogel containing liposomes for sustained delivery of cytarabine. *Drug Dev Ind Pharm.* 2009; 35: 49-56.
246. Nakamura S, Murayama N, Noshita T, *et al.* Progressive brain dysfunction following intracerebroventricular infusion of beta(1-42)- amyloid peptide. *Brain Res.* 2001; 912:128-136.
247. Nakano K, Tozuka Y, Takeuchi H. Effect of surface properties of liposomes coated with a modified polyvinyl alcohol (PVA-R) on the interaction with macrophage cells. *Int J Pharm* 2008; 354: 174-9.
248. Nair NG, Perry G, Smith MA, *et al.* NMR studies of zinc, copper, and iron binding to histidine, the principal metal ion complexing site of amyloid- β peptide. *J Alzheimer's Dis.* 2010; 20: 57-66.

249. Nallamothe R, Wood GC, Pattillo CB, *et al.* A tumor vasculature targeted liposome delivery system for combretastatin A4: design, characterization, and *in vitro* evaluation. *AAPS PharmSciTech.* 2006; 7: E1-E10.
250. Narita A, Takahara M, Ogino T, *et al.* Effect of gelatin hydrogel incorporating fibroblast growth factor 2 on human meniscal cells in an organ culture model. *The knee.* 2009; 16: 285-9.
251. Ngwuluka NC, Pillay V, Choonara YE, *et al.* Fabrication, Modelling and characterization of multi-crosslinked methacrylate copolymeric nanoparticles for oral drug delivery. *Int J Mol Sci.* 2011; 12: 6194-225.
252. Nihouannen LD, Guehennec LL, Rouillon T, *et al.* Micro-architecture of calcium phosphate granules and fibrin glue composites for bone tissue engineering. *Biomater.* 2006; 27: 2716-22.
253. Nishikawa K, Arai H, Inoue K. Scavenger receptor mediated uptake and metabolism of lipid vesicles containing acidic phospholipids by mouse peritoneal macrophages. *J Bio Chem.* 1990; 265: 5226-31.
254. Nixon JR, Yeung VW. Preparation of microencapsulated liposomes, II. Systems containing nylon-gelatin and nylon-gelatin-acacia walling material. *J Microencapsulation.* 1989; 6: 43-52.
255. Nobs L, Buchegger F, Furny R, *et al.* Current methods for attaching targeting ligands to liposomes and nanoparticles. *J Pharm Sci.* 2004; 93: 1980-92.
256. Nowacek A, Kosloski LM, Gendelman HE. Neurodegenerative disorders and nanoformulated drug development: Executive summary. *Nanomedicine.* 2009; 4: 541-55.
257. Ofokansi K, Winter G, Fricker G, *et al.* Matrix loaded biodegradable gelatin nanoparticles as new approach to improve drug loading and delivery. *Eur J Pharm Biopharm.* 2010; 76: 1-9.

258. Opazo C. Transition metals and Alzheimer's disease. *Rev Esp Geriatr Gerontol.* 2005; 40:365-70.
259. Paleos CM, Tsiourvas D, Sideratou Z. Hydrogen bonding interactions of liposomes simulating cell-cell recognition, A review. *Orig Life Evol Biosph.* 2004; 34: 195-213.
260. Pan H, Kopecek J. Multifunctional water-soluble polymers for drug delivery. *Curr Nanosci.* 2005; 1: 47-64.
261. Pardridge WM. Blood brain barrier genomics and the use of endogenous transporters to cause drug penetration into the brain. *Curr Opin Drug Discov Devel.* 2003; 6: 683-91.
262. Parenteau-Bareil R, Gauvin R, Berthod F. Collagen based biomaterials for tissue engineering applications. *Mater.* 2010; 3: 1863-87.
263. Park JH, Saravanakumar G, Kim K, *et al.* Targeted delivery of low molecular drugs using chitosan and its derivatives. *Adv Drug Deliv Rev.* 2010; 62: 28-41.
264. Patel RB, Solorio L, Wu H, *et al.* Effect of injection site on in situ implant formation and drug release *in vivo*. *J Control Release.* 2010; 147: 350-8.
265. Patel S, Zhang X, Collins L, *et al.* A small synthetic peptide for gene delivery via the serpin-enzyme complex receptor. *J Gene Med.* 2001; 3: 271-9.
266. Pavelić Z, Škalko-Basnet N, Filipović-Grčić J, *et al.* Development and *in vitro* evaluation of a liposomal vaginal delivery system for acyclovir. *J Control Release.* 2005; 106: 34-43.
267. Paula-Lima AC, Tricerri MA, Brito-Moreira J, *et al.* Human apolipoprotein A-I binds amyloid-beta and prevents a beta-induced neurotoxicity. *Int J Biochem Cell Biol.* 2009; 41: 1361-70.

268. Perry DP. Advancing Alzheimer's disease drug review as a national priority. *Alzheimer's & Dementia*, 2009, 5:180-1.
269. Pederson AW, Ruberti JW, Messersmith PB. Thermal assembly of a biomimetic mineral/collagen composite. *Biomater*. 2003; 24: 4881-90.
270. Peptu C, Popa M, Antimisiaris SG. Release of liposome-encapsulated calcein from liposome entrapping gelatin-carboxymethylcellulose films: a presentation of different possibilities. *J Nanosci Nanotechnol*. 2008; 8: 2249-58.
271. Perlmutter DH, Glover GI, Rivetna M, *et al*. Identification of a serpin-enzyme complex receptor on human hepatoma cells and human monocytes. *PNAS USA*. 1990; 87: 3753-7.
272. Perlmutter DH, Joslin G, Nelson P, *et al*. Endocytosis and degradation of alpha 1-antitrypsin-protease complexes is mediated by the serpin-enzyme complex (SEC) receptor. *J Biol Chem*. 1990; 265: 16713-6.
273. Pevion Biotech Ltd., "Virosomes," July 2010, <http://www.pevion.com/index.php?page=651>.
274. Phachonpai W, Wattanathorn J, Muchimapura S, *et al*. Neuroprotective effect of quercetin encapsulated liposomes: a novel therapeutic strategy against Alzheimer's disease. *Am J Appl Sci*. 2010; 7:480-5.
275. Pike CJ, Walencewicz AJ, Glabe CG, *et al*. *In vitro* aging of β -amyloid protein causes peptide aggregation and neurotoxicity. *Brain Res*. 1991; 563, 311.
276. Pike CJ, Burdick D, Walencewicz AJ, *et al*. Neurodegeneration induced by β -amyloid peptides *in vitro*: the role of peptide assembly state. *J Neurosci*. 1993; 13: 1676.
277. Pillai CKS, Paul W, Sharma CP. Chitin and chitosan polymers: chemistry, solubility and fiber formation. *Prog Polym Sci*. 2009; 34:641-78.

278. Pillay S, Pillay V, Choonara Y E, *et al.* Design, biometric simulation and optimization of a nano-enabled scaffold device for enhanced delivery of dopamine to the brain. *Int J Pharm.* 2009; 382: 277-90.
279. Pradhan P, Giri J, Rieken F, *et al.* Targeted temperature sensitive magnetic liposomes for thermo-chemotherapy. *J Control Release.* 2010; 142: 108-21.
280. Prabakaran M. Review paper: chitosan derivatives as promising materials for controlled drug delivery. *J Biomater Appl.* 2008; 23: 5-36.
281. Prentice P, Cuschieri A, Dholakia K, *et al.* Membrane disruption by optically controlled microbubbles cavitation. *Nature Phys.* 2005; 1:107-10.
282. Popovic N, Brundin P. Therapeutic potential of controlled drug delivery systems in neurodegenerative diseases. *Int J Pharm.* 2006; 314: 120-6.
283. Qi J, Yao P, He F, *et al.* Nanoparticles with dextran/chitosan shell and BSA/chitosan core-Doxorubicin loading and delivery. *Int J Pharm.* 2010; 393: 177-85.
284. Rai P, Vance D, Poon V, *et al.* Stable and potent polyvalent anthrax toxin inhibitors: raft-inspired domain formation in liposomes that contain PEGylated lipids. *Chem: A Eur J.* 2008; 14: 7748-51.
285. Rajput G, Majmudar F, Patel J, *et al.* Stomach-specific mucoadhesive microsphere as a controlled drug delivery system. *System Rev Pharm.* 2010; 1: 70-8.
286. Riche EL, Erickson BW, Cho MJ. Novel long-circulating liposomes containing peptide library-lipid conjugates: synthesis and *in vivo* behavior. *J Drug Target.* 2004; 12: 355-61.
287. Riemenschneider MJ, Reifenberger G. Molecular Neuropathology of Gliomas. *Int J Mol Sci.* 2009; 10: 184-212.

288. Reisberg B, Doody R, Stoffler A, *et al.* Memantine in moderate-to-severe Alzheimer's disease. *N Engl J Med.* 2003; 348:1333-41.
289. Roney C, Kulkarni P, Arora V, *et al.* Targeted nanoparticles for drug delivery through the blood brain barrier for Alzheimer's disease. *J Control Release.* 2005; 108: 193-214.
290. Rousseau V, Denizot B, Le Jeune JJ, *et al.* Early detection of liposome brain localization in rat experimental allergic encephalomyelitis. *Exp Brain Res.* 1999; 125: 255-64.
291. Rubin LL, Staddon JM. The cell biology of the blood brain barrier. *Ann Rev Neurosci.* 1999; 22: 11-28.
292. Ruizhen L, Lu G, Xiangliang Y, *et al.* Chitosan as a condensing agent induces high gene transfection efficiency and low cytotoxicity of liposome. *J Biosci Bioeng.* 2011; 111: 98-103.
293. Sahni JK, Doggui S, Ali J, *et al.* Neurotherapeutic applications of nanoparticles in Alzheimer's disease. *J Control Release.* 2011; 152: 208-31.
294. Sahoo SK, Labhasetwar V. Nanotech approaches to drug delivery and imaging. *Drug Discov Today.* 2003; 8: 1112-20.
295. Salerno A, Zeppetelli S, Maio ED, *et al.* Novel 3D porous multi-phase composite scaffolds based on PCL, thermoplastic zein and prepared via supercritical CO₂ foaming for bone regeneration. *Compos Sci Technol.* 2010; 70: 1838-46.
296. Samad A, Sultana Y, Khar RK, *et al.* Gelatin microspheres of rifampicin cross-linked with sucrose using thermal gelation method for the treatment of tuberculosis. *J Microencapsul.* 2009; 26: 83-9.

297. Sandor M, Riechel A, Kaplan I, *et al.* Effect of lecithin and MgCO₃ as additives on the enzymatic activity of carbonic anhydrase encapsulated in poly(lactide-coglycolide) (PLGA) microspheres. *Biochim Biophys Acta.* 2002; 1570: 63-74.
298. Sapra P, Allen TM. Ligand-targeted liposomal anticancer drugs. *Prog Lipid Res.* 2003; 42: 439-62.
299. Sasagawa T, Shimizu T, Sekiya S, *et al.* Design of prevascularized three-dimensional cell-dense tissues using a cell sheet stacking manipulation technology. *Biomater.* 2010; 31:1646-54.
300. Saude N, Ch`eze-Lange H, Beunard D, *et al.* Alginate production by *Azotobacter vinelandii* in a membrane bioreactor. *Process Biochem.* 2002; 38: 273-8.
301. Scherphof GL, Dijkstra J, Spanjer HH, *et al.* Uptake and intracellular processing of targeted and nontargeted liposomes by rat Kupffer cells *in vitro* and *in vivo*. *Ann NY Acad Sci.* 1985; 446: 368-84.
302. Schexnailder PJ, Schmidt G. Nanocomposite polymer hydrogels. *Colloid Polym Sci.* 2009; 287: 1-11.
303. Schnyder A, Krahenbuhl, Torok M, *et al.* Targeting of skeletal muscle *in vitro* using bionylated immunoliposomes. *Biochem J.* 2004; 377: 61-7.
304. Schnyder A, Huwyler J. Drug transport to brain with targeted liposomes. *NeuroRx.* 2005; 2: 99-107.
305. Schroeder A, Kost J, Barenholz Y. Ultrasound, liposomes, and drug delivery: principles for using ultrasound to control the release of drugs from liposomes. *Chem Physics of Lipids.* 2009; 162: 1-16.

306. Seely DMR, Wu P, Mills EJ. EDTA chelation therapy for cardiovascular disease: a systematic review. *BMC Cardiovasc.* 2005; 5:1-6.
307. Selkoe DJ. Cell biology of the amyloid beta-protein precursor and the mechanism of Alzheimer's disease. *Annu Rev Cell Biol.* 1994; 10:373-403.
308. Selkoe DJ. Deciphering the genesis and fate of amyloid beta-protein yields novel therapies for Alzheimer disease. *J Clin Invest.* 2002; 110: 1375-81.
309. Selkoe DJ. Translating cell biology into therapeutic advances in Alzheimer's disease. *Nature* 1999; 399:A23-A31.
310. Senior J, Gregoriadis G. Is half-life of circulating liposomes determined by changes in their permeability. *FEBS Lett.* 1982; 145: 109-14.
311. Shimizu N, Yamaguchi Y, Aoki T. Treatment and management of Wilson's disease. *Pediatr Int.* 1999; 4: 419-22.
312. Squitti R, Zito G. Anti-copper therapies in Alzheimer's disease: new concepts. *Recent Pat CNS Drug Discov.* 2009;4: 209-219.
313. Shmeeda H, Amitay Y, Gorin J, *et al.* Delivery of zoledronic acid encapsulated in folate-targeted liposome results in potent *in vitro* cytotoxic activity on tumor cells. *J Control Release.* 2010; 146: 76-83.
314. Shrivastava PK, Shrivastava SK. Dextran carrier macromolecule for colon specific delivery of celecoxib. *Curr Drug Deliv.* 2010; 7: 144-51.
315. Shytle RD, Mori T, Vendrame M, Sun N, *et al.* Cholinergic modulation of microglial activation by alpha7 nicotinic receptors. *J Neurochem.* 2004; 89: 337-43.

316. Sibambo RS, Pillay, Choonara Y, *et al.* A Novel Salted-out and subsequently crosslinked poly (Lactic-co-Glycolic Acid Polymeric Scaffold Applied to Monolithic Drug Delivery. *J Biol Comp Poly.* 2008; 23; 132-53.
317. Siepmann J, Gopferich A. Mathematical modeling of bioerodible, polymeric drug delivery systems. *Adv Drug Deliv Rev.* 2001; 48: 229-47.
318. Siepmann J, Siepmann F, Florence AT. Local controlled drug delivery to the brain: mathematical modeling of the underlying mass transport mechanisms. *Int J Pharm.* 2006; 314: 101-19.
319. Sihorkar V, Vyas SP. Potential of polysaccharide anchored liposomes in drug delivery targeted and immunization. *J Pharm Pharmaceut Sci.* 2001; 4: 138-58.
320. Sin D, Miao X, Liu G, *et al.* Polyurethane (PU) scaffolds prepared by solvent casting/particulate leaching (SCPL) combined with centrifugation. *Mater Sci Eng C.* 2010; 30: 78-85.
321. Simonis D, Schlesinger M, Seelandt C, *et al.* Analysis of SM4 sulfatide as a P-selectin ligand using model membranes. *Biophys Chem.* 2010; 150: 98-104.
322. Small DH, Mok SS, Bornstein JC. Alzheimer's disease and A β toxicity: from top to bottom. *Nat Rev Neurosci.* 2001; 2: 595-598.
323. Smith J, Zhang Y, Niven R. Toward development of a non-viral gene therapeutic. *Adv Drug Deliv Rev.* 1997; 26: 135-50.
324. Spicer PP, Mikos AG. Fibrin glue as a drug delivery system. *J Control Release.* 2010; 148: 49-55.

325. Soenen SJH, Brisson AR, DeCuyper M. Addressing the problem of cationic lipid-mediated toxicity: the magnetoliposome model. *Biomater.* 2009; 30: 3691-701.
326. Song CK, Jung SH, Kim DD, *et al.* Disaccharide-modified liposomes and their *in vitro* intracellular uptake. *Int J Pharm.* 2009; 380: 161-9.
327. Song S, Liu D, Peng J, *et al.* Peptide ligand-mediated liposome distribution and targeting to EGFR expressing tumor *in vivo*. *Int J Pharm.* 2008; 363: 155-61.
328. Soppirnath KS, Aminabhavi TM. Water transport and drug release study from cross-linked polyacrylamide grafted guar gum hydrogel microspheres for the controlled release application. *Eur J Pharm Biopharm.* 2002; 53(1): 87-98.
329. Soon SC, Stabenfeldt SE, Brown WE, *et al.* Engineering fibrin matrices: the engagement of polymerization pockets through fibrin knob technology for the delivery and retention of therapeutic proteins. *Biomater.* 2010; 31: 1944-54.
330. Stahl SM. The new cholinesterase inhibitors for Alzheimer's, Part 2: Illustrating their mechanisms of action. *J Clin Psychiatry.* 2000; 61: 813-4.
331. Stenekes RJH, Loebis AE, Fernandes CD, *et al.* Controlled release of liposomes from biodegradable dextran microspheres: a novel delivery concept. *Pharm Res.* 2000; 17: 690-695.
332. Stephan A, Laroche S, Davis S. Generation of aggregated beta-amyloid in the rat hippocampus impairs synaptic transmission and plasticity and causes memory deficits. *J Neurosci* 2001, 21:5703-14.
333. Stewart KM, Horton KL, Kelley SO. Cell penetrating peptides as delivery vehicles for biology and medicine. *Org Biomol Chem.* 2008; 6: 2242-55.

334. Strozyk D, Launer LJ, Adlard PA, *et al.* Zinc and copper modulate Alzheimer A β levels in human cerebrospinal fluid. *Neurobiol Aging*. 2009; 30: 1069-77.
335. Sultana Y, Jain R, Aqil M, *et al.* Review of ocular drug delivery. *Curr Drug Deliv*. 2006; 3: 207-17.
336. Sun G, Shen YI, Ho CC, *et al.* Functional groups affect physical and biological properties of dextran-based hydrogels. *J Biomed Mater Res Part A*. 2010; 93: 1080-90.
337. Suzuki R, Takizawa T, Negishi Y, *et al.* Gene delivery by combination of novel liposomal bubbles with perfluoropropane and ultrasound. *J Control Release*. 2007; 117, 130-6.
338. Suzuki R, Takizawa T, Kuwata Y, *et al.* Effective anti-tumor activity of oxaliplatin encapsulated in transferrin-PEG-liposome. *Int J Pharm*. 2008; 346: 143-150.
339. Suzuki R, Oda Y, Utoguchi N, *et al.* A novel strategy utilizing ultrasound for antigen delivery in dendritic cell based cancer immunotherapy. *J Control Release*. 2009; 133: 198-205.
340. Ta HT, Dass CR, Dunstan DE. Injectable chitosan hydrogels for localised cancer therapy. *J Control Release*. 2008; 126: 205-16.
341. Tabakovi A, Kester M, Adair JH. Calcium phosphate-based composite nanoparticles in bio-imaging and therapeutic delivery applications. *WIREs Nanomed Nanobiotechnol*. 2012; 4: 96-112.
342. Tabandeh H, Aboufazelia R, Ghasemi Z. Liposomes dispersed in two soluble types of collagens and the effect of collagens on the release rate of entrapped sodium shroma. *Iranian J Pharm Res*. 2003; 2: 161-5.

343. Tabesh H, Amoabediny GH, Nik NS, *et al.* The role of biodegradable engineered scaffolds seeded with Schwann cells for spinal cord regeneration. *Neurochem Int.* 2009; 54: 73-83.
344. Takara K, Hatakeyama H, Ohga N, *et al.* Design of a dual-ligand system using a specific ligand and cell penetrating peptide, resulting in a synergistic effect on selectivity and cellular uptake. *Inter J Pharm.* 2010; 396: 143-8.
345. Tang C, Yin L, Yu J, *et al.* Swelling behavior and biocompatibility of carbopol-containing superporous hydrogel composites. *J Applied Polym Sci.* 2007; 104: 2785-91.
346. Tierney CM, Jaasma MJ, O'Brien FJ. Osteoblast activity on collagen-GAG scaffolds is affected by collagen and GAG concentrations. *J Biomed Mater Res Part A.* 2009; 91: 92-101.
347. Tilakaratne HK, Hunter SK, Andracki ME, *et al.* Characterizing short-term release and neovascularization potential of multi-protein growth supplement delivered via alginate hollow fiber devices. *Biomater.* 2007; 28: 89-98.
348. Tran MA, Watts RJ, Robertson GP. Use of liposomes as drug delivery vehicles for treatment of melanoma. *Pigment Cell and Melanoma Res.* 2009; 22: 388-99
349. Torchilin VP. Recent advances with liposomes as pharmaceutical carriers. *Nat Rev Drug Discov.* 2005; 4: 145-60.
350. Torchilin VP. Tat peptide-mediated intracellular delivery of pharmaceutical nanocarriers. *Adv Drug Deliv Rev.* 2008; 60: 548-58.
351. Uchegbu IF. Parenteral drug delivery. *Pharm J.* 1990; 263: 309-18.
352. Unger EC, Porter T, Culp W *et al.* Therapeutic applications of lipid-coated microbubbles. *Adv Drug Deliv Rev.* 2004; 56:1291-314.

353. Vaidya B, Nayak MK, Dash D, *et al.* Development and characterization of site specific target sensitive liposomes for the delivery of thrombolytic agents. *Int J Pharm.* 2011; 403: 254-61.
354. Van Dijk-Wolthuis WNE, Hoogeboom JAM, van Steenbergen MJ, *et al.* Degradation and release behavior of dextran-based hydrogels. *Macromolecules.* 1997; 30: 4639-45.
355. Van Raaij ME, Lindvere L, Dorr A, *et al.* Functional micro-ultrasound imaging of rodent cerebral hemodynamics. *Neuroimage.* 2011; 58:100-8.
356. Van Tomme SR, Hennink WE. Biodegradable dextran hydrogels for protein delivery applications. *Expert Rev Med Devices.* 2007; 4: 147-64.
357. Vargas G, Patrikeev I, Wei J, *et al.* Quantitative assessment of microbicide-induced injury in the ovine vaginal epithelium using confocal microendoscopy. *BMC Infectious Dis.* 2012; 12:48.
358. Veerareddy PR, Vobalaboina V. Lipid-based formulations of amphotericin B. *Drug Today.* 2004; 40: 133-45.
359. Verma DD, Verma S, Blume G, *et al.* Particle size of liposomes influences dermal delivery of substances into skin. *Int J Pharm.* 2003; 258: 141-51.
360. Wallace DG, Rosenblatt J. Collagen gel systems for sustained delivery and tissue engineering. *Adv Drug Deliv Rev.* 2003; 55: 1631-49.
361. Wang N, Adams G, Buttery L, *et al.* Alginate encapsulation technology supports embryonic stem cells differentiation into insulin-producing cells. *J Biotechnol.* 2009; 144: 304-12.
362. Wang PP, J. Frazier J, *et al.* Local drug delivery to the brain. *Adv Drug Deliv Rev.* 2002; 54: 987-1013.

363. Wang SS, Yang MC, Chung TW. Liposomes/chitosan scaffold/human fibrin gel composite systems for delivering hydrophilic drugs-release behaviors of Tirofiban *in vitro*. *Drug Deliv*. 2008; 15: 149-57.
364. Wanga Y, Li X, Zhou Y, *et al*. Preparation of nanobubbles for ultrasound imaging and intracellular drug delivery. *Int J Pharm*. 2010; 384: 148-153.
365. Wang Y, Tu S, Li R, *et al*. Cholesterol succinyl chitosan anchored liposomes: preparation, characterization, physical stability, and drug release behavior. *Nanomedic Nanotechnol Biol Medic*. 2010; 6: 471-7.
366. Weers JG, Scheuing DR. Characterization of viscoelastic surfactant mixtures, I: fourier transform infrared spectroscopic studies. *Colloids Surf B: Biointerfaces*. 1991; 1: 41-56.
367. Weiner AL, Carpenter-Green SS, Soehngen EC. Liposome-collagen gel matrix: a novel sustained drug delivery system. *J Pharm Sci*. 1985; 74: 992-25.
368. Weller GE, Villanueva FS, Tom EM, *et al*. Targeted ultrasound contrast agents: *In vitro* assessment of endothelial dysfunction and multi-targeting to ICAM-1 and sialy Lewis(x). *Biotechnol Bioeng*. 2005; 92: 780-8
369. Weng L, Chen X, Chen W. Rheological characterization of in situ crosslinkable hydrogels formulated from oxidized dextran and N-carboxyethyl chitosan. *Biomacromol*. 2007; 8:1109-15.
370. Wiechens B, Neumann D, Grammer JB, *et al*. Retinal toxicity of liposome-incorporated and free ofloxacin after intravitreal injection in rabbit eyes. *Int Ophthalmol*. 1999; 22:133-43.
371. Willerth SM, Sakiyama-Elbert SE. Approaches to neural tissue engineering using scaffolds for drug delivery. *Adv Drug Deliv Rev*. 2007; 59: 325-38.

372. Willmann JK, Kimura RH, Deshpande N, *et al.* Targeted contrast-enhanced ultrasound imaging of tumor angiogenesis with contrast microbubbles conjugated to integrin-binding knottin peptides. *J Nucl Med.* 2010;51: 433-40.
373. Wittaya-areekul S, Prahsarn C, Sungthongjeen S. Development and *in vitro* evaluation of chitosan-eudragit RS 30D composite wound dressings. *AAPS PharmSciTech*, 2006;7.
374. Wolf K, Alexander S, Schacht V, *et al.* Collagen-based cell migration models *in vitro* and *in vivo*. *Seminars in Cell & Developmental Bio.* 2009; 20: 931-41.
375. Woodle MC, Lasic DD. Sterically stabilized liposomes. *Biochim Biophys Acta.* 1992; 1113: 171-99.
376. Xu JB, Bartley JP, Johnson RA. Preparation and characterization of alginate hydrogel membranes crosslinked using a water-soluble carbodiimide. *J Applied Polym Sci.* 2003; 90: 747-53.
377. Yagi N, Ogawa Y, Kodaka M, *et al.* Preparation of functional liposomes with peptide ligands and their binding to cell membranes. *Lipids.* 2000; 35: 673-9.
378. Yamada A, Taniguchi Y, Kawano K, *et al.* Design of folate-linked liposomal doxorubicin to its antitumor effect in mice. *Clin Cancer Res* 2008; 14: 8161-8.
379. Yang C, Hillas PJ, B´aez JA, *et al.* The application of recombinant human collagen in tissue engineering. *BioDrugs.* 2004; 18: 103-19.
380. Yang JM, Su WY, Leu TL, *et al.* Evaluation of chitosan/PVA blended hydrogel membranes. *J Membr Sci.* 2004; 236: 39-51.
381. Yeo Y, Kohane DS. Polymers in the prevention of peritoneal adhesions. *Eur J Pharm Biopharm.* 2008; 68: 57-66.

382. Yigit MV, Mishra A, Tong R, *et al.* Inorganic mercury detection and controlled release of chelating agents from ion-responsive liposomes. *Chem Biol.* 2009; 16: 937-42.
383. Ying X, Wen HE, Lu WL, *et al.* Dual-targeting daunorubicin liposomes improve the therapeutic efficacy of brain glioma in animals. *J Control Release.* 2010; 141:183-92.
384. Yin T, Wang P, Zheng R, *et al.* Nanobubbles for enhanced ultrasound imaging of tumors. *Int J Nanomedicin.* 2012; 7: 895-904.
385. Young S, Wong M, Tabata Y, *et al.* Gelatin as a delivery vehicle for the controlled release of bioactive molecules. *J Control Release.* 2005; 109: 256-74.
386. Young SL, Chaplin DJ. Combretastatin A4 phosphate: background and current clinical status. *Expert Opinion on Investigational Drugs.* 2004; 13: 1171-82.
387. Yousefi A, Esmaeili F, Rahimian S, *et al.* Preparation and *in vitro* evaluation of a pegylated nano-liposomal formulation containing docetaxel. *Sci Pharm.* 2009; 77: 453-64.
388. Yu B, Tai HC, Xue W, *et al.* Receptor targeted nanocarriers for therapeutic delivery to cancer. *Mol Membr Biol.* 2010; 27: 286-98.
389. Yu L, Chang GT, Zhang H, Ding JD. Injectable block copolymer hydrogels for sustained release of a PEGylated Drug. *Int J Pharm.* 2008; 348: 95-106.
390. Zatta P, Drago D, Bolognin S, *et al.* Alzheimer's disease, metal ions and metal homeostatic therapy. *Trends Pharmacol Sci.* 2009; 30: 346-55.

391. Ziady AG, Perales JC, Ferkol T, *et al.* Gene transfer into hepatoma cell lines via the serpin enzyme complex receptor. *Am J Physiol.* 1997; 273: 545-52.
392. Zhang HF, Zhong H, Zhang LL, *et al.* Modulate the phase transition temperature of hydrogels with both thermosensitivity and biodegradability. *Carbohydrate Polym.* 2010; 79: 131-6.
393. Zhang LW, Yang J, Barron AR, *et al.* Endocytic mechanisms and toxicity of a functionalized fullerene in human cells. *Toxicol Lett.* 2009; 191: 149-57.
394. Zhang X, Do MD, Casey P, *et al.* Chemical cross-linking gelatin with natural phenolic compounds as studied by high resolution NMR spectroscopy. *Biomacromol.* 2010; 11: 1125-32.
395. Zhua J, Xue J, Guo Z, *et al.* Vesicle size and stability of biomimetic liposomes from 3-Sulfo-Lewis a (SuLea)-containing glycolipids. *Colloids Surf B Biointerfaces.* 2007; 58: 242-9.
396. Zoldakova M, Kornyei Z, Brown A, *et al.* Effects of a combretastatin A4 analogous chalcone and its Pt-complex on cancer cells: a comparative study of uptake, cell cycle and damage to cellular compartments. *Biochem Pharm.* 2010; 80: 1487-96.
397. Zucker D, Marcus D, Barenholz Y, *et al.* Liposome drugs' loading efficiency: a working model based on loading conditions and drug's physicochemical properties. *J Control Release.* 2009; 139: 73-80.

APPENDICES

Appendix A: Research Publications

1: A Review on composite liposomal technologies for specialized drug delivery. Maluta S. Mufamadi, Viness Pillay, Yahya E. Choonara, Lisa C. Du Toit, Girish Modi, Dinesh Naidoo and Valence M. K. Ndesendo *Journal of Drug Delivery* doi:10.1155/2011/939851

Hindawi Publishing Corporation
Journal of Drug Delivery
Volume 2011, Article ID 939851, 19 pages
doi:10.1155/2011/939851

Review Article

A Review on Composite Liposomal Technologies for Specialized Drug Delivery

Maluta S. Mufamadi,¹ Viness Pillay,¹ Yahya E. Choonara,¹ Lisa C. Du Toit,¹ Girish Modi,² Dinesh Naidoo,³ and Valence M. K. Ndesendo¹

¹Department of Pharmacy and Pharmacology, University of the Witwatersrand, 7 York Road, Parktown, Johannesburg 2193, South Africa

²Department of Neurology, University of the Witwatersrand, 7 York Road, Parktown, Johannesburg 2193, South Africa

³Department of Neurosurgery, University of the Witwatersrand, 7 York Road, Parktown, Johannesburg 2193, South Africa

Correspondence should be addressed to Viness Pillay, viness.pillay@wits.ac.za

Received 28 July 2010; Revised 23 November 2010; Accepted 7 December 2010

Academic Editor: Guru V. Betageri

Copyright © 2011 Maluta S. Mufamadi et al. This is an open access article distributed under the Creative Commons Attribution License, which permits unrestricted use, distribution, and reproduction in any medium, provided the original work is properly cited.

The combination of liposomes with polymeric scaffolds could revolutionize the current state of drug delivery technology. Although liposomes have been extensively studied as a promising drug delivery model for bioactive compounds, there still remain major drawbacks for widespread pharmaceutical application. Two approaches for overcoming the factors related to the suboptimal efficacy of liposomes in drug delivery have been suggested. The first entails modifying the liposome surface with functional moieties, while the second involves integration of pre-encapsulated drug-loaded liposomes within depot polymeric scaffolds. This attempts to provide ingenious solutions to the limitations of conventional liposomes such as short plasma half-lives, toxicity, stability, and poor control of drug release over prolonged periods. This review delineates the key advances in composite technologies that merge the concepts of depot polymeric scaffolds with liposome technology to overcome the limitations of conventional liposomes for pharmaceutical applications.

2: Effect of surface-engineered nanoliposomes by chelating ligands on modulation of neurotoxicity associated with β -amyloid aggregates of Alzheimer's disease. Maluta S. Mufamadi, Yahya E. Choonara, Pradeep Kumar, Girish Modi, Dinesh Naidoo, Valence M. K. Ndesendo, Lisa C. Du Toit and Viness Pillay *Journal of Pharmaceutical Research*, 2012, 29(11):3075-3089.

Pharm Res (2012) 29:3075–3089
DOI 10.1007/s11095-012-0770-0

RESEARCH PAPER

Surface-Engineered Nanoliposomes by Chelating Ligands for Modulating the Neurotoxicity Associated with β -Amyloid Aggregates of Alzheimer's disease

Maluta S. Mufamadi • Yahya E. Choonara • Pradeep Kumar • Girish Modi • Dinesh Naidoo • Valence M. K. Ndesendo • Lisa C. du Toit • Sunny E. Iyuke • Viness Pillay

Received: 9 December 2011 / Accepted: 30 April 2012 / Published online: 15 May 2012
© Springer Science+Business Media, LLC 2012

ABSTRACT

Purpose To develop chelating ligand-bound nanoliposomes (NLPs) for the prevention and reversal of β -Amyloid ($A\beta$) aggregation associated with promoting neurotoxicity in Alzheimer disease (AD).

Methods Four different chelating ligands (CuAc, EDTA, histidine and ZnAc) were surface-engineered onto NLPs using either covalent or non-covalent conjugation. Successful conjugation of chelating ligands onto the surface of NLPs was confirmed by characterization studies: SEM, TEM and FTIR analysis. Chelation energetics of EDTA with Cu(II)/Zn(II)- $A\beta$ (10-21) and nanoformation of emulsified polymers were computed and corroborated with experimental and analytical data using chemometric molecular modeling.

Results The modified NLPs produced were spherical in shape, 127–178 nm in size, with polydispersity index from 0.217–0.920 and zeta potential range of -9.59 to -37.3 mV. Conjugation efficiencies were 30–76 %, which confirmed that chelating ligands were attached to the NLP surface.

Conclusions *In vitro* and *ex vivo* results elucidated the effectiveness of chelating ligand-bound NLPs for prevention of Cu $A\beta$ (1-42) or Zn $A\beta$ (1-42) aggregate buildup associated with neurotoxicity in PC12 neuronal cells, as well as promotion of intracellular uptake in the presence of Cu(II) or Zn(II) metal ions.

3: Ligand-functionalized nanoliposomes for targeted delivery of galantamine. Maluta S. Mufamadi, Yahya E. Choonara, Pradeep Kumar, Girish Modi, Dinesh Naidoo, Sannday van vuuren, Valence MK Ndesendo, Lisa C. du Toit, Sunny E. Iyuke, Viness Pillay. *International Journal of Pharmaceutics*, 2013, 448:267-281.

International Journal of Pharmaceutics 448 (2013) 267–281

Contents lists available at SciVerse ScienceDirect

 **International Journal of Pharmaceutics** 

Journal homepage: www.elsevier.com/locate/ijpharm

Pharmaceutical nanotechnology

Ligand-functionalized nanoliposomes for targeted delivery of galantamine 

Maluta S. Mufamadi^a, Yahya E. Choonara^a, Pradeep Kumar^a, Girish Modi^b, Dinesh Naidoo^c, Sandy van Vuuren^a, Valence M.K. Ndesendo^d, Lisa C. du Toit^a, Sunny E. Iyuke^e, Viness Pillay^{a,*}

^a University of the Witwatersrand, Faculty of Health Sciences, Department of Pharmacy and Pharmacology, 7 York Road, Parktown 2193, Johannesburg, South Africa
^b University of the Witwatersrand, Faculty of Health Sciences, Division of Neurosciences, Department of Neurology, 7 York Road, Parktown 2193, Johannesburg, South Africa
^c University of the Witwatersrand, Faculty of Health Sciences, Division of Neurosciences, Department of Neurosurgery, 7 York Road, Parktown 2193, Johannesburg, South Africa
^d St. John's University of Tanzania, School of Pharmacy and Pharmaceutical Sciences, Dodoma, Tanzania
^e University of the Witwatersrand, School of Chemical and Metallurgical Engineering, Private Bag 3, Wits 2050, Johannesburg, South Africa

A B S T R A C T

The purpose of this study was to design ligand-functionalized nanoliposomes that are proficient in providing effective intracellular delivery of an alkaloid drug (galantamine) into PC12 neuronal cells in response to managing Alzheimer's disease (AD). Ligand-functionalized nanoliposomes were produced and validated for their physicochemical properties, *in silico* molecular mechanics energy relationships, *ex vivo* cytotoxicity, peptide coupling efficiency (PCE), drug entrapment efficiency (DEE), drug release, fluorometry and confocal microscopy. Particle sizes of the nanoliposomes ranged from 127 nm to 165 nm (PDI= 0.39–0.03), zeta potential values of –18 mV to –36 mV, PCE from 40% to 78% while DEE ranged from 42% to 79%. The surface morphology of the nanoliposomes was stable, spherically and uniform in shape. Thermal behavior and Fourier transform infrared (FTIR) analyses confirmed that galantamine and the peptide-ligand were incorporated into the inner core and surface of the nanoliposomes, respectively. The optimized formulation showed sustained drug release (30% of drug released within 48 h). Fluorometry and confocal microscopy revealed that the ligand-functionalized nanoliposomes facilitated galantamine uptake into PC12 neuronal cells via the Serpin Enzyme Complex Receptor in a mediated manner. CytoTox-Glo™ cytotoxicity assay established the low cytotoxicity on PC12 neuronal cells when exposed to native nanoliposomes and the ligand-functionalized nanoliposomes. Response surface analysis demonstrated there was a high degree of correlation between the experimental and fitted values. Furthermore, *ex vivo* studies showed that the high galantamine accumulation into PC12 neuronal cells was influenced by the post-engineering of peptides on the surface of the galantamine-loaded nanoliposomes. MMR analysis aptly corroborated the experimental findings.

© 2013 Elsevier B.V. All rights reserved.

4: Design, biomolecular modeling and evaluation of surface-engineered nanoliposomes for the management of Alzheimer's disease. M.S. Mufamadi, Y.E. Choonara, L.C. du Toit, G. Modi, D. Naidoo, P. Kumar, V.M.K. Ndesendo, L. Meyer, S.E. Iyuke, V. Pillay EFNS European Journal of Neurology 2012, 19 (Suppl. 1), 90-457, Neurotoxicology.

© 2012 EFNS European Journal of Neurology 19 (Suppl. 1), 90-457
Neurotoxicity/ Occupational Neurology

Design, Biomolecular Modelling and Evaluation of Surface-Engineered Nanoliposomes for the Management of Alzheimer's disease

Maluta S. Mufamadi¹, Yahya E. Choonara¹, Lisa C. du Toit¹, Girish Modi², Dinesh Naidoo³, Pradeep Kumar¹, Valence M.K. Ndesendo¹, Leith C.R Meyer⁴ Sunny E. Iyuke⁵ and Viness Pillay^{1*}

¹University of the Witwatersrand, Faculty of Health Sciences, Department of Pharmacy and Pharmacology, Parktown, 2193, Johannesburg, South Africa

²University of the Witwatersrand, Faculty of Health Sciences, Department of Neurology, Parktown, 2193, Johannesburg, South Africa.

³University of the Witwatersrand, Faculty of Health Sciences, Department of Neurosurgery, Parktown, 2193, Johannesburg, South Africa.

⁴University of the Witwatersrand, Faculty of Health Sciences, Central Animal Services, Parktown, 2193, Johannesburg, South Africa

⁵University of the Witwatersrand, School of Chemical and Metallurgical Engineering, Private Bag 3, Wits 2050, Johannesburg, South Africa

*Correspondence: viness.pillay@wits.ac.za

Purpose: The purpose of this study was the design, modelling and evaluation of the surface engineered nanoliposomes (NLPs) coupled with chelating ligands [Zinc acetate (ZnAc), Histidine (His) and Ethylenediaminetetraacetic acid (EDTA)] for neuronal cell protections against A β aggregates.

Methods: NLPs were fabricated from distearylphosphatidylcholine (DSPC), Cholesterol (Chol), and distearylphosphatidylethanolamine (DSPE-mPEG2000) using the reverse phase evaporation technique. Chelating ligands were surface engineered onto the surface NLPs. Biomolecular modelling analysis was used as predictive approach in the design of surface-engineered NLPs to investigate the interaction of metal ions [Cu(II) and Zn(II)] with A β (1-42) peptide resulting in CuA β (1-42) or ZnA β (1-42) aggregates, and the effect of surface-modified NLPs in preventing A β aggregates. Cyto(neuro)toxicity studies were performed on the surface-modified NLPs in order to assess the effect on neuronal cell proliferation. Dead cells were assayed using CytoTox-Glo™ Cytotoxicity kit and counted employing a plate reader. The interaction of DSPC, Chol and DSPE-mPEG2000 during NLPs formulation and engineering of chelating ligands on the surface of NLPs was validated by Fourier Transmission Infrared (FTIR) and Scanning Electron Microscopy (SEM).

Results: Analytical-mathematical and geometrical configuration validated the interaction energy during protein/metal or metal/chelating ligands complexation. Ex vivo studies showed about 30-40% cell viability after exposure to CuA β (1-42)/ ZnA β (1-42) aggregates. Furthermore, about 60-80% cell viability was shown after treatment with surface-modified NLPs with ZnAc, histidine and EDTA

Conclusions: The in vitro and ex vivo experimental studies were well corroborated by the in silico molecular mechanistic studies, thus further confirming the potential of NLP/chelation therapy for Alzheimer's disease intervention.

5: Physicomechanical transitions of an implantable nano-enabled biorobotic intracranial device for Alzheimer's disease management for validation of *in vivo* behavior in a simulated brain environment. M.S. Mufamadi, Y.E. Choonara, L.C. du Toit, G. Modi, D. Naidoo, P. Kumar, V.M.K. Ndesendo, L. Meyer, S.E. Iyuke, V. Pillay. EFNS European Journal of Neurology 19 (Suppl. X), 66-343, Ageing and Dementia

© 2012 EFNS European Journal of Neurology 19 (Suppl. 1), 90-457
Ageing and dementia

Physicomechanical Transitions of an Implantable Nano-Enabled Biorobotic Intracranial Device for Alzheimer's Disease Management for Validation of *in Vivo* Behaviour in a Simulated Brain Environment

Maluta S. Mufamadi¹, Yahya E. Choonara¹, Lisa C. du Toit¹, Girish Modi², Dinesh Naidoo³, Pradeep Kumar¹, Valence M.K. Ndesendo¹, Leith C.R Meyer⁴ Sunny E. Iyuke⁵ and Viness Pillay^{1*}

¹University of the Witwatersrand, Faculty of Health Sciences, Department of Pharmacy and Pharmacology, Parktown, 2193, Johannesburg, South Africa

²University of the Witwatersrand, Faculty of Health Sciences, Department of Neurology, Parktown, 2193, Johannesburg, South Africa.

³University of the Witwatersrand, Faculty of Health Sciences, Department of Neurosurgery, Parktown, 2193, Johannesburg, South Africa.

⁴University of the Witwatersrand, Faculty of Health Sciences, Central Animal Services, Parktown, 2193, Johannesburg, South Africa

⁵University of the Witwatersrand, School of Chemical and Metallurgical Engineering, Private Bag 3, Wits 2050, Johannesburg, South Africa

*Correspondence: viness.pillay@wits.ac.za

Purpose: The purpose of this study was to evaluate the physicomechanical transitions of an implantable nanoenabled Biorobotic Intracranial Device (BICD) within simulated brain environment.

Methods: The BICD was fabricated by embedding galantamine-loaded functionalized nanoliposomes [f(x) NLPs] [Phosphocholine (DSPC), cholesterol, ethanolamine (DSPE-mPEG2000) with synthetic peptides] within a neuro-compliant scaffold [glutaraldehyde crosslinked chitosan, eudragit RSPO, and polyvinyl alcohol or polyethyleneoxide] followed by freeze-drying. Rheological, textural and SEM studies were employed to characterize the BICD behaviour *in vitro*. Hydration and degradation studies were conducted within artificial cerebrospinal fluid (aFCS). Images were acquired using a bench-top MRI over a period of 50 days. Labelled-f(x) NLPs distribution within the BICD was examined by micro-ultrasound imaging (Vevo@2100) and CLSM.

Results: SEM images validated the porous surface morphology of the scaffold, with pores that are relatively uniform in size and shape. Rheological and textural parameters demonstrated that the crosslinked scaffold was more firm and resilient when compared with the noncrosslinked scaffold. MRI images showed complete scaffold hydrated within 30min after submergence within aFCS, however the hydrated scaffold exhibited swelling and slight erosion. CLSM micrographs confirmed labelled f(x)NLPs encapsulation and distribution within the BICD. Fluorescence patterns postulate intact vesicles after BICD lyophilization. Ultrasound images confirmed that more even f(x)NLPs distribution was achieved in the slightly less viscous rather than highly viscous BICD.

Conclusions: The results validate that evaluation of BICD physicomechanical transitions is a useful tool for further investigation of the optimized formulation designed for prolonged delivery of the neuroprotectant-nanocarrier into targeted neuronal cells of Alzheimer's disease.

6: Exploration of a composite nano-medical device for the delivery of neuroprotectant- nanocarriers into targeted neuronal cells of Alzheimer's disease. M.S. Mufamadi, Y.E. Choonara, L.C. du Toit, G. Modi, D. Naidoo, P. Kumar, V.M.K. Ndesendo, L. Meyer, S.E. Iyuke, V. Pillay *European Journal of Neurology* 2012, 19 (Suppl. 1), 90-457, Ageing and Dementia.

© 2012 EFNS *European Journal of Neurology* 19 (Suppl. 1), 90-457
Ageing and dementia

Exploration of a Composite Nano-Medical Device for the Delivery of Neuroprotectant-Nanocarriers into Targeted Neuronal Cells of Alzheimer's Disease

Maluta S. Mufamadi¹, Yahya E. Choonara¹, Lisa C. du Toit¹, Girish Modi², Dinesh Naidoo³, Pradeep Kumar¹, Valence M.K. Ndesendo¹, Leith C.R Meyer⁴ Sunny E. Iyuke⁵ and Viness Pillay^{1*}

¹University of the Witwatersrand, Faculty of Health Sciences, Department of Pharmacy and Pharmacology, Parktown, 2193, Johannesburg, South Africa

²University of the Witwatersrand, Faculty of Health Sciences, Department of Neurology, Parktown, 2193, Johannesburg, South Africa.

³University of the Witwatersrand, Faculty of Health Sciences, Department of Neurosurgery, Parktown, 2193, Johannesburg, South Africa.

⁴University of the Witwatersrand, Faculty of Health Sciences, Central Animal Services, Parktown, 2193, Johannesburg, South Africa

⁵University of the Witwatersrand, School of Chemical and Metallurgical Engineering, Private Bag 3, Wits 2050, Johannesburg, South Africa

*Correspondence: viness.pillay@wits.ac.za

Purpose: The purpose of this study was to explore an implantable composite nano-medical device that is capable of prolonged delivery of the neuroprotectant-nanocarrier into targeted neuronal cells of Alzheimer's disease (AD).

Method: The device was fabricated by embedding galantamine-loaded/fluorescein-isothiocyanate (FITC)-labelled functionalized nanoliposomes [f(x)NLPs] [phosphocholine(DSPC), cholesterol, ethanolamine (DSPEmPEG2000)] with synthetic peptide [KVLFLS, KVLFLT and KVLFLM] within a neuro-compliant scaffold (glutaraldehyde crosslinked chitosan, Eudragit®-RSPO, and polyvinylalcohol or polyethyleneoxide) followed by freeze-drying. Drug release from drug-loaded f(x)NLPs was performed using an orbital shaker-bath (50days) and at predetermined time intervals samples were drawn and analyzed via UV ($\lambda_{max}=288nm$). PC12-cells were seeded on the device, ensued by air-drying/freeze-drying. Cells on the device were examined under SEM and stereomicroscopy. LDH release and antiproliferation were assayed using the CytoTox-96® Non-Radioactive and CytoTox-Glu® Cytotoxicity assays, respectively, thereafter Lactate Dehydrogenase (LDH)/dead cells was quantified employing plate reader. At pre-determined time intervals cell uptake was analyzed for 30 days employing plate reader and CLSM.

Results: In vitro study demonstrated that prolonged release of f(x)NLPs (60-100%) from the device over a period of 50 days. SEM and stereomicroscope results demonstrated that the device was suitable for neuronal cell attachment and proliferation. Ex vivo results exhibit less than 30% LDH release which validate that the designed device did not significantly induce cell injury. CLSM and plate-reader studies revealed that f(x) NLPs facilitated the drug uptake into PC12-cells via LDL receptor family.

Conclusions: The results revealed that the designed device had superior cytocompatibility and was suitable to fulfill prolonged delivery of neuroprotectants-nanocarrier into targeted neuronal cells of AD.

7. Biomedical Imaging and mechanical dynamics validated the physicochemical properties of the Bio-Robotic Intracranial Device *in vitro*. Maluta S. Mufamadi, Yahya E. Choonara, Lisa C. du Toit, Pradeep Kumar, Girish Modi, Dinesh Naidoo, Clement Penny, Sunny E. Iyu, Viness Pillay. Submitted to AAPS PharmTech

Biomedical Imaging and Mechanical Dynamics Validated the Physicochemical Properties of the Bio-Robotic Intracranial Device *in Vitro*

Maluta S. Mufamadi¹, Yahya E. Choonara¹, Lisa C. du Toit¹, Pradeep Kumar¹, Girish Modi², Dinesh Naidoo³, Clement Penny⁴, Valence M.K. Ndesendo⁵, Sunny E. Iyu⁶, Viness Pillay^{1,*}

¹ University of the Witwatersrand, Faculty of Health Sciences, Department of Pharmacy and Pharmacology, 7 York Road, Parktown 2193, Johannesburg, South Africa

² University of the Witwatersrand, Faculty of Health Sciences, Division of Neurosciences, Department of Neurology, 7 York Road, Parktown 2193, Johannesburg, South Africa

³ University of the Witwatersrand, Faculty of Health Sciences, Division of Neurosciences, Department of Neurosurgery, 7 York Road, Parktown 2193, Johannesburg, South Africa

⁴ University of the Witwatersrand, Faculty of Health Sciences, Department of Medical Oncology, 7 York Road, Parktown 2193, Johannesburg, South Africa

⁵ St. John's University of Tanzania, School of Pharmacy and Pharmaceutical Sciences, Dodoma, Tanzania

⁶ University of the Witwatersrand, School of Chemical and Metallurgical Engineering, Private Bag 3, Wits 2050, Johannesburg, South Africa

ABSTRACT

The purpose of this study was to explore the use of bio-imaging systems and mechanical dynamics as potential approaches to validate physicochemical properties of nano-enabled Bio-Robotic Intracranial Device (BICD). The BICD was constructed through embedment of the gas-filled functionalized nanoliposomes (NLPs) within hydrogel network, and thereafter cross-linked with glutaraldehyde (GA). The physicochemical properties of gas-filled NLPs were measured by Dynamic Light Scattering (DLS), the measurements revealed particles sizes ranging from 135-158nm, polydispersity index of 0.129-0.190 and zeta potential of -34mV. In addition, Transmission Electron Microscopy (TEM), real-time ultrasound, fluorescence imaging micro-ultrasound and optical immunofluorescence imaging data revealed that the gas-filled functionalized NLPs have uniformity and spherical shape, these were examined pre- and post embedment within BICD. Turbiscan Lab⁵ expert data further revealed that produced gas-filled functionalized NLPs in the suspension demonstrated a homogeneous state and stable system. FTIR spectra of the hydrogel networks revealed molecular structural variations formed during fabrication, in which 1560, 1650 and 1655cm⁻¹ were of the amide bands while 3500-3200cm⁻¹ corresponded to OH vibration. The mechanical dynamics of the hydrogel networks were shown to be governed by polymers concentrations and cross-linking agent. Real-time ultrasound, fluorescence imaging micro-ultrasound and optical immunofluorescence bio-imaging systems further validated that gas-filled functionalized NLPs were still at its intact form post embedment in the CEP hydrogel of the BICD construct. Overall, these findings signified that bio-imaging systems posed to be fundamental techniques for future characterization of BICD or tracking of labeled or gas-filled drug delivery vehicles in therapeutic delivery applications.

Keywords: Nanolipobubbles, hydrogel network, fluorescence, bio-imaging and Bio-Robotic Intracranial Device.

8 . Bio-construction of implantable nano-enabled bio-robotic intracranial device for advanced delivery galantamine into CNS. Maluta S. Mufamadi, Yahya E. Choonara, Lisa C. du Toit, Pradeep Kumar, Girish Modi, Dinesh Naidoo, Clement Penny, Sunny E. Iyu, Viness Pillay. Submitted to Journal of Pharmaceutical Sciences.

Bio-Construction of an Implantable Nano-Enabled Bio-Robotic Intracranial Device for Advanced Delivery Galantamine into CNS

Maluta S. Mufamadi¹, Yahya E. Choonara¹, Girish Modi ², Dinesh Naidoo³, Lisa C. du Toit¹, Sunny E. Iyuke⁵ and Viness Pillay^{1*}

¹ University of the Witwatersrand, Faculty of Health Sciences, Department of Pharmacy and Pharmacology, 7 York Road, Parktown 2193, Johannesburg, South Africa

² University of the Witwatersrand, Faculty of Health Sciences, Division of Neurosciences, Department of Neurology, 7 York Road, Parktown 2193, Johannesburg, South Africa

³ University of the Witwatersrand, Faculty of Health Sciences, Division of Neurosciences, Department of Neurosurgery, 7 York Road, Parktown 2193, Johannesburg, South Africa

⁴ University of the Witwatersrand, School of Chemical and Metallurgical Engineering, Private Bag 3, Wits 2050, Johannesburg, South Africa

ABSTRACT

The purpose of this study is to construct an implantable nano-enabled Bio-Robotic intracranial Device (BICD) that is capable of delivering galantamine (GAL) to a specific site in the brain, in response to Alzheimer's disease (AD). The BICD was engineered by embedding drug-loaded functionalized nanoliposomes (NLPs) (Particle sizes = 100-158nm, zeta potential of -34mV) into depot CEP scaffold. BICD was characterized for its physicochemical and physicochemical behaviours, *in vitro* prolong release of the drug-loaded functionalized NLPs in a simulated CSF environment (0.1M PBS; pH7.4; 37°C) and *ex vivo* for biocompatibility in cellular environment of the PC12 neuronal cells. SEM validated the surface morphology of the CEP scaffolds were spherical interconnected pores shape and ±100µm size, drug-loaded functionalized NLPs were also spherically and uniform in shape post embedment into depot CEP scaffold and PC12 neuronal cells proliferation within the surface of the BICD nano-enabled bio-structure. Swelling, erosion dynamics and porosity / diffusion, and particle size may have influence release behaviours of the drug-loaded functionalized NLPs post embedded into depot CEP scaffold of the BICD. High accumulation of GAL (about 50-90%) in a pellet validated that release drug-loaded functionalized NLPs post escape BICD was still at its intact form in simulated PBS environment over 50 days. The Lactate Dehydrogenase (LDH) level which is associated with cell membrane damage/injury post induced by drug-loaded functionalized NLPs, CEP scaffold and BICD were ±15%, ±30% and ±32%, respectively, this data demonstrated that there were no significant effects over 28 days when compared with untreated PC12 neuronal cells. High accumulation of the GAL and FITC intracellular validated that synthetic peptide potency for target delivery of the drug-loaded functionalized NLPs post escape BICD *ex vivo*.

Keywords: Alzheimer's disease (AD); drug-loaded functionalized nanoliposomes; scaffold; Bio-Robotic Intracranial Device (BICD); prolong release

Appendix B: Conference abstracts presented

1: Medical Research Council (MRC) of South Africa, Early Career Scientist Convention, Parow, Medical Campus, Cape Town, October 23, 2014.

An Implantable Composite Intracranial Device for Prolong Delivery of Liposomal Nanomedicine into the Brain

¹Maluta S. Mufamadi, ¹Yahya E. Choonara, ²Girish Modi, ³Dinesh Naidoo, ¹Lisa C. du Toit, ⁴Sunny Iyuke and ¹Viness Pillay

¹University of the Witwatersrand, Faculty of Health Sciences, Department of Pharmacy and Pharmacology, Parktown, 2193, Johannesburg, South Africa

²University of the Witwatersrand, Faculty of Health Sciences, Department of Neurology, Parktown, 2193, Johannesburg, South Africa.

³University of the Witwatersrand, Faculty of Health Sciences, Department of Neurosurgery, Parktown, 2193, Johannesburg, South Africa.

⁴University of the Witwatersrand, School of Chemical and Metallurgical Engineering, Private Bag 3, Wits 2050, Johannesburg, South Africa

*Correspondence: viness.pillay@wits.ac.za

OBJECTIVE

To design an implantable nano-enabled composite intracranial device (CID) that is capable of rendering optimized neuroprotectant delivery into a specific site in the brain in response to Alzheimer's disease (AD).

METHODS

The CID was formulated by embedding pre-formed drug (galantamine)-loaded functionalized-nanoliposomes (NLPs) within the polymeric scaffold. The functionalized-NLPs were formulated employing synthetic phospholipids (DSPC, cholesterol and DSPE-mPEG2000) thereafter surface engineered with synthetic peptide. The polymeric scaffold were formulated by cross-linked network of chitosan, Eudragit®-RSPO, and poly (vinyl alcohol) (PVA) followed by lyophilisation. Physicochemical dynamics were analysed by Electron Microscopy (EM), and Dynamic Light Scattering (DLS). Prolonged drug-loaded functionalized-NLPs release from CID were performed using an orbital shaker-bath over 50 days, drug quantity was analysed via UV. PC12 neuronal cells-uptake and lactate dehydrogenase (LDH) level post cells seeding on the device were validated by EM, confocal microscopy and Victor™X3 plate reader.

RESULTS

The produced drug-loaded functionalized-NLPs were spherical in shape with a nanometer size ranging from 100-158nm, a zeta potential of -18 mV to -36mV. Dissolution data revealed drug release from CID at a ranged between 50-90% over 50 days. The swelling or/and erosion dynamics and porosity and particle size may have influenced prolong diffusion release behaviours of the drug-loaded functionalized-NLPs post embedded into CID. Cellular studies confirmed that functionalized-NLPs facilitated the drug-uptake into PC12 neuronal cells via serpin enzyme complex receptor. The study also showed no significant effect on LDH level which is associated with cell membrane damage ranged between 15-32% post induced by CID when compared with untreated PC12 neuronal cells.

CONCLUSION

The results obtained in this study elucidated that CID may provide an improvement to existing brain drug delivery systems and may render satisfactory management of AD in terms of therapeutic efficacy, long-term pharmaceutical stability, targeted drug delivery and less frequent drug dosing intervals.

2: Medical Research Council (MRC) of South Africa, Early Career Scientist Convention, Parow, Medical Campus, Cape Town, October 16, 2013.

Bio-Architecture of an Implantable Nano-Enabled Bio-Robotic Intracranial Device for Optimized CNS Drug Delivery

Maluta S. Mufamadi¹, Yahya E. Choonara¹, Lisa C. du Toit¹, Girish Modi², Dinesh Naidoo³, Pradeep Kumar¹, Valence M.K. Ndesendo¹, Sunny E. Iyuke⁵ and Viness Pillay^{1*}

¹University of the Witwatersrand, Faculty of Health Sciences, Department of Pharmacy and Pharmacology, Parktown, 2193, Johannesburg, South Africa

²University of the Witwatersrand, Faculty of Health Sciences, Department of Neurology, Parktown, 2193, Johannesburg, South Africa.

³University of the Witwatersrand, Faculty of Health Sciences, Department of Neurosurgery, Parktown, 2193, Johannesburg, South Africa.

⁴St John's University of Tanzania, School of Pharmacy and Pharmaceutical Sciences, Dodoma, Tanzania

⁵University of the Witwatersrand, School of Chemical and Metallurgical Engineering, Private Bag 3, Wits 2050, Johannesburg, South Africa

*Correspondence: viness.pillay@wits.ac.za

Purpose: To design an implantable nano-enabled bio-robotic intracranial device that is capable of rendering optimized neuroprotectant delivery into the brain in response to Alzheimer's disease (AD).

Method: *Fabrication of the multicomponent Bio-Robotic Intracranial Device (BICD).* The BICD was formulated by embedding pre-formed drug-loaded functionalized-nanoliposomes within the "intelligent" polymeric scaffold. The functionalized-nanoliposomes were formulated employing synthetic phospholipids (DSPC, cholesterol and DSPE-mPEG2000) thereafter surface engineered with synthetic peptides. The "intelligent" polymeric scaffold were formulated by crosslinked network of chitosan, Eudragit®-RSPO, and poly(vinyl alcohol) (PVA) followed by lyophilization. Physicochemical dynamics were analyzed by FTIR, TEM, and Dynamic Light Scattering (DLS). Drug release from drug-loaded functionalized-nanoliposomes and prolonged drug-loaded functionalized-nanoliposomes release from BICD were performed using an orbital shaker-bath over 48hrs and 50 days respectively and analyzed via UV (λ_{max} = 288nm). PC12 neuronal cells-uptake and neuro-cytotoxicity post cells seeding on the device were validated by SEM, confocal microscope and Victor™X3 plate reader.

Results: The produced drug-loaded functionalized-nanoliposomes were spherical in shape with a nanometer size ranging from 118-165nm, a zeta potential of -18 mV to -36mV, coupling efficiency (CE) ranged between from 40-79% and a drug entrapment efficiency (DEE) ranged between from 42-74%. Dissolution data revealed drug release from drug-loaded functionalized-nanoliposomes at a ranged between 30-80% and drug-loaded functionalized-nanoliposomes release from BICD at a ranged between 60-100% over 48hrs and 50 days respectively. Cellular studies revealed no significant neuro-cytotoxicity and confirmed that functionalized-nanoliposomes facilitated the drug-uptake into PC12 neuronal cells via serpin enzyme complex receptor (SEC-R).

Conclusion: The results obtained in this study elucidated that BICD was suitable for application as a brain implant with potential for prolonged delivery of neuroprotectant-nanocarriers in response to AD.

2: Novartis Next Generation Scientist Research Day, D&I Development and NIBR, Basel, Switzerland, August 27, 2013.

Microfluidic Technology for Manufacturing of Stealth Liposomal Nanomedicine

Maluta Steven Mufamadi^{1,2}, Kewei Yang², Roman Ott², Andreas Fisch², Bernd Riebesehl², Harry Tiemessen²
¹WITS Advanced Drug Delivery Platform, University of the Witwatersrand, South Africa, ²PDU Parenteral and Topical, Nanomedicine Technology Platform, Technical R&D, Novartis Pharma AG, Basel.

Introduction

Liposomes are spherical vesicles composed of one or multiple phospholipid (PL) bilayers with an internal aqueous phase. (Fig. 1) Liposomes can entrap hydrophilic drugs in their internal aqueous compartment or lipophilic drugs within the lipid bilayer. Anti-tumor compounds can be delivered to solid tumors based on enhanced permeation and retention effect (EPR effect) by so-called "Stealth" gel-state liposomes, characterized by small size and composed of high melting PLs and PEGylated PLs. The purpose of this study is to employ a novel continuous-flow microfluidics technology to assess the manufacturability of nano-sized stealth gel-state liposomes while encapsulating model compounds. The aim is to achieve liposomes smaller than 100nm with a narrow size distribution (PDI, polydispersity index, smaller than 0.2).

Methods

Microfluidic manufacture

The microfluidic system is illustrated in Fig. 1.

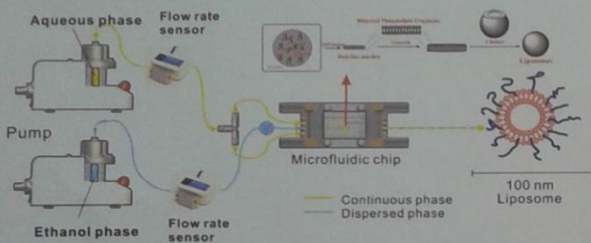


Figure 1. Schematic illustration of continuously manufacturing self assembly stealth liposomes using microfluidic technique.

Phospholipids are dissolved in ethanol phase, which is injected in the center channel, while aqueous phase is injected into two side channels. When ethanol diffuses into aqueous phase, the phospholipids self-assemble lipid bilayer fragments which then close to form liposomes.

Different process/formulation parameters were systematically investigated, including comparison of microfluidic chips, flow rate ratio (FRR), total flow rate (TFR), lipids concentrations, aiming to optimize the process for high yield production of high quality nano-sized liposomes. Furthermore, fluorescent dyes were encapsulated into liposomes to mimic the drug-loaded liposomes, i.e. lipophilic indocyanine green (ICG) and hydrophilic methylene blue (MB). Diameter and PDI are measured by dynamic light scattering.

Results

1. Comparison of microfluidic chips

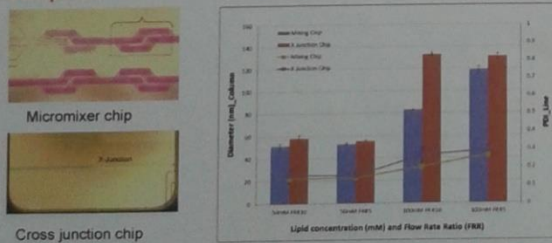


Figure 2. Comparison of microfluidic chips at different flow rate ratios (2 ml/min PBS and 0.2 ml/min lipid ethanol or 0.4 ml/min): Micromixer chip generates smaller liposomes with narrower size distribution compared to cross junction chip, and therefore is selected for all further experiments

2. Effect of flow rate ratio on liposomes size and PDI (FRR=Aqueous/Ethanol flow)

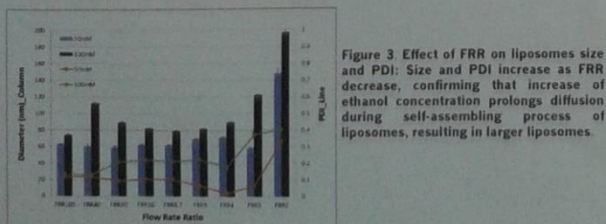


Figure 3 Effect of FRR on liposomes size and PDI: Size and PDI increase as FRR decrease, confirming that increase of ethanol concentration prolongs diffusion during self-assembling process of liposomes, resulting in larger liposomes.

3. Effect of total flow rate on liposomes size and PDI

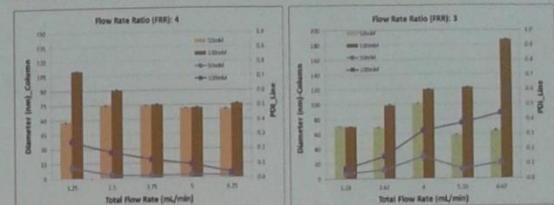


Figure 4. Effect of the total flow rate (TFR) on the size and PDI of the liposomes. At FRR4, small liposomes were attained even at highest total flow rate, demonstrating potential of high yield production; b) using FRR3, TFR showed no significant impact on the size of low concentration liposomes; while size of high concentration liposomes increased as TFR increased.

4. Effect of lipid concentration on liposomes size and PDI

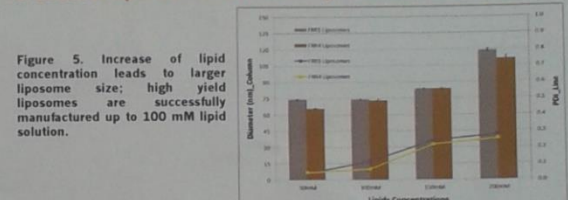


Figure 5. Increase of lipid concentration leads to larger liposome size; high yield liposomes are successfully manufactured up to 100 mM lipid solution.

5. Liposomes loaded with lipophilic or hydrophilic dye

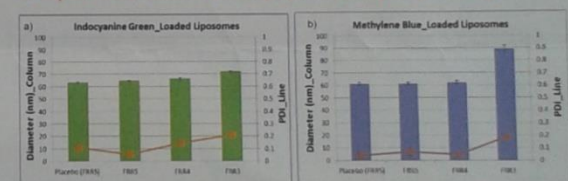


Figure 6. Encapsulation of lipophilic ICG dye in liposomal bilayer or hydrophilic Methylene blue (MB) in the aqueous phase showed no significant effect on liposomes size using FRR5

Conclusions

- *When producing liposomes by microfluidics technology, particle size and distribution can be controlled by flow rate ratio, total flow rate and lipids concentrations.
- *Using an optimized process, a liposome dispersion with high lipid load (20mM), a narrow size distribution, and a diameter of 70-80 nm can be produced at a rate of 6.25 ml/min. This means that one chip can produce 9L per day in a continuous, well controlled process.
- *Successful encapsulation of methylene blue and ICG dyes in liposomes indicates that this technique is promising for manufacturing liposome loaded with either lipophilic or hydrophilic compounds.
- *In general, the microfluidic technology is well suited for high yield continuously manufacturing liposomal nano-medicine in a well-controlled way.

Impact in Home Country

- The WITS Advanced Drug Delivery Platform (WADDP) and University of the Witwatersrand could implement this cutting edge technology and skills acquired for further manufacturing of nano-medicines.
- This opportunity endorses exchange of scientific knowledge and collaborations with TRD researchers at Novartis Pharma AG, Basel and WITS University of the Witwatersrand.

Reference

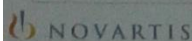
1. Allen, TM, Cullis, PR. Liposomal drug delivery systems: From concept to clinical applications. Adv Drug Deliv Rev. 2013. 65(1): 36-48.
2. Zook, JM, Vreeland, WN. Effects of temperature, acyl chain length, and flow-rate ratio on liposome formation and size in a microfluidic hydrodynamic focusing device. Soft Matter, 2010, 6, 1352-1360.
3. van Swaay, D, deMello, A. Microfluidic methods for forming liposomes. Lab Chip, 2013, 13, 752-767.

Note: The microfluidic system in Fig. 1 and Microfluidic chips in Fig.2 are cited from website of Dolomite Centre Ltd with their permission.

Acknowledgements

We want to acknowledge and thank the members of D&I office in Development, and the E, D&I Office in NIBR, Basel, Switzerland.

Copyright © 2013 Novartis Pharma AG. All rights reserved. Poster presented at the D&I Novartis Research Day, August 27th, 2013, Basel, Switzerland



3: 16th Congress of the European Federation of Neurological Societies (EFNS), Ageing and Dementia, Stockholm, Sweden, Europe, September 08 - 11, 2012.

Exploration of a Composite Nano-Medical Device for the Delivery of Neuroprotectant-Nanocarriers into Targeted Neuronal Cells of Alzheimer's Disease

Maluta S. Mufamadi¹, Yahya E. Choonara¹, Lisa C. du Toit¹, Girish Modi², Dinesh Naidoo³, Pradeep Kumar¹, Valence M.K. Ndesendo¹, Leith C.R Meyer⁴ Sunny E. Iyuke⁵ and Viness Pillay^{1*}

¹University of the Witwatersrand, Faculty of Health Sciences, Department of Pharmacy and Pharmacology, Parktown, 2193, Johannesburg, South Africa

²University of the Witwatersrand, Faculty of Health Sciences, Department of Neurology, Parktown, 2193, Johannesburg, South Africa.

³University of the Witwatersrand, Faculty of Health Sciences, Department of Neurosurgery, Parktown, 2193, Johannesburg, South Africa.

⁴University of the Witwatersrand, Faculty of Health Sciences, Central Animal Services, Parktown, 2193, Johannesburg, South Africa

⁵University of the Witwatersrand, School of Chemical and Metallurgical Engineering, Private Bag 3, Wits 2050, Johannesburg, South Africa

*Correspondence: viness.pillay@wits.ac.za

Purpose: The purpose of this study was to explore an implantable composite nano-medical device that is capable of prolonged delivery of the neuroprotectant-nanocarrier into targeted neuronal cells of Alzheimer's disease (AD).

Method: The device was fabricated by embedding galantamine-loaded/florescein-isothiocyanate (FITC)-labelled functionalized nanoliposomes [f(x)NLPs] [phosphocholine(DSPC), cholesterol, ethanolamine (DSPEmPEG2000)] with synthetic peptide [KVLFLS, KVLFLT and KVLFLM] within a neuro-compliant scaffold (glutaraldehyde crosslinked chitosan, Eudragit®-RSPO, and polyvinylalcohol or polyethyleneoxide) followed by freeze-drying. Drug release from drug-loaded f(x)NLPs was performed using an orbital shaker-bath (50days) and at predetermined time intervals samples were drawn and analyzed via UV ($\lambda_{max}=288nm$). PC12-cells were seeded on the device, ensued by air-drying/freeze-drying. Cells on the device were examined under SEM and stereomicroscopy. LDH release and antiproliferation were assayed using the CytoTox-96® Non-Radioactive and CytoTox-Glu® Cytotoxicity assays, respectively, thereafter Lactate Dehydrogenase (LDH)/dead cells was quantified employing plate reader. At pre-determined time intervals cell uptake was analyzed for 30 days employing plate reader and CLSM.

Results: In vitro study demonstrated that prolonged release of f(x)NLPs (60-100%) from the device over a period of 50 days. SEM and stereomicroscope results demonstrated that the device was suitable for neuronal cell attachment and proliferation. Ex vivo results exhibit less than 30% LDH release which validate that the designed device did not significantly induce cell injury. CSLM and plate-reader studies revealed that f(x) NLPs facilitated the drug uptake into PC12-cells via LDL receptor family.

Conclusions: The results revealed that the designed device had superior cytocompatibility and was suitable to fulfill prolonged delivery of neuroprotectants-nanocarrier into targeted neuronal cells of AD.

4: 16th Congress of the European Federation of Neurological Societies (EFNS), Ageing and Dementia, Stockholm, Sweden, Europe, September 08 - 11, 2012.

Physicomechanical Transitions of an Implantable Nano-Enabled Biorobotic Intracranial Device for Alzheimer's Disease Management for Validation of *in Vivo* Behaviour in a Simulated Brain Environment

Maluta S. Mufamadi¹, Yahya E. Choonara¹, Lisa C. du Toit¹, Girish Modi², Dinesh Naidoo³, Pradeep Kumar¹, Valence M.K. Ndesendo¹, Leith C.R Meyer⁴ Sunny E. Iyuke⁵ and Viness Pillay^{1*}

¹University of the Witwatersrand, Faculty of Health Sciences, Department of Pharmacy and Pharmacology, Parktown, 2193, Johannesburg, South Africa

²University of the Witwatersrand, Faculty of Health Sciences, Department of Neurology, Parktown, 2193, Johannesburg, South Africa.

³University of the Witwatersrand, Faculty of Health Sciences, Department of Neurosurgery, Parktown, 2193, Johannesburg, South Africa.

⁴University of the Witwatersrand, Faculty of Health Sciences, Central Animal Services, Parktown, 2193, Johannesburg, South Africa

⁵University of the Witwatersrand, School of Chemical and Metallurgical Engineering, Private Bag 3, Wits 2050, Johannesburg, South Africa

*Correspondence: viness.pillay@wits.ac.za

Purpose: The purpose of this study was to evaluate the physicomechanical transitions of an implantable nanoenabled Biorobotic Intracranial Device (BICD) within simulated brain environment.

Methods: The BICD was fabricated by embedding galantamine-loaded functionalized nanoliposomes [f(x) NLPs] [Phosphocholine (DSPC), cholesterol, ethanolamine (DSPE-mPEG2000) with synthetic peptides] within a neuro-compliant scaffold [glutaraldehyde crosslinked chitosan, eudragit RSPO, and polyvinyl alcohol or polyethyleneoxide] followed by freeze-drying. Rheological, textual and SEM studies were employed to characterize the BICD behaviour *in vitro*. Hydration and degradation studies were conducted within artificial cerebrospinal fluid (aFCS). Images were acquired using a bench-top MRI over a period of 50 days. Labelled-f(x) NLPs distribution within the BICD was examined by micro-ultrasound imaging (Vevo@2100) and CLSM.

Results: SEM images validated the porous surface morphology of the scaffold, with pores that are relatively uniform in size and shape. Rheological and textural parameters demonstrated that the crosslinked scaffold was more firm and resilient when compared with the noncrosslinked scaffold. MRI images showed complete scaffold hydrated within 30min after submergence within aFCS, however the hydrated scaffold exhibited swelling and slight erosion. CLSM micrographs confirmed labelled f(x)NLPs encapsulation and distribution within the BICD. Fluorescence patterns postulate intact vesicles after BICD lyophilization. Ultrasound images confirmed that more even f(x)NLPs distribution was achieved in the slightly less viscous rather than highly viscous BICD.

Conclusions: The results validate that evaluation of BICD physicomechanical transitions is a useful tool for further investigation of the optimized formulation designed for prolonged delivery of the neuroprotectant-nanocarrier into targeted neuronal cells of Alzheimer's disease.

5: 16th Congress of the European Federation of Neurological Societies (EFNS), Neurotoxicology/Occupational Neurology, Stockholm, Sweden, Europe, September 08 - 11, 2012.

Design, Biomolecular Modelling and Evaluation of Surface-Engineered Nanoliposomes for the Management of Alzheimer's disease

Maluta S. Mufamadi¹, Yahya E. Choonara¹, Lisa C. du Toit¹, Girish Modi², Dinesh Naidoo³, Pradeep Kumar¹, Valence M.K. Ndesendo¹, Leith C.R Meyer⁴ Sunny E. Iyuke⁵ and Viness Pillay^{1*}

¹University of the Witwatersrand, Faculty of Health Sciences, Department of Pharmacy and Pharmacology, Parktown, 2193, Johannesburg, South Africa

²University of the Witwatersrand, Faculty of Health Sciences, Department of Neurology, Parktown, 2193, Johannesburg, South Africa.

³University of the Witwatersrand, Faculty of Health Sciences, Department of Neurosurgery, Parktown, 2193, Johannesburg, South Africa.

⁴University of the Witwatersrand, Faculty of Health Sciences, Central Animal Services, Parktown, 2193, Johannesburg, South Africa

⁵University of the Witwatersrand, School of Chemical and Metallurgical Engineering, Private Bag 3, Wits 2050, Johannesburg, South Africa

*Correspondence: viness.pillay@wits.ac.za

Purpose: The purpose of this study was the design, modelling and evaluation of the surface engineered nanoliposomes (NLPs) coupled with chelating ligands [Zinc acetate (ZnAc), Histidine (His) and Ethylenediaminetetraacetic acid (EDTA)] for neuronal cell protections against A β aggregates.

Methods: NLPs were fabricated from distearylphosphatidylcholine (DSPC), Cholesterol (Chol), and distearylphosphatidylethanolamine (DSPE-mPEG2000) using the reverse phase evaporation technique. Chelating ligands were surface engineered onto the surface NLPs. Biomolecular modelling analysis was used as predictive approach in the design of surface-engineered NLPs to investigate the interaction of metal ions [Cu(II) and Zn(II)] with A β (1-42) peptide resulting in CuA β (1-42) or ZnA β (1-42) aggregates, and the effect of surface-modified NLPs in preventing A β aggregates. Cyto(neuro)toxicity studies were performed on the surface-modified NLPs in order to assess the effect on neuronal cell proliferation. Dead cells were assayed using CytoTox-Glo™ Cytotoxicity kit and counted employing a plate reader. The interaction of DSPC, Chol and DSPE-mPEG2000 during NLPs formulation and engineering of chelating ligands on the surface of NLPs was validated by Fourier Transmission Infrared (FITR) and Scanning Electron Microscopy (SEM).

Results: Analytical-mathematical and geometrical configuration validated the interaction energy during protein/metal or metal/chelating ligands complexation. Ex vivo studies showed about 30-40% cell viability after exposure to CuA β (1-42)/ ZnA β (1-42) aggregates. Furthermore, about 60-80% cell viability was shown after treatment with surface-modified NLPs with ZnAc, histidine and EDTA

Conclusions: The in vitro and ex vivo experimental studies were well corroborated by the in silico molecular mechanistic studies, thus further confirming the potential of NLP/chelation therapy for Alzheimer's disease intervention.

6: Wits Faculty of Health Sciences Research Day & Postgraduate Expo 2012. Wits Medical School, Parktown, JHB, South African. September 19, 2012.

Bio-Architecture of an Implantable Nano-Enabled Bio-Robotic Intracranial Device for Optimized CNS Drug Delivery

Maluta S. Mufamadi¹, Yahya E. Choonara¹, Lisa C. du Toit¹, Girish Modi², Dinesh Naidoo³, Pradeep Kumar¹, Valence M.K. Ndesendo¹, Sunny E. Iyuke⁵ and Viness Pillay^{1*}

¹University of the Witwatersrand, Faculty of Health Sciences, Department of Pharmacy and Pharmacology, Parktown, 2193, Johannesburg, South Africa

²University of the Witwatersrand, Faculty of Health Sciences, Department of Neurology, Parktown, 2193, Johannesburg, South Africa.

³University of the Witwatersrand, Faculty of Health Sciences, Department of Neurosurgery, Parktown, 2193, Johannesburg, South Africa.

⁴St John's University of Tanzania, School of Pharmacy and Pharmaceutical Sciences, Dodoma, Tanzania

⁵University of the Witwatersrand, School of Chemical and Metallurgical Engineering, Private Bag 3, Wits 2050, Johannesburg, South Africa

*Correspondence: viness.pillay@wits.ac.za

Purpose: To design an implantable nano-enabled bio-robotic intracranial device that is capable of rendering optimized neuroprotectant delivery into the brain in response to Alzheimer's disease (AD).

Method: *Fabrication of the multicomponent Bio-Robotic Intracranial Device (BICD).* The BICD was formulated by embedding pre-formed drug-loaded functionalized-nanoliposomes within the "intelligent" polymeric scaffold. The functionalized-nanoliposomes were formulated employing synthetic phospholipids (DSPC, cholesterol and DSPE-mPEG2000) thereafter surface engineered with synthetic peptides. The "intelligent" polymeric scaffold were formulated by crosslinked network of chitosan, Eudragit®-RSPO, and poly(vinyl alcohol) (PVA) followed by lyophilization. Physicochemical dynamics were analyzed by FTIR, TEM, and Dynamic Light Scattering (DLS). Drug release from drug-loaded functionalized-nanoliposomes and prolonged drug-loaded functionalized-nanoliposomes release from BICD were performed using an orbital shaker-bath over 48hrs and 50days respectively and analyzed via UV (λ_{max} = 288nm). PC12 neuronal cells-uptake and neuro-cytotoxicity post cells seeding on the device were validated by SEM, confocal microscope and Victor™X3 plate reader.

Results: The produced drug-loaded functionalized-nanoliposomes were spherical in shape with a nanometer size ranging from 118-165nm, a zeta potential of -18 mV to -36mV, coupling efficiency (CE) ranged between from 40-79% and a drug entrapment efficiency (DEE) ranged between from 42-74%. Dissolution data revealed drug release from drug-loaded functionalized-nanoliposomes at a ranged between 30-80% and drug-loaded functionalized-nanoliposomes release from BICD at a ranged between 60-100% over 48hrs and 50 days respectively. Cellular studies revealed no significant neuro-cytotoxicity and confirmed that functionalized-nanoliposomes facilitated the drug-uptake into PC12 neuronal cells via serpin enzyme complex receptor (SEC-R).

Conclusion: The results obtained in this study elucidated that BICD was suitable for application as a brain implant with potential for prolonged delivery of neuroprotectant-nanocarriers in response to AD.

7: Annual Meeting of the American Association of Pharmaceutical Scientists (AAPS), Washington DC, United States of America, October 23-27, 2011.

Elucidation of the cytotoxicity and intracellular uptake of surface modified nanoliposomes by chelating ligands

M. Mufamadi, V. Pillay, Y. Choonara, L. Du Toit, G. Modi, D. Naidoo, L. Meyer, S. Lyuke
Witwatersrand University

Purpose.

The purpose of this study was to assess the cytotoxicity and intracellular uptake of nanoliposomes surface modified by chelating ligands

Methods.

Preparation of the nanoliposomes

Nanoliposomes (NLPs) formulated with DSPC, cholesterol and DSPE-mPEG2000 using an adapted reverse phase evaporation technique. Nanoliposomes were surface modified with EDTA, L-Histidine and Zinc acetate (ZnAc).

Cytotoxicity assay of surface modified NLPs against PC12 cells

Cytotoxicity study of PC12 cells treated with modified NLPs was determined at 0, 12 and 24 hour intervals using a CytoTox-Glo™ Cytotoxicity Assay. Dead and live cell signals were measured by luminometer Victor™X3 Perkin Elmer 2030.

Intracellular uptake of surface modified NLPs

Intracellular uptake of the labeled-modified NLPs and control labeled-unmodified NLPs were performed in presence of zinc (Zn) or copper (Cu) ions. At 0, 6, 12, 18 and 24 hours interval cells were examined with a confocal scanning electron microscopy or quantified by flourometer Victor™X3 Perkin Elmer 2030.

Results.

The particle sizes of modified NLPs with chelating ligands were in a range of 125-175nm, polydispersity index (Pdi) 0.217-0.920 and zeta potential of -9.59 to -37.3mV. Cytotoxicity studies of the surface modified NLPs by chelating ligands did not show any significant effect against PC12 cells. FITC-labeled or rhodamine-labeled NLPs and surface modified NLPs were examined for their influence on intracellular uptake in the presence of transitions metal ion (Zn and Cu ions). The results validated that high intracellular uptake of the labeled modified NLPs (with ZnAc, Histidine and EDTA) when compared with labeled-unmodified NLPs

Conclusion.

High fluorescence intensity of the labeled surface modified NLPs by chelating ligands in the presence of biological metal ions were influence by ionophore process which mediates transport of metal ions into cells

8: Annual Meeting of the American Association of Pharmaceutical Scientists (AAPS), Washington DC, United States of America, October 23-27, 2011.

Surface-modified nanoliposomes by chelating ligands to modulate neurotoxicity associated with β -amyloid aggregation in Alzheimer disease

M. Mufamadi¹, V. Pillay¹, Y. Choonara², L. Du Toit², G. Modi², D. Naidoo², L. Meyer², S. Lyuke²

¹ University of the Witwatersrand, ² Witwatersrand University

Purpose.

The purpose of this study was to provide an ingenious solution to the neurotoxicity persuaded by $A\beta(1-42)$ aggregates using nanoliposomes (NLPs) surface-modified with chelating ligands such as zinc acetate (ZnAc), histidine, and ethylenediaminetetraacetic acid (EDTA).

Methods.

Preparation of the nanoliposomes

Nanoliposomes (NLPs) formulated with DSPC, cholesterol and DSPE-mPEG2000 using an adapted reverse phase evaporation technique. Chelating ligands were coupled within the surface NLPs consist of DSPE-mPEG-COOH conjugate.

Determination of size distribution and zeta potential

Determination of average particle size and zeta potential of modified nanoliposomes were analyzed by a Zetasizer NanoZS instrument.

In vitro $A\beta$ aggregation

$A\beta$ aggregation was induced by reacting 5mM of $A\beta(1-42)$ with 20mM of copper chloride ($CuCl_2$) or zinc chloride ($ZnCl_2$) incubation in 20mM Tris/150mM NaCl buffer (pH 7.4) at 37°C. Soluble $A\beta(1-42)$ was quantified by a NanoPhotometer spectrophotometer.

Ex vivo neurotoxicity

Neurotoxicity was established by exposing neuronal cell line (PC12 cells) to $ZnA\beta(1-42)$ or $CuA\beta(1-42)$, thereafter treated with modified NLPs in order to enhance neuronal cells protections. Neurotoxicity for this study was assayed using CytoTox-Glo Cytotoxicity kit. Dead and live cell signals were measured by luminometer Victor X3 Perkin Elmer 2030.

Results.

The results showed that NLPs produced have a nanometer size range 125-178nm and zeta potential range -35 to -37mV. *In vitro* studies showed that 30-40% soluble $A\beta(1-42)$ attained when $ZnA\beta(1-42)$ or $CuA\beta(1-42)$ formed. However, when modified NLPs were incorporated 70-80% soluble $A\beta(1-42)$ was recovered. *Ex vivo* studies showed about 60-80% cell viability after treatment with modified NLPs.

Conclusion.

High cellular survival postulated to be influenced by post surface-modified NLPs with EDTA, Histidine and ZnAc hampered $ZnA\beta(1-42)$ or $CuA\beta(1-42)$ aggregate formation while promoting high quantity of non-toxic soluble $A\beta(1-42)$.

9: Annual Meeting of the American Association of Pharmaceutical Scientists (AAPS), Washington DC, United States of America, October 23-27, 2011

Fabrication and characterization of an implantable nano-enabled Biorobotic Intracranial Device for enhanced drug delivery into targeted neuronal cells of Alzheimer's disease

M. Mufamadi, V. Pillay, Y. Choonara, L. Du Toit, G. Modi, D. Naidoo, L. Meyer, S. Iyuke
Witwatersrand University

Purpose.

The purpose of this study was to undertake *in vitro* characterization of a nano-enabled Bio-Robotic intracranial Device (BICD) fabricated by embedding FITC-loaded ligand functionalized nanoliposomes (FNLPs) within a depot "intelligent" scaffold

Methods.

Preparation of the functionalized nanoliposomes Nanoliposomes (NLPs) formulated with DSPC, DSPE-mPEG2000 and DSPE-PEG-Mal using an adapted reverse phase evaporation technique in accordance with a Box-Behnken experimental design. The fluorescence-loaded NLPs produced by hydrated dry NLPs with 48mM of FITC. Nanoliposomes were functionalized (FNLPs) with synthetic peptide ligands.

Peptide coupling efficiency (PCE)

FNLPs were treated with 1% Triton X 100 in methanol, absorbance were measured using a NanoPhotometer™ spectrophotometer.

Embedding FITC-loaded FNLPs within depot "intelligent" scaffold

FITC-loaded FNLPs were embedding within "intelligent" scaffold (chitosan, polyvinyl alcohol and eudragit RSPO) fabricated by freeze-drying method in order to generated nano-enabled Biorobotic Intracranial Device (BICD).

Modulating FITC-loaded FNLPs release from BICD

BICD was immersed in 20mL PBS buffer at pH 7.4, and at pre-determined time intervals PBS buffer was refreshed after sampling. Fluorescence activity, zeta-potential and size distribution associated with released FITC-loaded FNLPs release was quantified using Victor™X3 Perkin Elmer 2030 and Zetasizer NanoZS Malvern Instrument.

Results.

FNLPs produced were spherical in shape and PCE value of 78%. The designed "intelligent" scaffold had a surface morphology with pores that were relatively uniform in size ($\pm 10\mu\text{m}$) and shape. Confocal laser scanning microscopic profiles confirmed that FITC-loaded FNLPs were entrapped within the BICD and full preservation of their integrity. Sustained release kinetics of labeled FNLPs from the BICD depended on the BICD porosity and size of the FNLPs.

Conclusion.

In conclusion, we report here the development of a novel BICD with desired FITC-loaded FNLPs within an "intelligent" scaffold structure. BICD showed great potential as a FITC-loaded FNLPs depot and sustained release of FITC over a prolong period of time reaches 30 days in the study.

10: Annual Meeting of the American Association of Pharmaceutical Scientists (AAPS), Washington DC, United States of America, October 23-27, 2011

Development of functionalized nanoliposomes using a Box-Behnken experimental design

M. Mufamadi, V. Pillay, Y. Choonara, L. Du Toit, G. Modi, D. Naidoo, D. Naidoo, L. Meyer, S. Iyuke
Witwatersrand University

Purpose.

The purpose of this study was to design and develop functionalized nanoliposomes with the desired physicochemical properties, drug entrapment efficiency and release kinetics in order to improve drug uptake at a cellular level specifically to neuronal cells in the CNS

Methods.

Preparation of the functionalized nanoliposomes

Nanoliposomes (NLPs) formulated with DSPC, cholesterol, DSPE-mPEG2000 and DSPE-PEG-Mal using an adapted reverse phase evaporation technique in accordance with a Box-Behnken experimental design. Galantamine and FITC were loaded by hydrated liposomes film in 130mM ammonium sulfate. Nanoliposomes were functionalized (FNLPs) with synthetic peptide ligands.

Peptide coupling efficiency (PCE)

To estimate the quantity of synthetic peptide of surface of the FNLPs was performed by NanoPhotometer™ spectrophotometer.

Drug Entrapment Study (DEE)

Entrapment efficiency of broken FNLPs vesicles was determined by UV spectrophotometry method.

Drug Release Study

Galantamine release from FNLPs was measured by UV spectrophotometry.

Ex vivo antiproliferation and intracellular uptake

Antiproliferation and intracellular uptake of FNLPs by PC12 cells were evaluated using confocal microscopy and Victor™X3 Perkin Elmer 2030.

Results.

FNLPs produced were spherical in shape, physically stable (-34mV) and have a desirable nanometer size (129nm). An average DEE value of 79% and PCE value of 78% of galantamine-loaded FNLPs was achieved. Antiproliferative effects of the FNLPs against PC12 cells were synthetic peptide concentration dependent (10mg/mL). Intracellular uptake of FNLPs showed higher levels of fluorescence intensity and high galantamine (80%, 48hours) into targeted PC12 cells associated with Alzheimer's disease (AD).

Conclusion.

The data in this study revealed higher levels of fluorescence intensity and high galantamine activity within neuronal cell membranes to be associated with post-engineered synthetic peptide moieties on the surface of the NLPs.

11: Annual Meeting of the American Association of Pharmaceutical Scientists, Washington DC, United States of America, October 23-27, 2011.

Formulation and physicochemical characterization of surface-modified nanoliposomes by chelating ligands

M. Mufamadi, V. Pillay, Y. Choonara, L. Du Toit, G. Modi, D. Naidoo, L. Meyer, S. Iyuke
Witwatersrand University

Purpose.

The purpose of this study was to formulate and characterized nanoliposomes surface modified with chelating ligands such EDTA, histidine and ZnAc as new strategy to enhance the transport and distribution of chelating ligands into the brain

Methods.

Preparation of the nanoliposomes

Nanoliposomes (NLPs) formulated with DSPC, cholesterol and DSPE-mPEG2000 using an adapted reverse phase evaporation technique. Chelating ligands were coupled within the surface of NLPs consist of DSPE-mPEG-COOH conjugate.

Fourier Transmission Infrared Experiments (FTIR)

FTIR spectrophotometers of the surface modified nanoliposomes were analyzed using a Beckmann Hydraulic Press.

Morphological analysis by transmission electron microscopy (TEM)

TEM of the modified NLPs suspension in BPS buffer at pH7.4 was employed in order to determine the morphology of the modified nanoliposomes.

Surface morphological analysis by scanning electron microscopy (SEM)

SEM of the lyophilized modified NLPs was employed to determine surface morphology

Determination of size distribution and zeta potential

Determination of average particle size and zeta potential of modified nanoliposomes were analyzed by a Zetasizer NanoZS instrument

Results.

FTIR spectra of modified nanoliposomes confirmed an absorption band shift from 1561cm⁻¹ peak position to high frequency 1572cm⁻¹. TEM profiles of the established modified nanoliposomes were uniform in shape. SEM micrographs of the lyophilized modified NLPs showed the rough surface appearance. The average sizes of modified nanoliposomes were at arranged between 100-130nm with a polydispersity index (Pdi) between 0.235-0.445. The zeta potential of modified nanoliposomes ranged between -28.7 to -37.3mV.

Conclusion.

The present study revealed constructed nanoliposomes surface modified with EDTA, histidine and ZnAc was in good physical conditions, of an ideal nanometer size, zeta potential and was suitable for improvement of chelating ligands delivery into the brain.

12: 6th International Conference of South African Pharmaceutical and Pharmacological Sciences Society (ICPPS), ICPPS, University of KZN, South Africa, September 25-27, 2011.

An implantable nano-enabled Biorobotic Intracranial Device for neurotherapeutic applications

Maluta Steven Mufamadi¹, Viness Pillay^{1,*}, Yahya E. Choonara¹, Lisa C. Du Toit¹ Girish Modi²
Dinesh Naidoo² Leith C.R Meyer³ Sunny E. Iyuke⁴

¹ University of the Witwatersrand, Department of Pharmacy and Pharmacology, Johannesburg, South Africa

² University of the Witwatersrand, Department of Neurology, Johannesburg, South Africa.

³ University of the Witwatersrand, Department of Physiology, Brian Function Research Group and Central Animal Services, Parktown, 2193, Johannesburg, South Africa

⁴ University of the Witwatersrand, School of Chemical and Metallurgical Engineering, Private Bag 3, Wits 2050, Johannesburg, South Africa

*Correspondence: viness.pillay@wits.ac.za

Purpose

The purpose of this study was to design a nano-enabled Bio-Robotic intracranial Device (BICD) that is capable of delivering neuroactive drugs to a specific site in the brain in response to Neurodegenerative Disorders (NDs).

Methods

Nanoliposomes (NLPs) formulated with DSPC, cholesterol, DSPE-mPEG2000 and DSPE-PEG-Mal using an adapted reverse phase evaporation technique. Galantamine or FITC-loaded NLPs produced by hydrated NLPs film with 48mM of FITC or 5mg of galantamine in 130mM ammonium sulfate and 4mL PBS buffer (pH4.0 or pH7.4) thereafter functionalized with synthetic peptide ligands. Both NLPs and functionalized NLPs (FNLPs) were undertaken for in-depth physicochemical characterisation. Cytotoxicity and PC12 cell uptake of FNLPs were performed using a confocal laser scanning microscopy (CLSM), Victor™X3 Perkin Elmer 2030. BICD produced by embedding drug-loaded FNLPs within depot “intelligent” scaffold then subjected to lyophilization technique. Control release of drug-loaded FNLPs release from BICD was performed using orbital shaker bath (25rpm, 37°C) and at predetermined time intervals samples were drawn.

Results

Formation of FNLPs were validate by FTIR spectra which showed new absorption bands at in 1590cm⁻¹ and 1155cm⁻¹ associated with amine bond formation during NLP and ligand interactions. The particles size and zeta potential of FNLPs produced were in the range of 110-180nm and -27 to -35mV demonstrating superior stability. The FNLPs produced showed no impact in PC12 cell viability (80% cell viability in 48hours). FNLPs demonstrated improved cell uptake (70-85% FITC uptake within 48hrs) and drug release capacities (60-85% drug uptake within 48hrs) by targeting PC12 cells of Alzheimer’s disease when compared to non-functionalized NLPs (20% drug within 48hrs). Microscopic profiles confirmed that labeled FNLPs (spherical in shape) were entrapped within the BICD. These results demonstrate that control release of FNLPs from the BICD was influenced by the BICD porosity, diffusion and size of the FNLPs.

Conclusion

The fabricated BICD device may provide an improvement to existing drug delivery systems and may render satisfactory management of ND particularly in Alzheimer’s disease in terms of therapeutic efficacy, long-term pharmaceutical stability, targeted drug delivery and less frequent drug dosing intervals.

13: 6th International Conference of South African Pharmaceutical and Pharmacological Sciences Society (ICPPS), ICPPS, University of KZN, South Africa, September 25-27, 2011.

Application of ligand-functionalize nanoliposomes to reduce the neurotoxicity associated with β -amyloid aggregation in Alzheimer's disease

Maluta Steven Mufamadi¹, Viness Pillay^{1,*}, Yahya E. Choonara¹, Lisa C. Du Toit¹ Girish Modi²
Dinesh Naidoo² Leith C.R Meyer³ Sunny E. Iyuke⁴

¹ University of the Witwatersrand, Department of Pharmacy and Pharmacology, Johannesburg, South Africa

² University of the Witwatersrand, Department of Neurology, Johannesburg, South Africa.

³ University of the Witwatersrand, Department of Physiology, Brian Function Research Group and Central Animal Services, Parktown, 2193, Johannesburg, South Africa

⁴ University of the Witwatersrand, School of Chemical and Metallurgical Engineering, Private Bag 3, Wits 2050, Johannesburg, South Africa

*Correspondence: viness.pillay@wits.ac.za

Purpose

The purpose of this study was to provide an ingenious solution to the neurotoxicity persuaded by A β (1-42) aggregates using nanoliposomes (NLPs) surface-modified with chelating ligands such as zinc acetate (ZnAc), histidine, and ethylenediaminetetraacetic acid (EDTA).

Methods

Preparation of the nanoliposomes: Nanoliposomes (NLPs) formulated with DSPC, cholesterol and DSPE-mPEG2000 using an adapted reverse phase evaporation technique. Chelating ligands were coupled within the surface NLPs consist of DSPE-mPEG-COOH conjugate.

Determination of size distribution and zeta potential: Determination of average particle size and zeta potential of modified nanoliposomes were analyzed by a Zetasizer NanoZS instrument.

In vitro A β aggregation: A β aggregation was induced by reacting 5mM of A β (1-42) with 20mM of copper chloride (CuCl₂) or zinc chloride (ZnCl₂) incubation in 20mM Tris/150mM NaCl buffer (pH 7.4) at 37°C. Soluble A β (1-42) was quantified by a NanoPhotometer™ spectrophotometer.

Ex vivo neurotoxicity: Neurotoxicity was established by exposing neuronal cell line (PC12 cells) to ZnA β (1-42) or CuA β (1-42), thereafter treated with modified NLPs in order to enhance neuronal cells protections. Neurotoxicity for this study was assayed using CytoTox-Glo™ Cytotoxicity kit. Dead and live cell signals were measured by luminometer Victor™X3 Perkin Elmer 2030.

Results

The results showed that NLPs produced have a nanometer size range 125-178nm and zeta potential range -35 to -37mV. *In vitro* studies showed that 30-40% soluble A β (1-42) attained when ZnA β (1-42) or CuA β (1-42) formed. However, when modified NLPs were incorporated 70-80% soluble A β (1-42) was recovered. *Ex vivo* studies showed about 60-80% cell viability after treatment with modified NLPs.

Conclusion

High cellular survival postulated to be influenced by post surface-modified NLPs with EDTA, Histidine and ZnAc hampered ZnA β (1-42) or CuA β (1-42) aggregate formation while promoting high quantity of non-toxic soluble A β (1-42).

14. 2nd Annual Alzheimer's One-Day Seminar "Making it real: Living with Alzheimer's" Wednesday 21st September 2011, University of Witwatersrand, Parktown, Johannesburg.

Design of an Implantable Nano-Enabled Bio-Robotic Intracranial Device as a new approach to improve drug delivery for Alzheimer's patients

Maluta Steven. Mufamadi¹, Viness Pillay^{1,*}, Yahya E. Choonara¹, Lisa C. Du Toit¹ Girish Modi² Dinesh Naidoo² Sunny E. Iyuke³

¹ University of the Witwatersrand, Department of Pharmacy and Pharmacology, 7 York Road, Parktown, 2193, Johannesburg, RSA

² University of the Witwatersrand, Department of Neurology, 7 York Road, Parktown, 2193, Johannesburg, RSA

³ University of the Witwatersrand, School of Chemical and Metallurgical Engineering, Private Bag 3, Wits 2050, Johannesburg, RSA

Alzheimer's disease (AD) is the most common disease of the CNS and it is characterized by a progressive decline of mental function, deterioration in visual performance and an inability to function independently. Donepezil, galantamine, and rivastigmine are the most commonly used to treat the memory impairment associated with AD. However, these drugs are associated with the following disadvantages; 1) beneficial only at higher dose, 2) due to the oral administration of drugs there is limited bioavailability, severe gastrointestinal, and cardiovascular which influence majority of AD patients to stop treatment. The purpose of this work is to explore a unique nano-enabled Bio-Robotic intracranial Device (BICD), which is aimed on offering a comprehensive scientific solution associated with setback of current neuropharmaceutical therapies in the management of the AD. *Preparation of drug loaded bio-robotic nanoliposome:* Nanoliposomes (NLPs) was prepared from distearoyl-sn-glycero-phosphatidylcholine (DSPC), Cholesterol, 1,2-distearoyl-sn-glycero-3-phosphatidyl-ethanolamine - methoxypolyethyleneglycol conjugate (DSPE-mPEG 2000) and maleimide-[poly (ethylene glycol)]-1,2-dioleoyl-sn -glycero-3-phosphoethanolamine (DSPE-PEG-Mal) dissolved in an organic solvent phase. Galantamine was loaded by hydrated liposome film in 130mM ammonium sulfate and 4ml PBS buffer pH 4.0 for 30 min at 65°C, then cooling to 4°C, followed by dialyzing against 5% dextrose to remove ammonia and residual unloaded drug, thereafter surface engineered synthetic peptides (Lys-Val-Leu-Phe-Leu-Met, Lys-Val-Leu-Phen-Leu-Thr and Lys-Val-Leu-Phe-Leu-Ser sequences) in the presence of *N*-hydroxysulfosuccinimide and *N,N'*-dicyclohexylcarbodiimide. *Preparation of the device:* Pre-encapsulated drug loaded biorobotic NLPs were first expose to cryoprotectant in PBS buffer pH7.4. Thereafter, incorporated within a neuro-compliant "intelligent" polymeric scaffold prepared by blending chitosan, eudragit RSPO and PVA/PEO in a present of porogen, with agitation which followed by subsequently lyophilized after being frozen 24 hours at -80°C. Physicochemical dynamics and physicomechanical behavior were analyzed for/by FTIR, porosimeter, textural profiling, size, zeta potential, surface morphology, and TMDSC. Coupling, drug entrapment efficiency and *in vitro* drug release were analyzed using UV spectroscopy or nanophotometer. *Ex vivo* labeled biorobotic NLPs cellular uptake and antiproliferative activity were analyzed by Victor™X3, CSEM, and Cellvizio®LAB fluorescence microscope. Results showed that successful development of BICD with highly porous surface morphology (pores were relatively uniform in size and shape). Labeled biorobotic NLPs were shown to be distribution all over the interior of the BICD and the fluorescence patterns postulate that the NLPs were intact vesicle after incorporated within "intelligent" polymeric scaffold. TEM revealed spherical, uniform and galantamine loaded NLPs size of 127 nm (Polydispersity = 0.02), a zeta potential of -33.00mV, synthetic peptide coupling efficiency of 79% and a drug entrapment efficiency of 74% was obtained. TMDSC and FTIR profile confirmed that they were molecular structural changes or stretching which elucidate the formulation of biorobotic NLPs and BICD. High fluorescence intensity was visualized under Cellvizio®LAB fluorescence microscope and drug quantity confirm cellular uptake of biorobotic NLPs by cells associated with AD behavior. Results also confirm a control release of labeled/drug loaded biorobotic NLPs from BICD over prolong a period time. The above results validate that the BICD suitable for improve drug delivery for Alzheimer's patients.

Appendix C: Patent Publication

(12) INTERNATIONAL APPLICATION PUBLISHED UNDER THE PATENT COOPERATION TREATY (PCT)

(19) World Intellectual Property
Organization
International Bureau

(43) International Publication Date
31 May 2012 (31.05.2012)



(10) International Publication Number
WO 2012/070034 A1

(51) International Patent Classification:

A61K 9/26 (2006.01) A61K 9/51 (2006.01)
A61K 38/08 (2006.01) A61P 25/18 (2006.01)
A61P 25/28 (2006.01) B82Y 5/00 (2011.01)
A61K 31/5415 (2006.01)

(21) International Application Number:

PCT/IB2011/055345

(22) International Filing Date:

28 November 2011 (28.11.2011)

(25) Filing Language:

English

(26) Publication Language:

English

(30) Priority Data:

2010/03743 26 November 2010 (26.11.2010) ZA
2010/07276 26 November 2010 (26.11.2010) ZA

(71) Applicant (for all designated States except US): **UNIVERSITY OF THE WITWATERSRAND, JOHANNESBURG** [ZA/ZA]; 1 Jan Smuts Avenue, Braamfontein, 2050 Johannesburg, Gauteng (ZA).

(72) Inventors; and

(75) Inventors/Applicants (for US only): **GOVENDER, Thiresen** [ZA/ZA]; F48 Houghton Village, 6 Boundary Road, Houghton Estate, 2198 Johannesburg, Gauteng (ZA). **PILLAY, Viness** [ZA/ZA]; 91 Water Stone Estate, Benmore Sandton, 2196 Johannesburg, Gauteng (ZA). **CHOONARA, Yahya, Essop** [ZA/ZA]; 125 Robin Avenue, Extension 1 Lenasia, 1820 Johannesburg, Gauteng (ZA). **DU TOIT, Lisa, Claire** [ZA/ZA]; 61 Klinker Avenue, Fleurhof Florida Roodepoort, 1709 Johannesburg,

Gauteng (ZA). **MODI, Girish** [ZA/ZA]; 37 14th Avenue, Houghton, 2198 Johannesburg, Gauteng (ZA). **NAIDOO, Dinesh** [ZA/ZA]; 46 Bristow Street, Florida Park Roodepoort, 1709 Johannesburg, Gauteng (ZA). **MUFAMADI, Maluta, Steven** [ZA/ZA]; 17 Amagubi, Wits Junction, cnr Boundary / Ridge Road Parktown, 2193 Johannesburg, Gauteng (ZA).

(81) Designated States (unless otherwise indicated, for every kind of national protection available): AE, AG, AL, AM, AO, AT, AU, AZ, BA, BB, BG, BH, BR, BW, BY, BZ, CA, CH, CL, CN, CO, CR, CU, CZ, DE, DK, DM, DO, DZ, EC, EE, EG, ES, FI, GB, GD, GE, GH, GM, GT, HN, HR, HU, ID, IL, IN, IS, JP, KE, KG, KM, KN, KP, KR, KZ, LA, LC, LK, LR, LS, LT, LU, LY, MA, MD, ME, MG, MK, MN, MW, MX, MY, MZ, NA, NG, NI, NO, NZ, OM, PE, PG, PH, PL, PT, QA, RO, RS, RU, RW, SC, SD, SE, SG, SK, SL, SM, ST, SV, SY, TH, TJ, TM, TN, TR, TT, TZ, UA, UG, US, UZ, VC, VN, ZA, ZM, ZW.

(84) Designated States (unless otherwise indicated, for every kind of regional protection available): ARIPO (BW, GH, GM, KE, LR, LS, MW, MZ, NA, RW, SD, SL, SZ, TZ, UG, ZM, ZW), Eurasian (AM, AZ, BY, KG, KZ, MD, RU, TJ, TM), European (AL, AT, BE, BG, CH, CY, CZ, DE, DK, EE, ES, FI, FR, GB, GR, HR, HU, IE, IS, IT, LT, LU, LV, MC, MK, MT, NL, NO, PL, PT, RO, RS, SE, SI, SK, SM, TR), OAPI (BF, BJ, CF, CG, CI, CM, GA, GN, GQ, GW, ML, MR, NE, SN, TD, TG).

Published:

— with international search report (Art. 21(3))

Appendix D1: University of the Witwatersrand Animal Ethics Screening Committee (AESC) Clearance Certificates and Ethical Approval

AESC3



STRICTLY CONFIDENTIAL

ANIMAL ETHICS SCREENING COMMITTEE (AESC)

CLEARANCE CERTIFICATE NO. 2011/24/CMS

APPLICANT: Mr MS Mufumadi

SCHOOL: Therapeutic Sciences
DEPARTMENT: Pharmacy
LOCATION: Medical School

PROJECT TITLE: Evaluation of the in vivo performance of an implantable nano-enabled BICD in transgenic AD mouse model

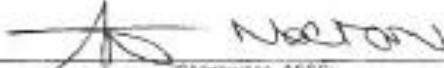
Number and Species

85 Transgenic Alzheimer mice

Approval was given for the use of animals for the project described above at an AESC meeting held on 20110329. This approval remains valid until 20130328.

The use of these animals is subject to AESC guidelines for the use and care of animals, is limited to the procedures described in the application form and to the following additional conditions:

1. A pilot study to be conducted using 2 normal mice in each of the five groups
2. Differing Galantamine doses must be justified
3. Proposals for the management of the breeding colony must be presented
4. Groups 3-5 should comprise 25 mice, not 20

Signed  Date 29/04/2011
(Chairperson, AESC)

I am satisfied that the persons listed in this application are competent to perform the procedures therein, in terms of Section 23 (1) (c) of the Veterinary and Para-Veterinary Professions Act (19 of 1982)

Signed  Date 29/04/2011
(Registered Veterinarian)

cc. Supervisor: Professor V Pillay
Director, CAS

Works 2000\ain2015\AESC\certs\app

Appendix D2: University of the Witwatersrand Animal Ethics Screening Committee (AESC) Clearance Certificates and Ethical Approval: Modifications and Extensions to experiments.

AESC 2012

Please note that only typewritten applications will be accepted. Should additional space be required for section "I" and/or "j", please use the back of this form.

ANIMAL ETHICS SCREENING COMMITTEE

MODIFICATIONS AND EXTENSIONS TO EXPERIMENTS

a. Name: Maluta Steven Mufamadi Department: Pharmacy and Pharmacology

c. Experiment to be extended AESC NO:2011/24/05

Original AESC number	2011	24	05
Other M&E's: No.			

d. Project Title: Evaluation of the *in vivo* performance of an implantable nano-enabled BICD intransgenic AD mouse model

e. Number and species of animals originally approved:	85	Transgenic Mice
f. Number of additional animals previously requested on M&Es:	100	Non-Transgenic Sprague Dawley Rats
g. Total number of animals allocated to the experiment to date:	100	Non-Transgenic Sprague Dawley Rats
h. Number of animals used to date:	0	Non-Transgenic Sprague Dawley Rats
i. Specific modification requested: <p>Change of injections procedure from stereotactically intraventricular injection to intra-cisterna magna (ICM) injection. We would like to change the injection model from stereotactically intraventricular injection to intra-cisterna magna (ICM) injection, for simplicity and that the procedure is standardized at CAS. Dr Lois Harden (Wits University, School of Physiology) recommended trying out this technique, which works very well for her research (Frank et al., 2012). The ICM is less painful and stressful for the animals. Therefore it is a preferred method.</p> <p>ICM Procedure Sprague Dawley rats will briefly anesthetize (as previous/below described). Then, the skull will be shaved and swab with 70% ETOH. A 26 gauge needle attached via PE50 tubing to a 50µl Hamilton syringe will be inserted into the cisterna magna. To verify entry into the cisterna magna, ~2µl of CSF will be collected (Frank et al., 2012). If collected CSF comes out clear of red blood cells this will indicate successful injection into the cisterna magna. B-amyloid peptide (25-35) will be administered in 5µl total volume per animal as previous stated in our M&E. All other procedure will be done as previous laid out in our previous M&E.</p> <p>Reference Frank MG, Barrientos RM, Thompson BM et al. IL-1RA injected intra-cisterna magna confers extended prophylaxis against lipopolysaccharide-induced neuroinflammatory and sickness responses. Journal of Neuroimmunology 2012, 252: 33-39.</p>		

Date: 04/12/2012

RECOMMENDATIONS:

Approved: Change of injection model to ICM.

Signature: 

Date: 7 December 2012

Signature: 
Chairman, AESC

Appendix E: Certificate to confirm that Novartis Next Generation Scientist Program Completion

Certificate

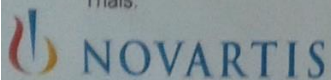
This is to confirm that

Maluta Steven Mufamadi

Has successfully completed:

Next Generation Scientist Program

This 3-month internship forms part of a Novartis program to build the next generation of scientific leaders. Candidates in the program completed a drug discovery or clinical development research project under the mentorship of a Novartis scientist, and presented their research findings as a scientific poster (available on request) during the Novartis Next Generation Scientist Research Day event. Their skills development training included ≥ 70 hours of presentation and communication skills, networking, giving and receiving feedback and scientific event organisation. Each candidate was an active participant in structured, interactive learning sessions on Pharmaceutical Research and Development topics, including: Health System, Ethics, Social Responsibility, Intellectual Property, Drug Targets, Drug Regulation, Technical Drug Development, Safety, Modeling and Simulation and Clinical Trials.



A handwritten signature in black ink, appearing to read "Colin Pillai".

Colin Pillai PhD
Pharma Development
Basel, Switzerland

A handwritten signature in black ink, appearing to read "Brigitta Tadmor".

Brigitta Tadmor PhD
NIBR, Cambridge, USA

August 27, 2013